



INSULATOR CHARGING IN RF MEMS CAPACITIVE SWITCHES

DISSERTATION

Jay F. Kucko, Captain, USAF

AFIT/DS/ENP/05-02

**DEPARTMENT OF THE AIR FORCE
AIR UNIVERSITY**

AIR FORCE INSTITUTE OF TECHNOLOGY

Wright-Patterson Air Force Base, Ohio

APPROVED FOR PUBLIC RELEASE; DISTRIBUTION UNLIMITED

The views expressed in this dissertation are those of the author and do not reflect the official policy or position of the United States Air Force, Department of Defense, or the United States Government.

INSULATOR CHARGING IN RF MEMS CAPACITIVE SWITCHES

DISSERTATION

Presented to the Faculty

Graduate School of Engineering and Management

Air Force Institute of Technology

Air University

Air Education and Training Command

In Partial Fulfillment of the Requirements for the

Degree of Doctor of Philosophy

Jay F. Kucko, BS, MS

Captain, USAF

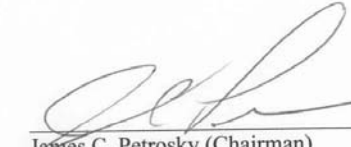
June 2005

APPROVED FOR PUBLIC RELEASE; DISTRIBUTION UNLIMITED

INSULATOR CHARGING IN RF MEMS CAPACITIVE SWITCHES

Jay F. Kucko, BS, MS
Captain, USAF

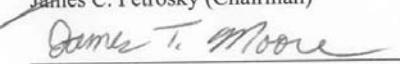
Approved:



James C. Petrosky (Chairman)

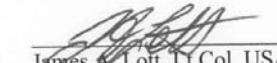
Date

01JUN05



James T. Moore (Dean's Representative)

15 Jun 05



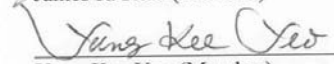
James A. Lott, Lt Col, USAF (Member)

01JUN05



James R. Reid (Member)

21 Mar 05



Yung Kee Yeo (Member)

12 May 05

Accepted:



Robert A. Calico, Jr.

Date

Dean, Graduate School of Engineering and Management

9 Jun '05

Abstract

While capacitive radio frequency microelectromechanical (RF MEM) switches are poised to provide a low cost, low power alternative to current RF switch technologies, there are still reliability issues limiting switch lifetime. Previous research identified insulator charging as a primary cause of switch failure. Changes in switch pull-in and release voltages were measured to provide insight into the mechanisms responsible for charging and switch failure. A spatial and temporal dependent model was developed to describe silicon nitride's time-dependent charging as a function of applied bias. This model was verified by applying constant biases to metal-silicon nitride-silicon capacitors and tracking flatband voltage shifts. This knowledge of silicon nitride was then applied to MEM switches. Using novel waveforms and exploiting differences in actuation characteristics allowed the determination of charging characteristics and the investigation of switch failure. Results show tunneling is responsible for changes in the pull-in voltages - this includes a super-saturation effect explained by a steady-state trap charge and discharge condition. A program that models switch actuation was enhanced to include the time-dependent tunneling model. Finally, it was discovered insulator charging cannot explain permanent switch failure; instead, stiction from a contaminant on the insulator surface is likely the cause.

Acknowledgements

A number of people at AFIT helped me complete this project. First and foremost is my advisor Dr James Petrosky. I could not have completed this project without his guidance throughout the process. His mentorship and friendship are also greatly appreciated. I'd also like to thank the members of my committee, Dr Yeo and Lt Col Lott, for agreeing to serve on the dissertation committee. I am also indebted to Eric Taylor for his technical help and insight throughout the process. Bill Trop and Rick Patton were patient in training and helping me with AFIT clean room equipment.

A number of folks in the AFRL Sensors Directorate contributed to this work. It was Dr Robert Reid of the Antenna Technology Branch initial idea to investigate radiation effects in these RF MEM devices, without this I would not have been able to pursue this fascinating line of research. I also want to thank him for agreeing to participate on the committee and for providing materials and technical assistance throughout the research. I'd also like to thank Dr Jack Ebel and Dr Kevin Leedy of the Aerospace Device and Component Branch for their help in depositing silicon nitride and for general advice and discussions on the RF MEMS capacitive switches. Dr Bill Cowan, currently with Sandia National Lab, was also supportive. He helped me establish initial research contacts and later on he was instrumental in making successful measurements.

I'd like to thank all of the people at AFRL/VSSE at Kirtland AFB that provided assistance. Bill Kemp, Roger Tallon, Richard Marquez, Dan Roley, and Todd Fitt all provided invaluable assistance to me. They understood when things did not always go as planned and always kept me motivated and moving forward. I'd also like to thank the

leadership of VSSE for supporting my work financially. Dr Joe Tringe's support was invaluable. He always willing to help me out, and, after he left VSSE, Dr Kitt Reinhardt and Major Tony Kadrovach continued to support this work. I'd also like to thank Dr Rod Devine for providing me wafers and discussions on radiation effects.

Andrew Kaufmann and Joe Talnagi of the Ohio State University were extremely helpful in planning and executing irradiations at their facility. They were always flexible and willing to help me take the measurements I needed.

Table of Contents

Abstract	iv
Acknowledgements	v
List of Figures	ix
List of Tables	xvi
1. Introduction	1-1
1.1. Microelectromechanical System (MEMS) Devices	1-1
1.2. Motivation	1-3
1.3. Objective, Approach, and Scope	1-4
1.4. Contributions	1-4
1.5. Overview	1-5
Bibliography	1-6
2. Switch Design and Operation	2-1
2.1. Switch Design	2-1
2.2. Switch Operation	2-3
2.3. Reliability Issues	2-10
2.4. Status of Research	2-11
2.5. Switch Operation with Insulator Charge	2-15
Bibliography	2-22
3. Charging Mechanisms	3-1
3.1. Introduction	3-1
3.2. Effect of Trapped Charge on Capacitors	3-1
3.3. Theory of Charging	3-4
3.4. Expectations from Model	3-20
Bibliography	3-27
4. Experimental Setup	4-1
4.1. Introduction	4-1
4.2. MNS Experiment	4-2
4.3. RF MEM Experiment	4-11
4.4. Summary	4-23
Bibliography	4-24
5. Results	5-1
5.1. MNS Capacitor Results	5-1
5.2. MEM Switch Results	5-6
5.3. Conclusion	5-24
Bibliography	5-25

6. Discussion	6-1
6.1. Introduction	6-1
6.2. MNS Capacitors	6-1
6.3. MEM Switches	6-13
Bibliography	6-53
7. Conclusions	7-1
7.1. Summary of Results	7-1
7.2. Summary of Contributions	7-4
7.3. Device Design Implications	7-5
7.4. Suggestions for Future Research	7-7
Bibliography	7-9
Appendix A. Theory of Radiation Effects on MEMS	A-1
A.1. Basics	A-1
A.2. Modeling Radiation Effects in Insulators	A-14
A.3. Radiation Effects on Silicon Nitride	A-17
A.4. Summary of Previous Radiation Experiments	A-23
Bibliography	A-25
Appendix B. Irradiation Experiment and Results	B-1
B.1. MNS	B-1
B.2. MEM	B-9
Bibliography	B-19

List of Figures

Figure

2-1: Schematic cross sectional diagram of MEM switch.....	2-1
2-2: Schematic plan view of switch.....	2-2
2-3: Parallel plate capacitor used to develop a simple model of switch operation	2-3
2-4: Free body diagram of forces on a section of beam.....	2-6
2-5: Calculated beam deflection as a function of applied bias (plotted using Reid's code).....	2-7
2-6: Single bipolar triangle wave.....	2-8
2-7: Calculated capacitance-voltage plot: historical path of switch operation	2-10
2-8: Trapped charge geometry	2-16
2-9: Calculated CV plot with and without trapped charge in insulator: 1) no trapped charge and 2) trapped charge at surface.	2-19
2-10: Calculated CV plot with trapped charge layer in different locations: 1) electrode interface, 2) half way between surface and metal interface, 3) metal interface. Line 3) is identical to having no trapped charge.....	2-20
2-11: Calculated pull-in and release voltages over time assuming a constant charging rate.....	2-21
3-1: Schematic design of arbitrary metal-insulator-conductor structure	3-1
3-2: Calculated high-frequency CV curve for a MIS capacitor.....	3-2
3-3: Band diagram for an arbitrary MIM capacitor with trap.....	3-5
3-4: Band diagram illustrating charging processes.....	3-6
3-5: Band diagram at metal-insulator interface in flat band condition	3-7

3-6: Band diagram at metal-insulator interface under a positive bias applied to opposite contact (not shown)	3-8
3-7: Band diagram illustrating Fowler-Nordheim tunneling mechanism	3-12
3-8: Field enhanced barrier lowering (Poole-Frenkel). Dashed line is conduction band in flat band condition.	3-15
3-9: Band diagram illustrating field ionization mechanism.....	3-16
3-10: Band diagram illustrating the hopping mechanism	3-17
3-11: Calculated local electric field under 0V bias but with holes trapped in insulator. Shaded region represents where trapped charge is located.	3-19
3-12: Calculated MNS charging behavior with negative applied biases. (-10V curve at $\Delta V=0$).....	3-22
3-13: Calculated MNS charging behavior for positive applied voltages.....	3-23
3-14: Effect of trapped charge density on charging behavior.....	3-25
3-15: Effect of trap depth on charging behavior.....	3-26
4-1: Bake results at 100 °C - four capacitors average for 100 kHz CV measurements. Times represent the cumulative number of minutes each capacitor was baked at that temperature.....	4-4
4-2: Bake results at 260 °C - two capacitors average for 100 kHz CV measurements. Times represent the cumulative number of minutes each capacitor was baked at that temperature.....	4-5
4-3: Bake results at 350 °C - two capacitors average for 100 kHz CV measurements. Times represent the cumulative number of minutes each capacitor was baked at that temperature.....	4-6
4-4: Schematic diagram of experimental setup during biasing.....	4-8
4-5: Schematic diagram of experiment during CV sweeps. Notice multiple coax leads at the K-590. This indicates that a CV sweep was taken for each capacitor.....	4-9
4-6: Schematic cross sectional view of an SNC-02 switch (not to scale).....	4-11

4-7: Plan view of SNC-02 capacitive switch. This particular switch design has a number of dimensional variations identified by the identifier (Br<x><y><z>).	4-12
4-8: SNC-02 die layout	4-14
4-9: Electrical measurement setup	4-18
4-10: Two triangle waves with different offset voltage. Notice wave two's peak voltage is larger than wave one's peak voltage. Also, notice the larger difference in time between pull-in (filled dots) and release (open dots). Finally, a portion of wave one has reversed polarity.	4-21
4-11: Modified triangular waveform	4-22
4-12: Single sweep triangular waveform	4-22
5-1: CV measurements on MNS devices taken during +10V biasing	5-2
5-2: Flatband voltage shift measurements based on CV sweeps. No bias applied between CV sweeps – quantifies the charging effects of successive CV sweeps.	5-3
5-3: Summary of MNS capacitor data from 0 to 22150 sec. The remainder of the data shows time dependent discharge at room temperature and no bias applied.	5-4
5-4: Logarithmic plot of flatband voltage shift while bias is applied	5-5
5-5: Waveform used for hold voltage experiment	5-9
5-6: Pull-in voltages shift in for various hold voltages ($t_r=25\text{ms}$, $t_s=25\text{ms}$, $t_h=25\text{ms}$)	5-9
5-7: Release voltage shifts for various hold voltages ($t_r=25\text{ms}$, $t_s=25\text{ms}$, $t_h=25\text{ms}$)	5-12
5-8: Comparison of 40V ΔV_{pi} and ΔV_r curves	5-13
5-9: Variable hold time waveform while maintaining constant frequency	5-14
5-10: Change in pull-in voltage for four hold times – constant 10 Hz frequency	5-15
5-11: Change in release voltage for four different hold/rest time combinations (hold time in parentheses) – 10 Hz frequency remains constant	5-16
5-12: Variable hold time waveform while maintaining constant rest time	5-17

5-13: Change in pull-in voltage for four hold/frequency combinations (hold times in parentheses) – a 25 msec rest time remained constant	5-18
5-14: Change in release voltage for four hold/frequency combinations (hold times in parentheses) – a 25 msec rest time remained constant	5-19
5-15: Comparison of change in pull-in voltages for constant rest and constant frequency.....	5-20
5-16: Single bipolar triangle wave (hatched portion indicates beam is in contact with insulator)	5-21
5-17: Pull-in and release results for positive offset voltage.....	5-22
5-18: Change in pull-in voltages plotted for positive and negative offset voltage cases. The negative offset voltage curve was multiplied by a factor of -1 for a better comparison of the two curves.	5-22
5-19: Change in release voltages plotted for the positive and negative offset voltage cases. The negative offset voltage curve was multiplied by a factor of -1 for a better comparison of the two curves.	5-23
6-1: A comparison of modeled (lines) and experimental (points) results for positive biases applied to MNS capacitors.....	6-5
6-2: Negative applied bias - comparing model to experiment results	6-7
6-3: First trapping region of insulator	6-10
6-4: All three trapping regions of insulator identified	6-11
6-5: Adjusted trap density based on -10V trap energy	6-12
6-6: Band diagram for a) MNS capacitor and b) MEM capacitor with bridge down (units are eV).....	6-14
6-7: Trap energy from MNS experiments placed on MEM band diagram.....	6-16
6-8: Trap energy from MNS experiments placed on MEM band diagram.....	6-17
6-9: Schematic of beam in contact with irregular insulator surface	6-18
6-10: Illustration of insulator 2D finite element array	6-19

6-11: a) Waveform for two cycles – the pull-in and release voltages. b) Simplified switch design corresponding to waveform showing charge becoming trapped while beam is down.	6-21
6-12: Tunneling is responsible for changes in pull-in and release voltages.	6-22
6-13: Modeled data points for five cycles assuming tunneling causes voltage shifts ...	6-24
6-14: Example of pull-in and release shift data	6-26
6-15: Least squares fit of pull-in voltage shifts (solid line is least squares fit with accompanying equation and R^2 value).....	6-27
6-16: Comparison of modeled results (dashed) to experimental results (points)	6-29
6-17: Pull-in voltage shifts for various hold times ($t_{rest}, t_{slope}, t_{hold}$) while frequency is constant plotted on a logarithmic scale.....	6-31
6-18: Comparison of hold time modeled results (solid) to actual results (points).....	6-33
6-19: Sample of super-saturation for a 36V peak voltage	6-35
6-20: Decay of pull-in voltage shift for various hold times.....	6-36
6-21: Pull-in voltage shift decay for various peak voltages.....	6-37
6-22: Illustration of the charging (t_c) and discharging (t_{nc}) portions of each cycle. Early in cycling, charging is much larger than discharge – later in cycling, the amount of charging and discharging that occurs per cycle equilibrates	6-39
6-23: Illustration of the four possible charging cases. 1.) No beam and insulator contact - no charging, 2.) Beam and insulator in constant contact – no equilibrium reached (similar to MNS case), 3.) Adequately large t_c allows equilibrium to be reached, and 4.) smaller t_c requires equilibrium to be reached from a large filled trap density – super-saturation.....	6-40
6-24: Release voltage shift for 36V peak voltage where hold time and rest time are varied to maintain a constant frequency (9 Hz)	6-41
6-25: Peak voltage comparison.....	6-45
6-26: Peak voltage comparison removing contribution of first shift	6-46
6-27: Comparison of various hold times while maintaining a constant frequency.....	6-47

6-28: Comparison of various hold times while maintaining a constant frequency. The contribution of the initial shift is removed.....	6-48
6-29: Comparison of various hold times while maintaining constant rest time	6-49
6-30: Comparison of various hold time while maintaining a constant rest time. The contribution of initial shift is removed.....	6-50
A-1: Schematic shows element 1 not in charged particle equilibrium	A-11
A-2: Absorbed dose through material depth	A-11
A-3: Plot from PHOTCOEF illustrating equilibrium thickness using 1 cm thick silicon exposed to 1 rad(Si) of 1 MeV photons.	A-12
A-4: Plot from PHOTCOEF comparing dose deposition calculations for the ideal, equilibrium assumption, and taking into account non-equilibrium of charged particles. Illustrates dose enhancement in the Au-Si-Au structure.	A-13
A-5: Schematic diagram of biased insulator.....	A-15
A-6: Irradiation calculation process.....	A-18
A-7: Charging behavior with -30V applied	A-21
A-8: Charging behavior with -10V applied	A-22
A-9: Charging behavior with 10V applied.....	A-23
A-10: Rockwell's novel RF MEMS switch design.....	A-24
B-1: Ohio State University's Co-60 gamma irradiator	B-2
B-2: Aluminum test fixture box at top of Co-60 gamma irradiator	B-3
B-3: CV sweeps while capacitor is biased with a +10V and irradiated.....	B-4
B-4: Summary of biasing data for MNS capacitors. From 0 to 1000 krad(SiO ₂) (6 hours, 38 min and 2 seconds) the capacitor is charged. The remainder of plot shows time dependent discharge at room temperature and no bias applied.....	B-5
B-5: Comparison of charging data for unirradiated and irradiated capacitors.....	B-6
B-6: Irradiated MNS flatband voltage shift results for three applied voltages. Points	

represent experimental data; lines are modeled result using various α values ...	B-8
B-7: LEXR facility at AFRL/VS, Kirtland AFB	B-10
B-8: Experimental setup inside LEXR facility	B-11
B-9: Experimental setup required to operate and measure capacitive MEM switches.	B-13
B-10: Change in pull-in voltages for non-irradiated and irradiated switches using the 48Vpp and +5V offset.....	B-14
B-11: Change in release voltages for non-irradiated and irradiated switches using the 48Vpp and +5V offset.....	B-16
B-12: Change in pull-in voltages for unirradiated and irradiated switches using the 48Vpp and -5V offset.....	B-17
B-13: Change in release voltages for unirradiated and irradiated switches using the 48Vpp and -5V offset.....	B-18

List of Tables

Table

1-1: Performance comparison of RF MEM switches to current switch technologies	1-2
5-1: Equations describing the data in Figure 5-4	5-6
6-1: Summary of best fit parameters for positive voltage case.....	6-6
6-2: Summary of best fit parameters for negative voltage case.....	6-7
6-3: Trap density, trap energy, and beginning of trapping	6-12
6-4: Material properties used for modeling peak voltage	6-28
6-5: Material Properties for 50,25,0 hold time case.....	6-32
6-6: Least-squares fits summary for release voltage shift curves in Figure 6-24.....	6-41
A-1: Summary of silicon dioxide parameters	A-19
A-2: Summary of silicon dioxide parameters	A-20

INSULATOR CHARGING IN RF MEMS CAPACITIVE SWITCHES

1. Introduction

1.1. Microelectromechanical System (MEMS) Devices

Government, academia, and industry have all invested a great deal of time, money, and effort into researching and developing MEMS devices. MEMS's utilize the fabrication techniques developed for the semiconductor industry to build miniature mechanical devices actuated by electrostatic and electrothermal forces. Examples of MEMS devices successfully fabricated include pressure and temperature sensors, accelerometers, and gas chromatographs [1].

One area of particular interest in the MEMS community is switching radio frequency (RF) signals. RF MEM devices use electrostatic force to induce mechanical movement in a metal beam. This beam movement induces open and short circuits that can be used in switching microwave or millimeter wave signals [1:2].

Before the advent of RF MEM devices, there were two main device alternatives for RF switching: 1) complementary metal-oxide-silicon (CMOS) field effect transistors (FETs) and 2) PIN diodes. MEM switch performance exceeds that of the devices listed above, with the added benefit of lower power consumption [2]. The main disadvantage of the MEM switch is the high voltage required for switch actuation. Table 1-1 summarizes performance characteristics for RF MEM switches, FETs and PIN diodes.

Table 1-1: Performance comparison of RF MEM switches to current switch technologies [1]

Parameter	RF MEMS	FET	PIN
Voltage (V)	20-80	3-5	3-5
Current (mA)	0	0	3-20
Power Consumption (mW)	0.05-0.1	0.05-0.1	5-100
Capacitance Ratio	40-500	n/a	10
Power Handling (W)	<1	<10	<10
Isolation (1-10 GHz)	Very High	Medium	High
Isolation (10-40 GHz)	Very High	Low	Medium
Isolation (60-100 GHz)	High	None	Medium
Loss (1-100 GHz) (dB)	0.05-0.2	0.4-2.5	0.3-1.2

The device characteristics described above mean the MEM switch lends itself to a wide variety of commercial and defense applications. For example, based on its isolation and insertion loss characteristics, RF MEM devices may provide a low power alternative to current GaAs switches in cellular telephones; lower power consumption means longer battery life. Other applications include tunable circuits and high performance instrumentation systems. Using MEM switches in phase shifters for phased array antennas is of particular interest to the defense community. MEMS based phased arrays will potentially be in future radar and communication systems for ground, airborne, missile and space applications [1:5-7].

In particular, DoD's space based radar could benefit from the use of RF MEM switches. Due to their larger size and weight, current GaAs PIN diode and FET technology in phase shifters do not lend themselves economically to a large scale project such as the space based radar. RF MEM switches may provide the technology necessary to make a space based radar an operational system.

There are two main types of RF MEM switches: contact and capacitive. Contact switches use an electrostatic force to pull a metal beam into direct contact with a metal electrode (transmission line). When the beam and transmission line are in contact, the circuit closes so the RF signal can pass, and the switch becomes a series resistor (0.5-2.0 Ω). Generally, the electrode responsible for pulling the beam down is separate from the transmission line. Therefore, no DC current passes. Capacitive switches also rely on pulling a beam onto an electrode; however, they incorporate an insulating layer between the beam and electrode. In the down state, the beam and electrode are capacitively coupled; therefore, only the RF signal passes. In a circuit, these switches can be placed either in series or in shunt across a transmission line. Contact switches are normally placed in series, while capacitive switches are placed in shunt because it provides better isolation with a smaller impedance ratio than it does in series [3].

1.2. Motivation

While the RF performance of the MEM switch makes it a promising alternative for a wide variety of applications, there are reliability issues preventing immediate use. The main reliability issue for contact switches is damage to the beam and electrode surfaces due to repeated impact. The damage can include pitting and hardening of the metal surfaces. Also, thin dielectric layers can form which increase the series resistance of the switch [1:192].

The main reliability issue for capacitive switches is believed to be trapped charge in the insulator. Trapped charge manifests itself as changes in switch actuation characteristics during operation. For example, the beam may remain stuck in the down position while no electrostatic force is present, the beam may release when a voltage is

applied, or operate with biases that deviate from the design voltages [2:250]. This research focuses specifically on insulator-trapped charge in capacitive switches. The mechanisms responsible for insulator charging are still not completely understood; however, the high electric field required to pull the beam down is capable of causing charge to transport in and out of the insulator. These reliability issues obviously influence any decision to use these switches in space-based systems. Understanding the fundamental physical processes involved in MEM capacitive switch charging will aid in designing reliable, long-lasting devices, capable of operating in the space environment.

1.3. Objective, Approach, and Scope

The objective of this research is to measure and explain insulator charging in RF MEM capacitive switches. This research focuses solely on the capacitive switch; no contact switches are investigated. The MEM capacitive switches used in this research were designed and fabricated by the Air Force Research Laboratory (AFRL) Sensors Directorate. Actuation parameters are examined to determine how they affect the charging behavior of the insulator. Since MEM devices are limited in quantity and somewhat difficult to measure, metal-insulator-silicon semiconductor (MIS) capacitors are investigated to isolate insulator charging from other issues inherent with MEM switches. A preliminary set of MEM irradiation results using AFRL Space Vehicles Directorate's low energy x-ray (LEXR) source are presented.

1.4. Contributions

A computer program that models time-dependent MIS insulator charging under bias and irradiation was developed. Based on experimental measurements, it was confirmed that charge tunneling from the silicon into the insulator is responsible for

charge accumulation; however, the model's single trap energy assumption was determined to be too simple.

The knowledge gained from the MIS capacitor was applied to research on MEM switch charging. First, an existing program was enhanced to include time-dependent charging. Other enhancements include a more flexible description of the voltage waveform as well as an option to include ionizing radiation in the calculations. Analyzing the experimental results using this enhanced model shows the MEM switch behavior agrees with tunneling early in testing. It was also shown that charging behavior depends on the length of time the beam spends in contact with the insulator. At longer operating times, charging continues to explain the changes in voltages required for closing the switch. Surprisingly, it was determined that insulator charging does not explain the changes in voltage required to open the switch, nor the switch's ultimate failure mechanism. Experiments to study radiation effects on MNS and MEM switches were developed. The first irradiation measurements on this MEM switch design were made, although, due to equipment problems, the results are only preliminary.

1.5. Overview

The next chapter describes the design of capacitive switches and how they operate, summarizes the current knowledge on switch reliability issues, and describes how trapped charge affects switch operations. With a basic knowledge of switch operation, the theory of insulator charging is presented in Chapter 3. The fourth chapter describes the experiments conducted on the MIS capacitors and MEM switches. In the fifth chapter, results of these experiments are presented and discussed. Chapter 6 provides a consolidated description of charging using the lessons learned from modeling

experimental results and discusses any short-comings in the models. The last chapter draws conclusions and discusses opportunities for follow-on research. Appendix A is a primer on radiation effects on insulators, and Appendix B summarizes data and modeling from the preliminary irradiation data.

Bibliography

1. Rebeiz, G.M. *RF MEMS: Theory, Design, and Technology*. Hoboken, New Jersey: Wiley, 2003.
2. Reid, J.R. "Simulation and Measurement of Dielectric Charging in Electrostatically Actuated Capacitive Microwave Switches," *Proceedings Modeling and Simulation of Microsystems*, 250-253 (April 2002).
3. Rebeiz, Gabriel M. "RF MEMS Switches: Status of the Technology," *12th International Conference on Solid State Sensors, Actuators and Microsystems*, 1726-1729 (June 2003).

2. Switch Design and Operation

This chapter provides an overview of the capacitive switch design and how it operates. Theory and a mathematical model will be presented to describe device physics. With an understanding of the switch, research published to date on switch reliability is summarized. Specifically, the issue of trapped charge is examined. Finally, the theory describing switch operation is redeveloped for the case when charges are present in the insulator.

2.1. Switch Design

A schematic, cross-sectional view of an RF MEM switch is shown in Figure 2-1. Generally, these switches consist of a metal beam suspended over a metal electrode that has been coated with an insulating material. Common substrate materials include silicon, GaAs, glass, quartz, or polished ceramics [1:15].

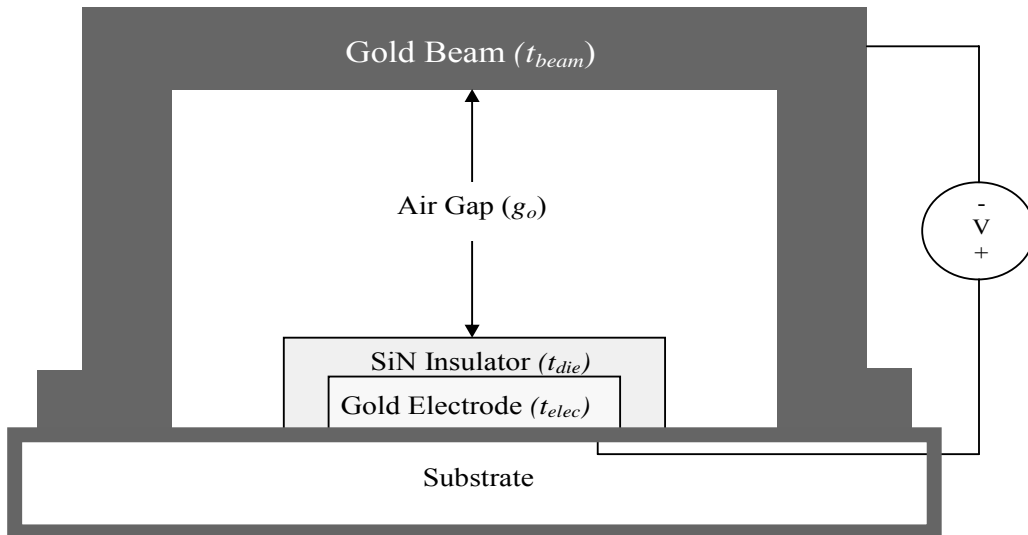


Figure 2-1: Schematic cross sectional diagram of MEM switch

A plan view of a capacitive switch is shown in Figure 2-2. Dimensions W , L , and w identify beam width, beam length, and electrode width, respectively. Since the switch will be included as part of a coplanar waveguide, it utilizes a ground-signal-ground configuration. The outside pads are connected to the beam and are maintained at ground. The middle path transmits the microwave and actuation signal.

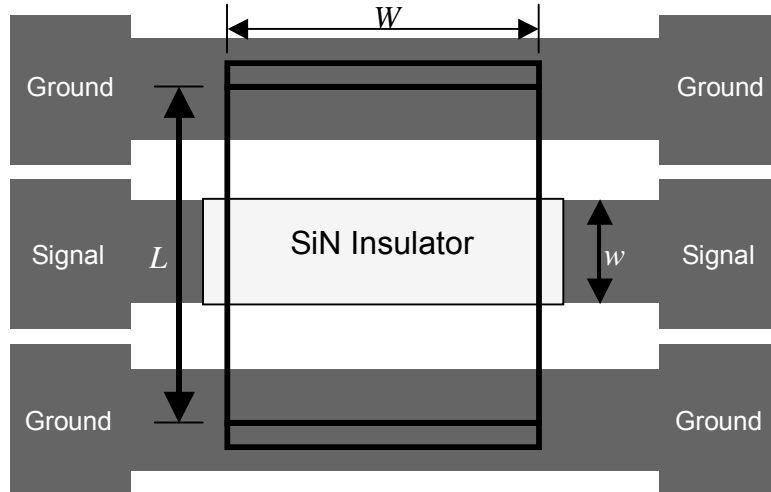


Figure 2-2: Schematic plan view of switch

In the zero bias state, the beam would be up as shown in Figure 2-1. In this position, the switch has a small total capacitance due to the large air gap between the beam and the silicon nitride. This small capacitance ensures only a small portion of the RF signal couples to the beam. Therefore, the signal passes under the bridge with extremely low losses.

To turn the signal off, the beam must be pulled into contact with the insulator. When the beam is in contact with the insulator, capacitance increases dramatically. A

large increase in capacitance leads to increased capacitive coupling. This capacitively coupled system allows the RF signal to pass from the transmission line to the bridge while blocking the dc component. Since the beam is held at ground, the RF signal passes from the transmission line to ground and the waveguide no longer propagates the RF signal.

2.2. Switch Operation

To simplify the description of the physical processes responsible for switch operation, the beam can be modeled as an equivalent circuit consisting of a series of parallel plate capacitors. The basic processes involved in modeling the beam can be described using one of these parallel plate capacitors. A diagram of a capacitor is shown in Figure 2-3. The top capacitor plate represents a section of the beam suspended by a spring which corresponds to the weight of the beam and its retaining force. The insulator is also shown, and the bottom plate represents the transmission line (t-line).

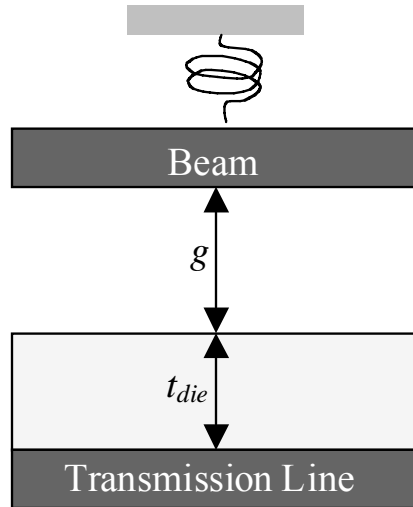


Figure 2-3: Parallel plate capacitor used to develop a simple model of switch operation

A voltage applied to the t-line relative to the top plate (ground) induces an electrostatic force, F_e [N]. The general definition of electrostatic force is the first derivative of work with respect to the air gap dimension, g [cm],

$$F_e = -\frac{d(\text{Work})}{dg}, \quad (2-1)$$

or

$$F_e = -\frac{d}{dg}\left(\frac{1}{2}CV^2\right), \quad (2-2)$$

which simplifies to

$$F_e = -\frac{1}{2}V^2 \frac{dC}{dg}, \quad (2-3)$$

where

C is the capacitance of the parallel plate capacitor [F], and V is the actuation voltage [V].

In the up state, capacitance is defined by the thick air gap, g , and the thin insulating layer in series.

$$C(g) = \frac{\varepsilon_r \varepsilon_o A}{t_{die} + \varepsilon_r g} \quad (2-4)$$

where

ε_r is the insulator's relative dielectric constant [-],
 ε_o is the permittivity of free space [F/cm],
 A is the overlap area of the beam and electrode, e.g. Ww [cm²], and t_{die} is the insulator thickness [cm].

Substituting $C(g)$ into the electrostatic force equation yields

$$F_e = -\frac{\varepsilon_r^2 \varepsilon_o A V^2}{2(t_{die} + \varepsilon_r g)^2} \quad (2-5)$$

Electrostatic force can also be expressed as a product of charge, Q [C], and the electric field, E [V/cm], where

$$E = -\frac{V}{2\left(\frac{t_{die}}{e_r} + g\right)} = -\frac{e_r V}{2(t_{die} + e_r g)} \quad (2-6)$$

and

$$Q = C \cdot V = \frac{e_r e_0 A}{(t_{die} + e_r g)} \cdot V. \quad (2-7)$$

It is clear Q and E are not only dependent on the applied voltage but also the air gap, g , i.e. $Q(V, g)$ and $E(V, g)$.

The polarity of Q depends on the polarity of the applied bias. For example, when a positive bias is applied to the t-line, positive charge is induced on the t-line and negative charge on the top plate. F_e from these opposite charges causes the beam to bend toward the t-line which, in turn, reduces g .

This behavior establishes a positive feedback as the beam approaches the insulator. As the beam bends toward the t-line, Q and E increase since they both depend on the size of the air gap which produces a larger F_e . Therefore, even though the applied bias remains constant in this case, F_e increases. This increase in F_e causes the beam to bend even further, and the process repeats.

Simultaneously, the beam's restoring force counters the electrostatic force. The restoring force prevents the beam from immediately collapsing onto the insulator surface due to the process described in the previous paragraph. This restoring force, F_r [N], is given by

$$F_r = k(g_o - g), \quad (2-8)$$

where

k is the normal spring constant of the beam [N/cm], and
 $g_o - g$ is the deflection of the beam relative to the relaxed position [cm].

Notice the restoring force increases as the beam deflects. Figure 2-4 is a free body diagram showing the electrostatic and restoring forces for this simplified spring-parallel plate capacitor model.

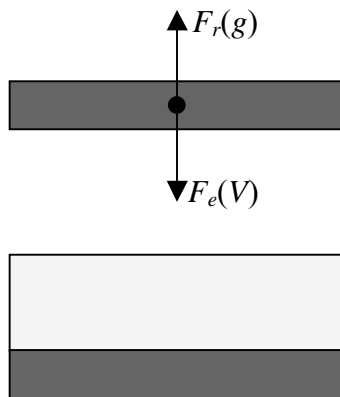


Figure 2-4: Free body diagram of forces on a section of beam

Both the electrostatic and restoring forces increase as the applied bias increases. At low applied voltages, changes in the restoring force are generally much larger than changes in the electrostatic force. Therefore, an equilibrium position is reached with the top plate only slightly deflected. The plate remains in this position as long as that particular voltage is applied. When a slightly larger bias is applied, the electrostatic and restoring forces will increase so the top plate deflects further. The electrostatic force is non-linear while the restoring force is linear. Therefore, the increase in F_e will eventually exceed the increase in F_r when the applied bias is large enough. Once this

condition is reached, the plate collapses onto the insulator surface. From theory, it can be shown this occurs when the top plate deflects $g_0/3$ [1:37].

As stated earlier, beam actuation can be described with a series of parallel plate capacitors. From this simplification, the entire switch can be modeled. Figure 2-5 is a plot of beam deflection as a function of applied bias. In the ideal case, positive and negative biases of the same magnitude result in the same electrostatic force. So, the deflection is also the same for both polarities, e.g. the beam deflects the same amount for +25V and -25V.

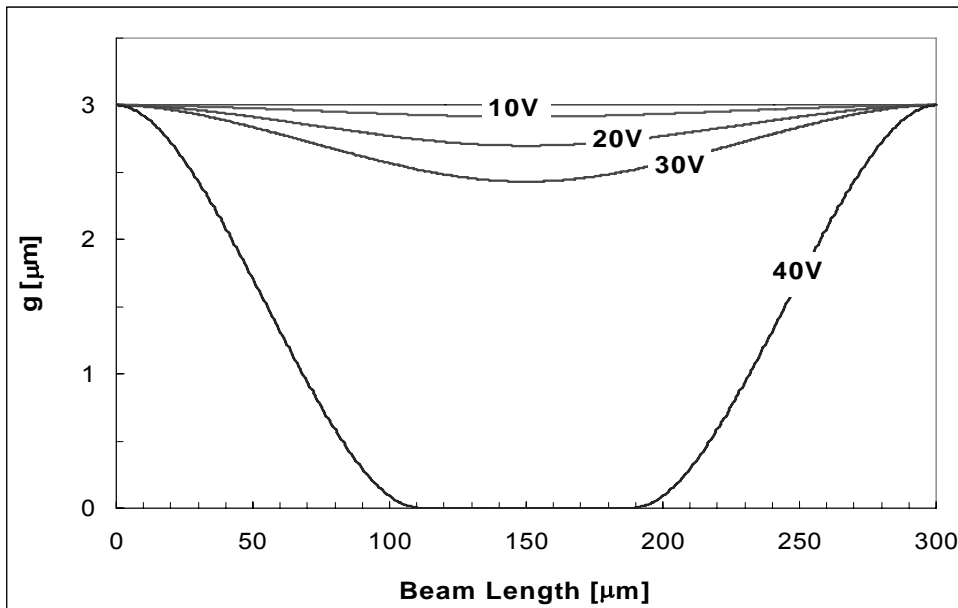


Figure 2-5: Calculated beam deflection as a function of applied bias (plotted using Reid's code)[2]

After the beam pulls onto the insulator surface, the next phase of switching is hold-down and release. The beam remains in contact with the insulator as long as the electrostatic force is larger than the restoring force. Since F_e 's response to a change in

voltage is non-linear and F_r 's response is linear, the beam remains in contact with the insulator at lower voltages than those required for the beam to collapse onto the insulator. This produces a hysteresis in the g - V (and C - V) relationship.

To illustrate this theory, a complete, bipolar actuation cycle is simulated using Reid's code [2]. Figure 2-6 shows the bipolar, triangle voltage waveform used to calculate the total switch capacitance with zero offset voltage.

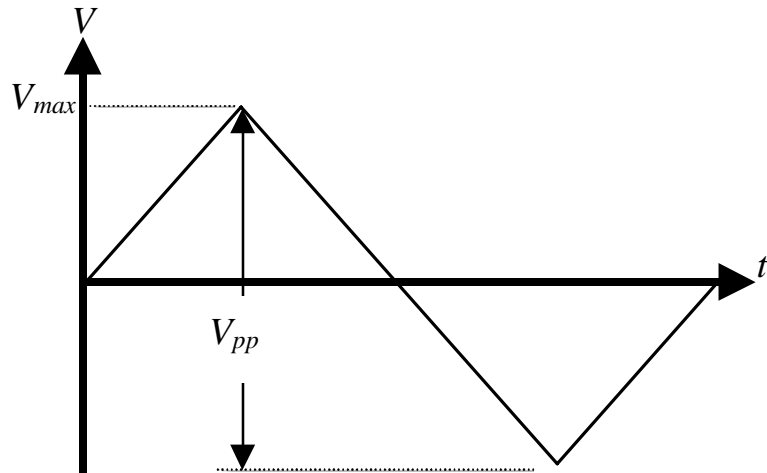


Figure 2-6: Single bipolar triangle wave

Figure 2-7 is a plot of capacitance as a function of the applied bias. The waveform starts at zero and ramps with a positive voltage. This is identified by the “1” arrow. During this phase, the total capacitance of the switch is very low, because of the series capacitance provided by the large air gap. When the ramped voltage reaches approximately 19V, the capacitance instantaneously jumps two orders of magnitude (arrow “2”) because the large air gap that was providing the series capacitance is gone. This indicates the beam has pulled-in and is resting on the insulator.

As the triangle voltage waveform reaches its maximum (arrow “3”), and begins to decrease (arrow “4”), the capacitance remains constant. Constant capacitance indicates the area of the formed parallel plate capacitor no longer changes. This is because the beam completely covered the electrode at pull-in. This also illustrates the point made earlier that the electrostatic force generated by a particular applied voltage depends on whether the beam is up or in contact with the insulator. At lower applied voltages, the capacitance decreases slightly as shown with arrow “5”. This indicates the beam restoring force is overcoming the decreasing electrostatic force, and the beam is beginning to peel off of the electrode. Peeling decreases the area of beam-electrode overlap and decreases the total capacitance. After a short period of the beam peeling off, it completely releases from the insulator, returning to the up position (arrow “6”). This is shown by the return to a small, total capacitance caused by the return of the series capacitance of the large air gap. The process repeats itself for the negative portion of the waveform (arrow “7”).

This analysis does not describe all of the factors contributing to the voltage required to hold the beam in contact with the insulator. First, the insulator surface is not perfectly smooth. When the beam is pulled down, true intimate contact is not made due to insulator roughness. This effectively leads to a large array of metal-insulator-metal and metal-air-insulator-metal capacitors in parallel. Therefore, the area described by A in the equations for Fe overestimates the force. A smaller effective area can be used in the model to account for this. An incomplete understanding of metal-insulator interface physics is an even larger issue. For example, localized adhesive and repulsive forces

exist at this interface. Experiments show that ignoring these forces underestimates the voltages required to hold the beam down.

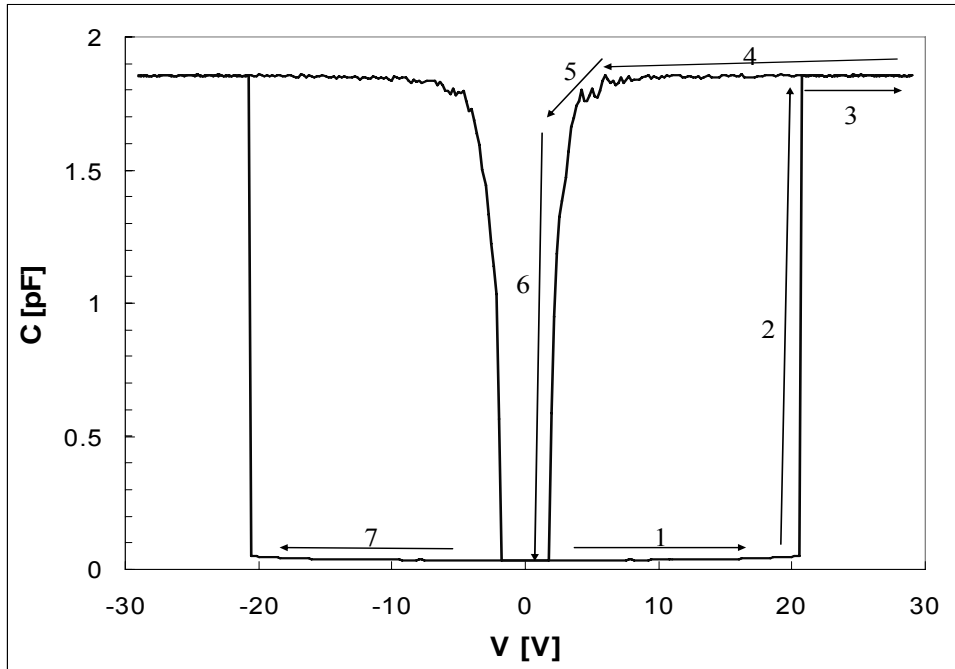


Figure 2-7: Calculated capacitance-voltage plot: historical path of switch operation

2.3. Reliability Issues

While the adhesive and repulsive forces just described affect switch operations, the literature identifies insulator trapped charge as the single most important factor in limiting capacitive switch lifetime [1:185]. Dielectric charging for semiconductor devices has been an area of concentrated research for more than 35 years [3]. The development of MIS transistors, including both silicon dioxide devices for MOSFET technology and dual insulator (e.g. nitride-oxide) devices, drove this research. In fact, metal-nitride-oxide-semiconductor (MNOS) capacitors utilize the long lasting charge

storage properties of silicon nitride for memory applications. MNOS research provides some insight into the MEM switch problem; however, the differences in device geometry are significant enough that previous dielectric charging research does not tell the whole story. The next section summarizes the research published to date on capacitive switch charging.

2.4. Status of Research

Chan, *et al.* [4] published one of the first papers to discuss capacitive switch charging. The switch used in this research was of a slightly different design than that shown in Figure 2-1. Their design used a silicon substrate as the electrode, a layer of silicon nitride deposited on the silicon, and a polysilicon beam suspended over the electrode and insulator. To actuate the switch, a bias was applied between the silicon and the beam. They determined that biasing the switch with a constant voltage caused charge to accumulate in the insulator over time. Their experimental procedure involved applying a constant voltage to the beam. The magnitude of the applied bias was between the pull-in and the release voltages. Since the applied voltage was insufficient to pull the beam in, the beam was physically pushed into contact with the insulator surface using a probe. With the beam down, a temporary polysilicon-silicon nitride-silicon capacitor was formed. In this configuration, they measured capacitance for an extended time. Using the theory developed for MOS capacitors [5:433], a change in capacitance at constant voltage was related to a change in insulator trapped charge density. Without any knowledge of the distribution of charge across the thickness of the insulator, charge is normally assumed to reside at the insulator-silicon interface. This is where an individual charge produces the largest change in capacitance (a charge at the polysilicon-silicon

nitride interface has no affect on the measured capacitance). The authors observed accumulation of charge with a polarity opposite that applied to the beam at the silicon nitride-silicon interface and assumed this charge tunneled from the electrode into the insulator. Again, this experiment does not provide information on charge trapped near the insulator surface.

Goldsmith, *et al.* [6] correlated switch lifetime to the equation for field dependent Frenkel-Poole emission (discussed further in Chapter 3). They assumed capacitive switch lifetime is directly related to charging. The bias required to actuate their switch design produced electric fields between 1 and 3 MV/cm. Fields of this magnitude are sufficient to cause Frenkel-Poole emission. Current varies exponentially with increasing applied voltage when Frenkel-Poole emission dominates. [6] compared the number of switch actuations to failure as a function of applied actuation voltage; as actuation voltage increased, switch lifetime decreased exponentially. This led the authors to conclude that switch lifetime is related to Frenkel-Poole emission.

Questions arise from the analysis presented by [6], so more experimental details are given here to illuminate these questions. First, a dual-pulse square waveform was used. The first pulse pulled the beam down, and was applied for 50 μ s. The second pulse held the beam down. (Remember from section 2.2 that the voltage required to hold the beam is much less than the voltage needed to pull the beam down.) The magnitude of the hold voltage was only a factor of two smaller than the release voltage, but it was applied nine times longer (approximately 450 μ s). While the actuation voltage only made up ten percent of the total biasing time, this is the voltage [6] chose to compare to lifetime. This analysis leaves one to wonder which is actually responsible for charging: the quicker,

higher voltage pulse or the longer, lower voltage pulse. In the course of 30 straight hours of switching with a 50% duty cycle, the switch spent 14 hours under a 20 - 25 V bias while only spending one hour at 50 – 60 V. The authors did not address these issues. While the article suggests a relationship between actuation voltage and lifetime, their experiment leaves doubt this actually explains switch failure.

Reid and Webster [7] used a switch (metal beam, silicon nitride insulator, metal electrode capacitive switch) similar to that shown in Figure 2-1 and compared their results to those presented in [4]. They observed that shifts of the pull-in and release voltages depend on the drive signal polarity (positive, negative, or bipolar). A unipolar signal shifted the voltages in the direction of the beam charge polarity. They explained these voltage shift characteristics as charge transfer from the beam into silicon nitride surface states. Over time the rate of charging decreased until a steady state voltage shift was reached. When a bipolar signal was applied, the pull-in voltages shifted only slightly during the actuation period, but the magnitude of all four actuation voltages decreased with time. They explained this as surface charge increasing over time, and the polarity of that charge switching with each cycle.

Reid and Webster point out that this contradicts the results in [4], where charge opposite the beam's polarity was trapped. Reid and Webster observed that beam and trapped charge polarity were the same, and suggested this contradiction is due to the testing method. The experiment in [4] maintained constant contact between the beam and the silicon nitride surface, while [7] experiment used a constantly cycling switch. Reid and Webster conclude both charging mechanisms may occur in their switch; however,

they only saw a fast surface charging mechanism. They suggest the other charging mechanism may show itself once the surface states saturate with extended cycling.

A few more experimental details from [4] and [7] work should be highlighted. The experiment in [4] measured charging with a capacitance measurement. This measurement provides no information about the charge trapped at the silicon nitride surface. On the other hand, the experiment in [7] provides the exact opposite information, providing surface information, but none on the amount of charge trapped at the electrode-insulator interface.

As previously discussed, [4] performed measurements with the beam in constant contact with the insulator. However, they also measured positive and negative pull-in voltages to determine a voltage shift. No information is given on the particular waveform, but their Figure 7 (b) implies it is similar to [7]. [4] made successive pull-in measurements with 5 minutes between each and compared them to measurements with less than 1 minute between each. The results from these measurements provided the motivation to make the constant contact measurements. The tunneling effect observed in [4] would also reach a steady state over time as trap states fill.

Finally, van Spengen, *et al.* [8] also tested capacitive RF MEM switches. They measured switch lifetime for three combinations of frequency and duty cycle. One was actuated at 1 kHz with a 50% duty cycle. A second switch was actuated at 10 kHz and a 50% duty cycle. A third switch was also actuated with a 10 kHz signal, but with a 20% duty cycle. The authors found that the 10 kHz lasted longer before sticking than the 1 kHz samples, and the 20% duty cycle lasted longer than the 50% duty cycle switch. However, when switch lifetime is compared to the total amount of time the switch spends

in the “on” position, the lifetimes are approximately the same regardless of the duty cycle. They conclude that total time in “on” position is a much better metric of switch reliability than the traditional cycles to failure.

The next section redevelops the equations in section 2.2 to include the effects of trapped charge. Fixed charge causes a constant, horizontal shift of the CV curves, i.e. the pull-in and release voltages are offset by the same magnitude and in the same direction.

2.5. Switch Operation with Insulator Charge

This section redevelops the equations of section 2.2 for the case of insulator trapped charge. This development was presented by Reid [2]. In the MEM switch geometry there are three general areas where charge may be trapped: 1) insulator surface, 2) bulk, and 3) insulator-electrode interface. When charge is trapped in the dielectric, charge conservation induces image charge in the beam and electrode. The total image charge induced on the beam is inversely proportional to the distance between the trapped charge and beam. The opposite relationship applies for induced charge on the electrode. Figure 2-8 shows the parallel plate capacitor geometry from Figure 2-3 with trapped charge included. The sheet of trapped charge is located at a distance, x , from the insulator-transmission line interface.

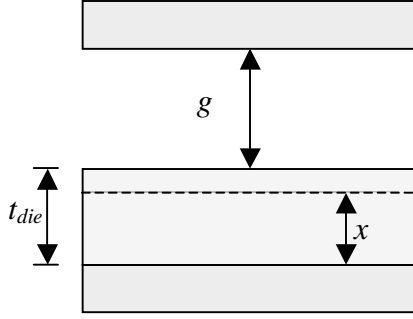


Figure 2-8: Trapped charge geometry

The number of charges on the beam (and electrode) when a voltage, V , is applied is equal to the product of capacitance and voltage plus a component independent of voltage but proportional to the trapped charge density. The amount of charge induced on the beam, Q_b [C], and electrode, Q_e [C], are given, respectively, by

$$Q_b = C(g) \cdot V + \rho_{b,image} A, \quad (2-9)$$

and

$$Q_e = -C(g) \cdot V + \rho_{e,image} A, \quad (2-10)$$

where $\rho_{i,image}$ is the induced image charge density [C/cm²] on either the beam (b) or electrode (e). The beam and electrode image charge density induced by insulator trapped charge is calculated by

$$\rho_{b,image} = - \int_0^{t_{die}} \rho_{trapped}(x) \frac{x}{t_{die} + \epsilon_r g} dx, \quad (2-11)$$

and

$$\rho_{e,image} = - \int_0^{t_{die}} \rho_{trapped}(x) \frac{t_{die} - x + \epsilon_r g}{t_{die} + \epsilon_r g} dx, \quad (2-12)$$

respectively, and $\rho_{trapped}(x)$ is the volume density of trapped charge [C/cm³] as a function of x in the insulator.

How does insulator and image charge affect switch actuation? When trapped charge is not present in the insulator, the electrostatic force pulling on the beam exists only between charge on the beam and charge on the electrode. When charge is trapped in the insulator, a combination of the charge on the electrode and the charge trapped in the insulator attracts the beam charge. The collective change in the number of charges on the beam and transmission line caused by insulator charging enhances or diminishes the electrostatic force depending on the polarity of the trapped charge and the polarity of the applied bias.

Calculating the effect of trapped charge on the electrostatic force, requires another look at the definition of electrostatic force, F_e [N], as presented in equation (2-5),

$$F_e = - \frac{\epsilon_r^2 \epsilon_o A V^2}{2(t_{die} + \epsilon_r g)^2}.$$

Equation (2-5) can be recast in terms of charge density

$$\begin{aligned} F_e &= - \frac{A}{2\epsilon_o} \frac{\epsilon_r \epsilon_o V}{t_{die} + \epsilon_r g} \frac{\epsilon_r \epsilon_o V}{t_{die} + \epsilon_r g} \\ F_e &= - \frac{A}{2\epsilon_o} \frac{CV}{A} \frac{CV}{A} = - \frac{A}{2\epsilon_o} \frac{Q}{A} \frac{Q}{A} \\ F_e &= - \frac{A \rho^2}{2\epsilon_o} \end{aligned} \quad (2-13)$$

It can be shown that the beam charge density equals the sum of the electrode charge density and the total insulator charge density, as described by

$$\rho_b = -\rho_e + \int_0^{t_{die}} \rho_{trapped}(x)dx. \quad (2-14)$$

Therefore, equation (2-13) can be rewritten as

$$F_e = -\frac{A\rho_b(\rho_e + \int_0^{t_{die}} \rho_{trapped}(x)dx)}{2\epsilon_0}. \quad (2-15)$$

The change in electrostatic force caused by trapped charge manifests itself as a change in pull-in and release voltages. In an equivalent analysis, McClure, *et al.* showed that the actuation voltage shift caused by insulator trapped charge is given by [9]

$$\Delta V = \frac{1}{\epsilon_r \epsilon_0} \int_0^{t_{die}} x \rho_{trapped}(x) dx. \quad (2-16)$$

The result of this analysis is that trapped charge induces a horizontal shift of the CV curve shown in Figure 2-7. In other words, the same capacitance is achieved with a different applied voltage.

Notice the entire CV curve shifts horizontally. Pull-in and release voltages (both positive and negative) shifted by the same amount. In this case, the density of trapped charge was $1 \times 10^{12} \text{ e}^-/\text{cm}^2$. This trapped charge density at the surface results in a voltage shift of 5.2V.

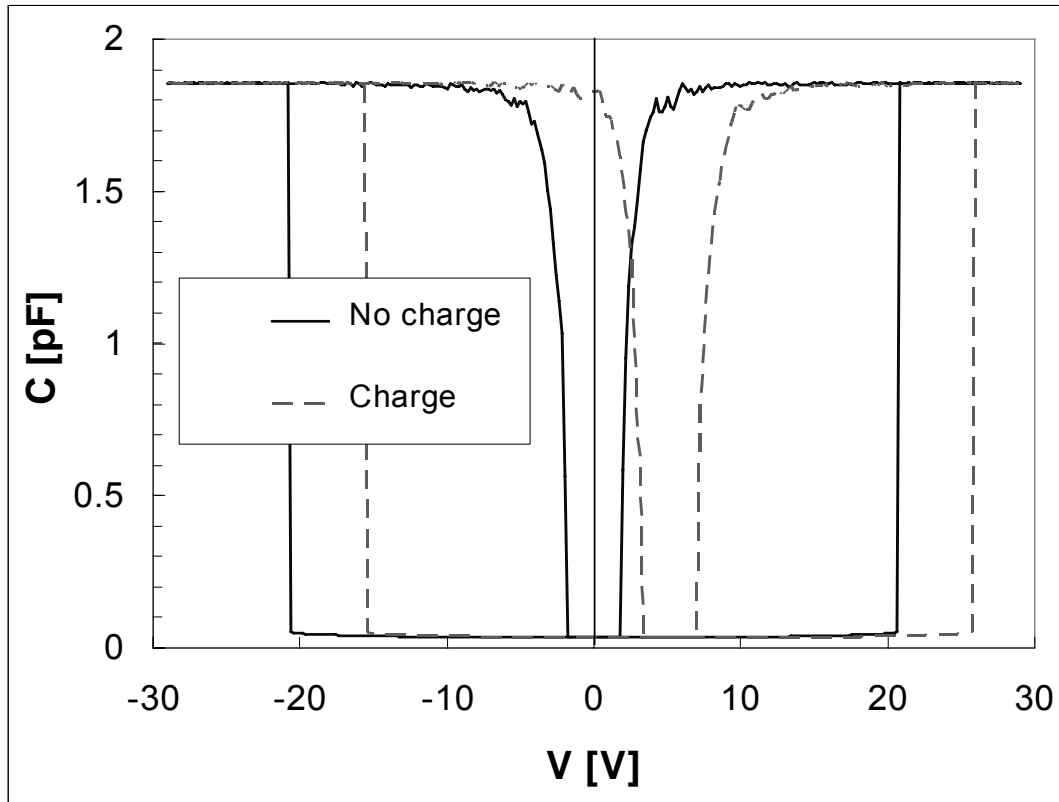


Figure 2-9: Calculated CV plot with and without trapped charge in insulator: 1) no trapped charge and 2) trapped charge at surface.

Referring to equation (2-16), ΔV is determined not only by the density of trapped charge, but also by the location of the trapped charge. In Figure 2-9, the trapped charge was located at the insulator surface. This location causes the largest shift in ΔV . When the layer of charge is deeper in the insulator, the effect is not as dramatic as shown in Figure 2-10. When the charge layer is in the middle of the $0.2 \mu\text{m}$ thick insulator, ΔV is reduced by a factor of two. Charge located at the electrode (t-line) interface has no effect on ΔV , so the CV curve is identical to Figure 2-7.

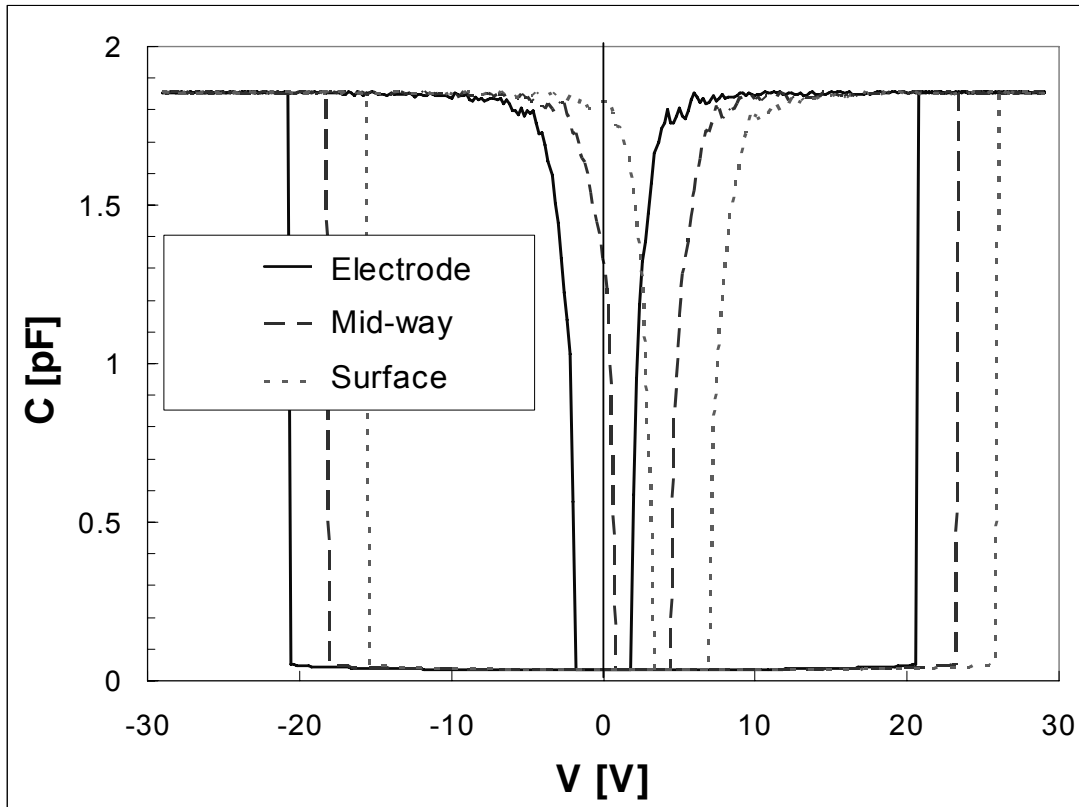


Figure 2-10: Calculated CV plot with trapped charge layer in different locations: 1) electrode interface, 2) half way between surface and metal interface, 3) metal interface. Line 3) is identical to having no trapped charge.

When the switch operates for extended periods, trapped charge density increases with time. For simplicity, consider only charges at the insulator surface and that the insulator charges at a constant rate of 2.5×10^9 electrons/cm²/sec. A plot of the pull-in and release voltages for the first 200 sec of operation is given in Figure 2-11.

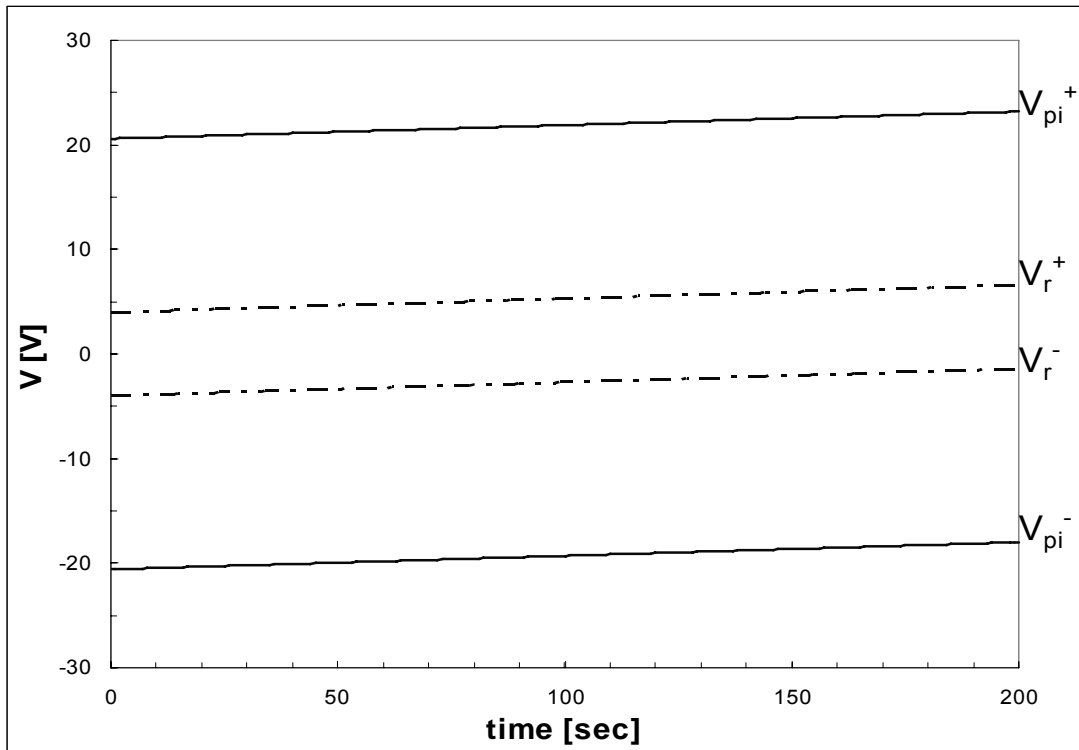


Figure 2-11: Calculated pull-in and release voltages over time assuming a constant charging rate.

A useful method of tracking charging behavior is the pull-in and release voltage shift.

This shift, $\Delta V(t)$, is the difference of the time dependent pull-in or release voltage, $V(t)$, relative to a base pull-in or release voltage. This base voltage can be an ideal pull-in or release voltage or the initial condition, $V(0)$.

This chapter discussed the theory and models necessary to describe switch operation. A brief summary was given of the current knowledge on the most important reliability concern for capacitive switches – trapped charge in the insulator. C - V and ΔV -time plots were introduced and discussed in detail. Later in this dissertation, extensive use will be made of these plots to describe more complex charging behavior. Finally, switch theory was adjusted to include the effects of trapped charge. The next chapter

discusses the mechanisms responsible for changes in the insulator trapped charge density including tunneling, conduction, and discharge.

Bibliography

1. Rebeiz, G.M. *RF MEMS: Theory, Design, and Technology*. Hoboken, New Jersey: Wiley, 2003.
2. Reid, J.R. "Simulation and Measurement of Dielectric Charging in Electrostatically Actuated Capacitive Microwave Switches," *Proceedings Modeling and Simulation of Microsystems*, 250-253 (April 2002).
3. Ross, E.C. and J.T. Wallmark. "Theory of the Switching Behavior of MIS Memory Transistors," *RCA Review*, 30: 366-381 (June 1969).
4. Chan, E., K. Garikipati, and R. Dutton. "Characterization of Contact Electromechanics Through Capacitance-Voltage Measurements and Simulations," *Journal of Microelectromechanical Systems*, 8: 208-217 (June 1999).
5. Neaman, Donald. *Semiconductor Physics & Devices*. Boston: Irwin, 1997.
6. Goldsmith, C., J. Ehmke, A. Malczewski, B. Pillans, S. Eshelman, Z. Yao, J. Brank, and M. Eberly. "Lifetime Characterization of Capacitive RF MEMS Switches," *2001 IEEE MTT-S Digest*, 227-230 (2001).
7. Reid, J.R. and R.T. Webster. "Measurement of Charging in Capacitive Microelectromechanical Switches," *Electronics Letters*, 38: 1544-1545 (21 November 2002).
8. van Spengen, W. M., R. Puers, R. Mertens, and I. De Wolf. "Experimental Characterization of Stiction Due to Charging in RF MEMS," *2002 International Electron Device Meeting Technical Digest*. 901-904. Piscataway, NJ: IEEE, 2002.
9. McClure, S.S., L.D. Edmonds, R. Mihailovich, A.H. Johnston, P. Alonso, J. DeNatale, J. Lehman, and C.Yui. "Radiation Effects in Micro-Electromechanical Systems (MEMS): RF Relays," *IEEE Transactions of Nuclear Science*, 49: 3197-3202 (December 2002).

3. Charging Mechanisms

3.1. Introduction

Chapter 2 described a mechanical model for MEM switch operation that included the effects of trapped charge. While potential charging mechanisms were suggested (e.g. tunneling [1][2][3] and Poole-Frenkel emission [4]), the mathematical model describing switch operation ignored how the charge was trapped. This chapter discusses possible mechanisms responsible for insulator charging behavior.

3.2. Effect of Trapped Charge on Capacitors

A schematic diagram of a capacitor is shown in Figure 3-1. Since silicon nitride was the insulator used in the MEM switches tested in this research, particular attention is paid to it throughout this discussion. The bottom layer is labeled “conductor.” This conductor serves as a source of carriers for injection into the insulator; it is a metal in the case of MEM switches and a semiconductor for MIS devices.

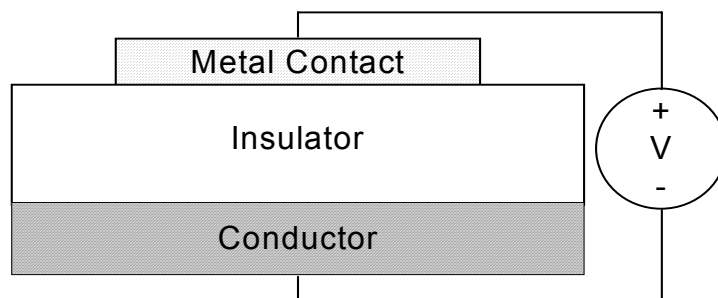


Figure 3-1: Schematic design of arbitrary metal-insulator-conductor structure

CV measurements on MIS devices are useful for studying insulator charging. A high-frequency CV curve is generated by applying a voltage sweep to the MIS structure and measuring the capacitance. This generates a characteristic capacitance curve. When a large negative bias is applied to a capacitor built with p-type material, the measured capacitance approaches the theoretical capacitance of a parallel plate capacitor of the same dimensions. This is referred to as accumulation because majority carriers accumulate at the insulator-semiconductor interface. As the voltage approaches zero, the curve begins an abrupt drop; this is referred to as depletion. After dropping, the capacitance reaches and maintains a minimum capacitance for further increases in positive voltages. For n-type material, the CV behavior is the exact opposite, i.e. accumulation for positive voltages, etc. Figure 3-2 shows an example of a high-frequency CV curve for p-type silicon. A thorough treatment of CV theory for MIS structures is found in most semiconductor physics texts [5][6][7].

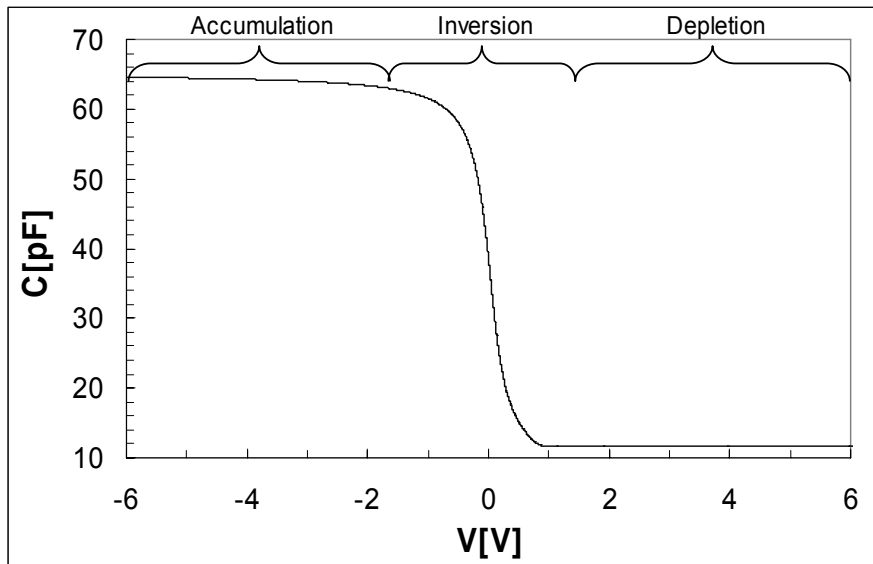


Figure 3-2: Calculated high-frequency CV curve for a p-type MIS capacitor

The CV curve in Figure 3-2 is ideal for 0.2 μm thick silicon nitride and a 0.5 mm diameter contact area. In reality, there are deviations to this curve. Since the work function of the top contact is likely different than the semiconductor work function, the insulator bands bend in order for the top and bottom contacts to achieve thermal equilibrium. Therefore, a voltage must be applied across the insulator to straighten the bands. The voltage required to straighten these bands is referred to as the flat band voltage. The flat band condition occurs in the depletion region of the curve. This flat band voltage manifests itself on the CV characteristics as a horizontal shift of the entire curve along the voltage axis. The magnitude and direction of this shift depends on the work function difference.

Trapped charge also induces a horizontal shift of the CV curve. This is analogous to the changes in pull-in and release voltage presented in Chapter 2 where trapped charge induces image charge in the silicon and top metal contact. Therefore, an additional voltage must be applied to the capacitor of an appropriate polarity (depends on the polarity of the trapped charge) and magnitude (depends on density and location of the trapped charge) to reach the flat band condition. Interface states also cause deviations in the CV curve - the slope of the CV curve in the depletion region is shallower.

The relationship between flat band voltage shift and trapped charge density is given by equation (3-1),

$$\Delta V_{fb} = -\frac{1}{C_{in}} \int_0^{t_m} \frac{x}{t_{in}} \rho(x) dx, \quad (3-1)$$

where

ΔV_{fb} is the CV curve shift [V],

C_{in} is the insulator capacitance $\epsilon_r \epsilon_0 / t_{die}$ [F/cm²],
 x is the distance into the insulator from the top contact [cm],
 t_{in} is the insulator thickness, and
 $\rho(x)$ is the density of trapped charge (volume) at depth x [C/cm³].

Since the distribution of trapped charge, $\rho(x)$, is generally not known, a sheet charge can be used. Assuming trapped charge is limited to a single sheet located at x , equation (3-1) simplifies to equation (3-2)

$$\Delta V_{fb} = -\frac{x}{t_{in}} \frac{Q_{in}}{C_{in}}, \quad (3-2)$$

where Q_{in} is the sheet charge density [C/cm²].

A sheet of trapped charge causes the largest voltage shift when it is located at the silicon-insulator interface, while charge located at the top contact interface produces no curve shift. A further simplification assumes the trapped charge resides at the insulator-silicon interface, therefore (3-2) simplifies to

$$\Delta V_{fb} = -\frac{Q_{in}}{C_{in}} \quad (3-3)$$

Since the voltage shift is directly measured during the experiment, equation (3-1), or one of its two simplifications, must be solved for trapped charge density.

3.3. Theory of Charging

Figure 3-3 shows the energy band diagram for a MIM capacitor structure. A metal bottom conductor is used for simplicity, and a representative trap site has been included in the bulk insulator.

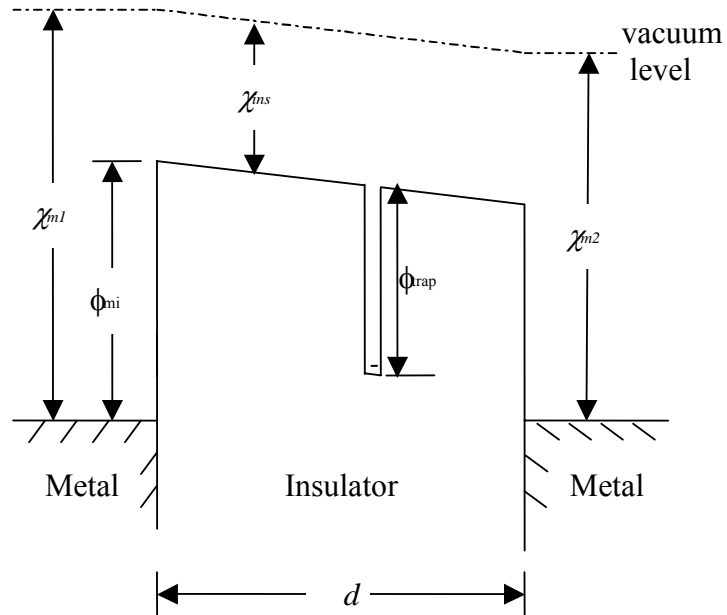


Figure 3-3: Band diagram for an arbitrary MIM capacitor with trap

Building a space charge in the insulator requires charge transport. The source of the charge can be from either inside or outside the insulator (i.e. a conductor). Charge from a conductor must overcome the ϕ_{mi} barrier shown in Figure 3-3. Charge originating within the insulator must overcome the ϕ_{trap} barrier. Once a charge moves within the insulator, it either becomes trapped or it leaves the insulator, enters the circuit, and contributes to the leakage current. These processes are shown on the schematic band diagram in Figure 3-4

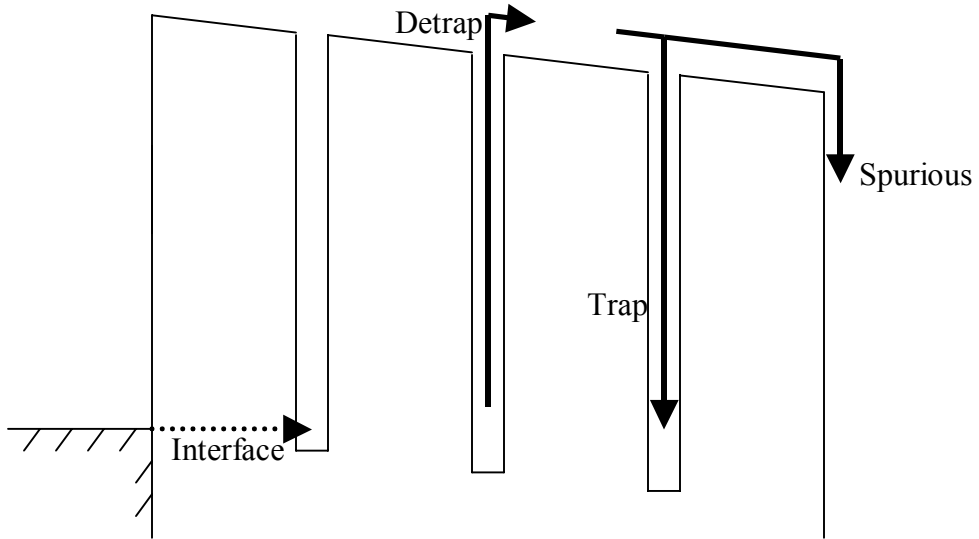


Figure 3-4: Band diagram illustrating charging processes

and summarized mathematically in the following equation

$$\frac{\partial n(x,t)}{\partial t} \Big|_{Total} = \frac{\partial n(x,t)}{\partial t} \Big|_{Interface} + \frac{\partial n(x,t)}{\partial t} \Big|_{Trap} - \frac{\partial n(x,t)}{\partial t} \Big|_{Detrap}, \quad (3-4)$$

where $n(x,t)$ is the density of filled trap sites as a function of time and location. The subsections that follow describe each of these elements in detail. For simplicity, the next section examines a single bias (positive) and a single carrier (electron); however, this knowledge is just as easily applied to positive biases and tunneling holes.

Interface Tunneling

The first aspect of insulator charging is injection across the insulator-conductor interface. The ϕ_{mi} barrier in Figure 3-3 is very large, so the probability of an electron overcoming ϕ_{mi} and entering the insulator conduction band is extremely low. However, an electron can still enter the insulator via tunneling.

Insulator tunneling is modeled as a quantum mechanical transition through a potential barrier. To tunnel, an electron must transition from the conductor's conduction band into an allowed insulator energy state. Ideally, the insulator's large forbidden band gap would be completely void of trap sites. However, most insulators have high densities of incomplete and dangling bonds that provide allowed energy states for trapping. Also, trap densities are often higher at material interfaces (e.g. insulator-metal interface and insulator-air interface) than they are in the insulator bulk.

Figure 3-5 depicts the band diagram at a metal-insulator interface. A single electron trap level has been included in the forbidden gap. For simplicity, these traps are initially assumed empty and neutral. As the bands are depicted in Figure 3-5, electrons will not tunnel from the conductor into the insulator because the traps are located at a higher energy than the electrons in the conduction band.

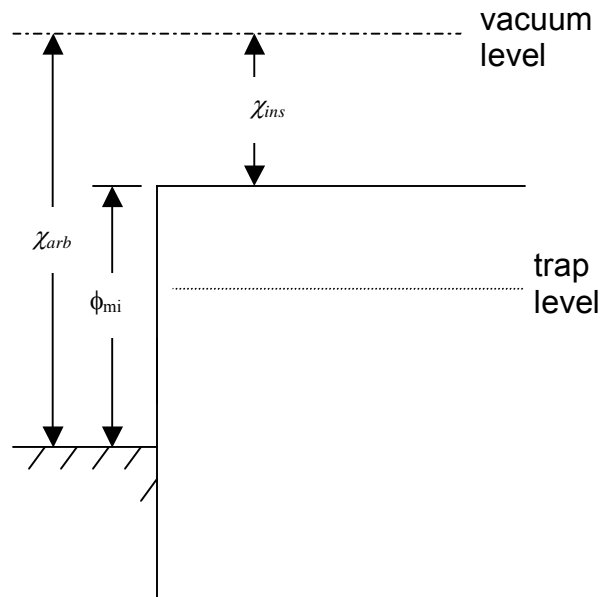


Figure 3-5: Band diagram at metal-insulator interface in flat band condition

For an electron to tunnel from the metal conduction band into an insulator trap, the energy of the trap must be aligned with the conduction band. This is accomplished when a large enough bias is applied between the top and bottom contacts. Applying a negative voltage to the top contact bends the bands down. When the bias is large enough and the bands bend enough, some of the traps overlap with the conduction band as depicted in Figure 3-6. The arrow on this figure indicates this transition. In this and the figures that follow, the positive bias is applied to the opposite contact (not shown). This is consistent with MIS and MEM experiments. Also, only a conduction band has been depicted on the conductor side of the interface. This is for simplicity; when a MIS capacitor is tested, a valence band also exists.

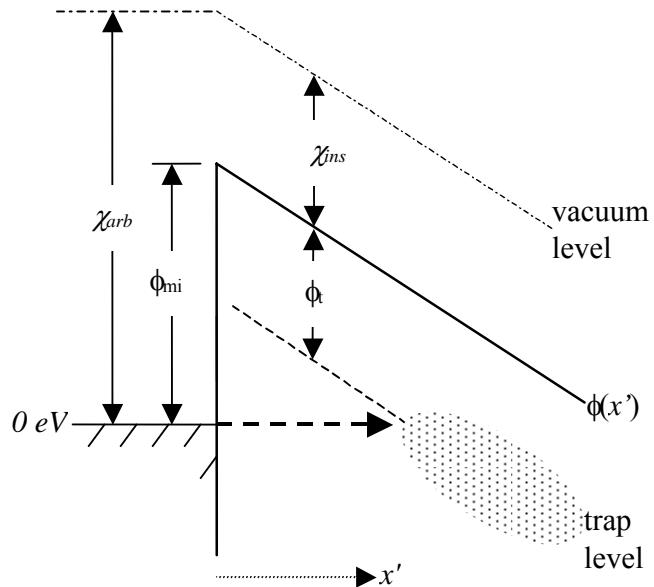


Figure 3-6: Band diagram at metal-insulator interface under a positive bias applied to opposite contact (not shown)

All traps to the right of the arrow (shaded area) overlap the conductor conduction band and can participate in tunneling; the traps to the left cannot participate in tunneling. As the bias increases, the bands bend further allowing the participation of additional traps that were previously unable to communicate with the conductor. This aspect provides voltage dependence to the model.

Describing this concept mathematically requires the development of relationships for the insulator conduction band and trap site energy. The equation that describes the energy of the insulator conduction band as a function of depth, x , relative to the conductor's conduction band is

$$\phi(x) = \phi_{mi} + \frac{V_a}{d}x, \quad (3-5)$$

where

$\phi(x)$ is the potential barrier as a function of insulator depth [eV],
 ϕ_{mi} is the barrier at the interface [eV],
 V_a is the applied voltage as it is applied to the contact [V], and
 d is the thickness of the insulator [cm].

The trap energy relative to the conductor's conduction band, $\phi_t(x)$, is determined by subtracting the trap energy, ϕ_t , from the conduction band energy, $\phi(x)$, as shown in equation (3-6)

$$\phi_t(x) = \phi(x) - \phi_t. \quad (3-6)$$

When $\phi_t(x) \leq 0$, tunneling into these trap sites is possible.

With the basics of tunneling and the problem's geometry established, a mathematical description of tunneling is developed. To begin, an equation for the transition rate of carriers transiting into the insulator is given in equation (3-7). This

transition rate is proportional to 1) the probability of tunneling, 2) the number of available sites, and 3) frequency of attempts to tunnel as shown [10]

$$T(x,t) = P(x,t) n_a(x,t) f \quad (3-7)$$

where

$T(x,t)$ is the transition rate [$\text{cm}^{-3} \text{ sec}^{-1}$],
 $P(x,t)$ is the probability of a transition occurring [-],
 $n_a(x,t)$ is the density of traps available for tunneling [cm^{-3}], and
 f is the tunneling frequency [sec^{-1}].

Each term from this equation is presented in detail in the paragraphs that follow. This discussion includes assumptions that simplify the equation to a point that it can be implemented in a computer program to model charging.

$P(x,t)$ is the probability a carrier will tunnel from conductor into the insulator. Tunneling probability is a function of barrier shape, $\phi(x)$, and depth into the insulator. It is assumed that probability is independent of time, $P(x)$. The implication of this assumption is that barrier height, ϕ_{mi} , is independent of applied bias. This is a reasonable assumption for the large barrier height at the metal-insulator interface [10]. The time independent probability of tunneling through a potential barrier, approximated using the Wentzel-Kramer-Brillouin (WKB) method [8], is given in (3-8). The insulator depth where $\phi_l(x)=0$ is identified as x_o . x_o is the insulator depth where the probability of tunneling, $P(x)$, switches from zero to non-zero, or

$$P(x) = \begin{cases} 0, & x < x_o \\ \text{Exp} \left(-2 \int_0^x \left(\frac{2mq\phi(x')}{\hbar^2} \right)^{1/2} dx' \right), & x \geq x_o \end{cases} \quad (3-8)$$

where

m is the effective mass of the carrier [kg],
 q is the elementary charge [1.6022×10^{-19} C], and

\hbar is Planck's constant [1.05457×10^{-34} J·s].

Note that time independence also means x_o is independent of time. This is discussed further in Chapter 6.

The probability function for this geometry can be determined by inserting (3-5) into (3-8) and integrating. This yields

$$P(x) = \text{Exp} \left(-\frac{4d}{3V_a \hbar} \sqrt{2mq} \left[\left(\phi_{mi} + \frac{V_a}{d} x \right)^{3/2} - \phi_{mi}^{3/2} \right] \right). \quad (3-9)$$

An even simpler case occurs when the barrier is assumed to be rectangular. One implementation of this assumption is to set $\phi(x')$ equal to the average of ϕ_{mi} and ϕ_t for all x' . In this case, equation (3-8) simplifies to

$$P(x) = \text{Exp} \left[-2 \left(\sqrt{\frac{2mq(\phi_{mi} + \phi_t)/2}{\hbar}} \right) x \right]. \quad (3-10)$$

A special case of this probability function occurs when the bias is large enough to make $\phi(x)$ equal zero. In this case, a triangular barrier is formed, and charge can tunnel through the triangular barrier. Tunneling through a triangular barrier is referred to as Fowler-Nordheim tunneling and is shown in Figure 3-7. Once through, the carrier is free to travel in the insulator's conduction band.

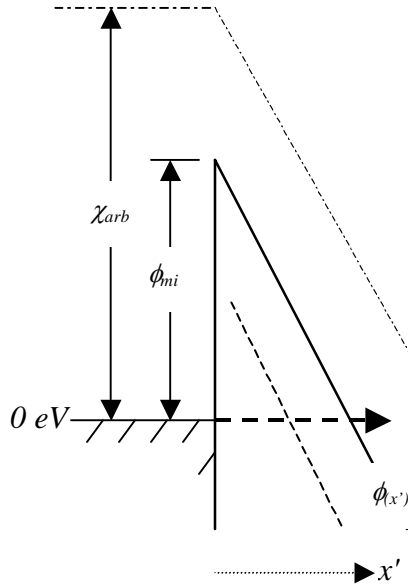


Figure 3-7: Band diagram illustrating Fowler-Nordheim tunneling mechanism

$n_a(x,t)$ from (3-7) is also the density of trap sites not filled. Assuming the total trap density is independent of insulator depth and time, $n_a(x,t)$ is given by

$$n_a(x,t) = N - n_t(x,t) \quad (3-11)$$

where

N is the total density of traps (cm^{-3}), and
 $n_t(x,t)$ is the density of filled traps (cm^{-3}).

The last parameter in the transition rate equation is tunnel frequency, f . A trap time constant, τ_o (sec), provides an average time per tunneling event. An estimate of τ_o is the inverse of the vibrational frequency of a carrier in the trap, $\tau_o=1/\nu$. The vibration frequency, ν , is estimated with $q\phi/(2\pi\hbar)$ [9]. For example, a 1 eV trap yields a time constant of 4×10^{-15} s.

Combining these three components together yields the time and depth dependent trap filling rate. Assuming no other processes are involved in filling or emptying these traps, the instantaneous change in filled trap density equals the transition rate [10]

$$\frac{\partial n_t(x,t)}{\partial t} = \frac{P(x,t) (N - n_t(x,t))}{\tau_o} \quad (3-12)$$

Equation (3-12) can be solved to yield a time and space dependent expression for trapped charge density assuming trap sites are initially empty, i.e. $n_t(x,0) = 0$, and produce the solution given by equation (3-13)

$$n_t(x,t) = N \left(1 - e^{-\frac{-P(x)}{\tau_o} t} \right) \quad (3-13)$$

Initially, the trapped charge density is zero for the entire insulator thickness. As a bias is applied, the trapped charge density increases based on how long the bias is applied and on the trap site distribution.

At $t = 0^+$, the tunneling rate is at a maximum since the rate is proportional to N .

Equation (3-14) expresses the initial charging rate as

$$\frac{\partial n_t(x,0)}{\partial t} = \frac{P(x)N}{\tau_o}. \quad (3-14)$$

Slightly later, at time dt , some traps have filled. Therefore, the tunneling rate is no longer proportional to N . Instead, the rate is smaller, because it is proportional to $N-n_t(x,dt)$ as shown in equation (3-15)

$$\frac{\partial n_t(x,dt)}{dt} = \frac{P(x)(N - n_t(x,dt))}{\tau_o}. \quad (3-15)$$

The tunneling probability continues to decrease as $n_t(x,t) \rightarrow N$. Equation (3-15) can be

substituted for the $\frac{\partial n_t(x,t)}{\partial t} \Big|_{Interface}$ term in equation (3-4).

Bulk Conduction

The next subsection discusses the transport processes occurring in the bulk insulator. Sze was the first to describe bulk charge transport in silicon nitride films [11]. He stated that three transport mechanisms contribute to this current: 1) Poole-Frenkel effect, 2) field ionization, and 3) thermal hopping - each discussed below.

Poole-Frenkel

Poole-Frenkel effect is the “field-enhanced thermal excitation of trapped electrons into the conduction band [11:2952].” To illustrate, an insulator trap site under the influence of an electric field is shown in Figure 3-8. In figure a), a small electric field is present, and the carrier’s thermal energy is small compared to the trap depth. Therefore, the carrier remains trapped. In figure b), the applied electric field lowers the barrier to the point that the carrier’s thermal energy is adequate to allow escape from the trap. Now, the carrier can transit the insulator’s conduction band until another site traps it or it leaves the insulator.

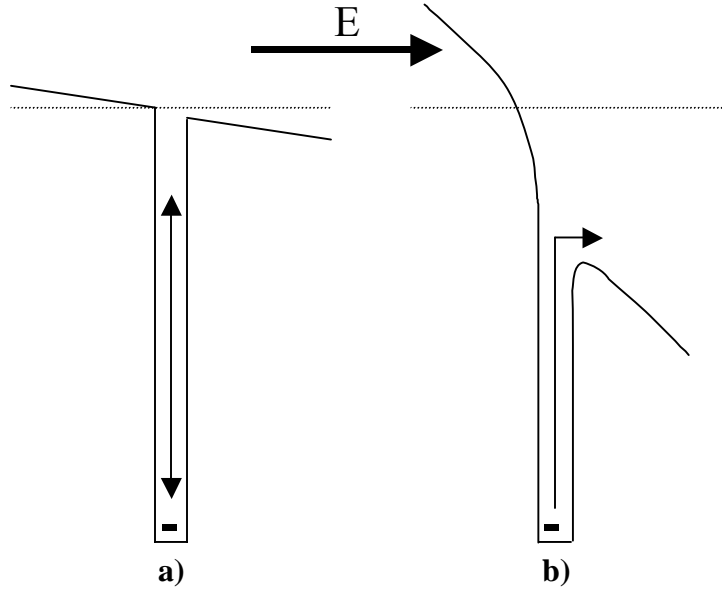


Figure 3-8: Field enhanced barrier lowering (Poole-Frenkel). Dashed line is conduction band in flat band condition.

The rate of detrapping from the Poole-Frenkel effect is given by [12]

$$\left. \frac{\partial n_t(x,t)}{\partial t} \right|_{P-F} = n_t(x,t) \cdot v \cdot \exp\left[-\frac{q}{kT}(\phi_t - \sqrt{\frac{qE}{\pi\epsilon_r\epsilon_0}})\right] \quad (3-16)$$

where

v is the vibration frequency of a carrier (s^{-1}),
 ϕ_t is the trap depth (eV),
 k is Boltzmann's constant ($1.3806503 \times 10^{-23} \text{ m}^2 \text{ kg s}^{-2} \text{ K}^{-1}$),
 ϵ_r is the relative dielectric constant of the insulator,
 ϵ_0 is the permittivity of free space ($8.85 \times 10^{-12} \text{ F/m}$), and
 E is the local electric field (V/m).

The $\sqrt{\frac{qE}{\pi\epsilon_r\epsilon_0}}$ term accounts for barrier lowering. This mechanism is extremely dependent

on both sample temperature and applied electric field [11][13][16]. Using case b) as an example, if the temperature had been significantly lower (i.e. lower thermal energy), the carrier's thermal energy (vertical motion on figure) would have been significantly less

not allowing it to leave. Therefore, this mechanism freezes out at low temperatures, and dominates at higher temperatures (>325 K) and high fields (> 1 MV/cm) [11].

Field Ionization and Thermal Assisted Tunneling

At lower temperatures, field ionization dominates [14]. Field ionization occurs when the electric field bends the insulator bands enough that a triangular barrier is formed as shown in Figure 3-9 (also see Fowler-Nordheim tunneling described in 0). If the barrier is thin enough, the carrier tunnels through the base of the triangular barrier and into the conduction band. Since this process does not require any additional thermal energy, it is independent of temperature [11:2952].

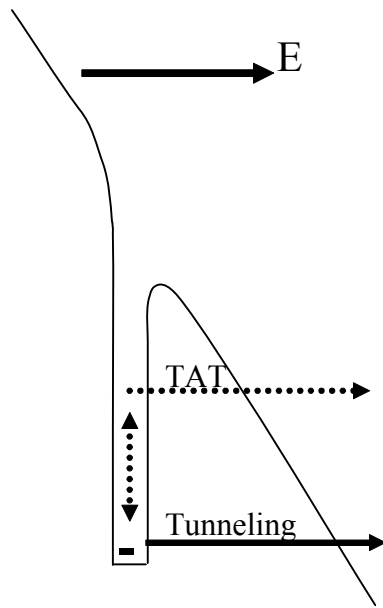


Figure 3-9: Band diagram illustrating field ionization mechanism

To quantify this detrapping mechanism, an approach similar to interface tunneling is used based on equation (3-12). A WKB approximation of tunneling probability yields

$$P = -\frac{4\sqrt{2m}}{3qh} \frac{\phi_t}{E}. \quad (3-17)$$

Substituting this probability into equation (3-12) yields a detrapping rate of

$$\left. \frac{\partial n_t(x,t)}{\partial t} \right|_{FI} = -\frac{4\sqrt{2m}}{3qh} \frac{\phi_t}{E} \frac{n_a(x,t)}{\tau_o} \quad (3-18)$$

Notice the field ionization rate depends on the density of trapped charge, i.e. a trap must be filled for a detrapping event to take place. “Thermal-assisted tunneling,” or TAT, is a similar process but requires additional thermal energy. The thermal energy provided by an elevated temperature allows the carrier to reach a narrow enough portion of the triangular barrier that the carrier is capable of tunneling through [13].

Hopping (Ohmic)

Hopping is a process where trapped carriers possess enough energy to tunnel into an adjacent trap site [11][14]. It dominates at low electric fields. Figure 3-10 shows a carrier hopping into an adjacent trap.

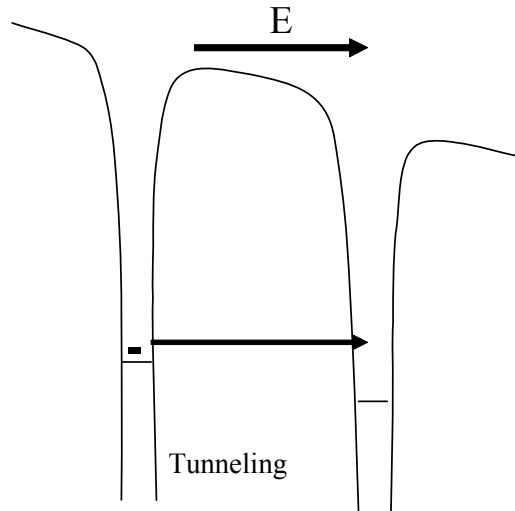


Figure 3-10: Band diagram illustrating the hopping mechanism

In hopping, current varies linearly with voltage, so it is often referred to as ohmic conduction. The hopping rate is given by

$$\left. \frac{\partial n_t(x,t)}{\partial t} \right|_{Hop} = \frac{n_a(x,t)}{\tau_o} \exp\left(\frac{-\phi_a}{kT}\right) \quad (3-19)$$

where ϕ_a is the thermal activation energy of the trap site.

Trapping

For Poole-Frenkel and field ionization emission, electrons reach the insulator conduction band and travel toward the bottom conductor. While they are transiting the conduction band, another site can trap the carrier. Trapping occurs when a free carrier moving in the conduction band approaches a coulombic trap in the forbidden band. Trapping is proportional to the density of free carriers, thermal velocity, the density of unfilled traps, and the trap's capture cross-section [15]. This term is written as

$$\left. \frac{\partial n_t(x,t)}{\partial t} \right|_{Trap} = n_c(x,t) \cdot \sigma \cdot v_{th} \cdot (N - n_t(x,t)), \quad (3-20)$$

where

$n_c(x,t)$ is the density of free carriers [cm^{-3}],
 σ is the capture cross-section [cm^2], and
 v_{th} is the carrier's thermal velocity [cm/sec],

Detrapping

When a bias is applied to the capacitor for an extended period of time, a considerable amount of charge becomes trapped. When the bias is removed, the insulator retains this trapped charge. Figure 3-11 illustrates the effect of trapped charge on the local electric field. With no bias applied, the electric field should be 0 V/ μm ; however, the electric field is distorted where the trapped charge is located (this charge density produced a voltage shift of -0.03 V).

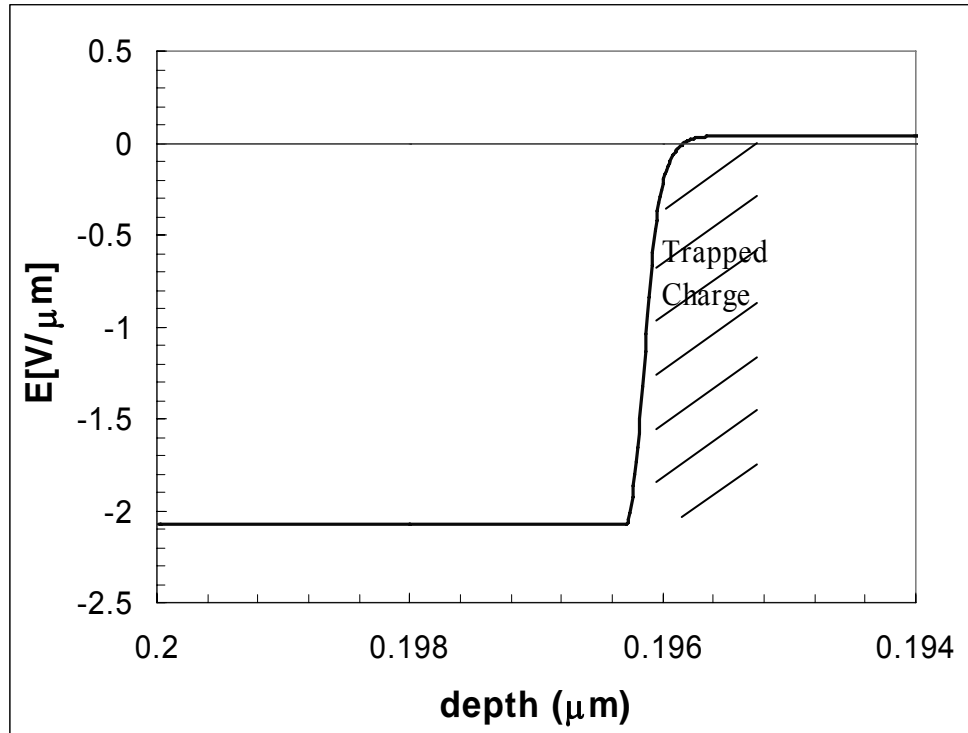


Figure 3-11: Calculated local electric field under 0V bias but with holes trapped in insulator. Shaded region represents where trapped charge is located.

With time, this charge dissipates. Since most of the charge is trapped in near surface states, one dissipation mechanism involves charge tunneling back to the conductor from the insulator. Other possible mechanisms for charge dissipation include ohmic conduction where carriers tunnel into adjacent trap sites, and electron-hole recombination [9].

Detrapping takes much longer than the time required to charge the insulator. The rate of tunneling into the insulator is proportional to the density of available traps, and at the start of charging all traps were available. The rate of tunneling out of the insulator is proportional to the density of filled traps. Since the filled trap density is always less than the density of trap sites, the detrapping rate will be less than the trapping rate.

Detrapping can be expedited by applying an opposite polarity bias. This is an example of tunnel annealing [7].

Summary

The charging mechanisms presented depend largely on electric field and temperature. Hopping conduction dominates in high temperature, low field conditions (<1 MV/cm). Field ionization dominates in low temperature situations. Poole-Frenkel dominates in high field conditions (>1.5 MV/cm) [11][16], so authors have pointed to this as a likely cause of MEM switch failure [4]. In this research, the highest fields reached were between 1.5 and 2 MV/cm. Only at these peak fields would Poole-Frenkel emission begin to dominate the insulator's charging behavior. The temperatures ranged from 5 °C to room temperature, which is low for Poole-Frenkel. Meanwhile, interface tunneling is independent of temperature. Therefore, it is reasonable to assume charging in MEM switches can be modeled with interface tunneling. This simplification is supported by other work in silicon nitride [10] where the tunneling model was successfully applied up to fields of 5 MV/cm.

In MEM operations, the switch spends a large fraction of the time in an unbiased state. Assuming the insulator charges, detrapping is likely to occur to some extent during the zero bias state. Therefore, this mechanism will also be discussed later.

3.4. Expectations from Model

A computer program was written to model MNS capacitor charging assuming carriers that tunnel from the conductor into insulator trap sites are responsible for charging. The program calculates the density of charge trapped in the insulator over time at a given applied bias. Assumptions made include a uniform distribution of traps in the

0.2×10^{-5} cm layer of silicon nitride closest to the silicon interface and mono-energetic traps. When a positive bias is applied, only electron trapping is tracked; when a negative bias is applied, hole trapping is tracked. This program does not model charge dissipation mechanisms. Refer to Chapter 6 for more details on this program.

Figure 3-12 shows the effect various negative applied biases have on charging. When the bias is initially applied, an abrupt voltage shift occurs. Approximately 80% of maximum charging occurs in the first time step due to the availability of unfilled trap sites early in testing. Over time, the density of empty trap sites decreases so the rate of charging also decreases. Larger applied bias magnitudes produce larger voltage shifts, because the voltage makes more trap sites available for tunneling. The program predicts essentially no charging when -10V is applied; the -10V curve cannot be differentiated from the time axis. The -20V and -30V curves initially shift approximately -5V and -7V , respectively. They both vary logarithmically for the remainder of the 900 seconds of calculation. The -20V curve shifts an additional -1.5V while the -30V curve shifts approximately -2V .

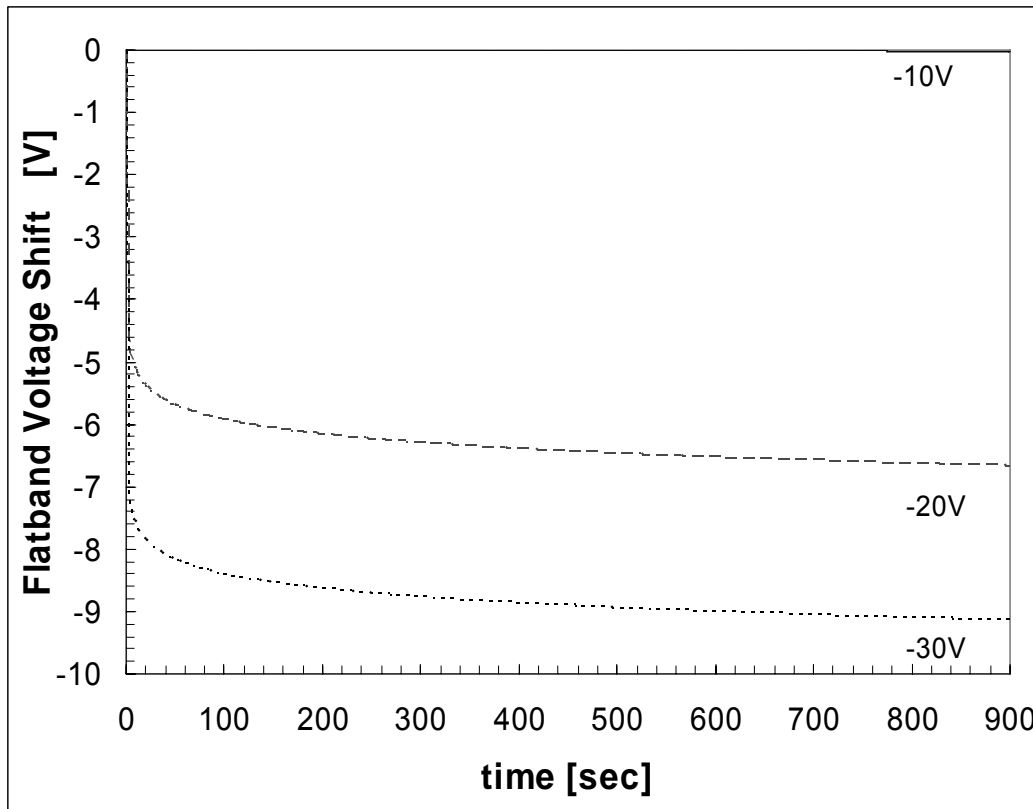


Figure 3-12: Calculated MNS charging behavior with negative applied biases (-10V curve at $\Delta V=0$), trap energy of 2.98 eV, and trap density of $2 \times 10^{19} \text{ cm}^{-3}$

Figure 3-13 shows the model results when a positive bias is applied. In this case, electrons trap in the insulator causing a positive shift of the CV curve. Unlike the -10V curve, the 10V case shows enough charging to separate from the time axis. The 20V and 30V curves initially shift 13V and 21V, respectively. After the initial shift, the 20V curve continues to increase another 2V, and the 30V curve increases an additional 7V.

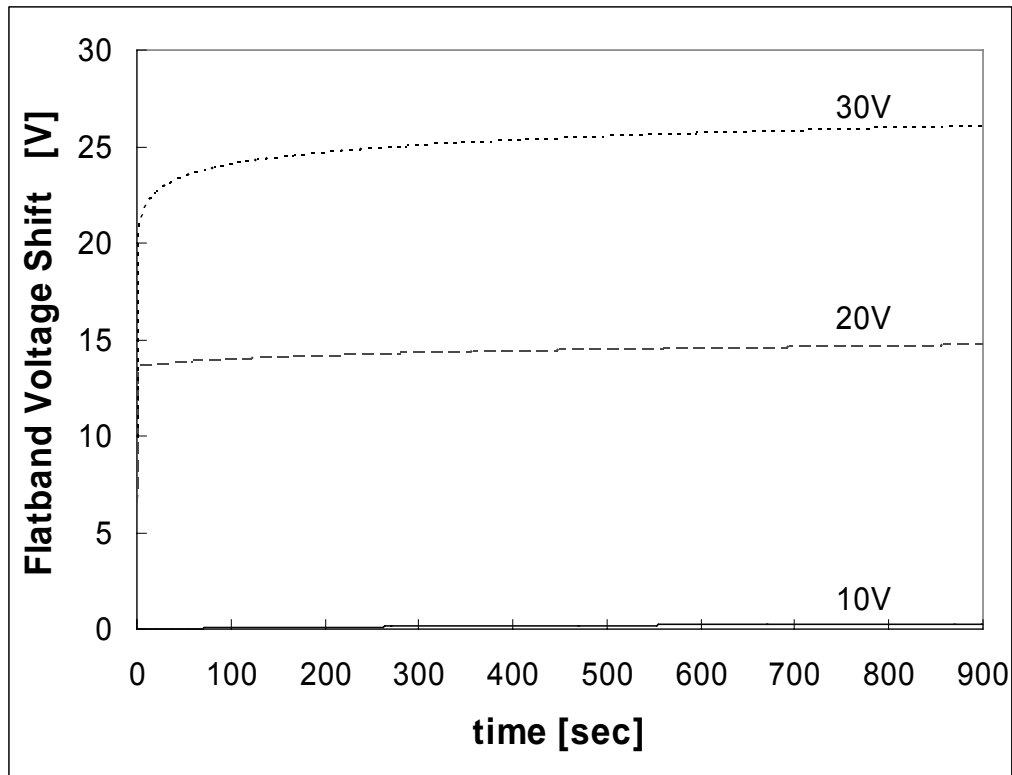


Figure 3-13: Calculated MNS charging behavior for positive applied voltages, trap energy of 2.98 eV, and trap density of $2 \times 10^{19} \text{ cm}^{-3}$

For MNS capacitors, there are a number of differences between positive and negative voltages of the same magnitude. A p-type silicon substrate is in accumulation when biased negatively and in inversion when biased with a positive bias. In accumulation, very little of the applied voltage drops across the silicon because majority carriers have accumulated at the interface. On the other hand, in inversion, the charge needed to balance the applied voltage comes from uncovering silicon atoms in the bulk. Therefore, in accumulation, nearly all of the applied bias drops across the insulator; in inversion, a portion of the voltage also drops in the silicon. This means that the same applied voltage magnitude produces different electric field magnitudes in the insulator

depending on bias polarity. For example, in p-type material a +20V applied bias produces a 0.9571 MV/cm electric field, while a -20V bias produces a 0.9844 MV/cm field.

The band structure also produces differences. The barrier height for a tunneling hole is 0.1 eV greater than the barrier to a tunneling electron. The effective mass of an electron and hole are also different in silicon nitride. Therefore, differences between Figure 3-12 and Figure 3-13 are not surprising.

Once a capacitor is fabricated, the only physical parameters that can be controlled during an experiment are the applied bias and the amount of time the bias is applied. Meanwhile, material properties are fixed but not well known, e.g. trap energy and trap density. The program has been run for a number of cases to show the effect material property uncertainty has on insulator charging.

Figure 3-14 examines changes in total trap site density. In this case, the bias is maintained at -20 volts and the trap energy is 1.98 eV. Since charging rate is proportional to the number of available trap sites, it is expected that a larger trap density results in a faster charging rate. Also, for a given voltage and bias time, more available trap sites lead to more trapped charge.

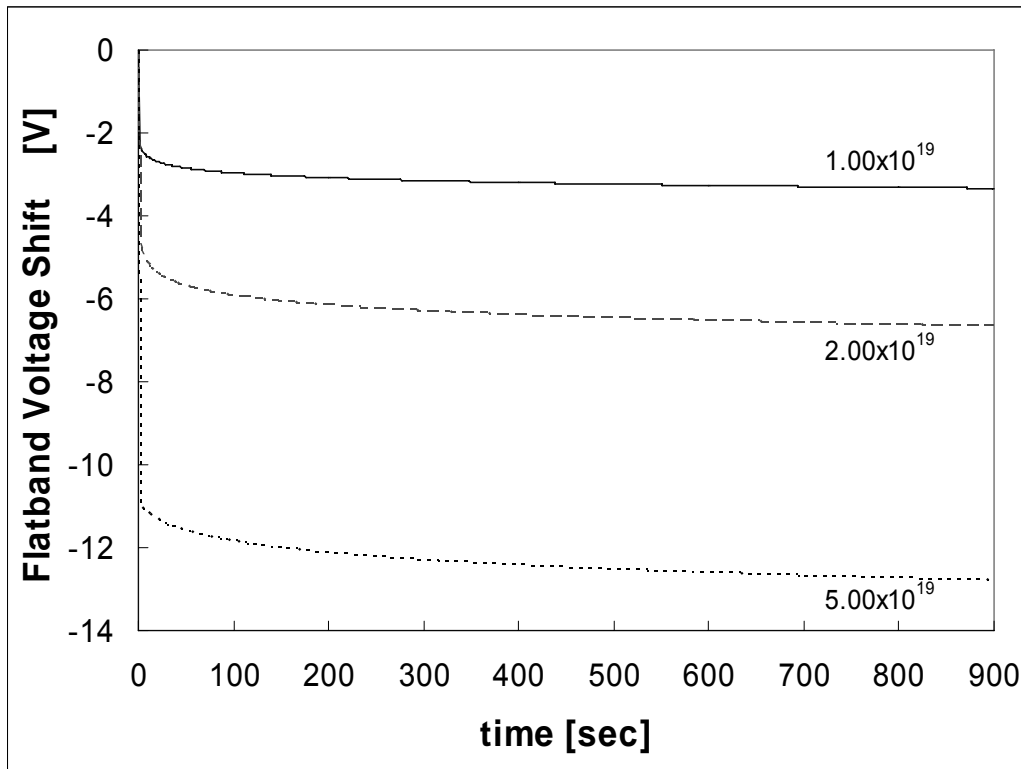


Figure 3-14: Effect of trapped charge density on charging behavior, trap energy of 2.98 eV, and applied voltage of -20V

Figure 3-15 shows the effect trap energy has on model results. In these calculations, the applied voltage is -10 V, the hole trap density is maintained at 1×10^{19} traps/cm³, and the hole trap energy varies between 2.9 eV and 3.04 eV. Deeper traps produce greater voltage shifts. Since the condition stated in equation (3-6) for a non-zero tunneling probability is reached at shorter distances from the silicon interface, a larger number of traps are able to participate in tunneling.

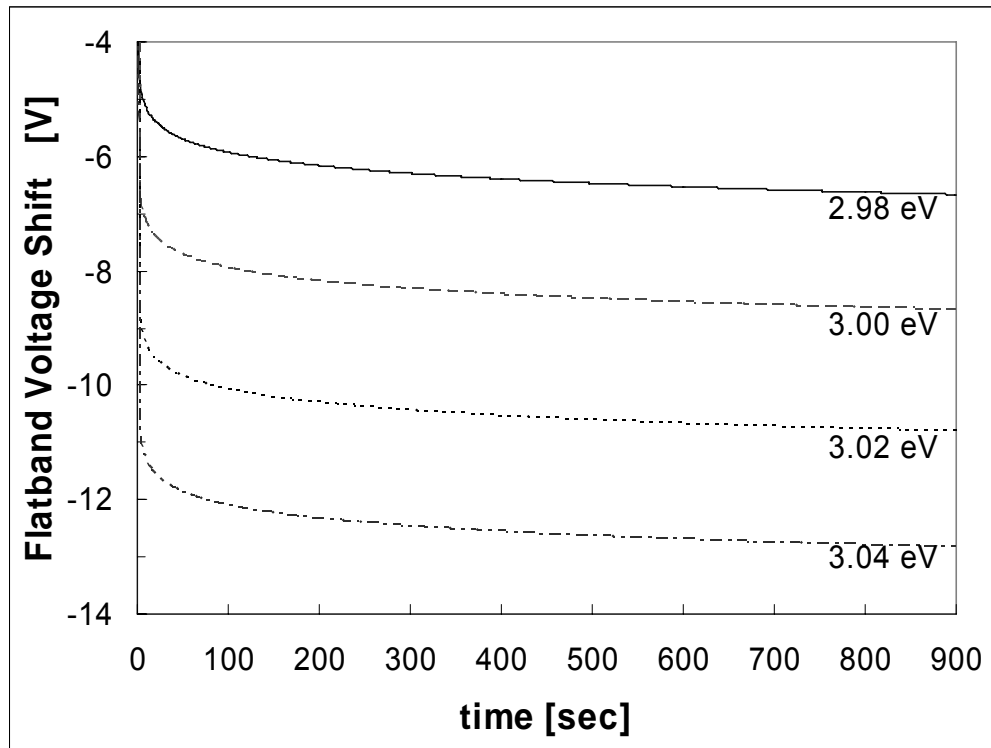


Figure 3-15: Effect of trap depth on charging behavior, trap density of $2 \times 10^{19} \text{ cm}^{-3}$, and applied voltage of -20V

Two categories of variables were modeled in this section: 1) variables from the experiment (applied bias and time), and 2) fixed material properties which are not well known. It was shown that bias magnitude and polarity each have a dramatic effect on the charging behavior of the insulator. Temporal dependence of charging cannot be avoided; its importance is great early in biasing, but diminishes with extended biasing. Trap densities and energies were also compared.

Bibliography

1. Reid, J.R. "Simulation and Measurement of Dielectric Charging in Electrostatically Actuated Capacitive Microwave Switches," *Proceedings Modeling and Simulation of Microsystems*, 250-253 (April 2002).
2. Reid, J.R. and R.T. Webster. "Measurement of Charging in Capacitive Microelectromechanical Switches," *Electronics Letters*, 38: 1544-1545 (21 November 2002).
3. Chan, E., K. Garikipati, and R. Dutton. "Characterization of Contact Electromechanics Through Capacitance-Voltage Measurements and Simulations," *Journal of Microelectromechanical Systems*, 8: 208-217 (June 1999).
4. Goldsmith, C., J. Ehmke, A. Malczewski, B. Pillans, S. Eshelman, Z. Yao, J. Brank, and M. Eberly. "Lifetime Characterization of Capacitive RF MEMS Switches," *2001 IEEE MTT-S Digest*, 227-230 (2001).
5. Sze, S.M. *Semiconductor Devices: Physics and Technology*. New York: Wiley, 1985.
6. Neaman, Donald A. *Semiconductor Physics and Devices*. Boston: McGraw, 1997.
7. Ma, T.P. and Paul V. Dressendorfer. *Ionizing Radiation Effects in MOS Devices and Circuits*. New York: Wiley, 1989.
8. Svensson, C. and I. Lundstrom. "Theory of the Thin-Oxide MNOS Memory Transistor," *Electronics Letters*, 6: 645-647 (1 October 1970).
9. Lundkvist, L., I. Lundstrom, and C. Svensson. "Discharge of MNOS Structures," *Solid-State Electronics*, 16: 811-823 (1973).
10. Buchanan, D.A., R.A. Abram, and M.J. Morant. "Charge Trapping in Silicon-Rich Si_3N_4 Thin Films," *Solid-State Electronics*, 30: 1295-1301 (1987).
11. Sze, S.M. "Current Transport and Maximum Dielectric Strength of Silicon Nitride Films," *Journal of Applied Physics*, 38: 2951-2956 (June 1967).
12. Williams, Ross A. and Moiz M. E. Beguwala. "The Effect of Electrical Conduction on Si_3N_4 on the Discharge of MNOS Memory Transistors," *IEEE Transactions on Electron Devices*, ED-25: 1019-1023 (August 1974).
13. Manzini, S. "Electronic Processes in Silicon Nitride," *Journal of Applied Physics*, 62: 3278-3284 (15 October 1987).

14. Hesto, P. "The Nature of Electronic Conduction in Thin Insulating Layers," in *Instabilities in Silicon Devices*, vol 1. Ed. G. Barbottin and A. Vapaille. Amsterdam: North-Holland, 1986.
15. Arnett, P. C. "Transient Conduction in Insulators at High Fields," *Journal of Applied Physics*, 46: 5236-5243 (December 1975).
16. Scarpulla, J., E. D. Ahlers, D. C. Eng, D.L. Leung, S. R. Olson, and C. S. Wu. "Dielectric Breakdown, Defects and Reliability in SiN MIMCAPs," *Proceedings of the 1998 GaAs Workshop*, 92-105 (1998).

4. Experimental Setup

4.1. Introduction

The previous chapters discussed theoretical aspects of insulator charging. This chapter provides details of the experiments used to measure insulator charging. The experiment to measure MEM charging is based on a technique developed by Reid [1][11]. Additionally, the experiments performed in this research were expanded to include new actuation waveforms, which help gain greater insight into the nature of insulator charging. The Air Force Research Laboratory's Aerospace Components and Subsystems Technology Division (AFRL/SND) developed the switches tested in this research and are at the forefront of MEM switch technology. While the performance of these switches is much better than most other technologies, there is still much variability between individual switches and even greater variability between wafers. Therefore, making reproducible and conclusive charging measurements on RF MEM capacitive switches is challenging. In addition, these switches are a limited resource.

In an effort to isolate the charging behavior of the insulator, metal-silicon nitride-silicon (MNS) capacitors were fabricated and tested. The MNS silicon nitride layer was deposited with the same equipment AFRL/SND uses to fabricate capacitive switches. This silicon nitride also shares the same thickness as the switch's insulating layer. While the same insulating material was used for both devices, device differences necessitate using different test methodologies for each device type.

4.2. MNS Experiment

The experimental method for investigating insulator charging in MEM switches is complicated, requires special equipment and parts, and does not lend itself to testing in hostile environments (e.g. radiation). Testing switches also consumes a limited resource – the switches themselves. Using MNS capacitors is a simpler test that isolates insulator charging effects. This section describes the experiment used to evaluate insulator charging with MNS capacitors.

Material Data

The MNS capacitors were built on p-type silicon wafers. The substrate was doped with boron to a resistivity of 0.008 to 0.02 $\Omega\text{-cm}$. A 15 to 18 μm thick silicon epilayer was then grown on top and doped to a resistivity of 30 to 50 $\Omega\text{-cm}$ also with boron. The wafers were initially dipped in hydrofluoric acid to remove unwanted oxides and later degreased with acetone, methanol, and de-ionized water. Then, 0.2 μm of silicon nitride was sputtered onto the epilayer surface by AFRL/SND. 0.2 μm thick metal contacts were fabricated on the top and bottom of the wafer using an Edwards electron beam evaporator at AFIT.

The wafer was diced into smaller pieces so it could fit on the evaporator's 2" diameter sample mount. First, 0.2 μm of aluminum was evaporated onto the entire backside of the silicon substrate (i.e. no silicon nitride). The samples were removed from the evaporator and mounted on a shadow mask for deposition of the front side contacts. The shadow mask is a steel plate with an array of 0.5 mm diameter holes. The front side

contact aluminum thickness was also 0.2 μm . Finally, these wafer pieces were diced by AFRL/SND into even smaller pieces containing two capacitors each.

The MNS capacitors leaving the final fabrication step contained high densities of interface states and bulk charge as determined by a high frequency (100 kHz) CV sweep. Interface states are seen as a shallow slope in the depletion region of the CV curve. Bulk charge appears as horizontal shifts of the CV curve (similar to the RF MEM CV curve).

All capacitors used in this research were baked at 270 °C for three separate 2 minute periods and 350 °C for 2 minutes; all of these bakes were performed in open air on a hot plate. It took some investigation to determine this preparation recipe. The temperature and duration of the three - 270 °C bakes mimics the baking procedure used during MEM switch fabrication. This bake improves interface quality, but there is still a considerable amount of trapped charge present. To reduce the density of bulk trapped charge, the wafer was baked at 350 °C an additional 2 min.

A study was required to determine the 350 °C bake temperature. Multiple capacitors were baked at 100, 150, 200, 260, 300, and 350 °C. Capacitors were not reused. At each temperature, CV sweeps were performed at the following cumulative time intervals of 0, 2, 4, 6, 8, and 13 min.

Figure 4-1 shows the results from the 100 °C series of bakes. 100 °C was used to see if moisture was present in the insulator. Baking at this temperature changes the slope of the CV curve and reduces the accumulation capacitance value from 80 pF to 65 pF. Changes in the curve's slope are explained by decreasing interface states. A decreasing accumulation capacitance is not as clear. In the relationship for capacitance, $C = \frac{\epsilon A}{t_{in}}$,

there are three terms: insulator permittivity, ϵ , capacitor area, A , and insulator thickness, t_{in} . It is unlikely the area of the capacitor changed. It is also unlikely there was a change in insulator thickness since the change in accumulation capacitance is permanent, i.e. when the capacitor is allowed to return to room temperature, accumulation capacitance remains at the lower value. The only parameter left is permittivity. Felix, *et al.* also observed this phenomenon in hafnium silicate and described it as a change in the dipole moment due to trapped water baking out of the insulator [2]. Since this also occurs at 100 °C, their explanation is plausible for this situation.

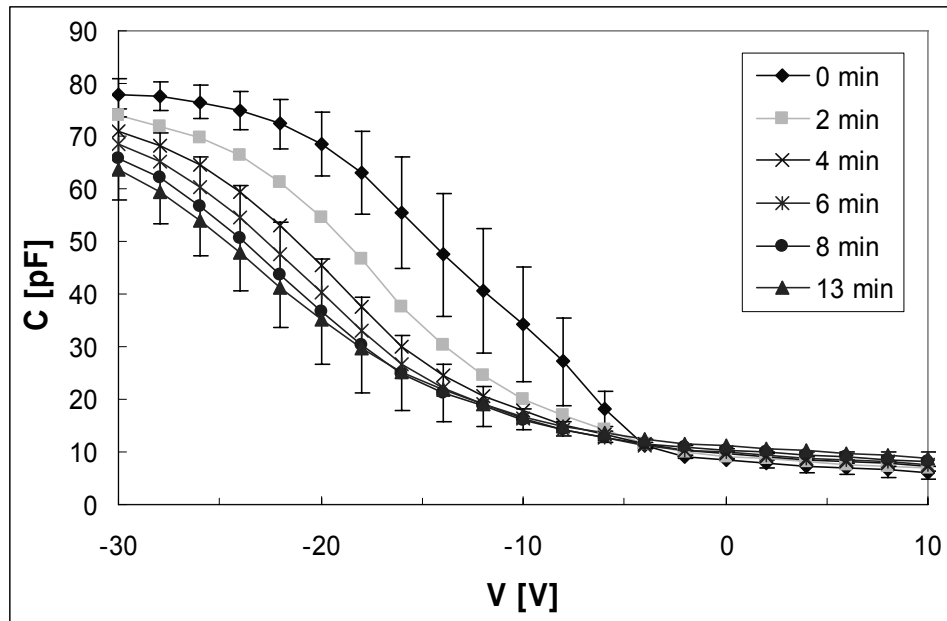


Figure 4-1: Bake results at 100 °C - four capacitors average for 100 kHz CV measurements. Times represent the cumulative number of minutes each capacitor was baked at that temperature.

Figure 4-2 shows the results for the 270 °C bakes. In this case, the drop in accumulation capacitance is apparent - as is the negative shift of the curve after the first 2

min bake which indicates the insulator trap site density increased. However, subsequent bakes at 270 °C cause a rightward shift of the CV curve. The 6 min curve indicates the quality of the insulator at the end of MEM switch fabrication. As bake time increases, the CV curve continues moving right suggesting that additional bake steps may be warranted in the switch fabrication process.

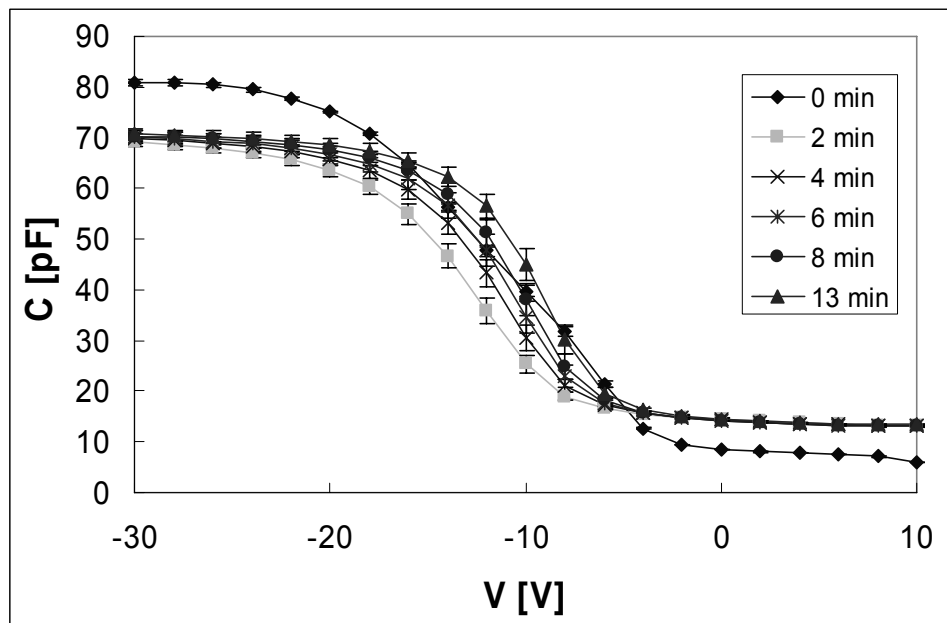


Figure 4-2: Bake results at 260 °C - two capacitors average for 100 kHz CV measurements. Times represent the cumulative number of minutes each capacitor was baked at that temperature.

Figure 4-3 shows the results from a series of 350 °C bakes. Notice these curves are even more vertical than the 270 °C bake curves, indicating even more interface states have annealed. There also appears to be a slight shift of the curve to the right indicating bulk traps have also annealed. Continuing to bake past 2 min at 350 °C does not dramatically improve the curve and even adds a low frequency component to the curve

(the upward portion of the curve at positive bias). Therefore, a single 2 min bake at 350 °C improves the curve dramatically. The bake recipe used in this research was three consecutive two-minute bakes at 270 °C bake for three separate 2 min periods followed by one two-minute bake at 350 °C. All of these bakes were performed in open air on a hot plate.

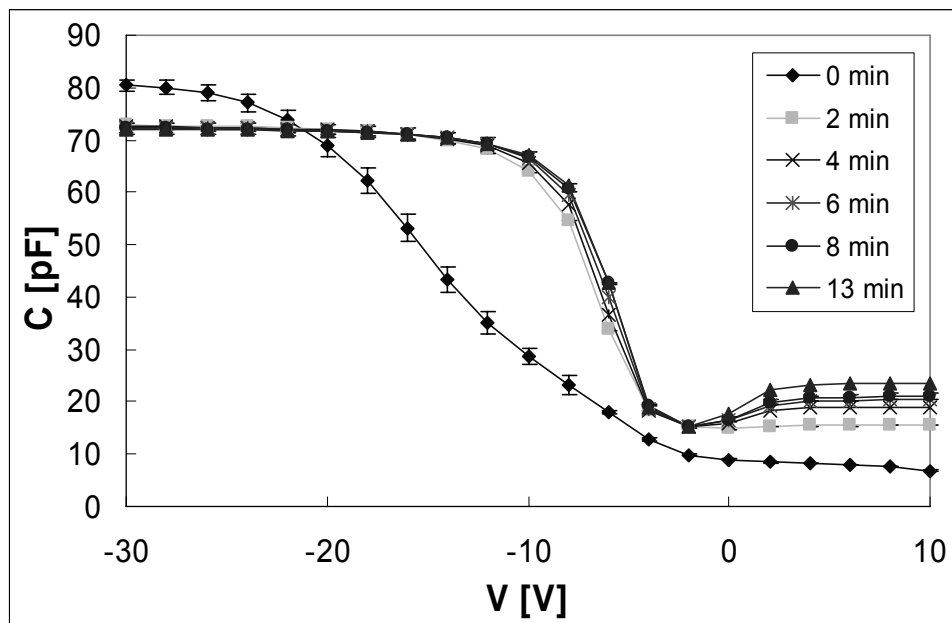


Figure 4-3: Bake results at 350 °C - two capacitors average for 100 kHz CV measurements. Times represent the cumulative number of minutes each capacitor was baked at that temperature.

To close the loop on the changing permittivity argument, the permittivity value calculated from the measured accumulation capacitance is compared to typical permittivity values. The thickness of the deposited silicon nitride layer was measured by AFRL/SNDD using variable-angle spectroscopic ellipsometry. This measurement yielded a thickness of 195.6 ± 1.6 nm. An average thickness of 195.6 nm and final

accumulation capacitance values ranging from 65 to 71 pF yield a dielectric constant between 7.5 and 8. The original, 0 min, accumulation capacitance value places the dielectric constant around 9. Most sources cite a dielectric constant between 7 and 8 [3][4][9].

Test Background

Testing involved biasing the MNS capacitors for extended periods of time and periodically taking high frequency CV sweeps. These CV sweeps were compared to an initial CV sweep to generate plots of flat band voltage shift as a function of bias time. The horizontal shift of successive high frequency CV curves provides an estimate of the trapped charge density. The theory relating voltage shifts to trapped charge density was presented in Chapter 3. The next section describes the equipment setup required to take these measurements.

MNS Experimental Setup

This experiment requires a capacitance measurement and the ability to apply a bias for extended periods of time. The bias was provided by a Keithley 237 Source Measurement Unit (K-237). Capacitance measurements were made with a Keithley 590 Capacitance Measurement System (K-590). The K-590's internal voltage source was not adequate for these tests, so a K-237 was connected to the K-590's external voltage source port when CV sweeps were made. During a given test period, it was desirable to apply two different bias voltages simultaneously (e.g. +20V and -20V). Therefore, a second K-237 was added. Figure 4-4 shows the experimental layout used during the constant biasing portion of the test.

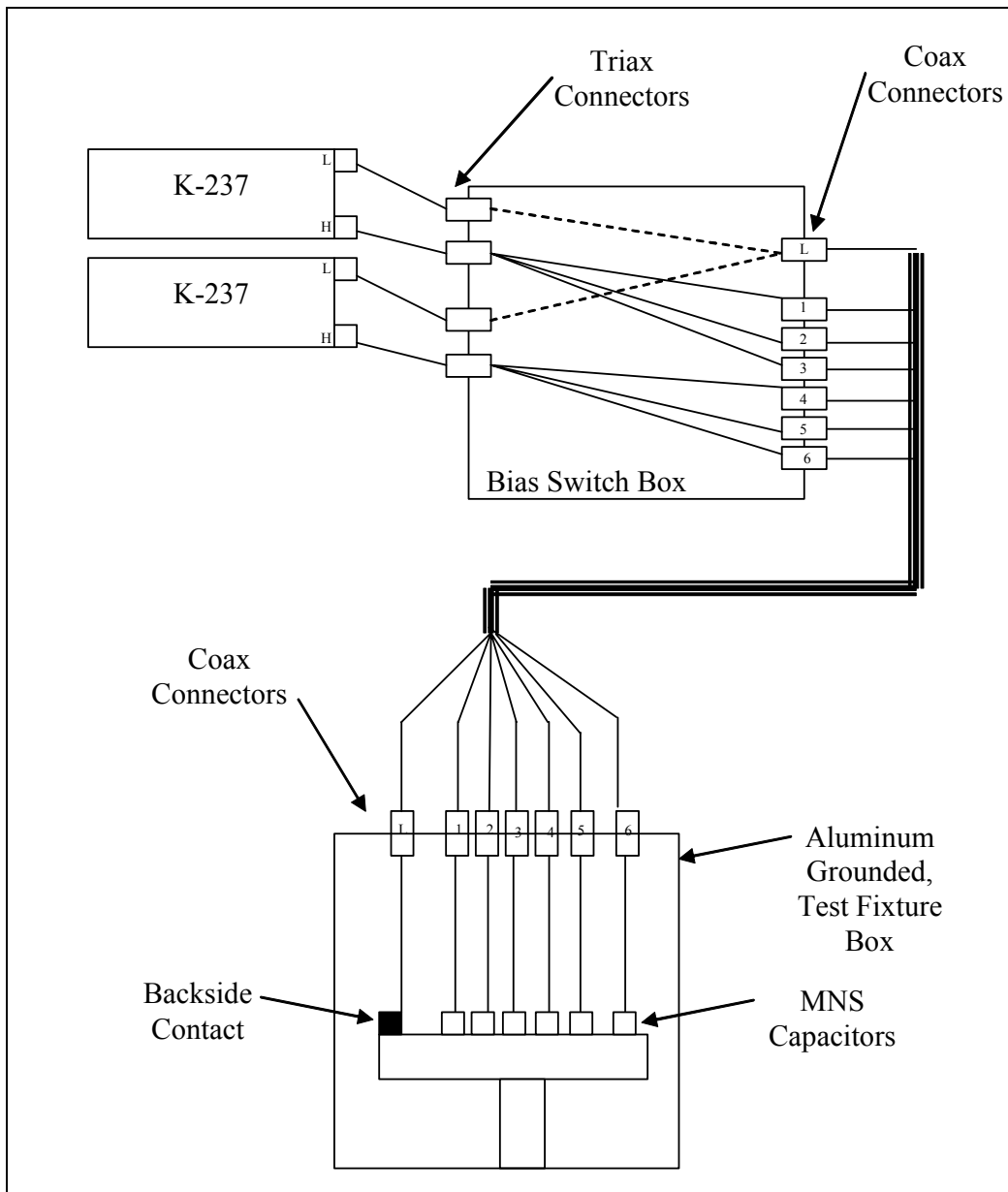


Figure 4-4: Schematic diagram of experimental setup during biasing.

There are four main parts to the setup: 1) two voltage sources, 2) bias switch box which splits incoming tri-axial bias lines into six different output lines that connect to individual capacitors, 3) RG-58 coax cables connect the bias switch box to 4) a hobby box holding the capacitors. The capacitors are mounted to a test fixture that is connected

to the hobby box wall. This ensures the test fixture, hobby box and coax connectors all share common ground. Copper wires connect the coax jacks on the hobby box to tungsten probes which are used to make contact with the capacitor. No data is collected during this portion of the experiment. As shown in Figure 4-5, a slightly different setup is required to make a CV sweep - a K-590 and a K-237 are required.

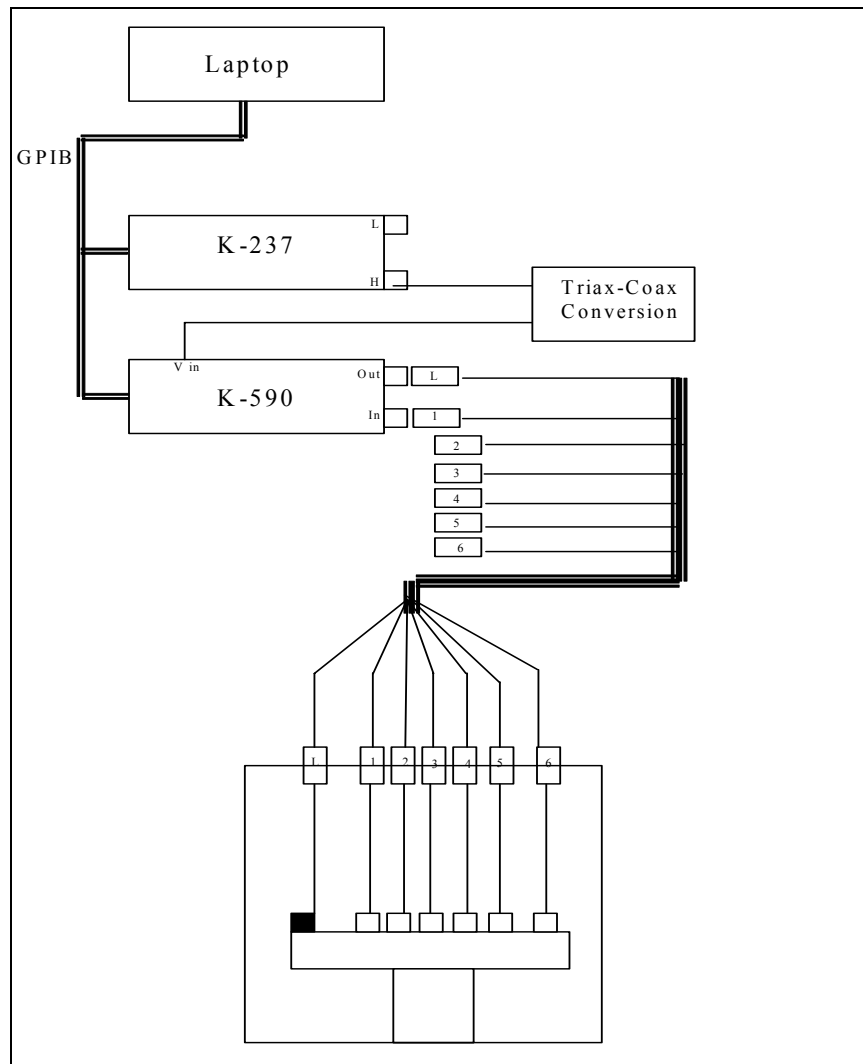


Figure 4-5: Schematic diagram of experiment during CV sweeps. Notice multiple coax leads at the K-590. This indicates that a CV sweep was taken for each capacitor.

The two instruments are controlled via GPIB cables with a program written in LABWINDOWS/CVI [5]. The program controls the two devices, collects the voltage and capacitance data collected by the K-590, displays it in a graphical user interface, and writes it to a Microsoft Excel .csv file.

The experimental setups shown in Figure 4-4 and Figure 4-5 were integrated into a single experiment using the following procedure. The first step is to take a CV sweep on each capacitor using the controller program (i.e. Figure 4-5). Next, the tri-axial cables from the two K-237s are connected to the seven coax cables coming from the test fixture box via the switch box (i.e. Figure 4-4). Once connected, the two K-237s are simultaneously triggered. When the predetermined bias time is over, the low cable is disconnected from the bias switch box and connected to the K-590. The high triax cable from K-237 #1 is disconnected from the bias switch box and is reconnected to the triax-coax conversion box. Capacitor 1's coax cable is connected to the other port of the K-590 (configuring setup back to Figure 4-5). A CV sweep is made on each capacitor. Once all capacitors are measured, the experiment is reconfigured back to Figure 4-4. It takes approximately two minutes to configure the measurement setup, take the six high-frequency CV sweeps, and reconfigure back to the bias setup. After the experiment is reconfigured, the capacitors are biased for the next predetermined bias time. The bias times were 1) 0, 2) 3m 42s, 36m 56s, 3) 3h 4m 38s, and 4) 6h 9m 16s. These bias times were determined by the amount of time required to reach irradiation total dose levels of 0, 100, 500, and 1000 krad[SiO₂], respectively, in Ohio State University's cobalt-60 source (further information is available in Appendix B).

4.3. RF MEM Experiment

This section provides details of the capacitive switch experiment. This includes details on the switches tested, equipment setup, testing philosophy, specific experimental parameters, and concludes with issues and weaknesses of this testing technique.

Material Data

AFRL/SND designed, developed the production process, and fabricated the capacitive switches tested. Their identification for this particular wafer design is SNC-02. Most measurements in this work were made on wafer 2 of this design (SNC-02/02). Both SNC-02 wafers were built on sapphire substrates. Figure 4-6 shows a schematic cross sectional view of a switch with typical dimensions indicated.

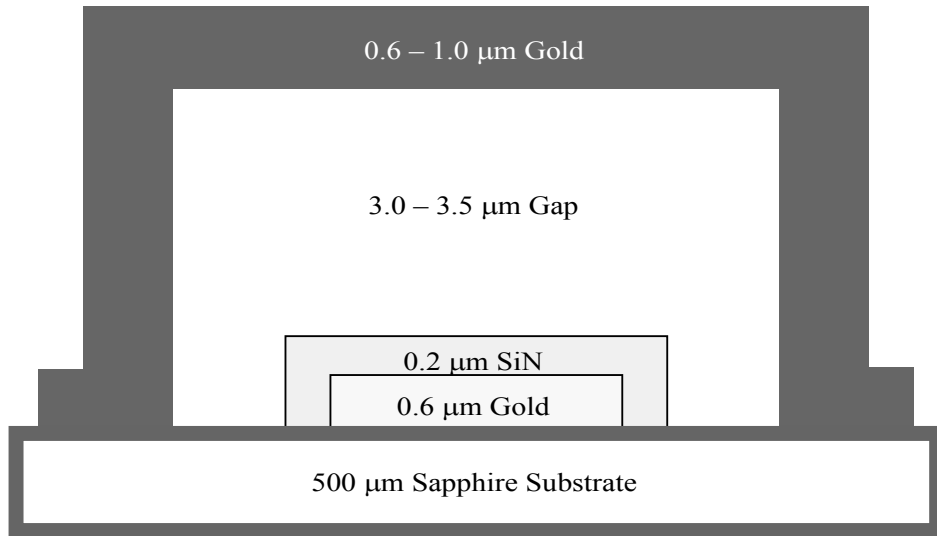


Figure 4-6: Schematic cross sectional view of an SNC-02 switch (not to scale)

A $0.6 \mu\text{m}$ thick gold electrode (t-line) was deposited on the substrate. The electrode has a $0.2 \mu\text{m}$ thick silicon nitride layer. Above the electrode spans a 0.6 to $1.0 \mu\text{m}$ thick gold beam. In the beam's relaxed state, a 3.0 to $3.5 \mu\text{m}$ air gap exists between the insulator and the beam. These dimensions vary from wafer-to-wafer and from switch-to-switch on an individual wafer.

A number of switch designs were available on SNC-02; however, only one design was used in this research – the bridge switch (“Br”). There were 23 variations of the “Br” switch on SNC-02. As shown in Figure 4-7, each bridge design is identified using the $\text{Br}_{<\text{x}>_{<\text{y}>_{<\text{z}>}}}$ format.

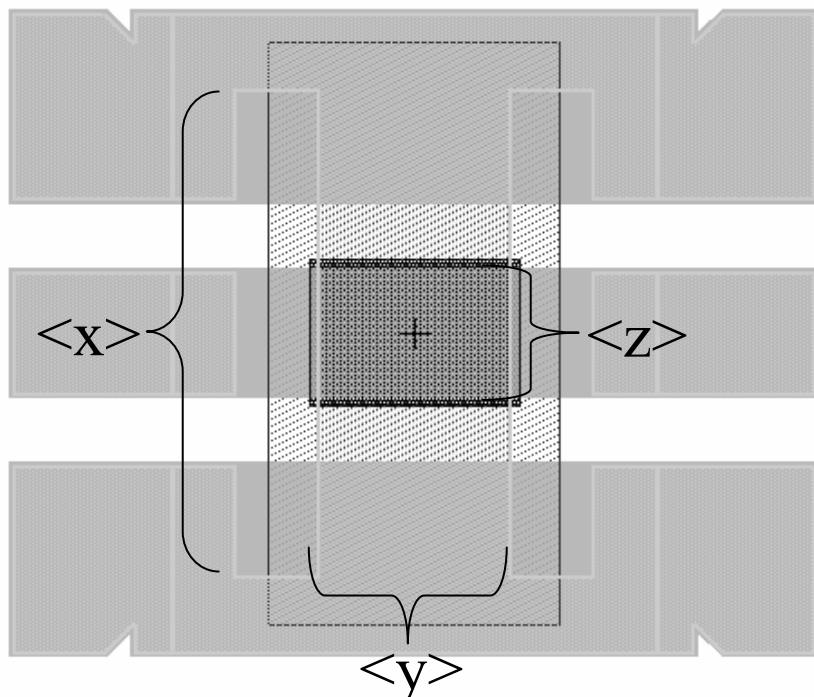


Figure 4-7: Plan view of SNC-02 capacitive switch. This particular switch design has a number of dimensional variations identified by the identifier ($\text{Br}_{<\text{x}>_{<\text{y}>_{<\text{z}>}}}$).

$\langle x \rangle$ holds the bridge length in μm ; $\langle y \rangle$ and $\langle z \rangle$ are the bridge and electrode widths in μm , respectively. These dimensions are also important to switch actuation. Smaller values of $\langle x \rangle$ are stiffer than larger values. Also, the product of $\langle y \rangle$ and $\langle z \rangle$ is the beam and electrode overlap area. The larger this area is, the larger the force pulling down on the beam at a given voltage. Larger forces lead to lower pull-in voltages. Out of the 23 “Br” switch variations, 3 were tested: Br_300_120_80, Br_300_100_80, and Br_300_80_80. These switch designs were chosen for their long beam length and large beam-electrode overlap area; they are highlighted and identified on Figure 4-8. Notice the die includes two columns of four switches for each of the three designs, as well as one of each switch design on the top row.

Ideally, this provides nine switches of each design in close proximity to each other per die. Approximately seven dies on the section of SNC-02/02 tested had functional switches. Unfortunately, not all of the switches on these dies were functional. Many arrived in the laboratory permanently stuck down. Others start off with the beam in the up position, but stick on the first cycle. Obviously, these switches cannot be used for lifetime testing. Other switches begin up but are shorted out because of incomplete removal of a sacrificial layer used in fabricating the bridge. There are also problems that occur during testing. The next few paragraphs describe the device physics associated with these problems and procedures used to work around them.

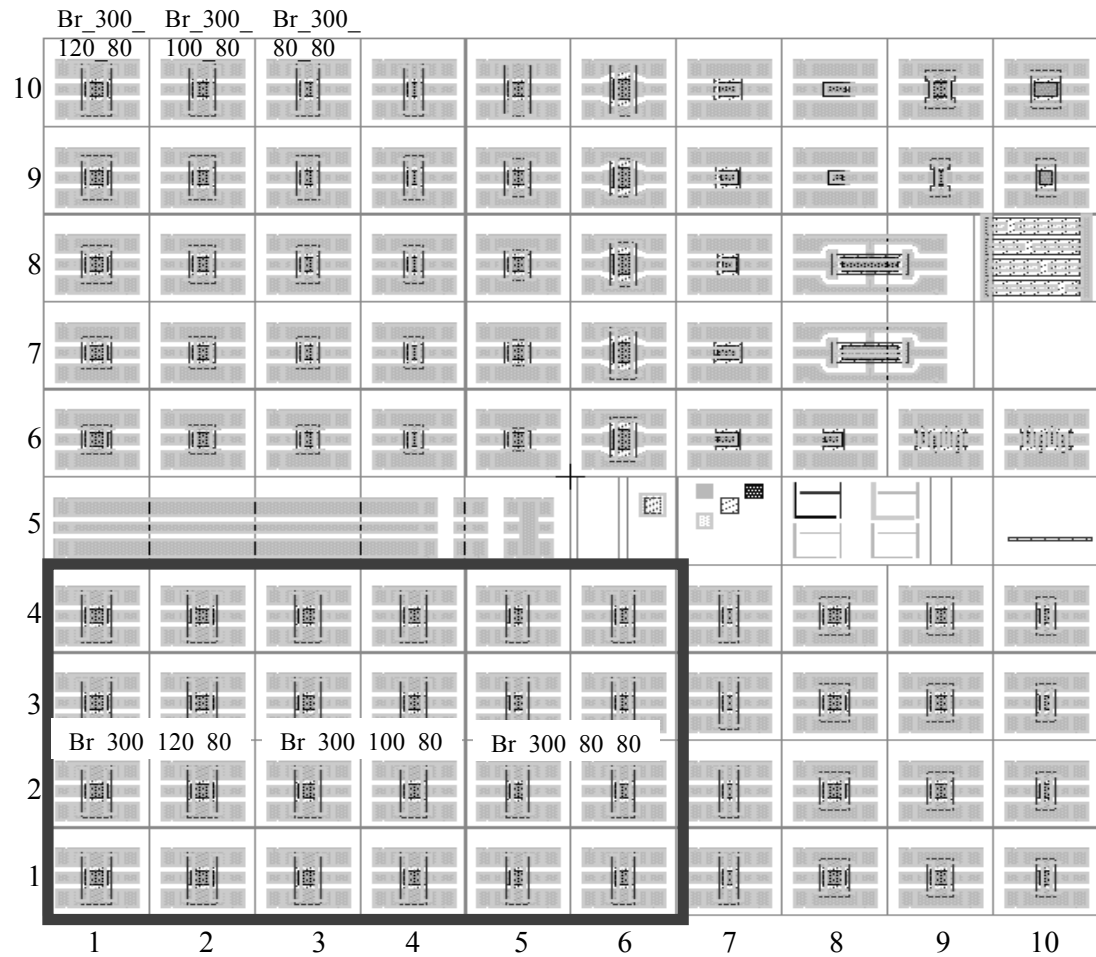


Figure 4-8: SNC-02 die layout

Switch performance depends strongly on device temperature. Temperature affects the switch by changing the amount of internal stress in the beam. Specifically, there are two competing stresses: residual stress from fabrication and thermal stress. Residual stress is compressive causing the beam to bow up or bow down at room temperature [8]. Fortunately, most beams bow up as they leave fabrication. One possible explanation for the preference to bow up involves the sacrificial layer deposited on the electrode and silicon nitride layer during fabrication. This layer is needed to deposit gold for the beam. The sacrificial layer mostly conforms to the electrode, leaving a relatively

flat surface. This surface is flattened further during a planarization step. Despite this, there may still be extra sacrificial material over the electrode so when gold is deposited, the beam has an upward bend. The upward bowing is maintained after the sacrificial layer is removed. It is likely downward bowing also occurs on the wafer and may explain why some switches are down immediately after leaving fabrication [8].

The competing stress is due to thermal expansion of the gold beam. The sapphire substrate and the gold beam have different coefficients of thermal expansion, (6.66×10^{-6} [6] and $14.2 \times 10^{-6} \mu\text{m}/\mu\text{m}/\text{K}$ [7], respectively). Therefore, an increase in temperature results in the gold expanding more than the substrate causing increased compressive stress which bends the beam. On the other hand, the beam contracts as the wafer cools. Initially, contraction reduces the bowing caused by the residual stress. At low enough temperatures, the compressive and tensile stresses balance leaving the beam completely flat with minimal internal stress. As the beam cools further, it goes from a zero stress condition to a tensile stress condition. Tensile stress causes the beam to become taught, or in other words, increases the restoring force.

Each of these phases change the pull-in and release voltages. The upward bend of the beam at higher temperatures means larger voltages are required to pull the beam down. Also, the spring constant is not as large at higher temperatures. It, therefore, takes less force to hold the beam down causing the release voltage to approach zero. When the release voltage reaches zero, the beam no longer releases and stays in the down position.

As the temperature is reduced, the beam does not bow as much and the spring constant increases, so the pull-in voltage decreases and the release voltage increases. At the point tensile and compressive stresses balance, the pull-in voltage reaches a minimum

value. As the switch is cooled even further and the beam becomes more taught, the beam becomes more difficult to pull-in. This increase in beam restoring force also means more force is required to keep the beam down, so the release voltages continue to increase. The bottom line is these switches require a stable, cool testing environment. For SNC-02, the minimum internal stress is reached between 0 and 5 °C [8].

Switches are also dramatically affected by humidity. This is due to water's extremely high surface tension [9:192]. Stiction resulting from water vapor can cause switches to stick down permanently. Some of these switches have been recovered by baking the switches for long periods of time [10]. Since these switches are not hermetically sealed and the temperatures required for cycling are often below the dew point, the environment in which testing occurs must be controlled. This is accomplished by testing in an inert gas environment such as nitrogen.

Test Background

Determining the charge trapping characteristics of the switch's insulating layer requires an experimental procedure much different from that previously described for the MNS devices. Taking CV sweeps over time to determine flatband voltage shifts are not viable. The capacitances associated with these devices are extremely small and would be difficult to measure (approximately 3 pF in the down position and 0.03 pF in the up position). Instead the pull-in and release voltages are utilized.

Experimental Setup

The experiment must provide accurate information on the voltages where beam pull-in and release occur. To do this, the switch must be opened and closed. To actuate

the switch, a low frequency (<100 Hz) waveform (or “dc” waveform) is applied to the switch. While actuating the switch is a vital part of the experiment, by itself it provides no information. Obtaining information requires sending a continuous-wave microwave signal into the switch and measuring the strength of the signal coming out. When the beam is up, the signal passes through. When the beam is down, the signal is shunted to ground. The continuous microwave signal has a negligible effect on beam actuation.

The experiment used to make this measurement is based on the description given in [11]. Figure 4-9 depicts this setup. A Hewlett Packard 3245A Universal Source supplies the dc waveform required to actuate the switch, and a Hewlett Packard 8720ES Network Analyzer supplies a 12 GHz, 5 dBm continuous microwave signal. A Narda 4946 Isolator protects the network analyzer by only allowing signals to leave the HP8720ES. An Ortel BN-1 bias-tee combines the microwave and dc waveforms. W.L. Gore 65474 101-162 3.5mm cables carry the combined signal to RF probes on a probe station. The cables connect to Cascade ACP-040W ground-signal-ground (GSG) microprobe, which in-turn probe the switches. The signal that makes it through the switch feeds into an Inmet 8141 DC-block. The DC-block removes the dc signal while leaving the microwave signal. The microwave signal passes to an Agilent 8474C microwave detector. The microwave detector converts the microwave power into a proportional DC voltage (e.g. $\text{mW} \rightarrow \text{mV}$). The output of the diode detector feeds into one channel on a Tektronics TDS 640 oscilloscope. A second oscilloscope channel receives the drive signal directly from the universal source. Feeding the drive signal and the detector output into the oscilloscope allows a microwave signal to be paired with the

corresponding applied voltage. The universal source and the oscilloscope are both controlled by a personal computer via GPIB controller.

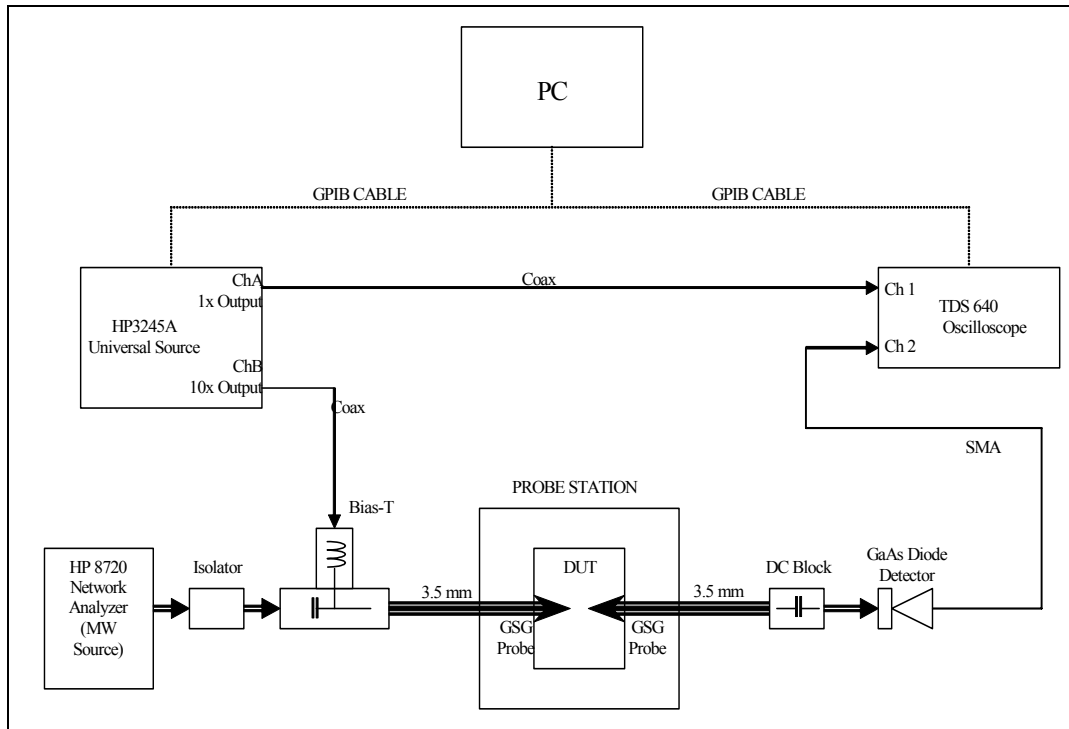


Figure 4-9: Electrical measurement setup

In addition to the electrical setup shown in Figure 4-9, environmental requirements need to be addressed. The temperature was controlled using a Temptronic Thermochuck capable of cooling the sample below -50 C and heating the sample well above room temperature. To cool the sample, the chuck was positioned in contact with the backside of the probe station stage. A thermocouple was placed near the sample on the front side of the stage for real time temperature monitoring.

Since the temperatures required for testing were well below the dew point, and switch operations are drastically affected by humidity, an inert gas atmosphere was

provided during testing. To create this atmosphere in the laboratory, a large plastic bag enclosed the probe station and nitrogen constantly flowed into the bag to provide a humidity free environment. In addition, to keep the sample from moving around during probing and testing, a vacuum line was attached to the backside of the probe station stage. Holding the sample with the vacuum line was vital during irradiation testing (see Appendix B).

Testing Parameters

The experiment presented provides the means for near continuous collection of pull-in and release voltage information. Determining pull-in and release voltages requires cycling the switch with a constantly changing voltage waveform. The last section stated this waveform is made up of two components: a high frequency and a low frequency (or dc) component. The high frequency component was set at a constant frequency for all tests. The dc component varied from test to test. Comparing results from different waveforms provides insight into the charging characteristics. The paragraphs that follow describe this waveform in more detail.

The simplest waveform for investigation purposes is the square wave. It fulfills the primary requirement of actuating the switch. However, the binary characteristic of the waveform provides no means of fulfilling the second requirement – determining pull-in and release voltages. The triangle waveform with its linear voltage ramp allows for determination of pull-in and release voltages. One experimental method for obtaining this information would be to use square pulses to actuate the switch, but periodically use single triangle pulses to determine actuation voltages. Unfortunately, the HP3245A universal source cannot be programmed to operate in this fashion. There is a delay when

the voltage source switches between square and triangle waves. Even more detrimental, the universal source sends a voltage spike with a magnitude that can exceed 100 V when it switches from a square wave to a triangle wave. This spike is enough to cause the switches to permanently stop actuating. Therefore, using a square wave in combination with a triangle wave is not a viable option.

Alternatively, a continuous triangle waveform can be used since it allows for uninterrupted determination of pull-in and release voltages while the switch is actuated. This waveform meets both requirements listed above while also not requiring a universal source function switch in the middle of testing.

The triangle waveform is characterized by peak-to-peak voltage, frequency, and offset voltage. When a symmetric triangle pulse is used (i.e. zero offset voltage), the switch actuates twice per cycle. The switch can be forced to actuate with a single polarity by including an offset voltage. The offset voltage shifts the entire triangle waveform by a constant amount. The frequency of this basic triangle waveform determines how often the switch opens and closes. This type of waveform has been successfully used to measure insulator charging [11].

While the triangle waveform allows uninterrupted actuation and frequent voltage measurement, there is one draw back. Increasing offset voltage (while frequency and peak-to-peak voltage remain constant) obviously changes the maximum voltage applied to the switch as shown in Figure 4-10. However, a closer look at the figure reveals that the single parameter change affects a number of other actuation characteristics. First, the amount of time the beam stays in contact with the insulator surface per cycle increases. Second, it decreases the amount of time between release and the next pull-in. Finally, it

changes the fraction of time the waveform has a negative polarity. A waveform that better isolates peak voltage from other timing issues is needed.

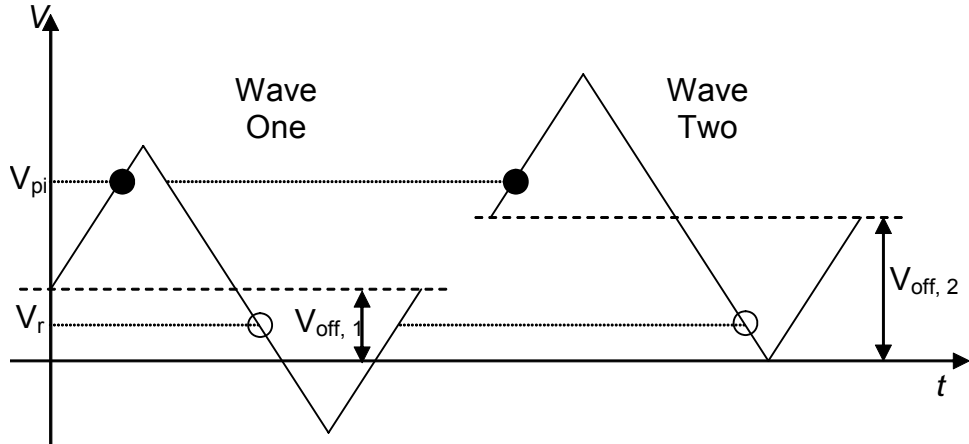


Figure 4-10: Two triangle waves with different offset voltage. Notice wave two's peak voltage is larger than wave one's peak voltage. Also, notice the larger difference in time between pull-in (filled dots) and release (open dots). Finally, a portion of wave one has reversed polarity.

A good compromise is a waveform that combines the best of the square and triangle pulses. The modified triangular waveform is a triangle wave with a variable time at the peak voltage, or hold time, and variable rest time at zero. This waveform and the parameters that describe it are shown in Figure 4-11. This waveform allows simultaneous switch actuation and measurement of pull-in and release voltages just as the triangle waveform does in [11]. At the same time, the coupling of the peak voltage and timing decreases as the hold time increases relative to the amount of time the beam is down during the ramped portion of the waveform. This waveform also dispenses with the need for an offset voltage.

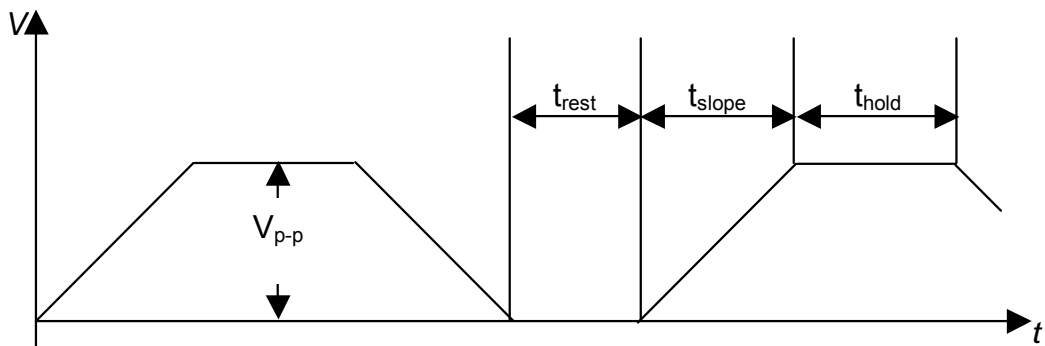


Figure 4-11: Modified triangular waveform

Regardless of the actuation waveform, the following test procedure is used to test the MEM switches. First, a single, symmetric, bipolar triangular wave is applied to the switch, and the output is recorded. The waveform (shown in Figure 4-12) causes the switch to close and open from both voltage polarities. This provides the switch's initial condition (e.g. minimum voltage required for actuation, initial trapped charge density, homogeneity of the switches, etc.).

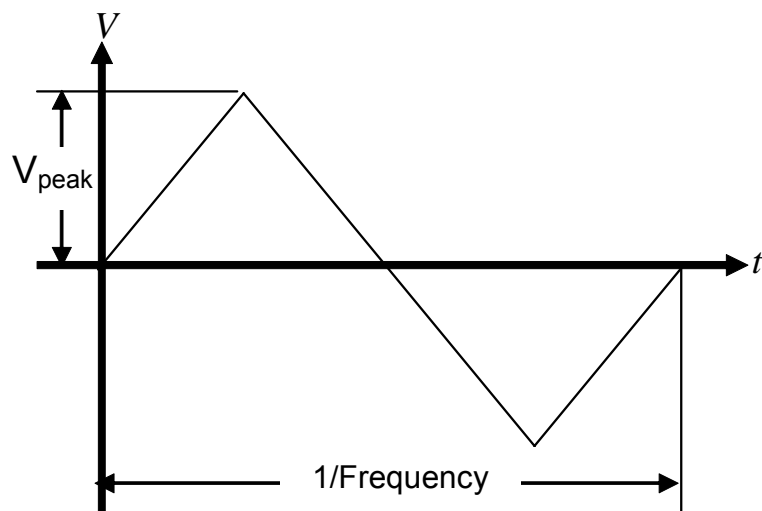


Figure 4-12: Single sweep triangular waveform

Once the switch's initial pull-in and release voltages have been determined, cycling with the modified triangular waveform begins. Without interrupting switch cycling, the oscilloscope triggers approximately every five to ten seconds. (The interval is user defined.) For each trigger event, drive voltage and diode detector output for one cycle are recorded and downloaded to the computer. The controller program on the computer extracts and records the pull-in and release voltages [11]. Later, pull-in and release voltage shifts are calculated relative to the initial sweep. Once the cycling period ends, a final symmetric, single sweep measurement is made. This sweep takes place a few seconds after the triangle waveform ends and provides information on initial discharge of trapped charge. Therefore, a basic three-step process is used for all testing: 1) single sweep for initial condition, 2) switch cycling with modified triangle waveform, and 3) single sweep for end state condition.

This process is fairly accurate in determining time dependent pull-in and release voltages. The number of voltage points used to describe the voltage waveform and the magnitude of the peak voltage determines the resolution of the pull-in voltage. For example, approximately 250 data points are used to describe the bipolar 25V triangular wave. This leads to a voltage resolution of about 0.4V and a timing resolution of 0.5 msec. The time it takes for actual pull-in and release events to occur is at least an order of magnitude faster than the time resolution provided by the oscilloscope. Therefore, little error is introduced from the timing of pull-in and release events.

4.4. Summary

This chapter presented the specifics of each experiment used in this research. This included two completely different tests. One set of experiments tests the charging of

the MEM switch. The other set of experiments focuses on the insulator using MNS capacitors. The next chapter presents the results of these experiments. Irradiation experiments were also performed and these results are presented in Appendix B.

Bibliography

1. Reid, J.R. "Simulation and Measurement of Dielectric Charging in Electrostatically Actuated Capacitive Microwave Switches," *Proceedings Modeling and Simulation of Microsystems*, 250-253 (April 2002).
2. Felix, J.A., D.M. Fleetwood, R.D. Schrimpf, J.G. Hong, G. Lucovsky, J.R. Schwank, and M.R. Shaneyfelt. "Total-Dose Radiation Response of Hafnium-Silicate Capacitors," *IEEE Transactions on Nuclear Science*, 49: 3191-3196 (December 2002).
3. Neaman, D.A. *Semiconductor Physics & Devices*. Boston: McGraw, 1997.
4. Sze, S.M. *Semiconductor Devices: Physics and Technology*. New York: Wiley, 1985.
5. *LABWINDOWS/CVI*. Version 6.0. Computer Software. National Instruments, Austin, TX, 2001.
6. "Sapphire Properties Table," n. pag. <http://www.mkt-intl.com/sapphires/sapphphotos.htm> 19 April 2004.
7. WebElements. "Gold Properties." n. pag. <http://www.webelements.com/webelements/elements/text/Au/heat.htm>. 19 April 2004.
8. Starman, L.C. Air Force Research Laboratory Antenna Technology Branch (AFRL/SNHA), Hanscom AFB MA. Personal Interview. 20 Nov 2003.
9. Rebeiz, G.M. *RF MEMS: Theory, Design, and Technology*. Hoboken, New Jersey: Wiley, 2003.
10. Reid, J. Robert. Air Force Research Laboratory Antenna Technology Branch (AFRL/SNHA), Hanscom AFB MA. Personal Interview. 1 Oct 2003.

11. Reid, J.R. and R.T. Webster. "Measurement of Charging in Capacitive Microelectromechanical Switches," *Electronics Letters*, 38: 1544-1545 (21 November 2002).

5. Results

The previous chapter presented the experimental procedures in detail. This chapter provides the results of those experiments. Results from metal-nitride-semiconductor (MNS) charging experiments are given first and MEM switch results follow.

5.1. MNS Capacitor Results

MNS capacitors allow investigation of the time and electric field dependence of silicon nitride charging. In this experiment, capacitors were biased for extended periods at six different voltages. Typically, six capacitors were tested simultaneously using the same voltage magnitude - half biased negatively and the remainder biased positively.

Figure 5-1 shows a series of CV sweeps taken on a capacitor biased at +10V. The voltage sweep that produced these CV curves started at +30V and ended at -24V using -2V steps lasting 0.25 sec each. As discussed in the previous chapter, the CV sweep is distorted by interface states and trapped charge. The initial CV curve (0 sec) indicates the existence of interface states trapped charge (horizontal shift of approximately -8V). As the capacitor is biased positively during testing, successive CV curves shift further to the left.

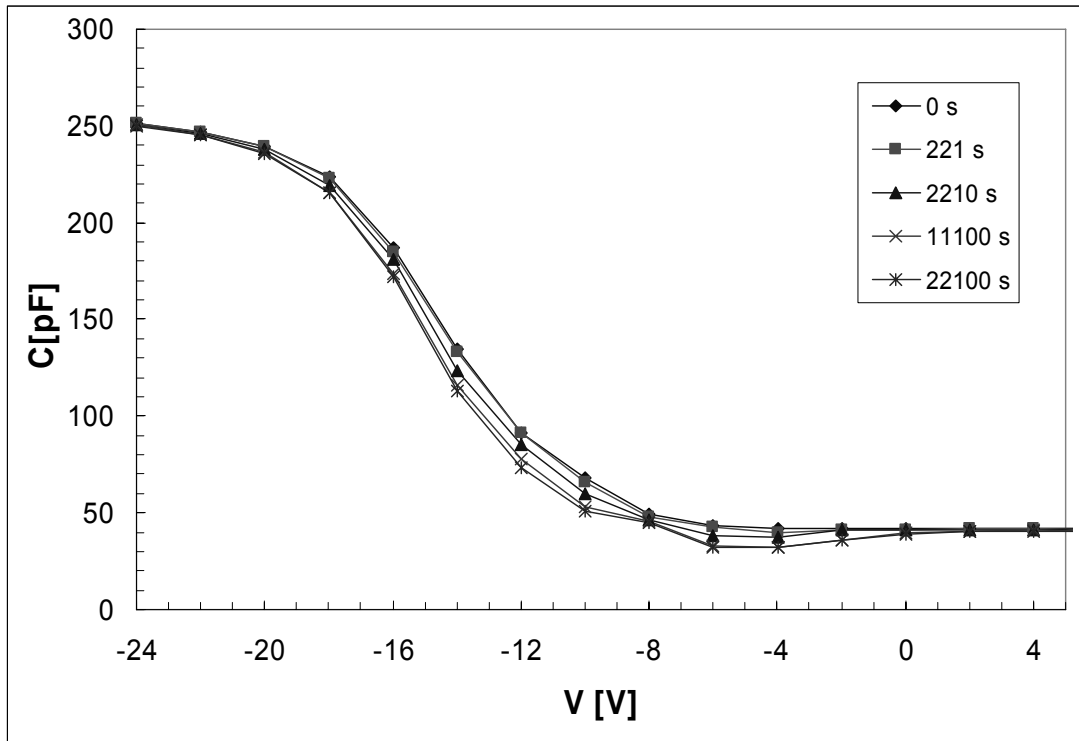


Figure 5-1: CV measurements on MNS devices taken during +10V biasing

Notice the curves translate horizontally, but do not change shape appreciably during biasing. This means interface state density, while initially great, remains relatively constant throughout testing. The impact of the interface state density is reduced by tracking changes in flat band voltage. These interface states were not investigated further in this research because an insulator-semiconductor interface does not exist on the MEM switch. Although, the silicon nitride surface (top) of a MEM switch forms a silicon nitride-air interface that may have characteristics similar to the MNS interface. A study of silicon nitride surface states may be worth investigating; however, experimental techniques (e.g. optical) other than capacitance measurements are better suited for this surface study.

Although the sweep voltage was optimized to minimize net charging, a small amount caused by the CV sweep still occurs. Five capacitors were tested with no bias applied between successive CV sweeps. Figure 5-2 shows the flat band voltage shift over a period of approximately 12000 sec (33 hours). This data was used to correct the biased capacitor data.

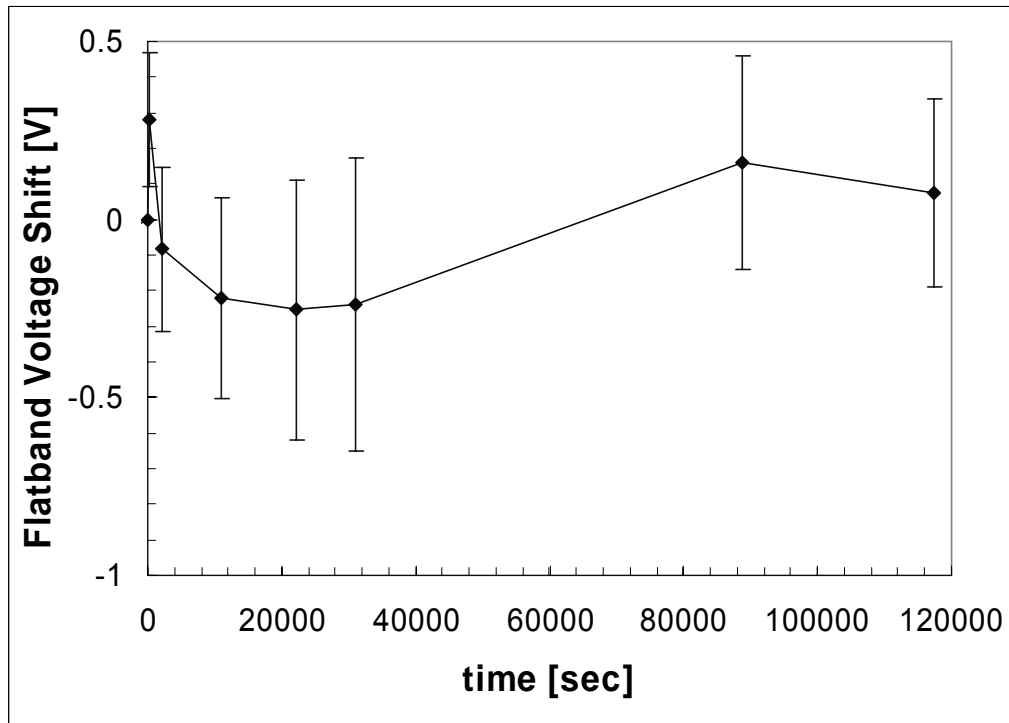


Figure 5-2: Flatband voltage shift measurements based on CV sweeps. No bias applied between CV sweeps – quantifies the charging effects of successive CV sweeps.

Figure 5-3 shows the data from all MNS tests. Each curve and associated set of one-sigma error bars represents corrected data from three individual capacitors. There are two phases to the measurement shown in Figure 5-3. For the first 22150 sec (~6 hours), the capacitor was stressed with the indicated applied bias. For the remaining

time, the bias was removed and charge dissipation was tracked. This research focuses on the charging portion of the data since it is most applicable to the MEM switch.

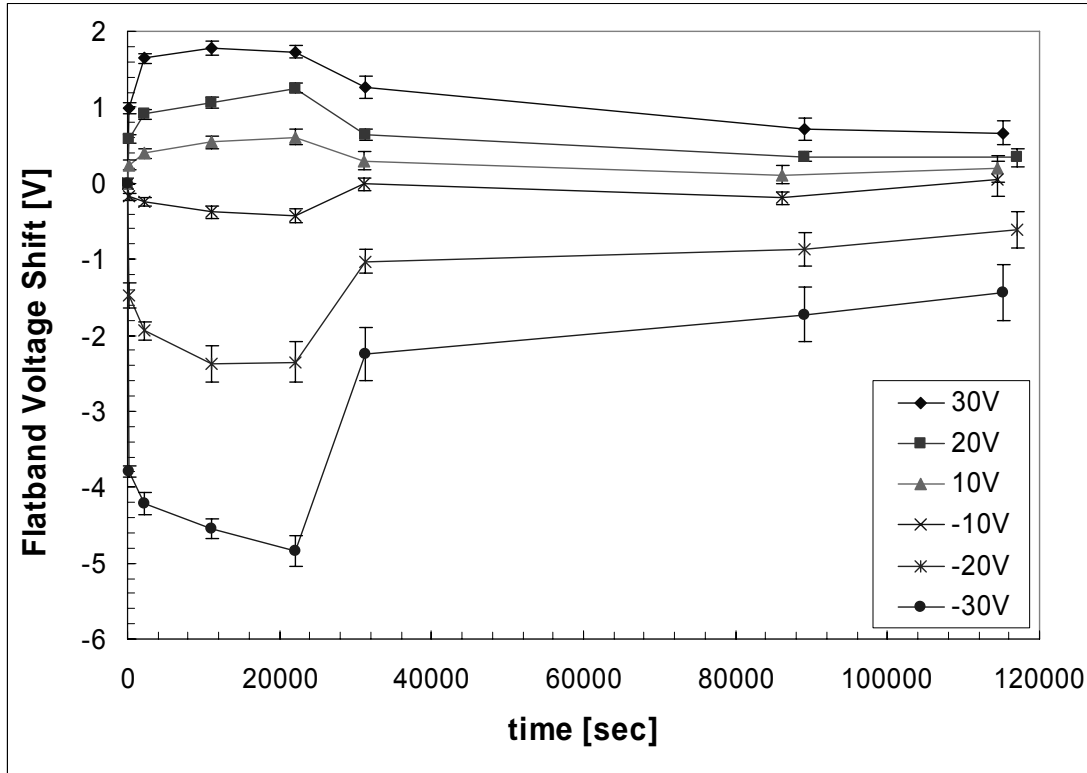


Figure 5-3: Summary of MNS capacitor data from 0 to 22150 sec. The remainder of the data shows time dependent discharge at room temperature and no bias applied.

Figure 5-4 shows the charging data (first 22150 sec). Larger applied biases result in larger voltage shifts. To show the strong logarithmic behavior of the data, time is plotted on a logarithmic scale. The polarity of the voltage shift depends on the polarity of the applied bias. This is explained by the net polarity of the charge trapped in the insulator. Not quite as obvious is the polarity dependence. The voltage shift for biases of

the same magnitude but opposite polarity differ, e.g. the $-30V$ shift is much larger than the $+30V$ shift. This is addressed in Chapter 6.

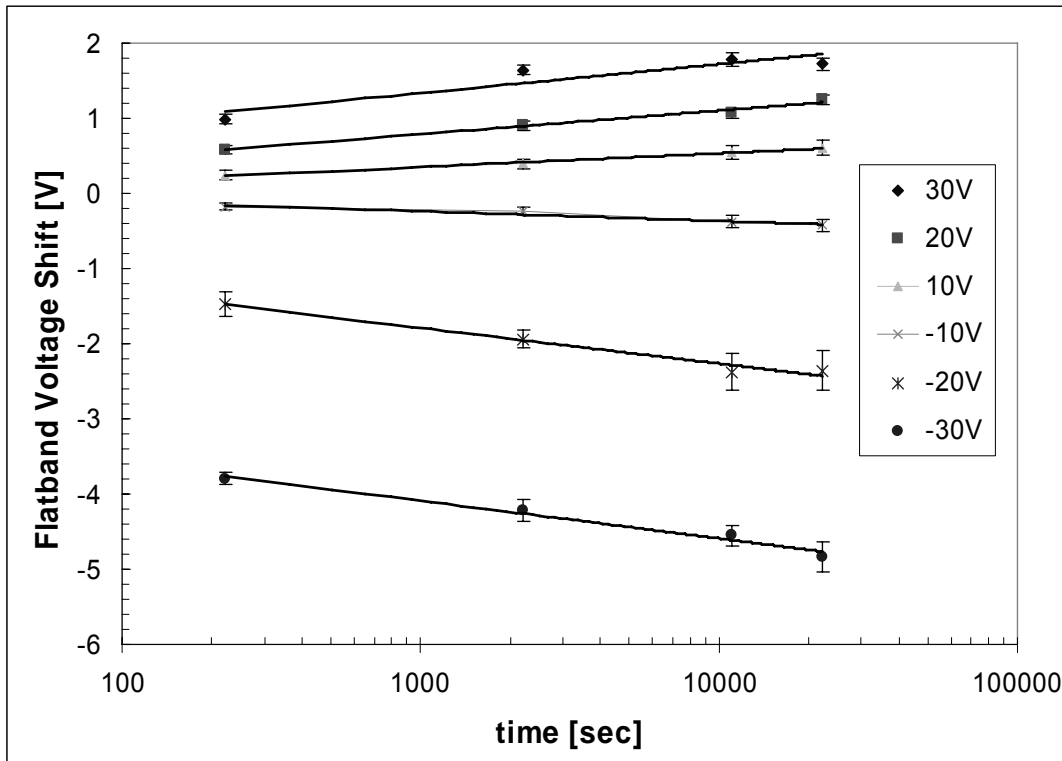


Figure 5-4: Logarithmic plot of flatband voltage shift while bias is applied

Table 5-1 lists the logarithmic least squares fit line for the data presented in Figure 5-4. There is good agreement between the lines of best fit and the data as indicated by the high values for R^2 . The $+30V$ curve has a lower R^2 value, which may be due to oscillation about the line of best fit, rather than a large continued deviation from the logarithmic estimate, i.e. the equations for the line is close, but the degree that the data points hug the line differ. The charging rate is also proportional to the applied voltage. Notice that the first data points in Figure 5-4 increase with increasing bias

magnitude. Also notice that the slope of the least squares fit is larger for larger bias magnitudes. Therefore, the charging rate is faster for larger biases.

Table 5-1: Equations describing the data in Figure 5-4

Bias (V)	Least Squares Best-Fit (V)	R² (-)
30	$1.7 \times 10^{-1} \ln(t) + 1.8 \times 10^{-1}$	0.857
20	$1.4 \times 10^{-1} \ln(t) - 1.5 \times 10^{-1}$	0.982
10	$7.9 \times 10^{-2} \ln(t) - 1.9 \times 10^{-1}$	0.991
-10	$-5.5 \times 10^{-2} \ln(t) + 1.4 \times 10^{-1}$	0.938
-20	$-2.1 \times 10^{-1} \ln(t) - 3.7 \times 10^{-1}$	0.974
-30	$-2.2 \times 10^{-1} \ln(t) - 2.6$	0.978

The strong logarithmic behavior of these results agrees with the explanation presented in Chapter 3 that tunneling is responsible for the filling of silicon nitride traps. Larger voltage shifts and faster charging rates also agree with tunneling theory since larger voltages allow more trap sites to participate in tunneling. The next section discusses a related set of experiments that were carried out on MEM switches.

5.2. MEM Switch Results

It was pointed out in Chapter 3 that once a switch is fabricated the only adjustable parameters that effect insulator charging are voltage magnitude, voltage polarity, and the amount of time the voltage is applied to the switch. Environmental parameters, such as temperature, humidity, and atmosphere, can also be changed; however, switch performance is extremely sensitive to these environmental changes. Therefore, great effort went into maintaining constant environmental conditions throughout testing. Care had to be taken in biasing the MEM switch; keeping the beam biased and in contact with

the insulator surface for more than 100 msec can cause the switch to stick down permanently.

Chapter 4 described a waveform that provides flexibility in the length of time a switch is open and closed while also allowing the determination of a switch's pull-in and release voltages. Parameters such as peak voltage, hold time, frequency, and polarity can be varied using this waveform. This section presents the data collected utilizing this waveform. Based on tunneling theory and the MNS results, it is expected that the longer the beam is held in contact with the insulator surface the faster the insulator charges. It is also expected that larger peak voltages result in higher levels of charging.

It should be pointed out there is a competing explanation for the changes in pull-in and release voltages. It involves the charging of surface states and would be proportional to the number of times the beam contacts the insulator. If this is true and tunneling is incorrect, charging would not be directly related to voltage and hold time. Instead, it would depend on the number of times the beam contacts the insulator surface. Chapter 6 relates the results in this chapter to the theory presented in chapter 3.

Before the results are presented, the variability of the data is briefly discussed. An assumption was made in chapter 3 that all traps are initially empty and neutral. The figures in this section show there is latent charge present in the insulator; however, it is small ($\Delta V_o < 1V$) relative to steady state voltage shifts. It is possible this observed latent charge is caused by the initial voltage sweep itself.

The raw data was adjusted based on an estimate of initial charging. As discussed in Chapter 4, the first step of the measurement procedure is to take a simple, symmetric voltage sweep to determine the pull-in and release voltages for both polarities. From this

data, corrections are calculated in the following manner. The pull-in adjustment is determined by taking the difference in magnitude of the positive and negative pull-in voltages and dividing this difference by two. This is the magnitude of both pull-in voltages when no trapped charge is present. The next step is to subtract the two pull-in voltages from this ideal pull-in voltage. The same procedure is performed for the release voltages. Both the adjustments should be approximately the same.

Often the $\Delta V(t)$ results of two adjacent switches were quite different from each other. In this section these differences are indicated with error bars. In chapter 6, reasons for these large differences are given based on Chapter 5 results. The sections that follow describe the waveforms used and present the data collected using that waveform. Discussion of the data is limited to observations and general trends; explanations tied to theory are saved for Chapter 6.

Variations in Hold Voltage

To determine how the magnitude of the applied bias affects charging, unipolar, triangular waveforms, as shown in Figure 5-5, were applied with various peak voltages. The waveform starts at 0V and ramps up reaching the peak voltage in 25 msec. The peak voltage is held for 25 msec followed by a ramp down period to 0V which also lasts 25 msec. Between each pulse there is a 25 msec rest period. Switches were tested with peak voltages of 32V, 36V, 38V, and 40V. Each test lasted a total of 900 seconds.

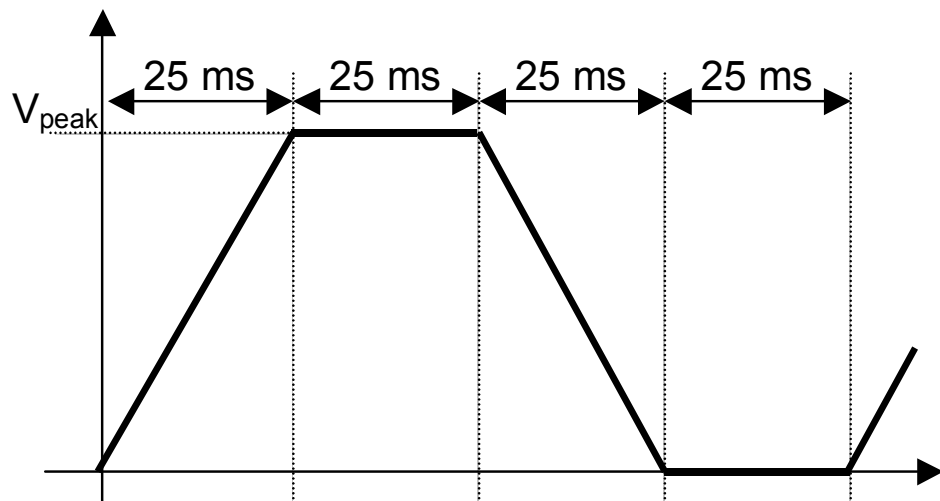


Figure 5-5: Waveform used for hold voltage experiment

The pull-in voltage results for these four peak voltages are displayed in Figure 5-6.

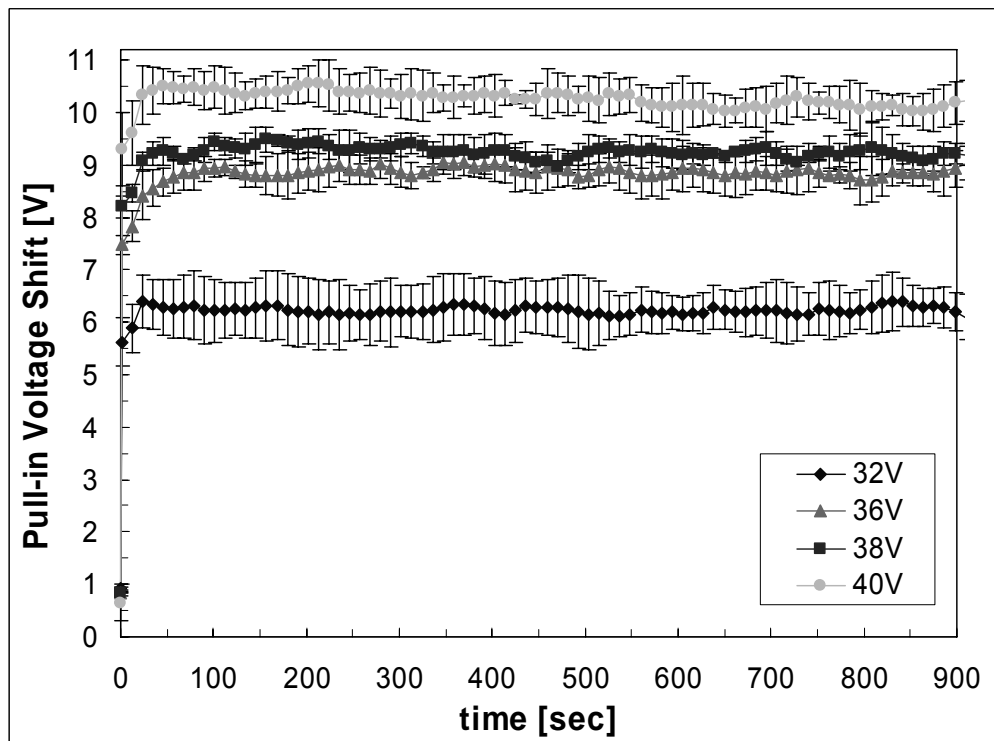


Figure 5-6: Pull-in voltages shift in for various hold voltages ($t_r=25\text{ms}$, $t_s=25\text{ms}$, $t_h=25\text{ms}$)

The first observation is that the 32V curve is different from the others. It charges quickly similar to the other curves, but reaches a maximum voltage shift value of 6.4V after 40-50 sec of testing. Charging caused the pull-in voltage to reach the peak voltage of 32V (voltage shift is approximately 6.5V). Pull-in voltage exceeding the waveform's peak voltage highlights a common failure mechanism for these switches. If a triangle waveform were applied (i.e. $t_h=0$) and the pull-in voltage reached the peak voltage, the beam would cease closing. Fortunately, this is not a permanent failure mechanism. All it takes for the switch to actuate again with this waveform is either time for the trapped charge to dissipate, or the application of a waveform with a higher peak voltage.

For the data presented in Figure 5-6, the switch continues to operate after the pull-in voltage reaches the peak voltage. This is because the 32V peak voltage is held for an extended period. Therefore, the beam does not close immediately when 32V is reached, but at some later time in the pulse while the waveform is still 32V. As the insulator continues to charge, the delay between the waveform reaching 32V and the pull-in event occurring grows. Thus, pull-in also has a time component. Tracking the delay between reaching peak voltage and the pull-in event provides an alternate metric for charge tracking. While it is possible to collect this type of data, it requires extensive reprogramming of the current controller software. It also requires storing and maintaining extremely large data files. This effort was not pursued because of its low payoff compared to other work that could be done with the existing code. The bottom line is that the 32V data is not useful once the pull-in voltage reaches 32V, so there is only about 40 seconds worth of useful data. The experiments with the larger peak voltages did not run into this problem and provide useful data on insulator charging.

It is apparent from the data that larger peak voltages yield larger maximum pull-in voltage shifts. The 36V curve's maximum shift is about 8.8V. The 38V curve shifts slightly more, 9.2V, although there is overlap on a majority of the one standard deviation error bars. The maximum shift of the 40V curve is approximately 10.6V.

Charging rate also depends on peak voltage. Comparing the voltage shift from the first to the second data points, the 32V curve (data still useful) shifts 5.5V, the 36V curve shifts 7.5V, the 38V curve shifts 8.2V, and the 40V curve shifts 9.3V. The time required to reach the maximum voltage shift is also indicative of charging rate. The 36V and 38V curves reach maximum voltage shifts in approximately 100 sec. The 40V curve reaches its maximum voltage shift even quicker, taking approximately 50 sec. Figure 5-7 displays the release voltage shifts from the same experiment. Just as with pull-in voltage shifts, higher applied biases lead to larger ΔV_r levels and faster increases in ΔV_r early in cycling.

The 32V release shift curve is discussed briefly. Even though the 32V ΔV_{pi} curve saturates when V_{pi} reaches 32V, the release voltage curve does not saturate when V_{pi} reaches 32V. The release voltage shift continues to change and eventually reaches saturation after about 200 sec of cycling. After the pull-in voltage reaches 32V, the release shift data does not provide a valid comparison with the other data since the switch actuates later in the waveform than the other three cases.

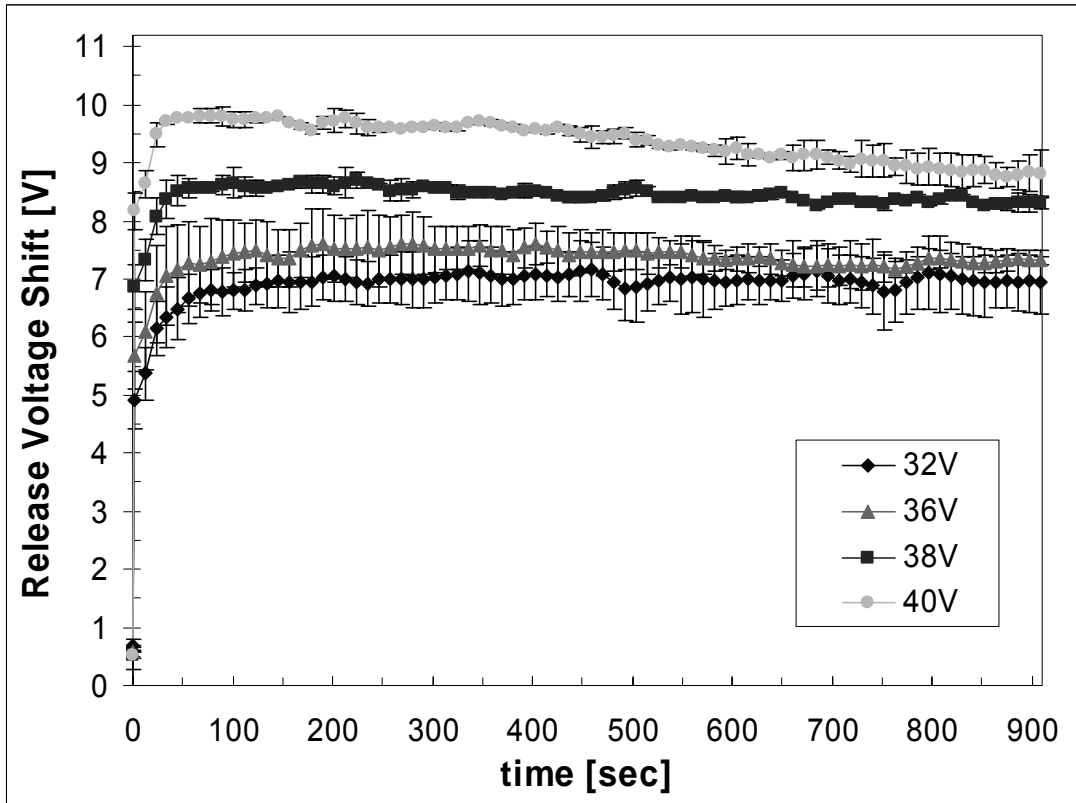


Figure 5-7: Release voltage shifts for various hold voltages ($t_r=25\text{ms}$, $t_s=25\text{ms}$, $t_h=25\text{ms}$)

ΔV_{pi} and ΔV_r also provide an interesting comparison. Figure 5-8 plots the 40V ΔV_{pi} curve and ΔV_r curve together. The two curves deviate in the following ways: 1) the release voltage maximum shift is less than the pull-in voltage shift, and 2) after ΔV_{pi} reaches a steady state condition, ΔV_r steadily decreases for the remainder of testing. At $t=0$, the difference between the pull-in and release voltages is 0.1 V. After one second, the difference between the two is 1.1 V. By the end of testing, the two deviate 1.4 V. Chapter 6 examines the relationship between ΔV_{pi} and ΔV_r in detail.

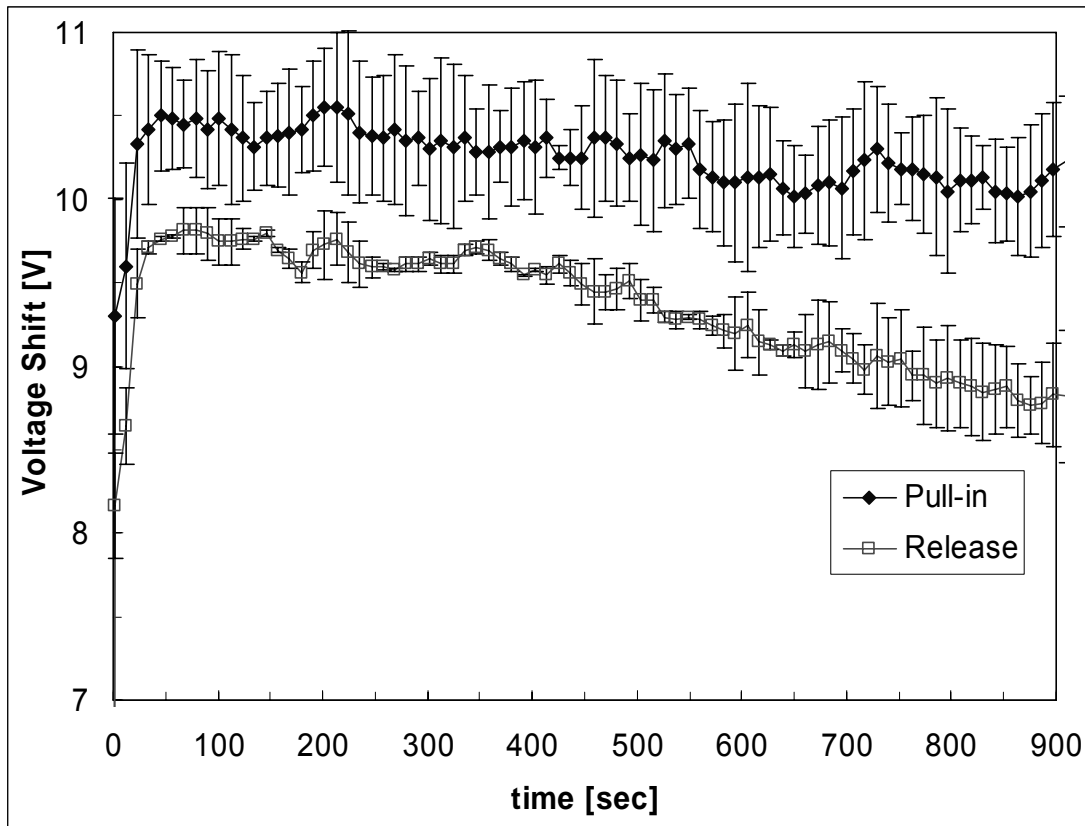


Figure 5-8: Comparison of 40V ΔV_{pi} and ΔV_r curves

Variations in Hold Time (Constant Frequency)

In this section, the triangular waveform was used to determine the importance of beam-insulator contact time. The peak voltage was maintained at 36V for all tests. To test the effect beam-insulator contact time has on charging, the hold time was varied (0 msec, 10 msec, 25 msec, and 50 msec). To isolate changes in hold time from changes in the number of beam insulator collisions, a constant frequency of 10 Hz was maintained for all hold times by adjusting the rest time accordingly as shown in Figure 5-9.

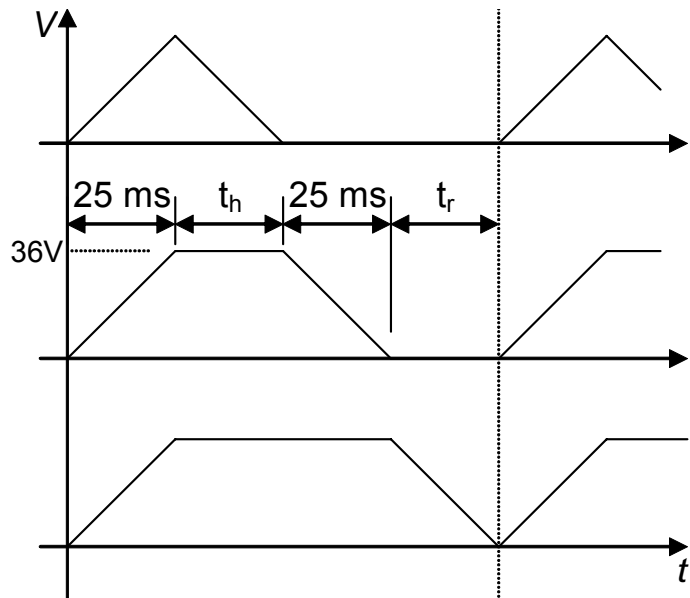


Figure 5-9: Variable hold time waveform while maintaining constant frequency

Figure 5-10 shows the pull-in voltage shift results for these four hold times.

Observe all curves share the same steady state voltage shift of 5.8V, even though the route to the steady state condition is different for each hold time. The charging rate is faster for longer hold times which is highlighted by the initial voltage shift and the time required to reach the maximum voltage shift. The initial shift for the 0 msec hold time is 3.6V, the 10 msec initial shift is 4.4V, the 25 msec curve is 5.6V, and the 50 msec curve is 6.5V. Longer hold times produce larger initial voltage shifts. Similarly, the shorter the hold time, the longer it takes to reach maximum voltage shift. The 0 msec curve takes all 900 sec of testing, the 10 msec data takes 150 sec, the 25 msec takes 110 sec, and the 50 msec curve only takes 20 sec to reach the maximum voltage shift. For the 25 and 50 msec data, the maximum voltage shift was larger than the steady state voltage shift. This is referred to as “super saturation” and discussed in chapter 6.

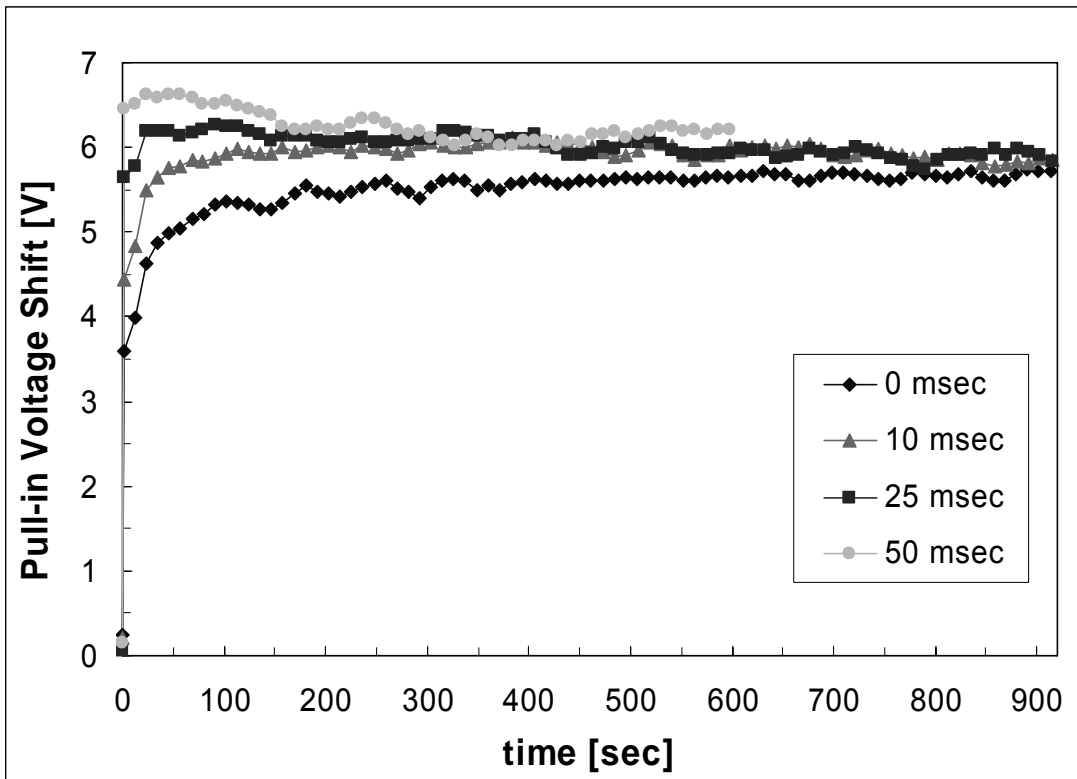


Figure 5-10: Change in pull-in voltage for four hold times – constant 10 Hz frequency

The release voltage results are shown in Figure 5-11. A comparison of ΔV_{pi} and ΔV_r reiterates the same observations made about the peak voltage test: the release voltage shift is smaller than the pull-in voltage shift (4.4V versus 5.8V, respectively), and in the case of 25 msec and 50 msec curves, the release shift curves steadily decrease after reaching a maximum. The slope is larger for the 50 msec than the 25 msec slope. In fact, the 50 msec case eventually sticks down and ceases to operate.

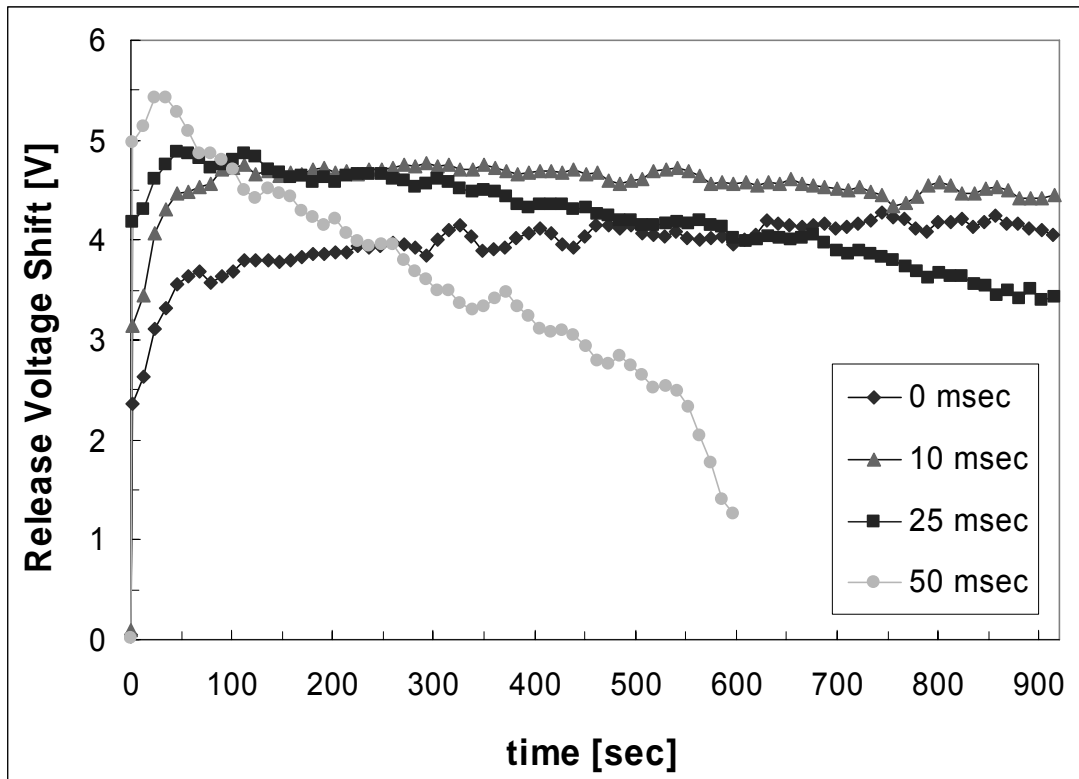


Figure 5-11: Change in release voltage for four different hold/rest time combinations (hold time in parentheses) – 10 Hz frequency remains constant

Variations in Hold Time (Constant Rest Time)

In the previous section, hold time varied while frequency was held constant. This was done to examine the effect hold time has on charging while eliminating any effect the number of beam-to-surface collisions may have on charging. It is seen that hold time has a dramatic effect on charging. In order to maintain a constant frequency, the rest time also had to change. This experiment assumes the rest period has little effect on charging behavior.

To evaluate this assumption, a similar experiment was conducted. However, in this case as hold time increased, the rest time remained constant; therefore, the frequency

changed as shown in Figure 5-12. If the assumption is valid, the hold time results for the various frequencies should be approximately the same.

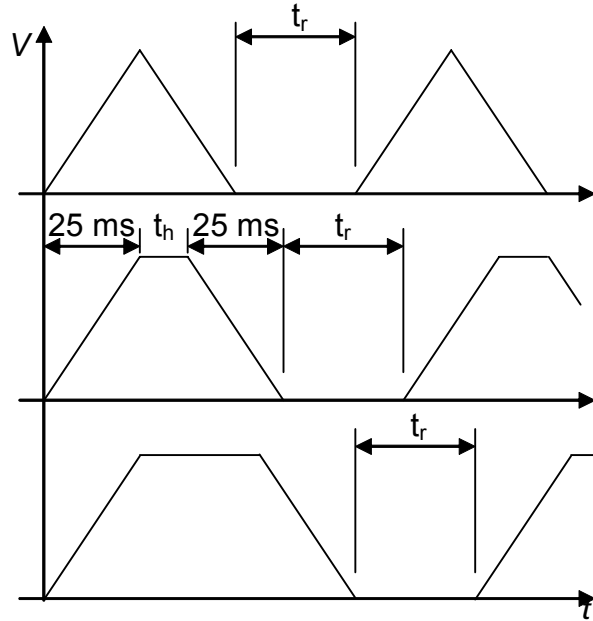


Figure 5-12: Variable hold time waveform while maintaining constant rest time

These ΔV_{pi} results are shown in Figure 5-13. The 0 msec (13.3 Hz) curve reaches a steady state shift of 6.0V in approximately 400 sec. The 25 msec (10.0 Hz), 50 msec (8.0 Hz), and 100 msec (5.7 Hz) curves are similar. They reach a maximum shift of 6.8 V in about 40-50 sec. After reaching a maximum shift, they slowly decrease before reaching a steady state voltage shift of approximately 6.0 V. The steady state pull-in voltage shift agrees with the curves in Figure 5-10.

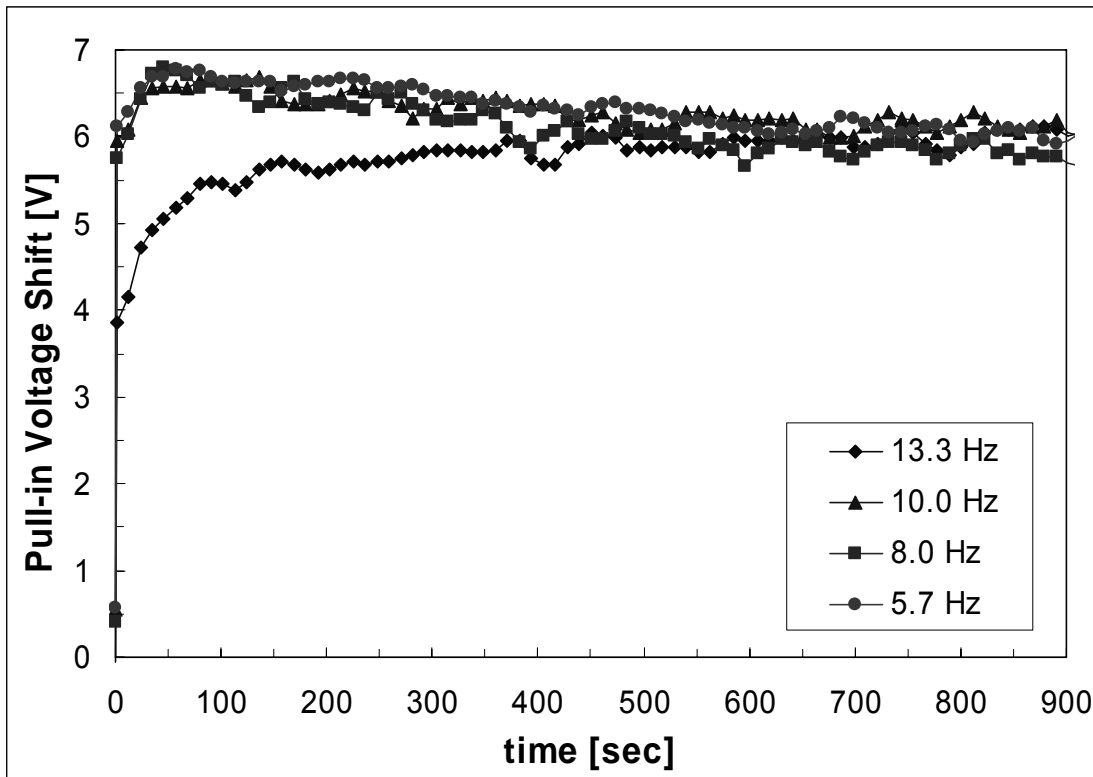


Figure 5-13: Change in pull-in voltage for four hold/frequency combinations (hold times in parentheses) – a 25 msec rest time remained constant

Figure 5-14 presents the corresponding release voltage shifts from Figure 5-13.

For the pull-in data, the only outlier was the 0 msec curve; the other three were essentially identical. In Figure 5-14 this is not the case – no two release curves are identical. The 0 and 25 msec release data are very similar to the pull-in data. The 50 and 100 msec release voltages show an initial increase, but not as large as the pull-in's initial increase. The 50 msec release voltage increases approximately 2V initially before eventually reaching a maximum shift of 2.9V. The 100 msec release voltage initially shifts 5.25V with a maximum shift of 5.75V. After reaching the maximum shift, the 50 and 100 msec release curves decrease for the remainder of testing.

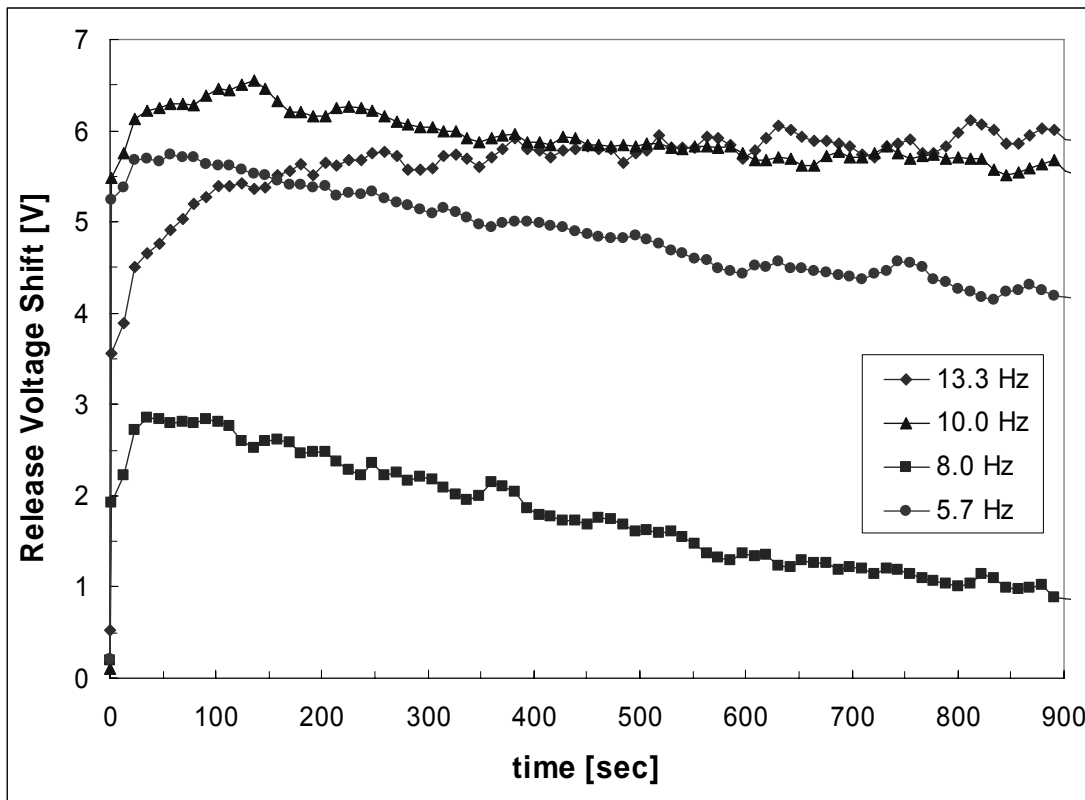


Figure 5-14: Change in release voltage for four hold/frequency combinations (hold times in parentheses) – a 25 msec rest time remained constant

Figure 5-15 is a comparison of Figure 5-10 and Figure 5-13 to verify the assumption that rest time differences can be ignored. For clarity, only two sets of pull-in voltage shift curves with different hold times (0 msec and 50 msec) are displayed in Figure 5-15. The curves from the two frequency comparisons track together for the 600 sec of operation (at 600 sec the 50 msec 10 Hz data ends). Rest time differences can be ignored, and the pull-in voltages are insensitive to the number of collisions that occur. Therefore, the hold time is important to charging.

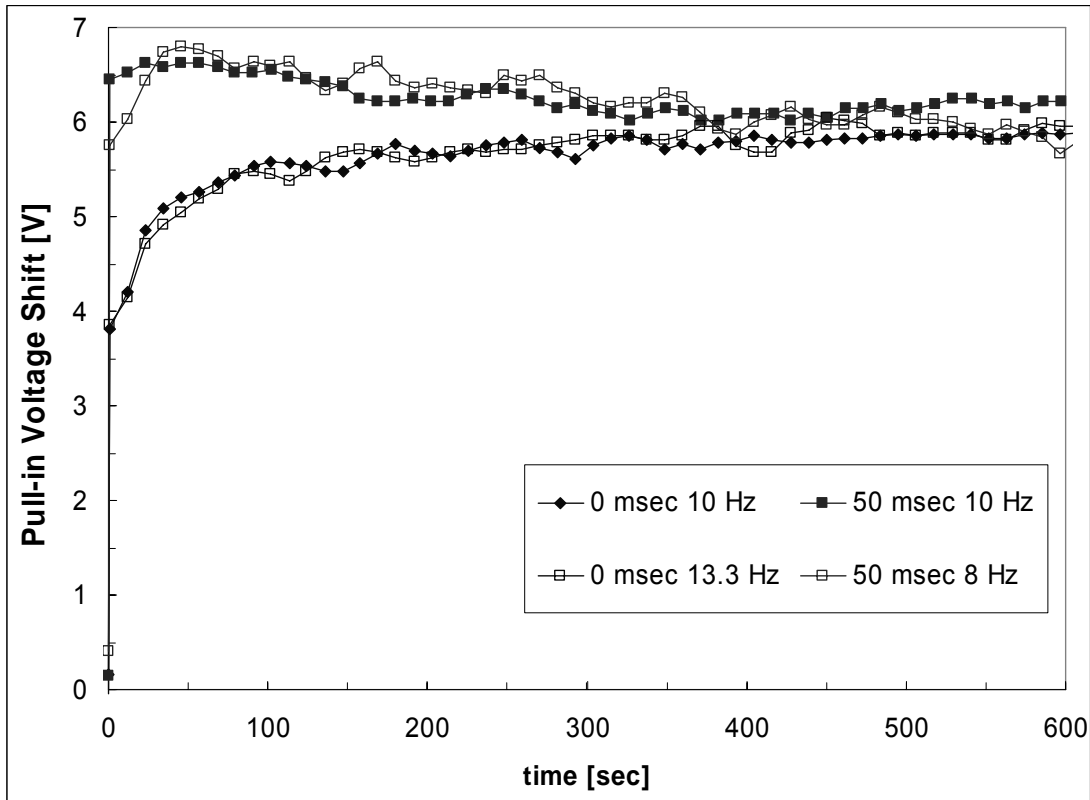


Figure 5-15: Comparison of change in pull-in voltages for constant rest and constant frequency

Polarity

Tests were performed to determine the importance of bias polarity on charging. A slightly different waveform was used for this test. In this case, a bipolar waveform with an offset voltage was used as shown in Figure 5-16. This same waveform used by Reid and Webster [1]. For the case shown in, the offset voltage is sufficiently positive to ensure pull-in occurs at the positive voltages and actuation does not occur during the negative portion of the waveform. Therefore, the beam is only in contact with the insulator for the positive portion of the curve.

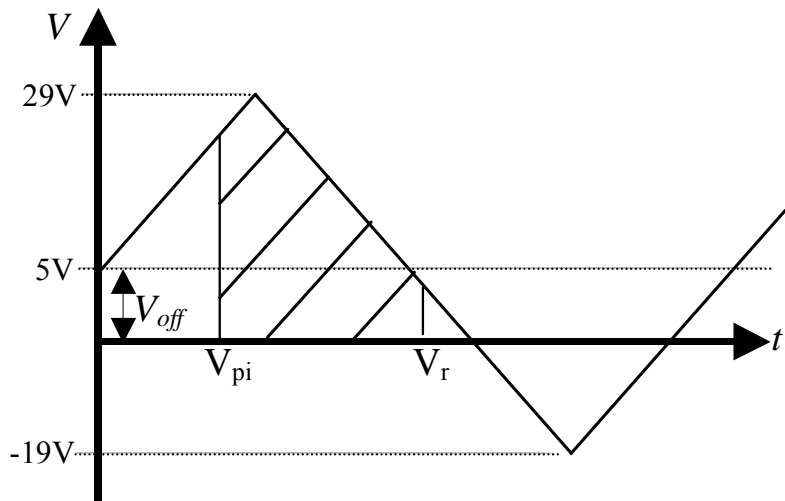


Figure 5-16: Single bipolar triangle wave (hatched portion indicates beam is in contact with insulator)

The peak-to-peak voltage of the waveform used in testing was 48 V with either a positive or negative 5V offset. Figure 5-17 shows the pull-in and release data (not voltage shift) for a +5V offset. The -5V offset results are a mirror image.

To facilitate a comparison of the data for both polarities, voltage shift plots have been constructed. Figure 5-18 compares the pull-in voltage shift results for the +5V and the -5V waveforms. The -5V results have been multiplied by a factor of -1 to allow a direct comparison of the two pull-in data sets. In the first 20 to 30 seconds of switching, there is a significant difference between the positive and negative curves (greater than one standard deviation). The negative curve increases faster than the positive case. After the first the 30 seconds, the two curves' error bars consistently overlap making them indistinguishable from each other.

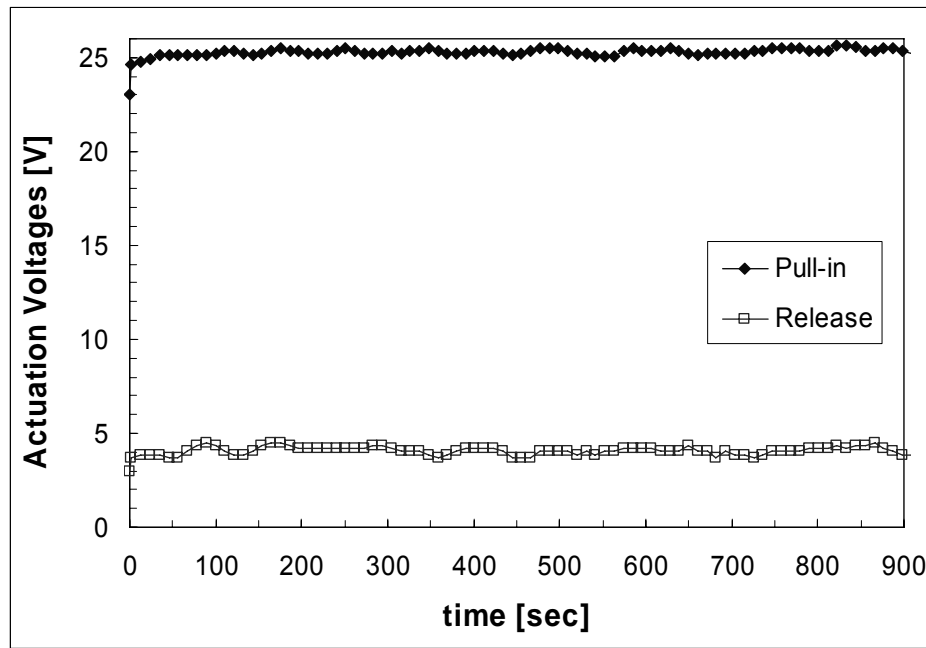


Figure 5-17: Pull-in and release results for positive offset voltage

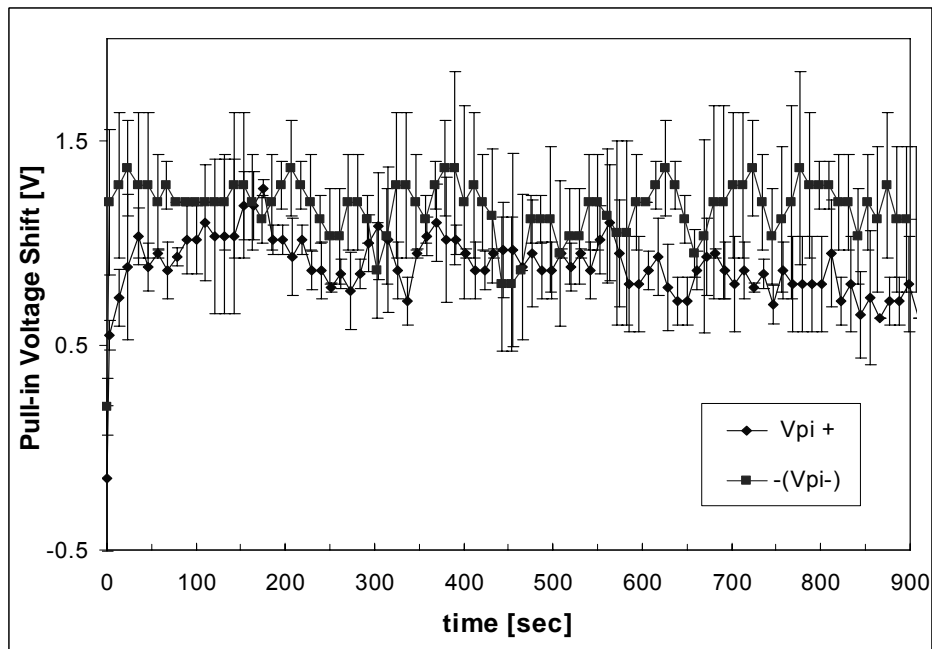


Figure 5-18: Change in pull-in voltages plotted for positive and negative offset voltage cases. The negative offset voltage curve was multiplied by a factor of -1 for a better comparison of the two curves.

Figure 5-19 shows the release voltage shifts during the same period of time. Again, the positive and negative release curves are indistinguishable from each other after the first 20 to 30 seconds of actuation. The negative case is characterized by a steady decrease in the release voltage throughout testing. On the other hand, during the first 150 seconds of positive bias testing, the release voltage increases. At that point, the curve drops rapidly and operates in a manner similar to the negative bias until testing ends.

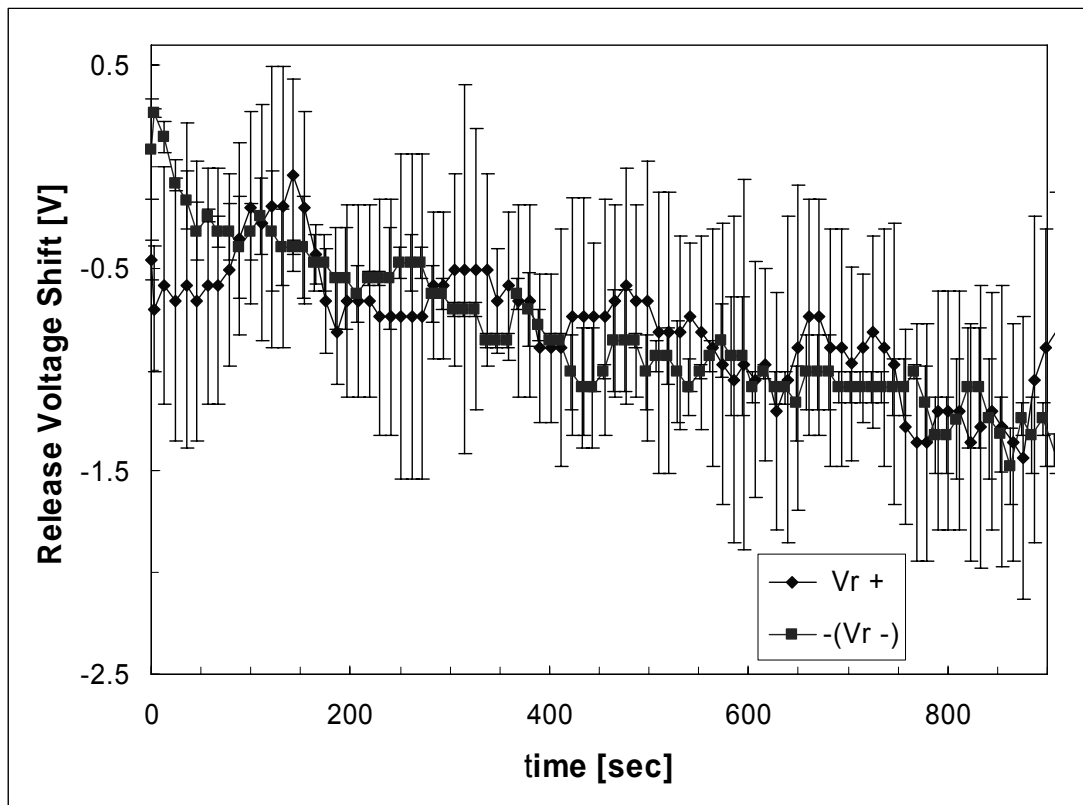


Figure 5-19: Change in release voltages plotted for the positive and negative offset voltage cases. The negative offset voltage curve was multiplied by a factor of -1 for a better comparison of the two curves.

The bottom line is there is little difference between the positive and negative biases. This is not surprising. Polarity differences that exist in silicon semiconductor devices are not present here, e.g. depletion versus accumulation at the same voltage magnitude. The differences that do exist are trap depth, trap density, barrier height, and effective mass of the carriers. It is likely that these differences are either not significant or average out within the error of the measurement.

5.3. Conclusion

This chapter presented results from MNS and MEM experiments. The MNS experiment involved biasing silicon nitride capacitors for extended periods while flat band voltage shifts were tracked. These experiments were performed to isolate insulator charging from the complicating issues inherent with MEM switches. This effort provides confidence in the charging theory applied to the MEM switch.

Operating MEM switches while tracking the changes in their pull-in and release voltages provides valuable information on MEM charging. Insight into the mechanisms of charging is gained by using a number of novel waveforms; specifically, charging dependence on voltage, polarity and hold time. These experiments also highlight an unusual behavior in the release voltages. Therefore, the next chapter will look at the voltage and timing dependence of charging. It also discusses the relationship between pull-in and release voltages and gives reasons for the unusual behavior of the release voltage. Appendix B provides experimental data from MNS and MEM irradiation experiments.

Bibliography

1. Reid, J.R. and R.T. Webster. "Measurement of Charging in Capacitive Microelectromechanical Switches," *Electronics Letters*, 38: 1544-1545 (21 November 2002).

6. Discussion

6.1. Introduction

This chapter provides analysis and discussion of the data presented in Chapter 5. This analysis includes both device types discussed in Chapters 4 and 5: MNS capacitors and MEM switches. The MNS capacitor results are analyzed for insulator charging. This includes modeling the capacitors and determining values for the insulator trap energy and density that best describe the charging behavior. This work provides confidence in tunneling theory as the discussion transitions to the MEM switch results. The MEM analysis begins by presenting the results best explained using tunneling theory as presented in Chapter 3 including the direct relationships between voltage and charging, and hold time and charging. Then results not explained using tunneling theory are presented. This includes the super-saturation effect and differences between pull-in and release voltages. Radiation results are discussed in Appendix B.

6.2. MNS Capacitors

This section analyzes the MNS capacitor results. First, the program used to model the capacitors is described, then the results are modeled and analyzed using the program, and, finally, the limitations of the model are discussed.

MNS Model

MNS data has been modeled using the tunneling theory described in Chapter 3. Differential equation (6-1) describes the change in trapped charge density (filled traps) over time.

$$\frac{\partial n_t(x,t)}{\partial t} = \frac{P(x,t)}{\tau_o} [N - n_t(x,t)]. \quad (6-1)$$

The following assumptions were made in developing this charging model:

- 1) a single trap energy participates in tunneling,
- 2) insulator trap sites are uniformly distributed in the 10 nm of insulator closest to the silicon interface,
- 3) an initial voltage shift of -8V (based on an initial, experimental CV sweep) caused by a net excess of trapped positive charge,
- 4) initial trapped charge is uniformly distributed in the trapping region,
- 5) a trap site remains filled once it traps a carrier, and
- 6) $P(x,t)$ is assumed constant at each location, x , during an individual time step - therefore, $P(x,t)$ is assumed $P(x)$.

The differential equation in (6-1) is solved as given in (6-2). For each discrete time step, the charge density for a user defined number of insulator thickness layers is calculated.

Each time step calculation depends on the charge density from the previous time step.

$$n_t(x,t_{i+1}) = n_t(x,t_i) + [N - n_t(x,t)] e^{-\frac{P(x)}{\tau_o} (t_{i+1} - t_i)} \quad (6-2)$$

The probability calculation assumes a square barrier of constant height for all calculations. In the case of tunneling electrons, the barrier height is an average of the trap depth and the height of the insulator conduction band relative to the silicon valence band. The barrier height to a tunneling hole is an average of the hole trap depth and the energy of the insulator valence band relative to the silicon conduction band.

$P(x)$ should actually be referred to as pseudo-time dependent, since the minimum insulator depth where tunneling transitions occur, x_o , is updated for each time step. Transitions into trap sites are allowed ($P(x) > 0$) when the bands bend enough for the trap site to overlap with the silicon's injecting band. (The probability is zero when the trap sites do not overlap in energy with the injecting band.) The depth x_o depends on trap energy and the local electric field, and the local electric field is a function of applied bias,

insulator thickness and trapped charge density. While the bias is maintained at a constant level throughout testing, x_o still changes over time due to changes in the band shape caused by increased levels of trapped charge in the insulator.

This model was used as the basis for a computer program that calculates insulator charging as a function of time and applied bias. A general outline of the program follows. After reading user input and initializing variables, a time loop begins. For each time step, the following calculations are made:

1. Calculate the shape of insulator energy band structure,
2. Calculate x_o for each time step,
3. Loop through each insulator thickness depth to calculate the new density, using equation (6-2) with the simplifications described, and
4. Calculate the voltage shift caused by the new trapped charge density.

Once all time steps have been made, the time dependent voltage shift data is written to an output file along with the user-defined input.

This program accounts for 1) the variable depth of x_o , 2) the changing capacitance associated with particular voltages as the CV curve shifts due to previous charging, and 3) permittivity of capacitor based on an experimental capacitance measurement while capacitor is in accumulation. The program does not account for stretch-out of the CV curve due to interface states. Even though the initial CV results show a large density of interface states, this is still a good approximation since the experimental results show no change in interface state density as the capacitor is biased or irradiated. So, this does not affect ΔV results, although it does add uncertainty to the initial voltage shift. The program also does not account for the non-square potential barrier that actually exists. This is a good approximation considering the depth of the trap (vertical axis) relative to the trap's distance from the silicon interface (horizontal axis). Finally, the program only

accounts for an initial, net trapped charge density (i.e. assumes either trapped electrons or trapped holes) and does not separately account for an insulator initially containing both trapped electrons and holes.

MNS Charging

In Chapter 5, the MNS capacitor data was described using a logarithmic least squares fit (equation in the form $y=a\ln(t)+b$). Since a numerical method was used to model charging, many of the parameters that describe charging (e.g. x_0) change with time. Therefore, the slope and constant terms (a and b) used to describe the logarithmic fit to the experimental (and modeled) results cannot be expressed analytically in terms of modeled parameters. To provide some context on how trap energy and density affect the slope and constant terms, an analytical approximation developed by Buchanan, *et. al.* is presented. Their analytical approximation for modeling tunneling [1] is similar to the method used in this research and is given in the following equation

$$\Delta V(t) = qN\lambda d_{ins}/\epsilon_r \epsilon_0 [\ln(t/t_0) + \gamma]. \quad (6-3)$$

where

q is the elementary charge [1.609×10^{-19} C],
 N is the trap density [cm^{-3}],
 λ is the effective tunneling depth [cm],
 d_{ins} is the insulator thickness [cm],
 t_0 is a time constant [sec], and
 γ is Euler's constant [0.57721].

Therefore, on a plot of ΔV vs $\ln(t)$, slope is given by $qN\lambda d_{ins}/\epsilon_r \epsilon_0$ and the constant is $qN\lambda d_{ins}/\epsilon_r \epsilon_0[\gamma - \ln(t_0)]$. The effect of N is apparent, while trap energy indirectly affects the value of λ and t_0 . Trap energy and density each affect both terms of the equation. While this analytical method provides a simple and fast solution, it ignores the time

dependence of many of the terms including t_0 , x_0 , and λ . It also does not provide an explicit voltage dependence.

The program described in the MNS Model section was run to generate time and voltage dependent calculations that approximate the best-fit results in Chapter 5 (given as $y=a \ln(t)+b$). Since time and applied bias were the experimental variables, trap energy and trap density were chosen as model fit parameters. The differential equation dictates that model results are fit with a logarithmic function, $y=c \ln(t)+d$. Trap energy and density were adjusted until the logarithmic fit for the model results matched the logarithmic fit from experiment, i.e. $a \approx c$ and $b \approx d$. Figure 6-1 displays the results for positive biases applied to the capacitor, where electrons from the p-silicon semiconductor tunnel into insulator trap-sites.

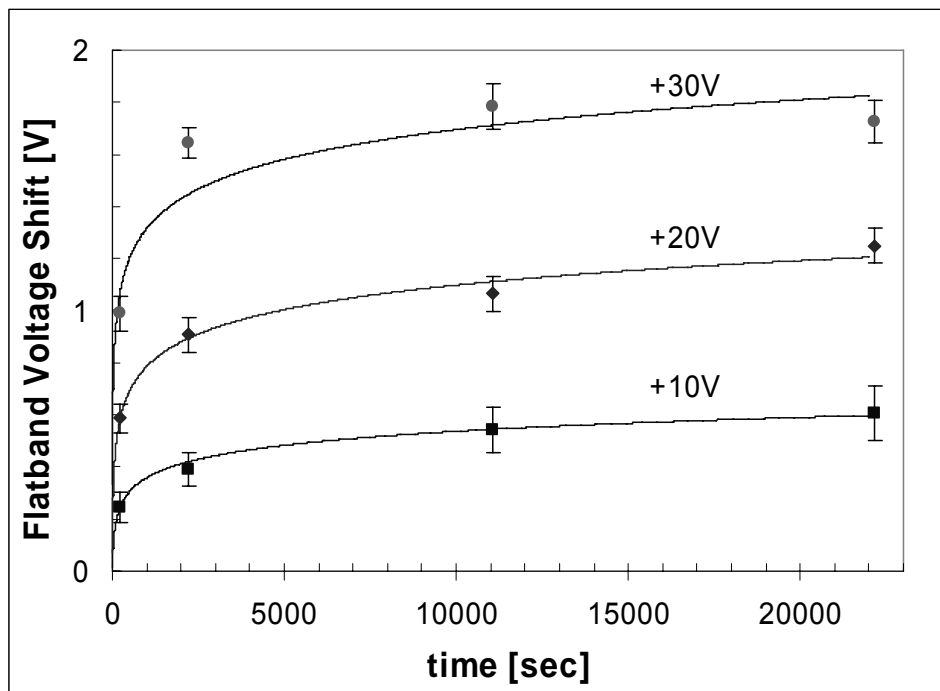


Figure 6-1: A comparison of modeled (lines) and experimental (points) results for positive biases applied to MNS capacitors

Table 6-1 summarizes the trap density and energy values used to generate these model best fit results. For the +10V case, an electron trap density of $1.68 \times 10^{18} \text{ cm}^{-3}$ and a trap energy of 3.0125 eV were used. For the +20V case, an electron trap density of $2.88 \times 10^{18} \text{ cm}^{-3}$ and a trap energy of 2.9848 eV were used. For the +30V case, an electron trap density of $3.50 \times 10^{18} \text{ cm}^{-3}$ and a trap energy of 2.9635 eV were used. As applied bias increases, trap density increases and trap energy decreases. This will be discussed further in the next section.

Table 6-1: Summary of best fit parameters for positive voltage case

V	N (traps/cm³)	Trap Energy (eV)
10	1.68×10^{18}	3.0125
20	2.88×10^{18}	2.9848
30	3.50×10^{18}	2.9635

Figure 6-2 displays the results when a negative bias is applied to the capacitor, and holes tunnel from the p-silicon semiconductor into insulator trap-sites. Table 6-2 summarizes the trap characteristics for negative biases. For the -10V case, a hole trap density of $5.28 \times 10^{18} \text{ cm}^{-3}$ and a trap energy of 3.0370 eV were used. For the -20V case, a hole trap density of $1.42 \times 10^{19} \text{ cm}^{-3}$ and a trap energy of 2.9850 eV were used. For the -30V case, a hole trap density of $1.47 \times 10^{19} \text{ cm}^{-3}$ and a trap energy of 2.969 eV were used. Again, notice that trap density increases and trap energy decreases as the bias magnitude increases.

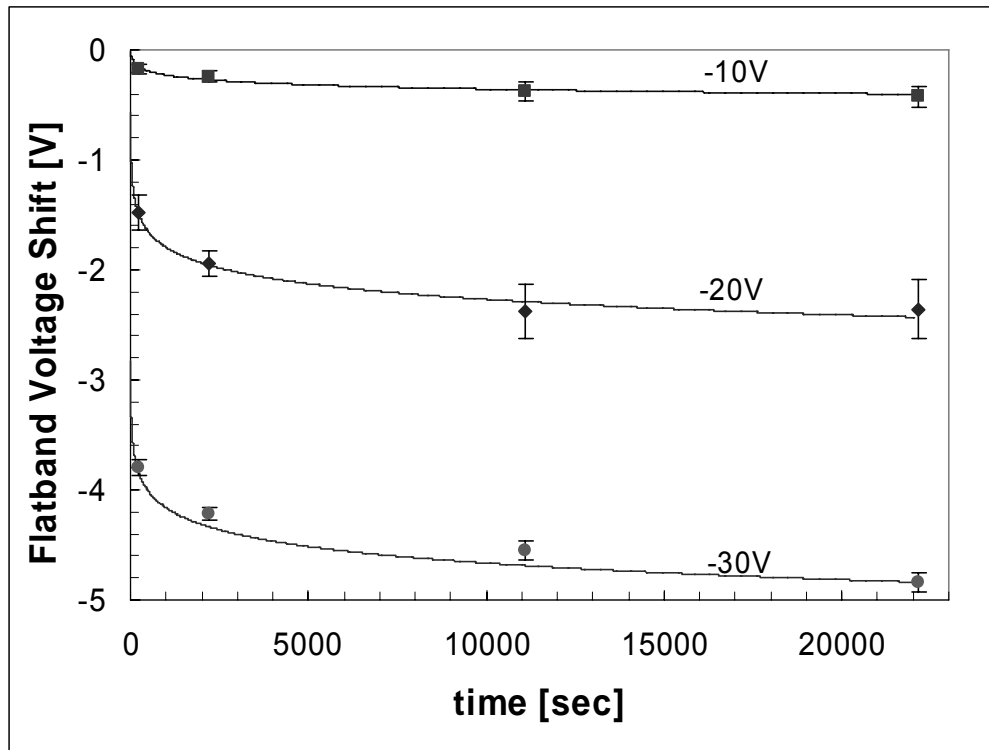


Figure 6-2: Negative applied bias - comparing model to experiment results

Table 6-2: Summary of best fit parameters for negative voltage case

V	N (traps/cm³)	Trap Energy (eV)
-10	5.28×10^{18}	3.0370
-20	1.42×10^{19}	2.9850
-30	1.47×10^{19}	2.9690

The results of the program fit the experimental data well when the trap density and trap energy are changed for each applied bias. These changes in density and energy are consistent for all biases and both polarities. The density increases and the energy decreases as the magnitude of the applied bias increases. Physical arguments for this behavior are provided in the next subsection.

Limitations of Model

If insulator charging followed all of the assumptions made in this model, matching charging behavior for any applied bias would only require an adjustment of applied bias; however, this is not the case. Trap density and energy also have to be adjusted to achieve an appropriate fit. The assumptions obviously do not hold for this range of applied biases. Physical arguments are suggested to explain these results in the two paragraphs that follow.

First, the reasons for increased trap density at higher applied voltages are discussed. Insulator quality tends to be lower near interfaces resulting in a higher trap density. Separately, increases in applied voltage magnitude are accompanied with further band bending. As the bands bend, x_o moves closer to the silicon interface so the probability of transitions into trap sites located closer to the interface is no longer zero. Combining these two arguments, carriers are more likely to tunnel into an insulator region with a higher density of trap sites. Therefore, it is not surprising that the charging behavior at higher applied voltage magnitudes is better characterized with larger trap densities.

The model results are extremely sensitive to changes in trap energy. Using the -10V case as an example, changing the trap energy value given in Figure 6-2 (3.0370 eV) to the average trap energy for all negative bias cases (2.997 eV) results in no voltage shift after 22000 sec. Therefore, a 0.04 eV difference in trap energy makes the difference between matching experimental results and seeing no charging. Increasing trap density cannot compensate for this difference. It is likely multiple trap sites exist in the insulator.

When a single trap site is used, it represents a weighted average of all trap sites participating in tunneling.

As stated above, a single trap energy and density do not describe the MNS charging behavior for all applied voltages. This was investigated further with the model by describing the insulator thickness with multiple regions, each with its own combination of trap energy and trap density. Specifically, the insulator was divided into three layers. The thickness of each layer was determined using the minimum x_o values from the -10V, -20V, and -30V tests.

The first step is to determine the layer furthest from the silicon-silicon nitride interface using the -10V data. The boundary furthest from the interface is predetermined by the width of the major divisions. In this case, the 0.2 μm insulator was divided into 10 major divisions, so the far boundary is 2.0×10^{-6} cm from the silicon-insulator interface. The closer boundary is determined by the smallest value of x_o for the -10V data (1.193×10^{-6} cm). Placing 3.0370 eV traps with a density of 5.25×10^{18} cm^{-3} in this first trapping layer while assuming no traps in the remainder of the insulator replicates the -10V results in Figure 6-2. (Again, trap sites located between the interface and x_o do not participate in tunneling.)

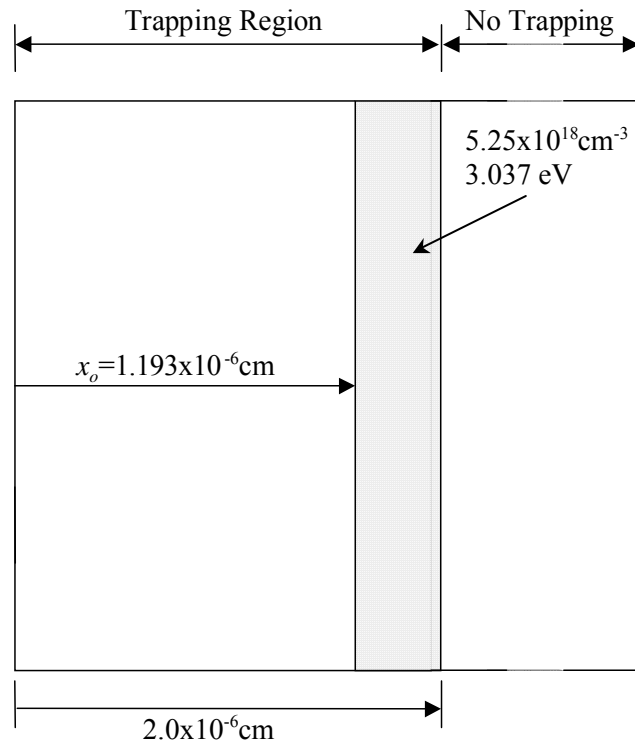


Figure 6-3: First trapping region of insulator

With the trap information for the layer furthest away from the interface established, the second and third layers can also be determined using the -20V and -30V results, respectively. The next closest layer's boundaries span from the smallest value of x_o calculated for the -20V run in Figure 6-2 and the x_o value for -10V. The third layer is defined by the silicon interface and the -20V x_o value. Figure 6-4 shows these boundaries.

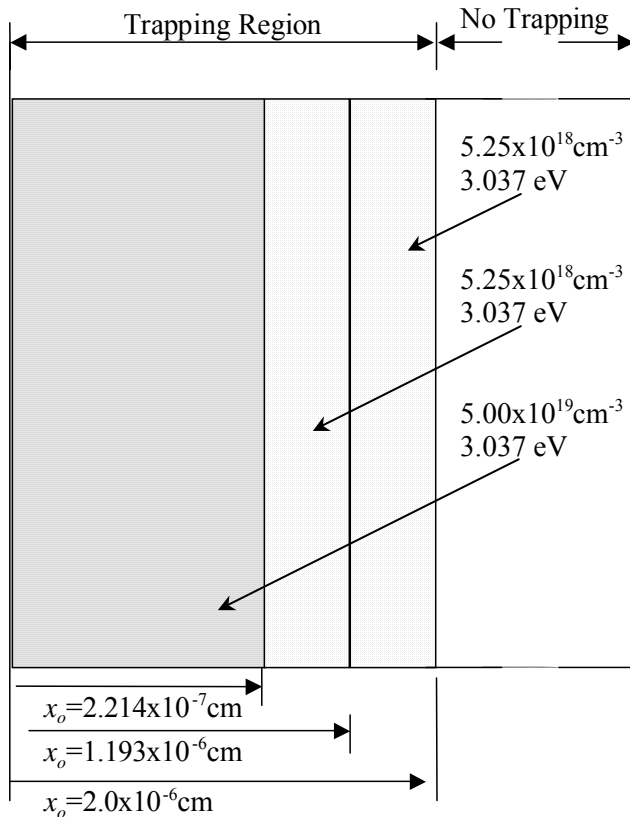


Figure 6-4: All three trapping regions of insulator identified

The 3.037 eV trap energy also provides the best fit for the -20V and -30V cases.

The best fit for the -20V curve was achieved maintaining the -10V trap density of $5.25 \times 10^{18} \text{ cm}^{-3}$, while the trap density had to be raised to $5.0 \times 10^{19} \text{ cm}^{-3}$ for the -30V case. The results are shown in Figure 6-5 and Table 6-3.

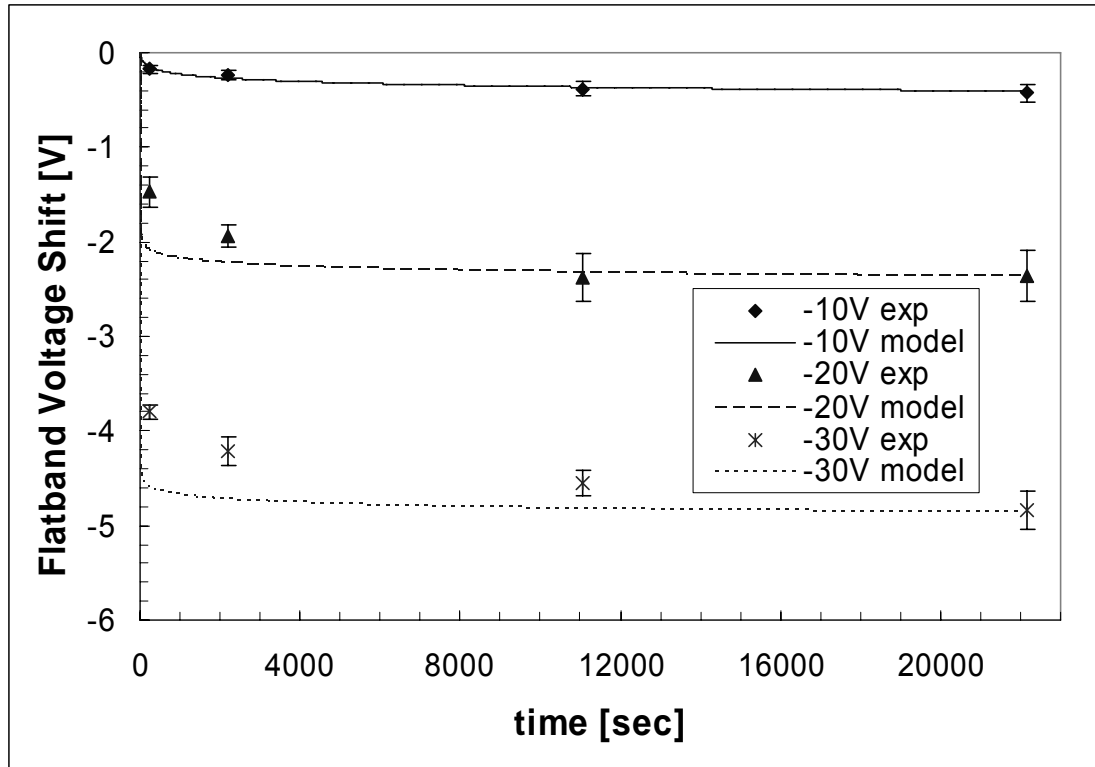


Figure 6-5: Adjusted trap density based on -10V trap energy

Table 6-3: Trap density, trap energy, and beginning of trapping

N_t (cm $^{-3}$)	E_t (eV)	x (cm)
5.25×10^{18}	3.037	1.193×10^{-7}
5.25×10^{18}	3.037	2.214×10^{-8}
5.00×10^{19}	3.037	0.0

As expected, the -10V data are fit well with this method. All bias levels are fit well at late times but do not match the -20V and -30V data at early times. Adjusting trap energy in these cases does not help – over-estimation at early times. The model predicts that insulator traps charge too quickly due to the deep trap energy in a large portion of the insulator thickness (defined by the furthest trapping region). The trap density value appears to be a good match as evidenced by the data fit at later modeled times. It appears

this trap density would need to be split across at least one other trap energy level to more accurately model the early data.

6.3. MEM Switches

Limitations of Model

MEM and MNS Comparison

Many of the fundamental charging processes described for MNS capacitors also apply to MEM switches. The two devices are also dissimilar in a number of ways including material and geometry differences. The MEM structure has a silicon nitride insulator deposited on a gold electrode and a gold beam that makes temporary contact with the insulator surface. The MNS structure has a silicon nitride insulator deposited on a silicon substrate with aluminum deposited permanently on the insulator surface for a top contact. Figure 6-6 illustrates the band structures associated with the two devices when no voltage is applied. (The MEM beam is assumed to be in contact with the insulator.)

Even with 0V applied and no trapped charge present, the MNS conduction and valence bands bend due to the work function difference between the aluminum contact and the silicon substrate. On the other hand, there is no band bending for the MEM switch under the same conditions since the beam and electrode share the same materials.

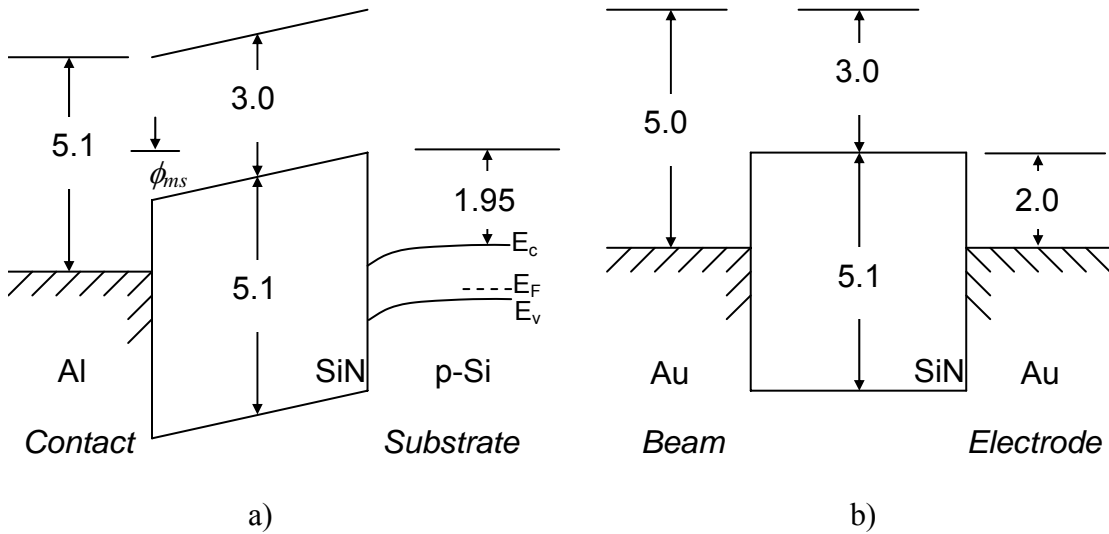


Figure 6-6: Band diagram for a) MNS capacitor and b) MEM capacitor with bridge down (units are eV).

Not all charges affect device operation equally. The discussion that follows provides the charging scenario that has the largest affect on device operation – specifically, the source of these charges and their ultimate location. For the MEM structure, charge trapped closest to the beam causes the greatest change in device operation, while charge located near the electrode has little effect. Charge injection occurs at both insulator interfaces; however, it is reasonable to assume that charge transport through the entire thickness of the insulator is minimal at the fields and temperatures of interest. Therefore, the interface closest to the trap site is assumed the source of trapped charge. Since charges trapped near the electrode have a negligible effect on device operation and charges trapped in sites closest to the beam have the largest effect, only charges transiting from the beam into the insulator are tracked. This

interface is referred to as the injecting contact. For the MNS device, the injecting contact was the silicon substrate.

Another difference between the MEM and MNS devices is how the material interface at the injecting contact affects the barrier height for tunneling. In the MNS, a 3.05 eV barrier exists for electrons tunneling from the silicon valence band into an insulator trap, while a 3.15 eV barrier characterizes hole tunneling from the silicon conduction band into the trap. For the MEM device, these barriers are lower; the barrier to electron tunneling is 2.0 eV and the barrier to hole tunneling is 3.1 eV (see Figure 6-6).

The effect of these material differences lies in how quickly charge builds in the insulator via tunneling probabilities. For example, tunneling rate increases as the probability of tunneling increases. The tunneling probability for electrons transiting from the gold beam into the silicon nitride is higher than the probability of electrons tunneling from the silicon into the MNS insulator, because the gold-silicon nitride barrier is lower than the silicon-silicon nitride barrier (2.0 eV vs. 3.05 eV). A related issue is electron trap depth. Voltage dependence of charging requires a portion of the trap sites lie energetically above the injecting band so that the application of a bias causes band bending which makes additional trap sites available to participate in tunneling. In Figure 6-7, the nominal electron trap energy determined in the MNS capacitor section is superimposed on the MEM band diagram. Notice that a 3 eV electron trap lies below the gold conduction band. This means the minimum tunneling depth, x_o , equals zero, regardless of the applied bias. If this were true, insulator charging would be independent of applied voltage. The data from Chapter 5 does not support this. Also, the results of the MNS experiment suggest that multiple trap energies in the insulator are likely. So,

alternative trap energy and density values are needed that represent the average trap in the 2.0 eV of insulator that lie above the beam conduction band and participate in tunneling.

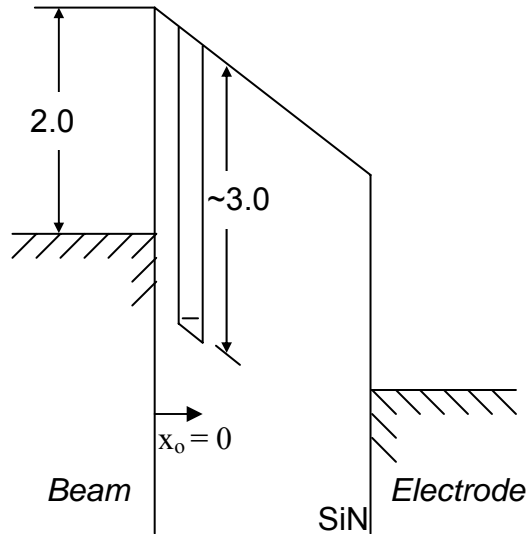


Figure 6-7: Trap energy from MNS experiments placed on MEM band diagram

There is a final difference between the two devices. The band diagrams shown in Figure 6-6 represent the 0V case; however, a working MEM switch will not be in this configuration (closed). Instead, the band diagram should include the large air gap as shown in Figure 6-8. This highlights another major difference between the MNS capacitor and the MEM switch – the temporary interface that exists between the insulator and the injecting contact.

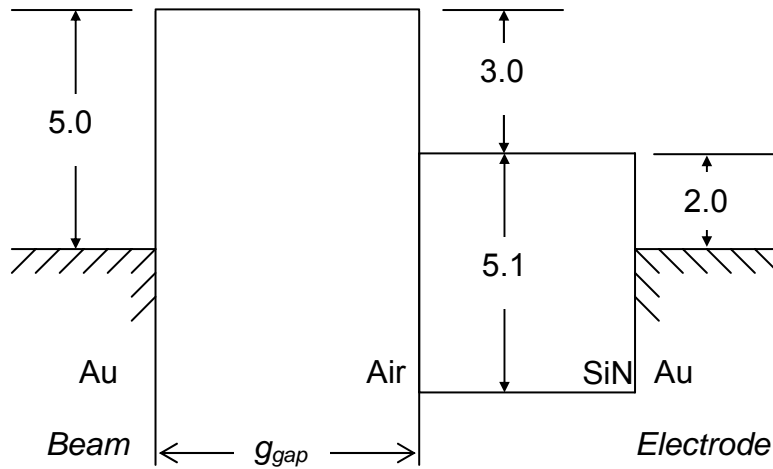


Figure 6-8: Trap energy from MNS experiments placed on MEM band diagram

Ideally, this gap would only result in high isolation while the beam is open. This temporary contact also introduces further complexity in understanding switch operation. The insulator surface is actually a rough surface on the order of 10 nm [2]. Therefore, as the beam meets the insulator surface, intimate contact is not made between the two surfaces. Instead, the beam contacts the insulator in some locations while small air gaps remain in other locations as shown in Figure 6-9. Since this effectively forms metal-air-nitride-metal capacitor in parallel with metal-nitride-metal capacitors, a reduced, effective permittivity can be used. A typical value for silicon nitride permittivity is between 7 and 8 (see 0) while an effective permittivity value for MEM switches is around 4 [2].

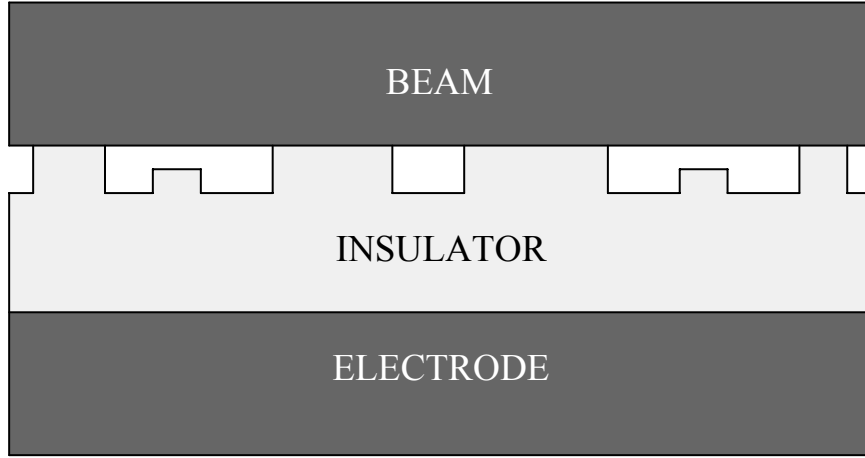


Figure 6-9: Schematic of beam in contact with irregular insulator surface

Model

As part of this research, an existing computer program [3] that modeled switch operations was modified to include charging from tunneling holes and electrons. The original program calculates beam position for a single applied voltage using a quasi-2D approach. The method is quasi-2D because the beam length dimension is broken into 250 finite elements, and the vertical deflection of each element is calculated. The original program also includes a voltage sweep option which sequences together a series of individual applied voltage steps and uses the previous beam position as an initial guess for the next voltage step. The voltage sweep is limited to a triangular waveform based on a user defined voltage range and step size. The amount of time required to complete the voltage sweep is not incorporated into this program in any way, so each voltage step occurs in an arbitrary amount of time. At the end of each voltage step, the program calculates the total capacitance of the switch. At the conclusion of a voltage sweep, the program generates a capacitance-voltage plot similar to those presented in Chapter 2.

The original program also allows the placement of a single sheet of trapped charge of a user-defined density halfway between the electrode and the insulator surface.

This program was enhanced to allow for the investigation of spatial and temporal changes in trapped charge density. These program enhancements include:

- 1) A time-dependent voltage waveform,
- 2) Tunneling of carriers from beam to insulator (carrier type depends on applied voltage),
- 3) Insulator divided into a two dimensional array of finite elements (shown in Figure 6-10) which allow spatial and temporal tracking of insulator charging,
- 4) The top row of elements can be subdivided into a user defined number of elements allowing greater resolution in the region where essentially all tunneling occurs,

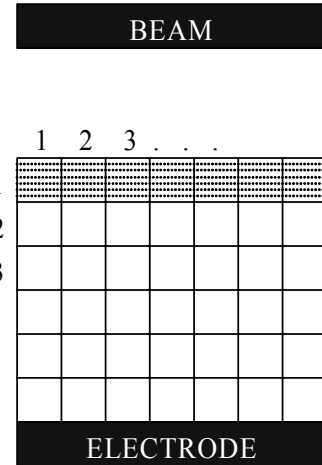


Figure 6-10: Illustration of insulator 2D finite element array

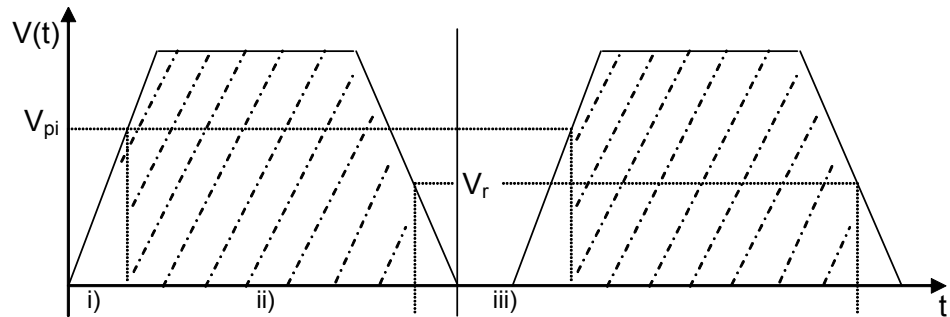
- 5) Calculation of local electric field in insulator,
- 6) Radiation induced charge in insulator using a user-defined radiation dose rate, and
- 7) Calculation of radiation induced trapped electrons and holes (both carrier types tracked during irradiation).

Next, expectations of device operation based on the tunneling theory used to develop this model are presented.

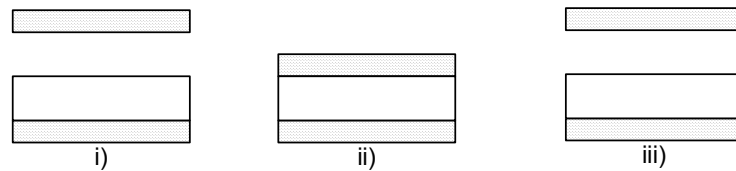
Expectation

In Chapter 2, a simplistic simulation of $\Delta V_{pi}(t)$ and $\Delta V_r(t)$ was presented. To generate this plot, the charging rate was assumed constant over time. Also no detrapping mechanisms were present - once a trap filled it remained filled for the remainder of testing. Under these assumptions, $\Delta V_{pi}(t)$ and $\Delta V_r(t)$ were linear and indistinguishable from each other. However, this is not the behavior seen in the experimental results shown in Chapter 5. The theory in Chapter 3 explained why the curves are not linear. This section develops the expected relationship between the pull-in voltage shift and the release voltage shift assuming tunneling is responsible for charging.

The discussion begins with the simplest case - no insulator charging. Even though the experiment shows the insulator accumulates charge, this no charging case provides a baseline for the discussions that follow. Figure 6-11 a) shows two cycles of a typical waveform used to actuate the switch. The shaded regions indicate when the beam is in contact with the insulator surface. This is further illustrated in figure b) where the parallel plate capacitors represent a switch opening and closing. Each capacitor corresponds to the lower case Roman numeral (i, ii, etc.) annotated on figure a). Due to the simplifying assumption that charging processes do not occur, the pull-in voltage for the second cycle is identical to the initial pull-in voltage, and the second cycle release voltage is the same as the first cycle release voltage. This represents the ideal case where the pull-in and release voltages are only determined by the mechanical properties of the beam, device geometry, and the voltage waveform.



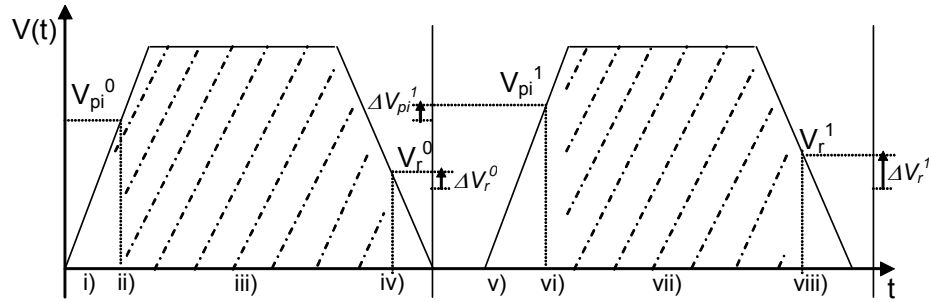
a)



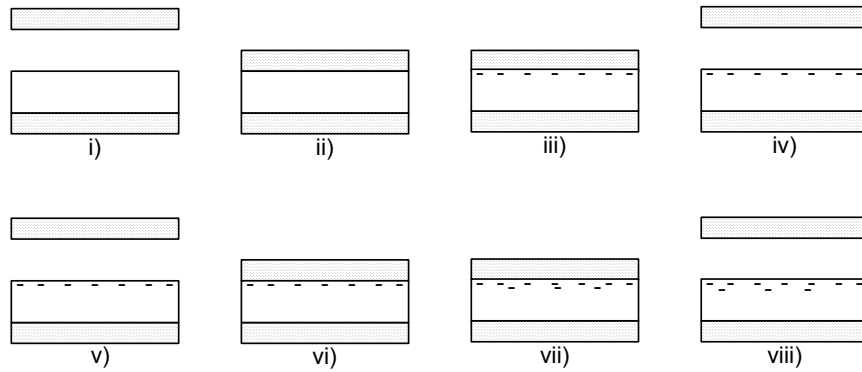
b)

Figure 6-11: a) Waveform for two cycles – the pull-in and release voltages. b) Simplified switch design corresponding to waveform showing charge becoming trapped while beam is down.

In the next case, charge is allowed to tunnel into the insulator. The expected ΔV_{pi} and ΔV_r deviations relative to the ideal case are again discussed for two complete unipolar cycles where the waveform's positive bias is applied to the electrode. A graphical representation of these cycles is given in Figure 6-12.



a)



b)

Figure 6-12: Tunneling is responsible for changes in pull-in and release voltages.

These two cycles are explained in detail below.

- i) Assume the insulator initially has no trapped charge and is neutral,
- ii) Voltage shifts are relative to the ideal pull-in and release voltages. Since there is no charge trapped at this point, ΔV_{pi}^0 is 0V (ΔV_{pi}^0 not shown in Figure 6-12).
- iii) After pull-in, electrons from the beam tunnel into trap sites near the insulator surface.
- iv) With electrons trapped in the insulator, the electrostatic force pulling the beam towards the electrode is reduced for any applied positive voltage. Therefore, the beam releases from the insulator surface at a higher voltage than the ideal, so ΔV_r^0 is greater than zero.
- v) Assume no charging (or discharge) processes occur while the beam is not in contact with the insulator. Also assume charge does not move within the insulator.

vi) As pointed out in Chapter 2, ΔV is independent of beam location. Since there is no change in charge density or the location of the charge, ΔV_{pi}^1 is identical to ΔV_r^0 .

vii) After pull-in, electron tunneling resumes at a rate proportional to the density of empty trap sites.

viii) With more electrons trapped in the insulator, the beam releases at an even larger applied bias which increases the release voltage shift.

Summarizing, the pull-in and release voltage shift relationships shown in Figure 6-12

$$0 = \Delta V_{pi}^0 < \Delta V_r^0 = \Delta V_{pi}^1 < \Delta V_r^1.$$

The data collected during an experiment associates the pull-in and release voltages from a single cycle with a single time (time at the beginning of cycle). The model also associates time with the pull-in and release voltages in this way. Figure 6-13 is an example of model results using the enhanced program for modeling MEM switch charging. Notice the release voltage shift is greater in magnitude than the pull-in voltage shift for each cycle. At later times, ΔV_{pi} and ΔV_r converge. When the difference between ΔV_{pi} and ΔV_r reaches the sensitivity of the measurement, the two curves become indistinguishable.

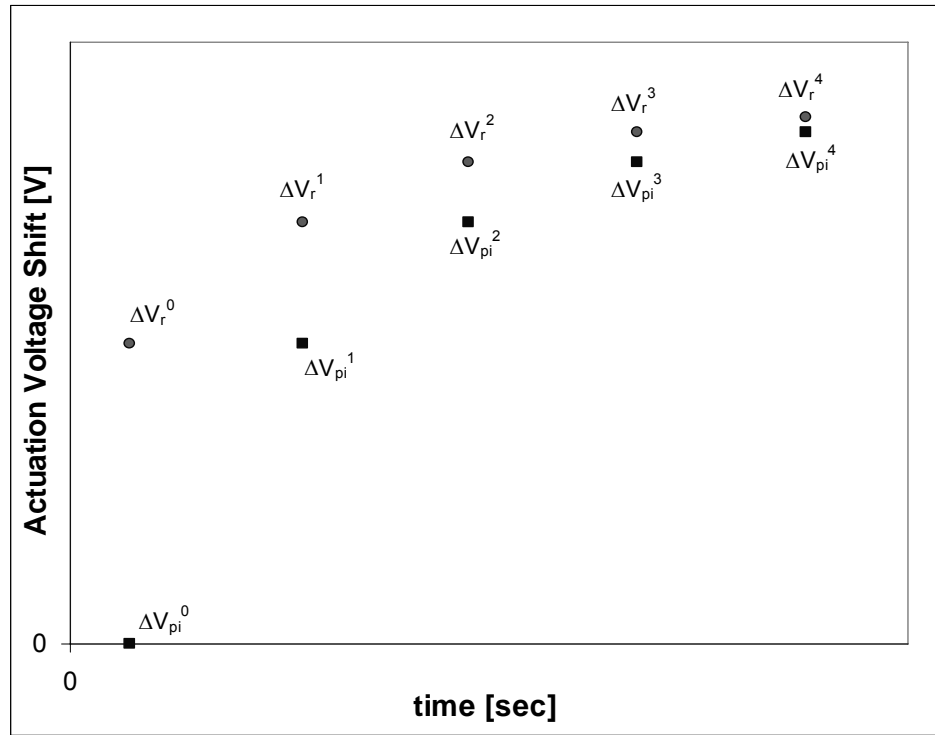


Figure 6-13: Modeled data points for five cycles assuming tunneling causes voltage shifts

Deviations from this theory are discussed further in the next section. These deviations between $\Delta V_{pi}(t)$ and $\Delta V_r(t)$ are important, because permanent failure of a switch is normally preceded by a large decrease in ΔV_r magnitude and eventually leads to the beam no longer releasing from the insulator surface. At the same time, ΔV_{pi} changes very little.

The next section analyzes, models, and discusses the MEM results presented in Chapter 5. Admittedly, the program does not successfully model all facets of the results. In these cases, alternate explanations are presented. These cases provide opportunities for future research.

Explanation of MEM Results

Chapter 5 examined the effect different waveform parameters have on MEM switch operation with a goal of better understanding the mechanisms responsible for insulator charging. To do this, pull-in and release voltages were tracked during switch operation. It was shown in Chapter 2 that a voltage shift can be related to the net charge density trapped in the insulator.

Figure 6-14 is an example of capacitive switch ΔV_{pi} and ΔV_r results from experiment. There are four areas identified on the graph. First, ΔV_{pi} and ΔV_r vary linearly on a logarithmic scale for approximately the first 100 seconds of testing indicating they follow the tunneling model. This behavior is similar to that shown for the MNS capacitor in section 6.2. The second characteristic is the decreasing ΔV_{pi} for the remainder of testing. In Chapter 5, this was referred to as “super-saturation.” The third feature is the vertical separation between the pull-in and release curves, ΔV_r lies below ΔV_{pi} , for the entire testing period. This counters the expectation described in the previous sub-section. The fourth characteristic is the growing separation between ΔV_r and ΔV_{pi} for the remainder of testing. The pull-in data during this period was fit with a logarithmic function while the release data was fit with a linear function. This indicates two separate processes drive the pull-in and release of the beam. All MEM switch data collected in this research exhibit the first and third characteristics. Most of the switch data also show the other two characteristics. The remainder of this section discusses these characteristics in detail for a better understanding of the mechanisms responsible for limiting switch lifetime.

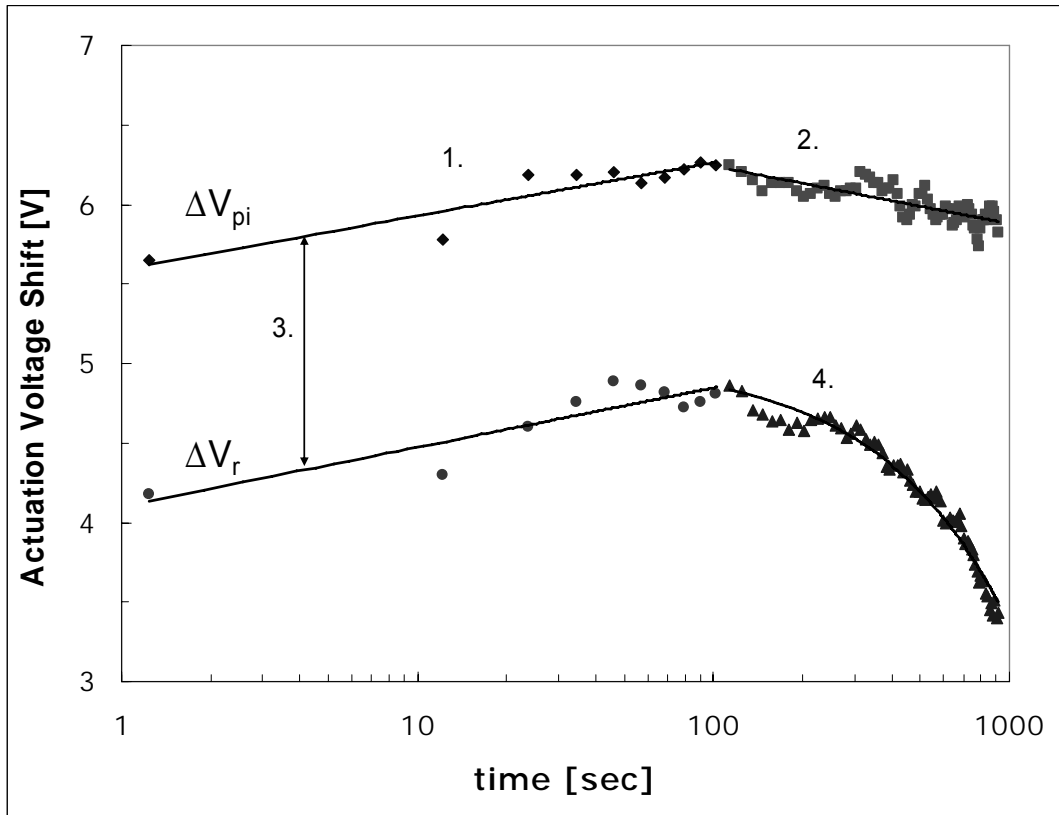


Figure 6-14: Example of pull-in and release shift data

Tunneling

During the first 100 seconds of testing, ΔV_{pi} and ΔV_r vary logarithmically and are parallel to each other. The vertical offset between the two curves, as shown in Figure 6-14, is unexpected. Since ΔV_{pi} is closer to the expected results throughout testing and ΔV_r deviates dramatically from theory, ΔV_{pi} data is assumed to be the standard. Therefore, it is modeled using the enhanced program. The ΔV_r results are described later in this section.

The voltage shift results for the first 100 seconds of testing are in Figure 6-15 for the 36, 38 and 40V peak voltage waveforms. For these cases, the waveform had a t_{slope} of

25 msec, a t_{hold} of 25 msec, and a t_{rest} of 25 msec. In addition to the data points, the corresponding R^2 value for each data set is shown. The fits to the 38V and 40V data are not as good as the 36V fit. As discussed for the MNS capacitors, this logarithmic fit to the data indicates that it agrees with tunneling.

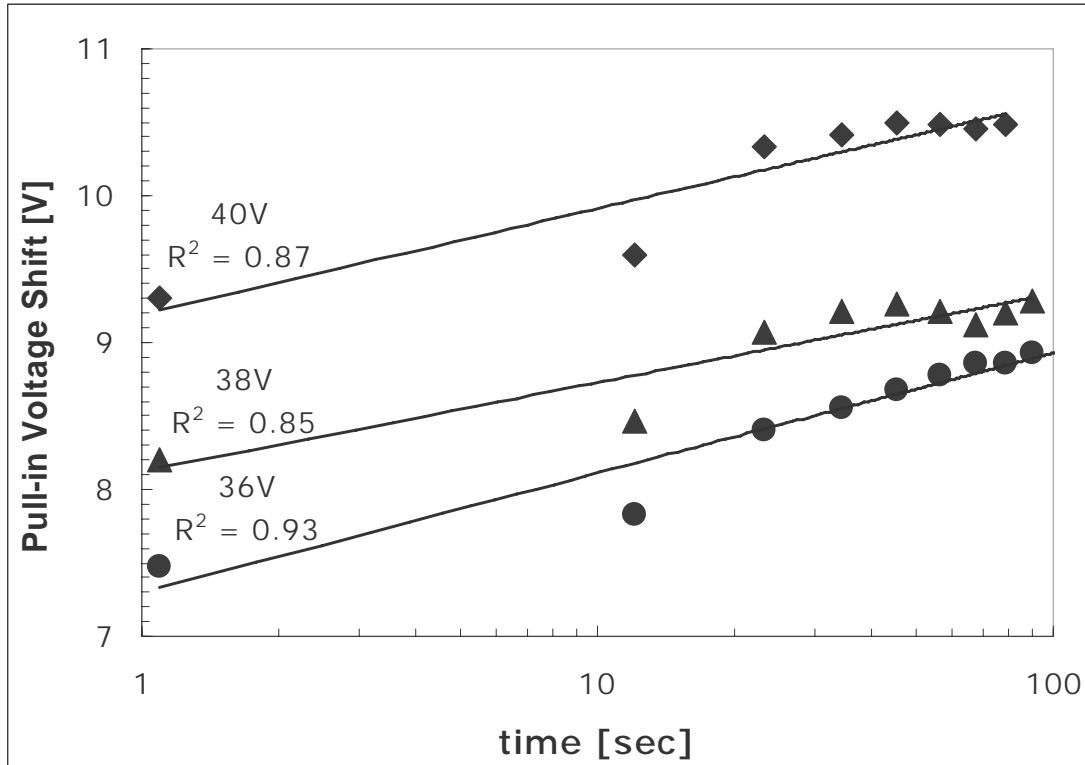


Figure 6-15: Least squares fit of pull-in voltage shifts (solid line is least squares fit with accompanying equation and R^2 value)

Table 6-4 contains the beam and insulator properties used to model the switch. The choice of material properties matched an initial, experimental CV sweep created using a 30V, 20 Hz, bipolar sweep performed before testing began. As discussed in 0, the effective dielectric constant is lower than the dielectric constant normally associated

with silicon nitride. This effective value is consistent with the dielectric constant used in previous switch modeling [2][4].

Table 6-4: Material properties used for modeling peak voltage

Property	36 V	38 V	40 V
Young's Modulus [GPa]	30.0	30.0	30.0
Residual Stress [MPa]	3.2	3.2	3.2
Poisson's Ratio	0.35	0.35	0.35
Beam Thickness [μm]	1.0	1.0	1.0
Beam-Insulator Gap [μm]	3.0	3.0	3.0
Effective Dielectric Constant [-]	4.3	4.3	4.3
Trap Energy [eV]	1.72	1.72	1.72
Trap Density [$\times 10^{18} \text{ cm}^{-3}$]	4.00	4.00	4.60

Figure 6-16 compares the data points shown in Figure 6-15 to model results using the input parameters given in the table above. The stair-step feature of the modeled curve is due to the coarseness of the sloped portion of the voltage waveform which is used to determine the pull-in voltage. The sloped portions of an ideal waveform would be smooth, as shown in Figure 6-11; however, in experiment and modeling this slope is approximated with a series of steps in voltage. Fidelity depends on the number of time steps made to approximate a slope. In the experiment, the step size made by the function generator was on the order of 10 mV; while, the step size used in modeling was a much larger 0.25V. Reducing the size of the time steps dramatically increases the computation time to model the switch. Therefore, the tradeoff between computing time and the resolution of the pull-in and release voltages was balanced.

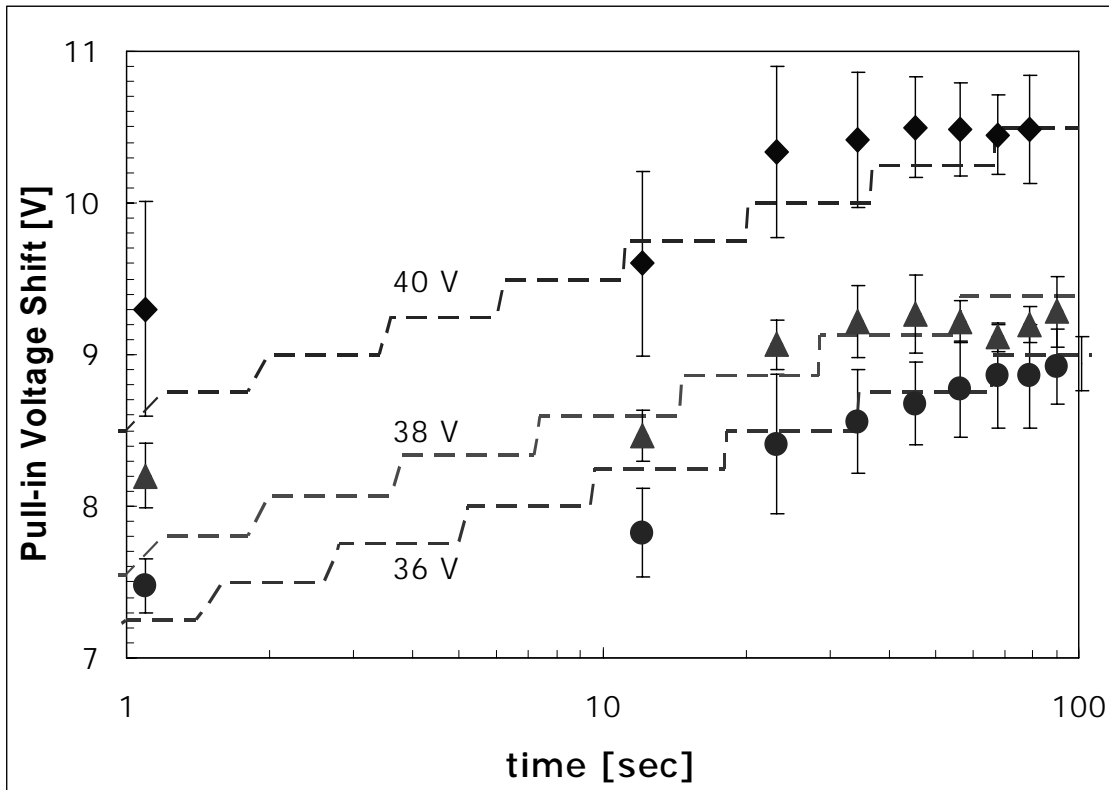


Figure 6-16: Comparison of modeled results (dashed) to experimental results (points)

From Table 6-4, notice the trap energies and densities used to produce the modeled results above. The trap density varies while the trap energy remains constant for all peak voltages. From the MNS results, it was discussed that the insulator has multiple trap energies and each energy has its own density. This average trap energy and density represents all trap energies and densities participating when a single bias is applied. For the MEM case, it is even more complicated. That single trap energy and density does not just represent the trap energies and densities participating at a single bias, this weighted average represents all trap energies and densities participating for a wide range of applied voltages. In the figure above, the voltage range was slightly different for each case run (0

to 36V, 0 to 38V, and 0 to 40V). Therefore, due to the averaging of material properties, it is not surprising a single trap energy does a reasonable job describing these three voltages for the relatively small voltage difference that exists between the 36V peak voltage and a 40V peak voltage. The trap density increases slightly when the peak voltage increases from 36V to 40V, which is consistent with the MNS results.

The insulator's sensitivity to length of hold time (while maintaining a constant number of beam-to-insulator collisions, i.e. frequency) was also investigated. In Figure 6-17, the amount of time the beam spends in contact with the insulator per cycle is smallest for the bottom curve and largest for the top curve. All other things being equal, the more time the beam is in contact with the insulator, the quicker insulator trap sites fill. Previous research had not addressed which is responsible for charging, the length of time the beam is in contact with the insulator or the number of beam-insulator collisions. This data shows that hold time dramatically affects charging. The experimental data, logarithmic least squares fit, and corresponding R^2 value for each data set is shown. The fit to 50,25,0 and 40,25,10 is good while the other two waveform cases are fair. Notice the amount of time that passes before the insulator enters super-saturation is inversely proportional to the hold-time length.

It is also interesting that the transition to the super-saturation regime depends on the hold time per cycle. The 50,25,0 waveform never enters that super-saturation regime, while it takes less than 50 sec for the 0,25,50 waveform to reach this point. Super-saturation is discussed further in the next subsection.

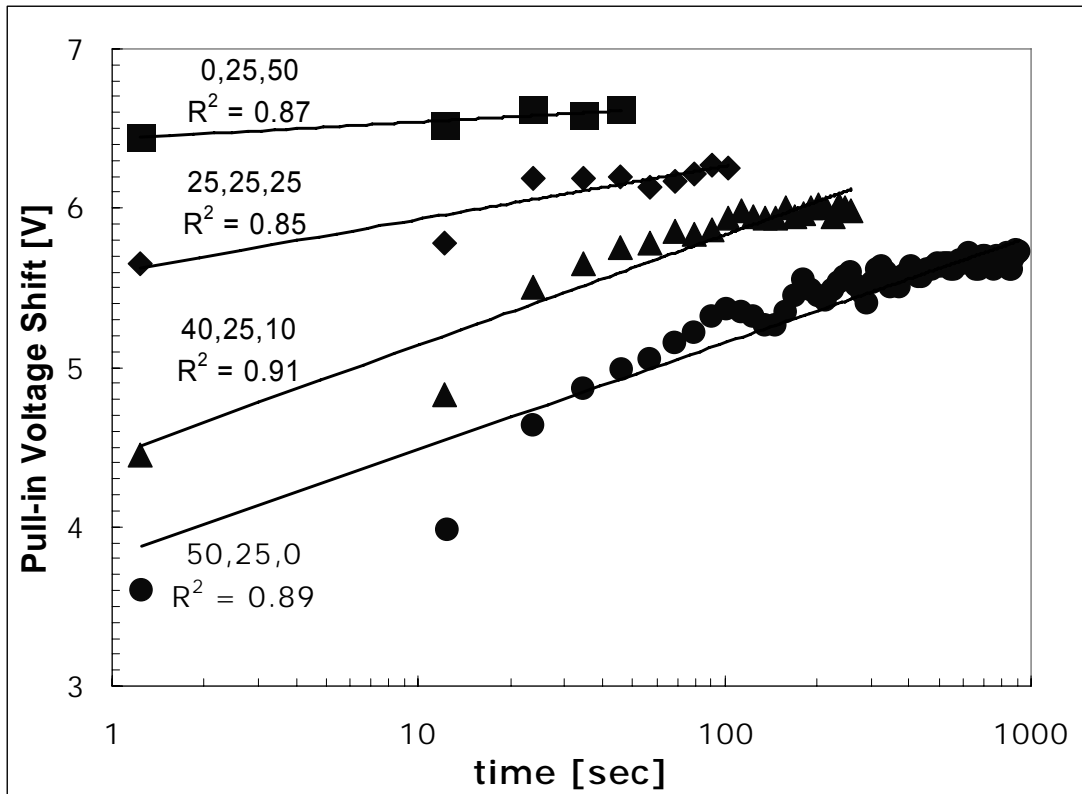


Figure 6-17: Pull-in voltage shifts for various hold times ($t_{rest}, t_{slope}, t_{hold}$) while frequency is constant plotted on a logarithmic scale

The material properties in Table 6-5 were used to model the data shown in Figure 6-17 and were arrived at in the same manner as the properties given in Table 6-4. Only the 50,25,0 data was modeled to fit the data, since there was no sign of super-saturation in the experimental data. Since the program does not have the ability to model super-saturation, fitting the other three hold time data sets was not attempted.

Table 6-5: Material Properties for 50,25,0 hold time case

Property	50,25,0
Young's Modulus [GPa]	30.0
Residual Stress [MPa]	3.2
Poisson's Ratio	0.35
Beam Thickness [μm]	1.0
Beam-Insulator Gap [μm]	3.0
Effective Dielectric Constant [-]	5.0
Trap Energy [eV]	1.48
Trap Density [$\times 10^{18} \text{ cm}^{-3}$]	5.2

Figure 6-18 shows the first 100 sec of experimental data and model results for the 50,25,0 waveform ($t_{rest}, t_{slope}, t_{hold}$) based on the switch material properties given in the table above. The three other waveforms were also simulated using the same material properties. While these three additional simulations do not match the data points, they do demonstrate a major feature expected from tunneling theory. There are two major points to notice from the experimental and modeled data. First, the magnitude of the initial voltage shift is proportional to the length of the hold time. Longer hold times per cycle lead to more trap sites filling during the first few cycles, hence longer initial voltage shifts. The model demonstrates this feature.

The slope of the experimental data decreases for larger initial shifts. Since tunneling rate is proportional to the density of available trap sites, the tunneling rate will be smaller in cases where more trap sites filled in the first cycle. Therefore, based on the previous discussion on initial voltage shift, long hold time have fewer traps available so the ΔV -time slope is smaller. Conversely, short hold times have many traps available so the ΔV -time slope is much larger.

This feature is not picked up with this model for reasons previously described for the MNS capacitor. The weight averaged trap energy and density for the 50,25,0 case is representative of traps that participate at a lower voltage, say 20V. The 0,25,50 case requires trap characteristics much closer to 36V since such a large fraction of the cycle time is spent at that voltage. Therefore, based on MNS results, one would expect the trap energy to decrease slightly and the trap density to increase to match the longer hold time results.

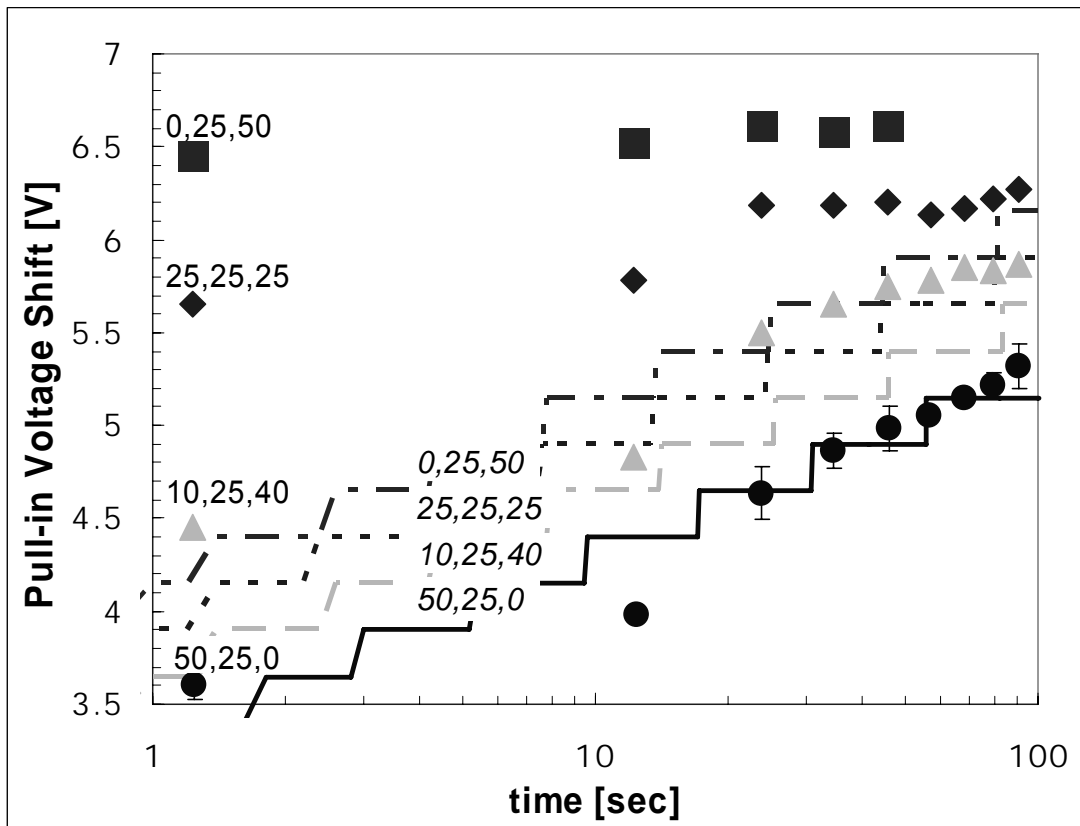


Figure 6-18: Comparison of hold time modeled results (solid) to actual results (points)

This section discussed the pull-in voltage shifts early in testing when they agree with the theory presented in Chapter 3. To support this, peak voltage and waveform time parameters were perturbed to determine if the charging response of the switch matches expectations based on tunneling. Variations in trap density were consistent with the MNS results from the previous section of this chapter. In an effort to answer the question - is beam-insulator contact time more important than the number of beam-insulator collisions, it was shown that variations in hold time, while frequency remains fixed, have a large effect on device operation. This data also illustrates major deviations from tunneling theory, and these are discussed in the paragraphs that follow.

Super-saturation

In many instances, it was observed that the pull-in voltage shift presented a deviation from the expected results referred to as super-saturation. In MNS capacitors, charging behavior for tunneling was characterized by a continual increase in trapped charge density while the charging rate decreased. In this case, ΔV curves either approach an asymptote defined by the maximum voltage shift for that peak voltage waveform, or when super-saturation occurs, the voltage shift increases until it reaches a maximum value. Then the curve gradually decreases and approaches the asymptote from above rather than below. The comparison of ΔV_{pi} using a waveform with a peak voltage of 36V and various hold times in Figure 6-19 shows that regardless of the level of super-saturation, all ΔV_{pi} curves converge on the same voltage shift, approximately 5.7V.

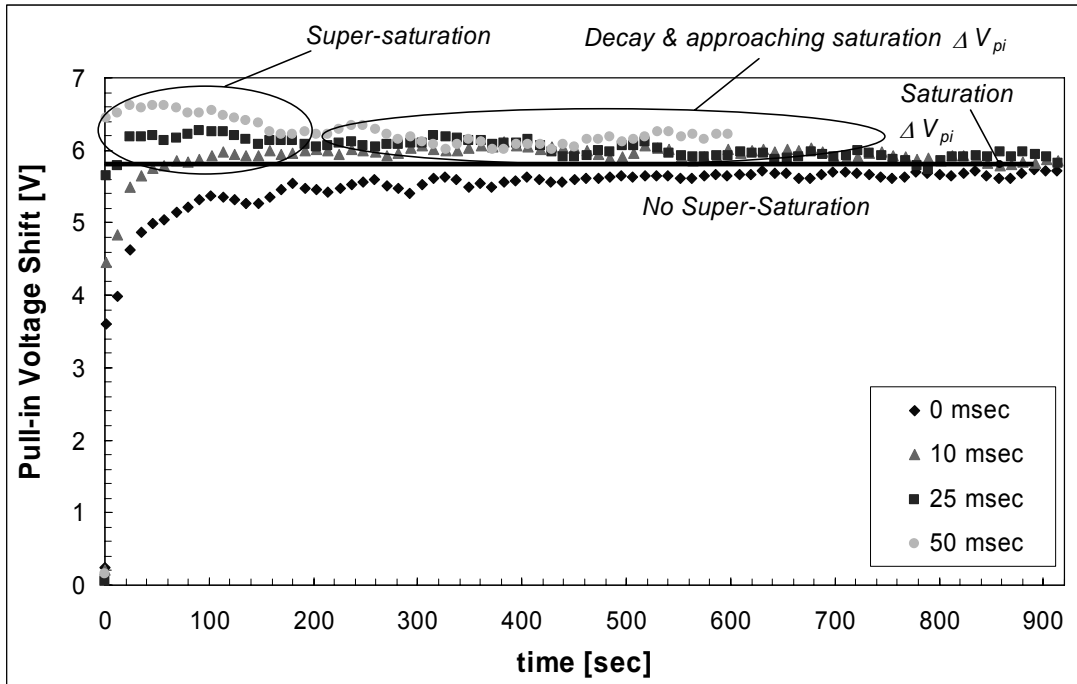


Figure 6-19: Sample of super-saturation for a 36V peak voltage

In Figure 6-20, the data from Figure 6-19 has been re-plotted on a logarithmic time scale. First, notice that the longer the beam is in contact with the insulator, the greater the super-saturation effect. In the 50,25,0 case, there is no super-saturation. During the super-saturation phase of the 0,25,50 case, the pull-in curve reaches a maximum value that is 1V higher than the saturation value. Intermediate hold times fall in between these two. Also notice longer hold times per cycle for the same frequency lead to earlier initiation of super-saturation. The increase in magnitude of the slope is proportional to the level of super-saturation.

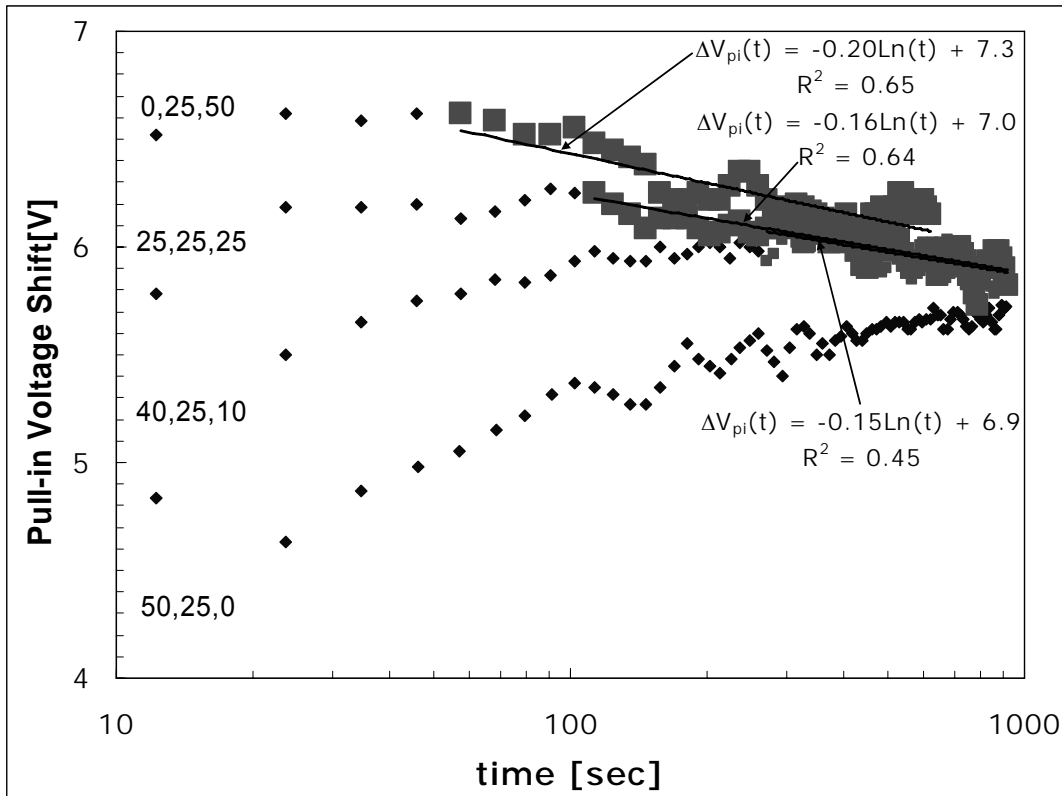


Figure 6-20: Pull-in voltage shift decay for various hold times

Figure 6-21 shows the entire pull-in voltage results for comparison. The second half of each curve with the negative slope (squares) is the super-saturation portion of the data. Notice slope magnitude is proportional to the magnitude of the super-saturation. In other words, the greater the excess charge, the faster discharge occurs. As presented in Chapter 3, discharge is proportional to the density of trapped charge, just as the level of charging is proportional to the density of available traps.

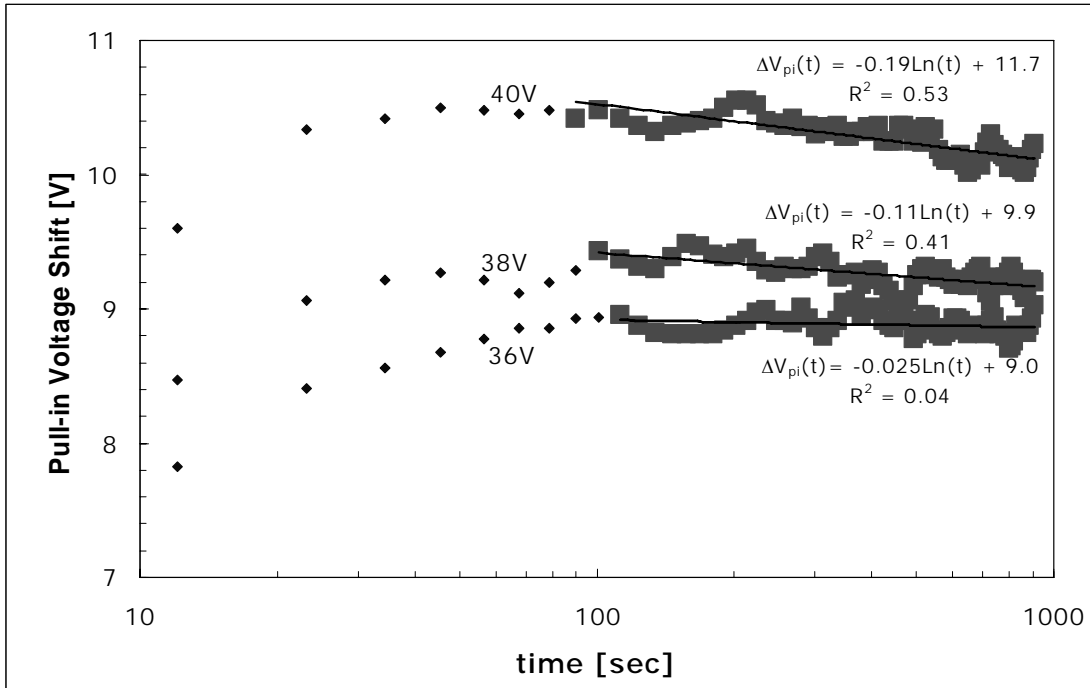


Figure 6-21: Pull-in voltage shift decay for various peak voltages

Based on these results, an explanation of super-saturation must include insulator charging above the saturation voltage shift, and the slow decay of the charge back to the saturation voltage shift. Also, the decay rate must depend on the density of excess trapped charge which is a function of hold-time and waveform peak voltage. An explanation of super-saturation follows.

Assume that charges only trap in the insulator while the beam is in contact with the insulator and that charges can only leave their traps sites (detrap) when the beam is not in contact with the insulator. Detrapping occurs by tunneling deeper into the insulator from a region with a high trapped charge density to a region with a low trapped charge density. Detrapping may also occur through a recombination process at the surface of the insulator. The rate that charges enter insulator trap sites, $T_t(x, t)$, was

discussed in Chapter 3 and presented in equation (3-15). The number of charges that actually transition into the insulator, $\Delta n_t(x,t)$, in one cycle is proportional to this rate

$$T_t(x,t) = P_t(x,t)[N - n_t(x,t)]f \quad (6-4)$$

and the amount of time the beam is in contact with the insulator, t_c .

$$\Delta n_t(x,t) = T_t(x,t) \cdot t_c \quad (6-5)$$

Similarly, the transition rate out of traps will be proportional to the density of filled traps.

$$T_d(x,t) = -P_t(x,t)n_t(x,t)f \quad (6-6)$$

The total number of charges that leave trap sites will be proportional to the detrapping rate, $T_d(x,t)$, and the amount of time the beam is not in contact with the insulator, t_{nc} .

$$\Delta n_d(x,t) = T_d(x,t) \cdot t_{nc} \quad (6-7)$$

Early in operation, n_t , will be very small, so $T_t(x,t) \gg T_d(x,t)$. Later in operation, as n_t becomes large, $T_t(x,t)$ will decrease as $T_d(x,t)$ increases. As the switch continues to actuate, an equilibrium or saturation voltage shift, ΔV_{sat} , is established when $T_t(x,t) \cdot t_c \approx T_d(x,t) \cdot t_{nc}$ as illustrated in Figure 6-22.

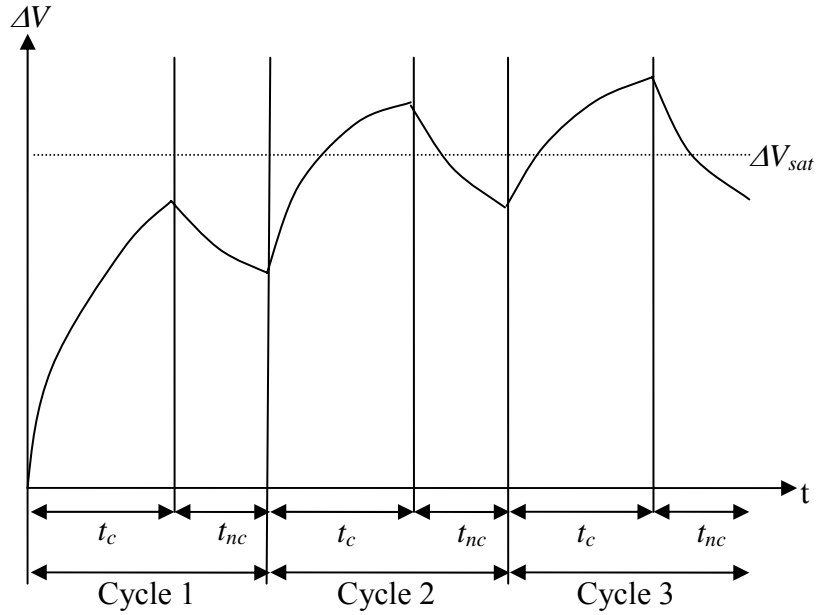


Figure 6-22: Illustration of the charging (t_c) and discharging (t_{nc}) portions of each cycle. Early in cycling, charging is much larger than discharge – later in cycling, the amount of charging and discharging that occurs per cycle equilibrates

The path to equilibrium (shape of the ΔV curve) is determined by the relationship between $T_t(x,t) \cdot t_c$ and $T_d(x,t) \cdot t_{nc}$. Four cases are described below and are illustrated in Figure 6-23.

1. The $t_c = 0$ case is trivial. The beam never makes contact with the insulator so no charging occurs.
2. When $t_{nc} = 0$, the beam never leaves contact with the insulator. ΔV continually increases logarithmically with time as $n_t(x,t)$ asymptotically approaches the condition where all traps are filled. This is the case in MNS capacitor testing.
3. When t_{nc} is long enough, there is adequate time between successive beam closing events to allow charge to dissipate from trap sites. This additional time allows a steady state condition to be eventually reached as illustrated in Figure 6-22.
4. In the super-saturation case, t_{nc} is so short that the equilibrium cannot be reached based on timing. The amount of discharge needed to establish equilibrium

cannot occur in the amount of time between successive beam closing events. Therefore, the insulator continues to charge until n_t is so large that $T_t(x,t)$ is small and $T_d(x,t)$ is large. At this point, more charge leaves trap sites while the beam is up than enters when the beam is down. Therefore, ΔV decreases. As n_t decreases during this phase, $T_t(x,t) \cdot t_c$ and $T_d(x,t) \cdot t_{nc}$ eventually equilibrate and ΔV achieves a steady state at ΔV_{sat} .

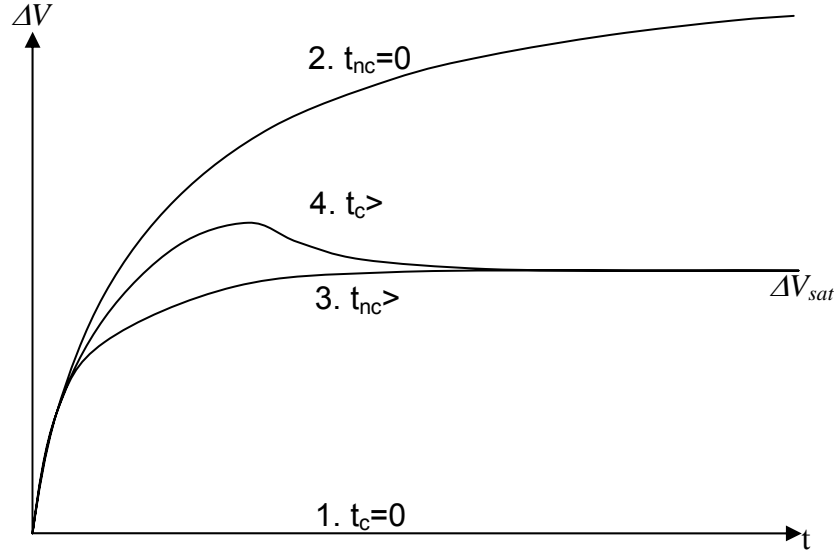


Figure 6-23: Illustration of the four possible charging cases. 1.) No beam and insulator contact - no charging, 2.) Beam and insulator in constant contact – no equilibrium reached (similar to MNS case), 3.) Adequately large t_c allows equilibrium to be reached, and 4.) smaller t_c requires equilibrium to be reached from a large filled trap density – super-saturation

Differences between Pull-in and Release Voltage Shifts

Earlier in this section it was pointed out that the release voltage shift deviated from the pull-in shift in two ways. First, ΔV_r is always less than ΔV_{pi} , which counters expectations from tunneling theory. Early in testing, the difference between ΔV_r and ΔV_{pi} is constant. The second deviation is the increasing differences between ΔV_r and ΔV_{pi} at later times. A comparison of ΔV_{pi} in Figure 6-20 and ΔV_r in Figure 6-24 illustrates these

two issues. Notice in Figure 6-20 that the least squares fit for the decay portion of ΔV_{pi} is logarithmic, while ΔV_r in Figure 6-24 is best approximated using a linear fit indicating two separate processes occur.

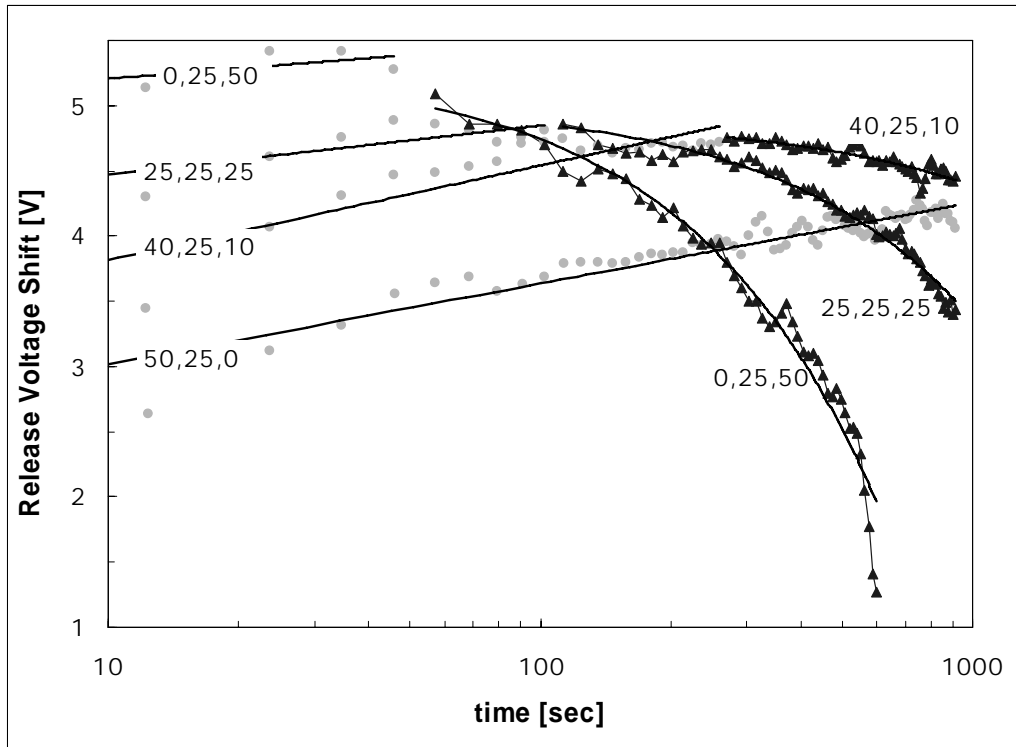


Figure 6-24: Release voltage shift for 36V peak voltage where hold time and rest time are varied to maintain a constant frequency (9 Hz)

Table 6-6: Least-squares fits summary for release voltage shift curves in Figure 6-24

Waveform ($t_{rest}, t_{slope}, t_{hold}$)	Early		Late	
	Fit Equation	R^2	Fit Equation	R^2
50,25,00	$\Delta V_r(t) = 0.27\ln(t) + 2.4$	0.91	-	-
40,25,10	$\Delta V_r(t) = 0.31\ln(t) + 3.1$	0.88	$\Delta V_r(t) = -0.0005t + 4.9$	0.79
25,25,25	$\Delta V_r(t) = 0.16\ln(t) + 4.1$	0.80	$\Delta V_r(t) = -0.0017t + 5.0$	0.97
00,25,50	$\Delta V_r(t) = 0.11\ln(t) + 4.9$	0.75	$\Delta V_r(t) = -0.0056t + 5.3$	0.96

Before discussing the results further, a reminder that pull-in and release measurements are made consecutively, rather than independent of one another. Assuming voltage shifts are only caused by trapped charge, the pull-in shift is a measure of the trapped charge at the end of a period when the beam was not in contact with the insulator and only a small electric field is applied to the insulator. The release shift measures the trapped charge density as the beam leaves the insulator surface. Therefore, for the release shift to be consistently lower than the pull-in shift, the trapped charge density must rapidly increase and decrease between each switch opening event and each closing event.

From the tunneling theory presented earlier, ΔV_r should be greater in magnitude than ΔV_{pi} , but this is not the case. A comparison of the ΔV_{pi} and ΔV_r curves in Figure 6-14 shows a consistent 1.5V separation for the first 100 sec. Explaining a pull-in voltage that is consistently 1.5V higher than the release voltage requires a net increase of 3×10^{11} electrons/cm² (assuming a sheet charge located at the insulator surface) and must occur between the beam's release from the insulator and the next pull-in event. This trapped charge increase must occur every single cycle. The next few paragraphs attempt to explain this behavior with charging; however, these charging arguments cannot explain the differences between the pull-in and release curves. They are presented to eliminate charging as the cause for switch failure.

Explaining the ΔV_r results relative to ΔV_{pi} requires a two-step process: 1) charge compensation to decreases the net trapped electron density while the beam is in contact with insulator, and 2) increase the net trapped electron density when the beam is up. Electron or hole transport must provide this compensation. The applied bias in this case

dictates that electrons must travel towards the electrode and holes must move towards the beam. Therefore, the possible forms of charge compensation are: 1) electrons moving out of near surface traps and traveling deeper into the insulator, or 2) holes moving from the insulator bulk to near surface traps. The first possible compensation mechanism involves electrons transporting deeper into the insulator and away from the surface. This is similar to the description of super-saturation. However, if this were the mechanism, consistency would be expected. The pull-in and release curves should run parallel with each other, or at a minimum share the same general form. Instead, the two curves behave completely different. Explaining the pull-in and release oscillation using this mechanism requires the trapped charge to travel from one side of the insulator to the other when no bias is applied across the insulator. This does not explain this process. The second possible compensation mechanism involves holes traveling from the bulk towards the insulator surface. To allow the constant oscillation of the net trapped electron density, it is assumed recombination does not occur. Rather, holes and electrons trap in separate sites near the insulator surface. Trapping holes from the bulk near the insulator surface would reduce the net negative charge caused by electrons tunneling from the beam and explains why ΔV_r is smaller than ΔV_{pi} .

Continuing the argument with the second compensation mechanism, the second step of the two-step process explains how the compensating positive charge dissipates before the next pull-in event occurs. Once the beam releases from the insulator surface, the applied electric field drops substantially (e.g. for a 5V release voltage, the field drops from 0.25MV/cm to 0.01MV/cm). Since a unipolar waveform was used, an electrostatic force capable of driving holes back into the bulk of the material is never established.

Also, while the applied electric field is small, the trapped charge density in the insulator is large so a substantial internal field exists. Since the insulator surface has a larger density of electrons trapped, the internal field points in the same direction as the applied field. Therefore, this field would actually attract more holes to the surface rather than drive them away as needed to explain the pull-in voltage that follows. Therefore, there is no electrical impetus for trapped holes to leave the insulator surface, so the observed differences between the pull-in and release results cannot be explained using a charging model.

If a charging model cannot explain the offset results (e.g. 50,25,0 in Figure 6-20 and Figure 6-24), it would be more difficult to explain the widening difference between the two curves at later times in switch operation. It is likely that a mechanism other than insulator charging is responsible for these issues.

To aid the investigation of this other mechanism, a difference of voltage shifts, ΔV_A^i , is defined

$$\Delta V_A^i = \Delta V_r^i - \Delta V_{pi}^i \quad (6-8)$$

where i is an integer identifying an individual pull-in and release cycle. From tunneling theory a typical ΔV_A curve would begin positive and gradually decrease towards a 0V asymptote, see Figure 6-13.

The figures that follow show the difference of voltage shifts for various parameter studies. Figure 6-25 shows a comparison of peak voltage results. All three voltages have the same general behavior. Between 0 sec and the first cycle shown, there is a large

negative shift ranging from -1.6V to -0.9V . After this initial, large shift, the curves decrease in magnitude briefly and then level out.

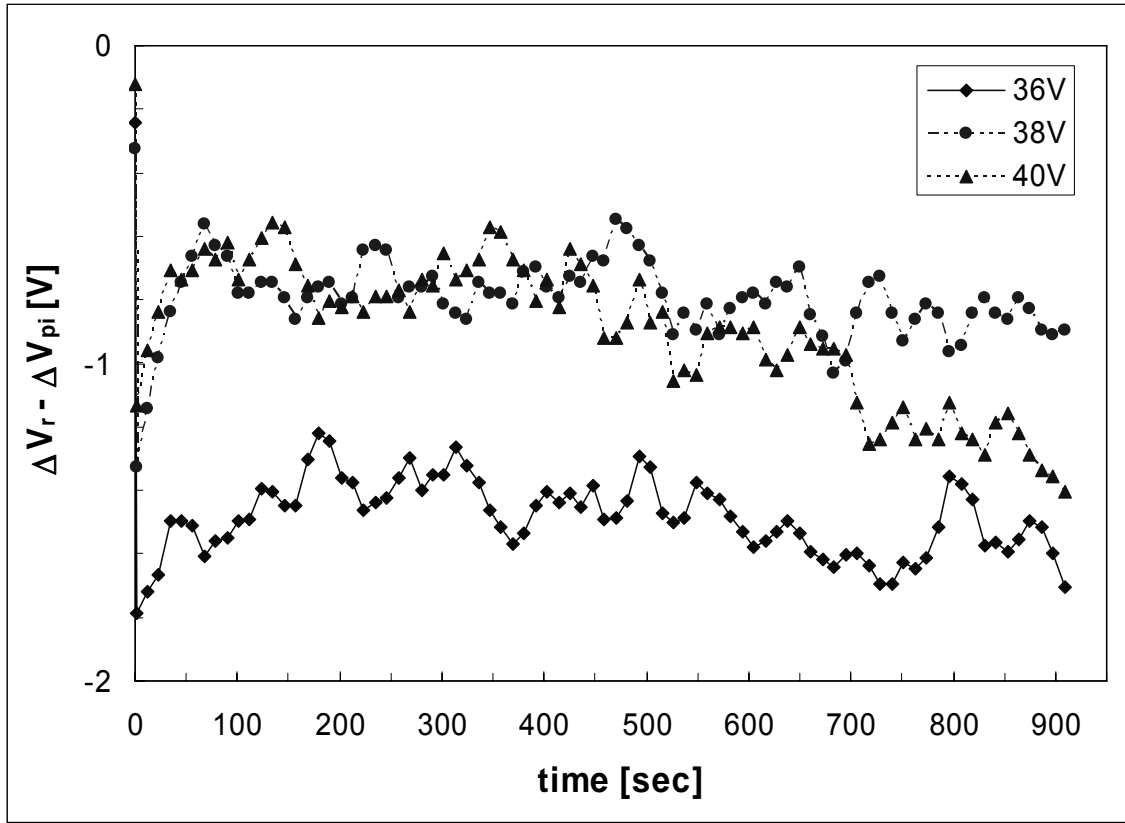


Figure 6-25: Peak voltage comparison

In Figure 6-26, the contribution of the initial shift has been removed to highlight the remainder of testing. Notice there is little difference between the curves. They begin with a decrease in magnitude for approximately 200 sec. While the 36V and 38V curves level out, the 40V curve steadily decreases for the remainder of testing. The 40V ΔV_{pi} curve supersaturates and is followed by a slow decrease ($\sim 0.3\text{V}$ over 840 sec) while the ΔV_r curve reaches a maximum value and decreases at a faster rate ($\sim 1.0\text{V}$ over 840 sec).

Still, the differences between these three curves are quite small relative to the error in the measurements. Therefore, the pull-in voltage difference may depend only slightly on the peak voltage.

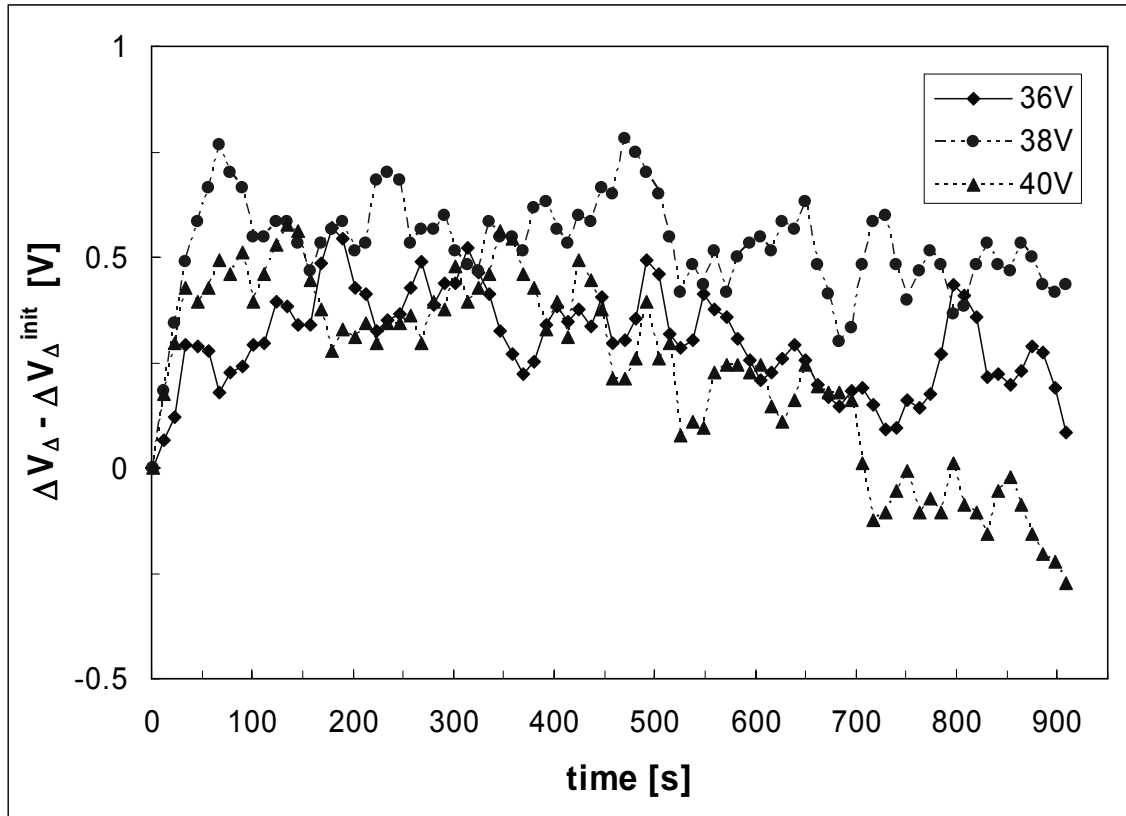


Figure 6-26: Peak voltage comparison removing contribution of first shift

In Figure 6-27, the hold time at the peak voltage varied from 0 msec to 50 msec while maintaining a constant 8 Hz frequency in all cases. The initial shift was approximately $-1.3V$ for all hold times (they fall within $0.5V$ of each other).

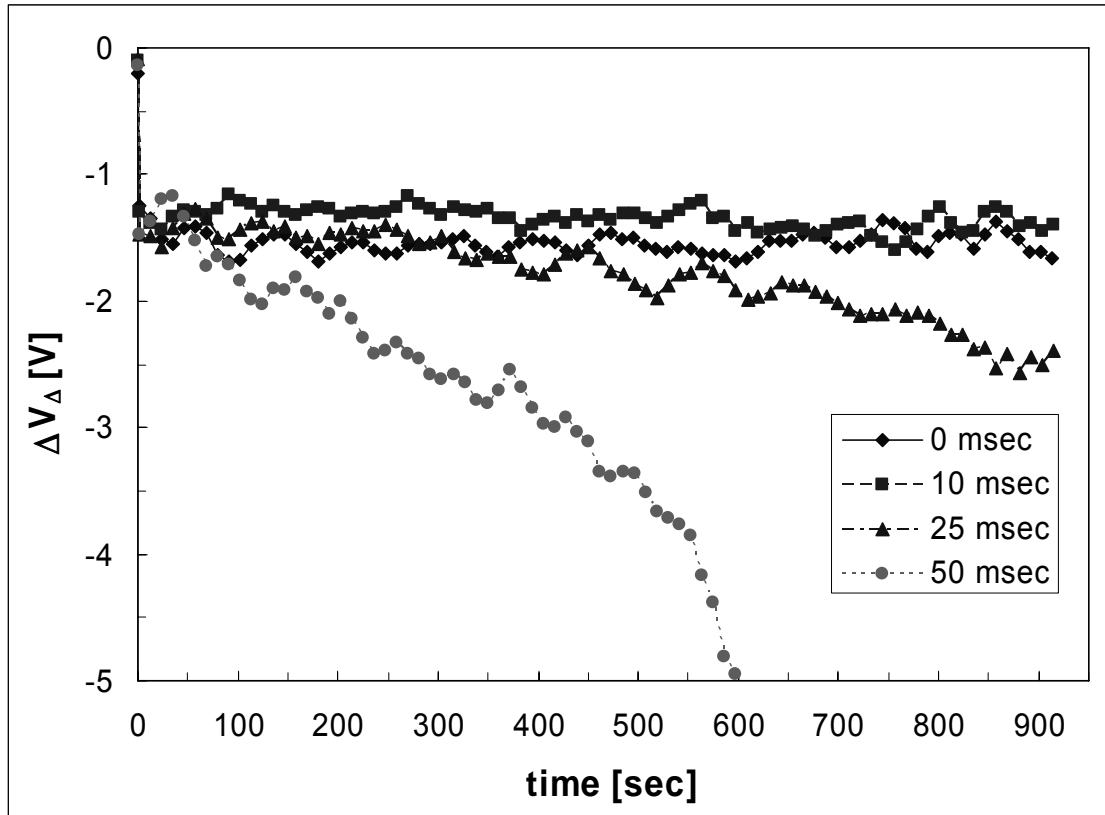


Figure 6-27: Comparison of various hold times while maintaining a constant frequency

To produce Figure 6-28, the initial voltage shift was subtracted from all data points. Notice that for shorter hold times (0 msec and 10 msec), there is little change in $\Delta V_r - \Delta V_{pi}$. On the other hand, for 25 msec hold time, there is a small, but consistent decrease over time. For 50 msec hold time, there is a much more rapid decrease in the voltage shift. This rapid decrease led to switch failure (beam never released) after 600 sec of operation. The switch's behavior after failure also supports the hypothesis that charging is not responsible for switch failure - after the switch fails (i.e. beam no longer releases), the application of a bias with opposite polarity does not release the beam from the insulator surface.

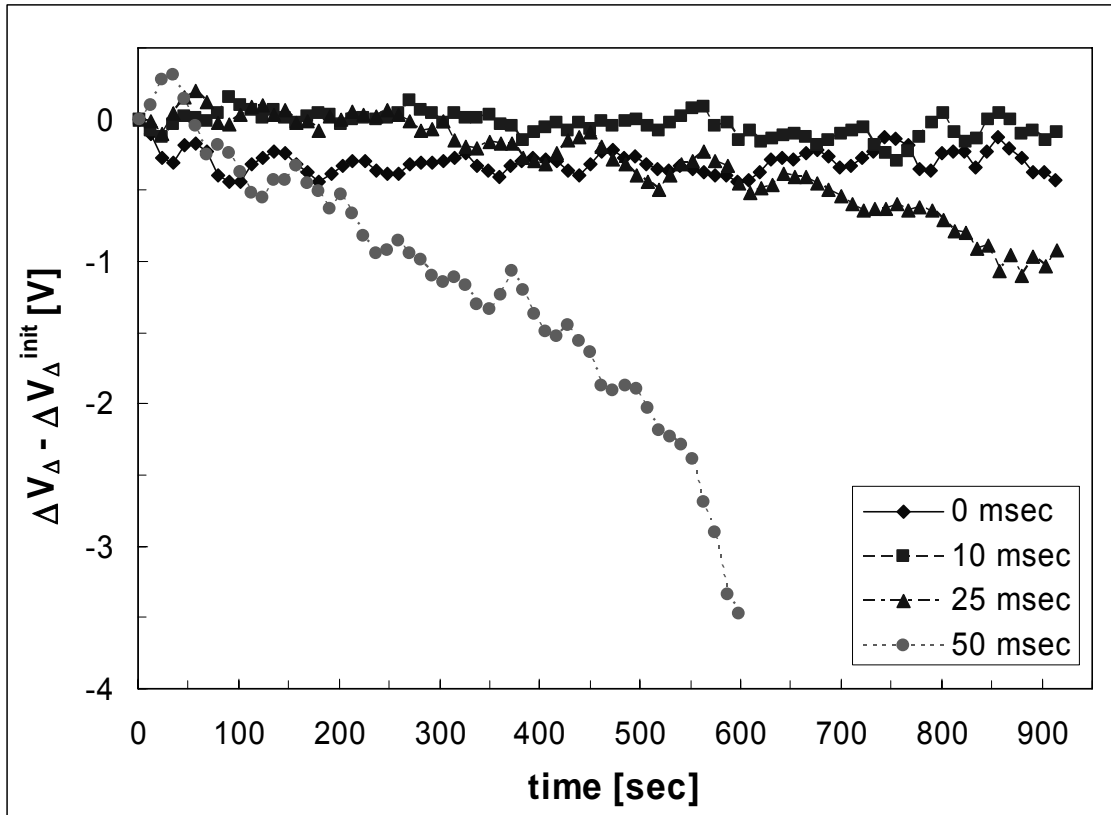


Figure 6-28: Comparison of various hold times while maintaining a constant frequency. The contribution of the initial shift is removed.

Figure 6-29 shows $\Delta V_r - \Delta V_{pi}$ for four hold time cases where the rest time remained fixed at 25 msec. Notice, the 10Hz and 13 Hz curves are very similar, while the 8Hz and 5.7Hz curves are not. The 13Hz and 10Hz cases begin with a $-0.5V$ shift followed by minimal change for the remainder of testing (staying near 0V). The 8Hz curve initially shifts nearly $-1V$ and the 5.7Hz data shifts about $-4V$, followed by a gradual decrease for the remainder of testing.

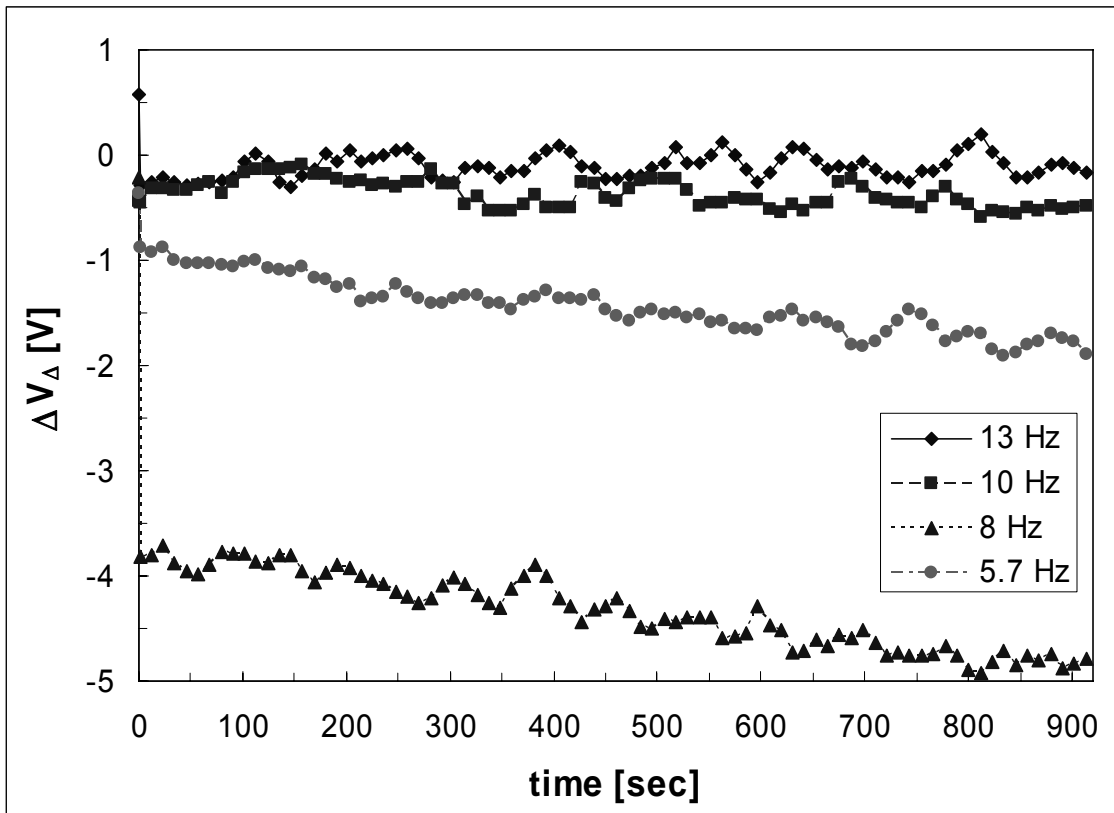


Figure 6-29: Comparison of various hold times while maintaining constant rest time

In Figure 6-30, the initial voltage shifts are eliminated for each case. With the initial shift eliminated, the similarities between the two sets of data become even more apparent. The 13 and 10 Hz curves are essentially indistinguishable from each other, and the 8 and 5.7 Hz curves are also indistinguishable from one another. This suggests the long-term voltage shift difference increases as the beam spends more time in contact with the insulator surface. Curiously, in this case the effect is binary. Possibly there is a threshold frequency that leads to more extreme voltage shifts.

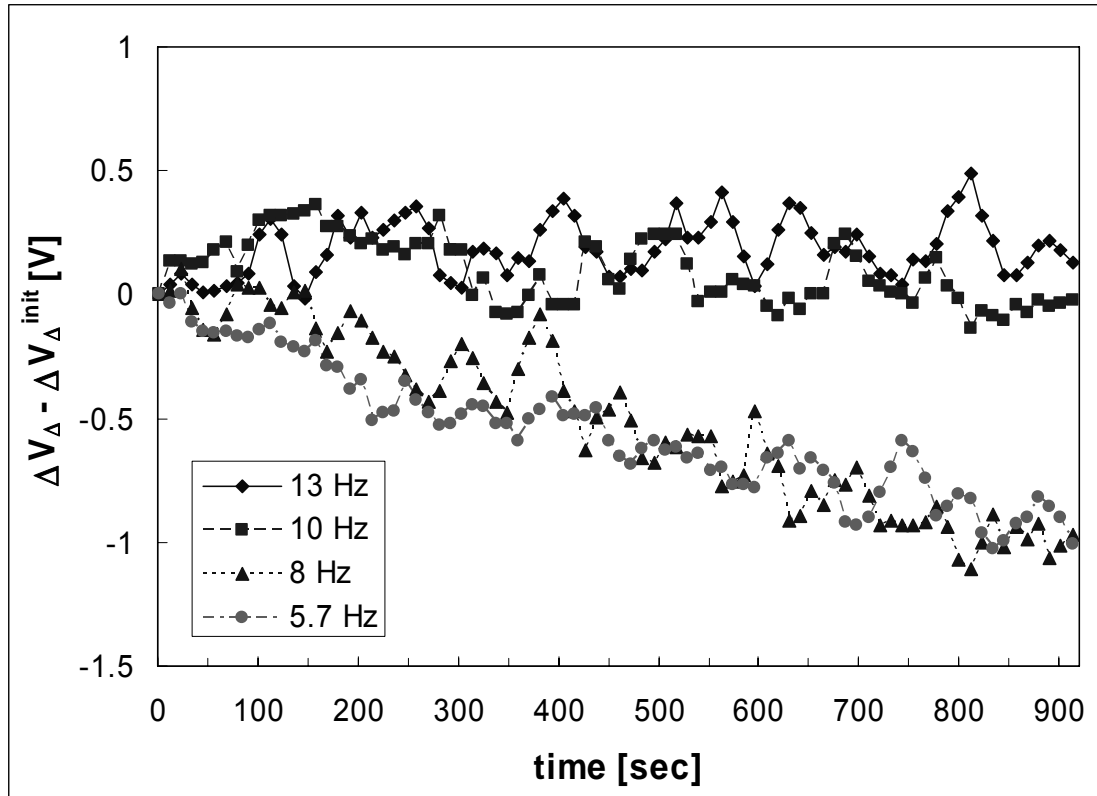


Figure 6-30: Comparison of various hold time while maintaining a constant rest time. The contribution of initial shift is removed.

To summarize, there are two components to the $\Delta V_r - \Delta V_{pi}$ data: an initial shift and a time-dependent decrease. These two processes appear independent of one another. For example, after the first measurement, Figure 6-29 displays a 3V difference between the 8 and 5.77 Hz curves, while Figure 6-30 shows no separation for the remainder of testing. In Figure 6-25, the largest initial shift occurs for the middle peak voltage. The range of initial voltage shifts in Figure 6-29 compared to the tight grouping of initial shifts shown in Figure 6-27 shows that the initial shift is not strongly related to the waveform used to actuate switch. Instead, it appears to vary from switch to switch.

On the other hand, there is a strong relationship between waveform hold time and the time-dependent decrease. Figure 6-28 is the best example of this. The 0 and 10 msec curves have essentially no time dependent component, while the 25 msec and 50 msec curves have negative slopes over the entire testing period. As pointed out earlier, the 50 msec curve's slope was so large that after 600 sec of cycling the switch permanently stopped releasing. The voltage relationship is much weaker than the hold time relationship, at least over the limited peak voltage range tested.

If charging does not explain these release voltage results, what can? One possible explanation is mechanical fatigue of the metal beam. Release at progressively lower applied voltages could indicate the metal beam is weakening from repeated cycling, i.e. a beam with a lower spring constant requires less force (voltage) to maintain contact with the insulator; however, this seems unlikely. If the beam weakened, the force required to pull the beam down should also decrease. Therefore, the data does not support beam weakening. This secondary mechanism must only affect switch operation while the beam is very close to the insulator surface.

Examples of mechanisms that operate at small distances include van der Waals force and capillary forces. The van der Waals force exists from the interaction of dipole moments of atoms very close to one another. The magnitude of the force depends on the materials and the distance between the atoms [5]. Capillary forces occur when a contaminant, such as water, is present between switch surfaces. Humidity was kept to a minimum by operating the switches in a nitrogen atmosphere. However, it is possible that another contaminant, perhaps latent water from fabrication, a film of oil, or a

hydrocarbon introduced during or after fabrication, is present in the insulator or on its surface. A possible scenario using the idea of contamination follows.

The insulator begins testing with a small layer of contamination present. This layer provides an additional force that attracts the beam to the surface. Assuming the fraction of the surface covered with contaminant dictates the magnitude of the additional force and each switch has a unique fraction of its surface area covered with contaminant. Then contamination explains the variable initial shift, and its independence with respect to waveform parameters. Contaminant may also reside in pores at the insulator surface. As the switch cycles and the beam impacts the insulator surface, a compressive force on the order of 0.01 N/cm^2 squeezes the insulator. This compression emits additional contaminant out of the pores on to the insulator and beam surfaces. The additional surface area covered in contaminant increases the force holding the beam down which causes a further decrease in the release voltage. This contaminant only affects device operation when the beam and insulator are in contact, so it would have no affect on pull-in. This argument has not been independently confirmed; however, it provides opportunity for further research to determine the true cause of this failure mechanism.

While these results are not tidy, they are still important findings. Studies previously pointed to insulator charging as the mechanism that determines switch lifetime (see Chapter 2). These were often done using switch lifetime as the metric. However, this does not provide much information on the physical processes that cause device failure - only how long or how many cycles it takes to reach failure.

It is true insulator charging affects switch operations; however, based on the tunneling theory presented and the pull-in voltage results, insulator charging does not

explain device failure. The effect of insulator charging eventually reaches a steady state condition in time, after most trap sites have filled. While not ideal, if the system has the excess capacity required to provide the extra potential needed to compensate, the effects of charging can be overcome. Therefore, there must be another mechanism affecting these devices. In most cases where the switch permanently fails, it can be traced back to the beam failing to release. This secondary mechanism was shown to strongly depend on the amount of time the beam spends in contact with the insulator surface.

Bibliography

1. Buchanan, D.A. "Charge Trapping in Silicon-Rich Si_3N_4 Thin Films," *Solid-State Electronics*, 30, 1295-1301 (1987).
2. Rebeiz, G.M. *RF MEMS: Theory, Design, and Technology*. Hoboken, New Jersey: Wiley, 2003.
3. Reid, J.R. *beamDeflect*. Version 1.3, PC, LabWindows. Computer software. Air Force Research Laboratory Sensors Directorate, Hanscom AFB MA, 2001.
4. Reid, J.R. "Simulation and Measurement of Dielectric Charging in Electrostatically Actuated Capacitive Microwave Switches," *Proceedings Modeling and Simulation of Microsystems*, 250-253 (April 2002).
5. Maboudian, R. and R.T. Howe. "Critical Review: Adhesion in Surface Micromechanical Structures," *J. of Vacuum Science and Technology B*, 15, 1-20 (1997).

7. Conclusions

7.1. Summary of Results

Previous research on RF MEM switches suggested that charging of the insulating layer limits capacitive switch lifetime. The goal of this research was to investigate the mechanisms responsible for charging behavior. Performing this research required the development and execution of two separate experiments. For each experiment, an instrument controller program was developed to collect and process data. Separately, a program to model the charging behavior of each device was also developed. The results from each experiment were modeled to understand the processes involved in MEM insulator charging.

The first experiment tested metal-silicon nitride-silicon (MNS) capacitors. These simple capacitors allowed the isolation of insulator charging from other possible MEM switch issues (e.g. mechanical changes). Capacitors were fabricated in the AFIT cleanroom and at AFRL/SN. The experimental procedure included applying a constant bias across the insulator and periodically taking CV measurements. Based on the voltage shift between successive CV sweeps, the amount of trapped charge was estimated. An instrument controller program was developed to collect and process the data from these measurements.

Another computer program was developed to model the accumulation of trapped charge based on tunneling theory. Experimental results were evaluated with this program using trap energy and density as fit parameters. A good fit of the data was accomplished using this model if adjustments to the fit parameters were made at each voltage tested.

The adjustments to trap energy and density were always consistent, and plausible physical arguments for these adjustments were presented. Knowing the tunneling model approximates silicon nitride charging provided confidence in this approach moving into the MEM portion of the research.

The second experiment involved operating capacitive MEM switches (fabricated by AFRL/SN) for extended periods to investigate insulator charging. Similar to MNS capacitor flatband voltage shifts, MEM pull-in and release voltage shifts also indicate the amount of charge trapped in the insulator. Generally, these switches are actuated with voltage pulses that keep the beam biased and in contact for no more than 100 msec. If the beam is in contact for too long, it sticks to the insulator permanently. While this time constraint complicates testing in a number of ways, it also provides an alternate method for investigating charging. Previously, triangle and square waveforms had been used to actuate MEM switches for reliability testing. In this research, a modified triangular waveform was used which allowed the determination of pull-in and release voltages while maximizing the decoupling of the voltage and timing parameters. An existing MEM instrument controller program was revised to include the modified triangular waveform.

From experiment, it was shown that longer hold times increase insulator charging rates. It was also shown that increases in the waveform's peak voltage result in larger pull-in and release voltage shifts. Switch charging was far less sensitive to changes in the switch's actuating frequency.

An existing program was enhanced to model time dependent charging of the MEM insulator with modified triangular waveforms. Using a method similar to that

described for MNS devices, the experimental data was modeled with this program using trap energy and density as fit parameters. Modeling shows that tunneling theory describes pull-in voltage shift results early in testing.

It was stated earlier that the final voltage shift was independent of the hold time. While this is true, the path to the saturation voltage was not the expected logarithmic rise seen in MNS results. Instead, the pull-in voltage steadily increased until it reached a saturation voltage shift. For longer hold times, the curve surpassed the saturation voltage shift, reached a maximum shift, and steadily decayed back to the saturation level. This process was referred to as super-saturation. While not described previously in the literature and, therefore, unexpected, it is clear that it is the result of a competition between the charging and discharging the insulator.

The pull-in/release voltage relationship does not agree with expectations from tunneling or even charging. From tunneling theory, the release voltage shift should be larger in magnitude than the pull-in voltage shift and over time the two should converge. Instead, the release voltage shift was always substantially lower in magnitude than the pull-in curve and the two ran approximately parallel. The third deviation involves the pull-in and release voltages diverging from each other later in testing. When the switch was operated with a waveform that included long hold times, the pull-in voltage maintained a constant shift while the release voltage shift steadily decreased linearly over time. For the longest hold time, the release voltage (not release voltage shift) reached approximately 0V - shortly after reaching 0V, the beam ceased releasing from the insulator surface. This is the mode for permanent switch failure. It was concluded that while charging affects device operations, it is not responsible for switch failure as

previously postulated in the literature. The failure mechanism is likely a contaminant on the insulator surface, which creates a short-range force (similar to stiction) that affects the release voltage but not the pull-in voltage.

Determining the effect ionizing radiation has on capacitive MEM switch charging is required if these switches are to be used in space. Therefore, both the MNS and MEM experimental setups also incorporated a capability to make in situ irradiation measurements. In the case of MNS capacitors, the devices were biased and CV sweeps were made in the presence of a 2600 Ci Co-60 source. For the MEM radiation experiment, the switches were tested with a 3.2 kW x-ray source. In both cases, radiation measurements were successfully made. Unfortunately, the x-ray source stopped working after only a few tests. Therefore, based on the limited data collected, conclusive statements on irradiation induced MEM charging are impossible. Preliminary results suggest there is a charging effect at very high dose rates, although the effects are small compared to bias induced charging. Even though the data collected is not conclusive, this research produced the first successful radiation measurements on this RF MEM switch design. Also, the programs developed to model capacitor and MEM switch charging also incorporate radiation charging mechanisms. These tools will be useful in further exploration of radiation effects on MEM switches. The MNS and MEM experimental results are provided in Appendix B.

7.2. Summary of Contributions

Insulator Charging: It was determined that tunneling is responsible for changes in the actuation voltages early in switch cycling. This work verified temporal and voltage dependence of charging matches expectations from tunneling theory. For longer hold

times, a super-saturation effect was discovered and explained as a competition between charging and discharging of insulator trap sites.

Failure Mechanism: It was discovered that charging is not responsible for switch failure as previously thought. Failure is likely due to stiction caused by a contaminant introduced at fabrication or between fabrication and operation.

Modeling: A spatial and temporal dependent model that describes charging of silicon nitride insulators as a function of an applied bias was developed. The model was verified with experiment. An existing capacitive switch model that calculated beam position as a function of applied bias was enhanced by including a time dependent tunneling model.

Experimental Method: This work developed a new experimental method that perturbs waveform parameters to determine charging characteristics. Differences in the pull-in and release voltages were exploited to investigate the switch failure mechanism.

Radiation Testing: An experimental set-up to test MEM switches in an ionizing radiation environment was successfully developed and implemented. Radiation effects were incorporated into the models for MNS and MEM devices.

7.3. Device Design Implications

The summary above points out that charging can change switch pull-in or release voltages to the point the switch no longer actuates for a given actuation waveform; however, there is no evidence that charging leads to the permanent failure of a switch. There are a number of potential solutions to these switch lifetime problems. Further switch development must address both charging and the stiction mechanism that is likely responsible for device failure.

Obviously, any solution for a reliability problem must be balanced with the switch's ability to transmit and block the RF signal passing through the switch. One option is to separate the signal line from the bias line so that the large actuation bias is not applied across the insulator. Rockwell fabricated a switch using this approach [1] by incorporating three electrodes in parallel. The center electrode carries the RF signal while the two outside electrodes are biased to pull the beam down. The electrode carrying the signal does not induce a large bias across the insulator. While this reduces insulator charging, it also creates a number of new problems. The magnitude of the voltage required to pull the beam down is two to three times larger (60 - 90V) than the AFRL switch's pull-in voltage. This creates the undesirable requirement of providing a high voltage source for each switch. This design is also much more complicated, so it takes up more surface area on the die, is more difficult to fabricate, requires more processing steps, and includes more points of failure which can lead to lower fabrication yields and lower reliability.

Another solution is to use a thicker insulator, which reduces the magnitude of the electric field across the insulator for any given voltage. A smaller field reduces the electron or hole tunneling probability and the electrostatic force across the insulator while the beam is in contact with the insulator. The downside to this solution - the device's ability to switch the RF signal on and off is degraded. By thickening the insulator, the down state capacitance is reduced which reduces its ability to shunt the signal to ground.

An advantage of the AFRL design is its elegance and simplicity. If the device design remains unchanged, one philosophy for extending switch lifetime is to work around the insulator problem rather than fixing it. Workarounds include providing an

adequate applied voltage to keep the switch actuating despite charging and using waveforms that stress the insulator less. A hold voltage that is larger than the pull-in voltage and provides excess potential to cover the voltage shift caused by trapped charge could be used. This approach was used in this research just to collect data, but this does not address the problems responsible for the ultimate failure of the switch.

Changing the waveform provides another solution. Bipolar waveforms have been suggested, because they reduce the effects of charging. Another waveform solution uses one voltage magnitude for actuating the switch and a second, lower voltage to hold the beam in contact with the insulator [2]. Holding the beam in place with a lower voltage reduces charging and the squeezing force. This approach would limit the level of charging and extend the life of the switch. Unfortunately, this comes at the cost of supplying a more complicated waveform. With the appropriate equipment, this is not terribly difficult in a laboratory; however, in low earth orbit, providing this capability to millions of switches on a space-based radar would be difficult and expensive. These waveform solutions can reduce or eliminate the effect of charging; it may even reduce how quickly stiction kills the switch, but it will not eliminate the effects of stiction. Therefore, the best solution is to continue researching the fundamental problems and continue to improve switch materials and design.

7.4. Suggestions for Future Research

The issues uncovered in this research require further research to develop a complete description of the mechanisms limiting device operation and lifetime. The biggest questions involve the mechanisms causing the initial difference between the pull-in and release voltage shifts and their divergence over time. Chapter 6 points out that the

deviation between these voltages is likely due to a contaminant on the insulator surface since it only affects the release voltage. Determining and reducing the cause of this problem would be a big step forward in improving the lifetime of these switches. One potential source of this contaminant is in the fabrication step. As an example, it was reported in Chapter 4 that to produce useful CV curves, the MNS capacitor had to be baked at a higher temperature than the temperature used in fabricating the MEM switches – possibly baking a contaminant out. Since these devices were not packaged, the contaminant could also have been introduced between the end of fabrication and switch testing. While testing was always performed in a clean, nitrogen environment, long term storage of the wafer was not in a clean room environment.

Another area of research needed is in alternative insulator materials. An insulating material with a lower trap density and/or one not as susceptible to contamination problems would aid in the reliability of these switches. Investigating higher permittivity insulating materials is also needed. A higher- ϵ insulator would allow the use of thicker insulating layers thus reducing the electric field while maintaining a high capacitance.

Finally, research in radiation effects on MEM switches should be revisited when the effects of these other issues has been reduced or eliminated.

MEMS is an exciting, growing field of study. Continued research in this field is vital to the development of future defense systems, as well as everyday applications such as cellular phones and automobile safety systems. Increases in RF MEM reliability and lifetime will allow the manufacture of systems previously impossible to develop.

Bibliography

1. McClure, S.S., L.D. Edmonds, R. Mihailovich, A.H. Johnston, P. Alonzo, J. DeNatale, J. Lehman, and C.Yui. "Radiation Effects in Micro-Electromechanical Systems (MEMS): RF Relays," *IEEE Transactions of Nuclear Science*, 49: 3197-3202 (December 2002).
2. Rebeiz, G.M. *RF MEMS: Theory, Design, and Technology*. Hoboken, New Jersey: Wiley, 2003.

Appendix A. Theory of Radiation Effects on MEMS

A.1. Basics

Environment

Radiation environments of concern to the electronics community include: space, nuclear reactor, nuclear weapons, semiconductor processing and medical. Of these, the space environment is described in detail. Space has been chosen for two reasons: 1) the MEM switches are intended to be used in a space based radar system, and 2) lessons on the damage mechanism encountered in space can be applied to other environments of interest.

A large part of what makes space difficult to operate in is the solar and galactic radiation encountered. Protecting electronic components from this environment contributes to the extremely high costs associated with launching space systems. The information in the next four paragraphs is taken from Braunig [1].

Space systems are exposed to solar radiation, galactic cosmic rays, and the radiation belts around earth. Also, exposing system materials to energetic electrons generates bremsstrahlung (x-ray) radiation. Solar radiation is composed of solar wind and solar flares. Solar winds consist mostly of the low energy protons and helium ions constantly expelled from the sun. Low energy electrons also comprise a small fraction of the solar wind. While the solar wind is a fairly constant emission, solar flares are bursts of radiation corresponding to sunspots on the surface of the Sun. The sunspot cycle lasts 22 years, and during these cycles, large magnetic field fluctuations take place in the upper layer of the solar atmosphere. These fluctuations result in large emissions of x-rays, UV-

radiation, and radio waves, in addition to the solar wind plasma and energetic particles.

The fluxes emitted during these flares can vary by several orders magnitude.

Galactic cosmic rays are distributed uniformly and omni-directionally. They primarily consist of protons and helium ions, with a small fraction consisting of heavier nuclei. Universally, particle energies range from 10 to 10^{14} MeV, while the flux is approximately four nuclei per cm^2 per second. However, near earth, the rays interact with the solar wind and the geomagnetic field which changes their energy and flux. The highest energy cosmic ray ions in the vicinity of earth are 1 GeV and the flux is reduced at lower energies.

The environment encountered by satellites orbiting earth consists of a combination of electron, proton, heavy ion, and photon radiation. Electrons and protons are trapped in the geomagnetic field lines of earth. The motion of these particles is a complicated combination of gyro motion around the geomagnetic field lines, a bouncing motion between mirror points, and drift around the earth [2:445]. These electrons and protons come from solar winds and nuclear reactions with cosmic ray protons in the atmosphere. Charge levels will cycle up and down with the solar cycle. Therefore, wide variations in the charge flux should be anticipated. Trapped electrons have energies on the order of keV to MeV. Trapped protons have energies up to 800 MeV.

For space systems to avoid catastrophic effects while operating in this environment, electronics are often shielded with thin layers of metal. Slowing and stopping energetic particles results in the emission of bremsstrahlung radiation. This leads to a further complication in the requirements for space mission protection.

Laboratory Radiation Sources

Obviously, the space environment is a complex mix of charged particles. The radiation mix becomes even more complex as it passes through spacecraft structures. These devices in space absorb their dose slowly over long periods of time (in many cases several years). In the laboratory, testing is performed using machines or radioisotopes that produce radiation within a small band of energy. Any conclusions drawn from laboratory data must be modified in order to develop accurate predictions of a device's performance in a radiation environment [3:341-346]. At the basic science level, radiation testing provides insight into damage mechanisms that may limit device performance in a space environment. Radiation testing can also be used as a tool to investigate material and device performance characteristics.

Assessing a device's radiation hardness does not necessarily require testing in space or even a proton/electron radiation environment. For example, a major portion of the interactions in insulator field effect devices (e.g. MOS) are caused by ionization, rather than displacement. Therefore, radiation sources producing high-energy ionizing radiation can be used to assess radiation effects.

The most common source used is the radioisotope cobalt-60. As it beta decays to nickel-60, it produces 1.17 and 1.33 MeV gamma rays. The high energy gammas produced by Co-60 deposit their energy relatively evenly across thick samples. Since this source is widely used and discussed in the literature, dosimetry information is readily available.

An alternative is the low energy x-ray (LEXR) tester. Instead of a radioisotope, an x-ray tube is used. Electrons are accelerated toward a tungsten target. The collision

creates an energy spectrum of L-line radiation peaks superimposed on a lower intensity bremsstrahlung base. It has been shown that 80 percent of the absorbed energy comes from the L-lines that lay near 10 keV. While the dosimetry is not as well known, the LEXR is a much safer and easier to use alternative to Co-60. Research that relates Co-60 and LEXR dosimetry is still ongoing [2:454-459].

Radiation Interactions

Radiation affects materials by entering the material and depositing some or all of its energy. Charged particle and photon interaction mechanisms will be examined since they are the primary radiation concerns in the space environment.

Effects of Charged Particles

Charged particle interactions are different than photon interactions because of coulombic repulsion. Coulombic repulsion results in two charge deposition mechanisms: ionization and displacement. Due to the mass difference between electrons and protons, they will be discussed separately.

Electrons lose energy through three interaction types: elastic and inelastic collisions with nuclei, and inelastic collisions with shell electrons. Inelastic collisions with the nuclei produce the bremsstrahlung radiation discussed earlier. Elastic collisions can be neglected for incident electron energies above 100 eV. Generally, electron elastic collisions with nuclei result in a large electron deflection and little effect to the nuclei due to the large mass difference. However, it is possible for an electron to possess enough energy to displace an atom from its lattice position with an elastic collision. This is most likely to occur with a head on collision.

Inelastic interactions with shell electrons occur when incident electrons deflect due to the coulombic repulsion by the shell electrons. As the incident electrons slow down, the energy difference is transferred to the shell electron [4:585-586].

Protons (and other ions) deposit their energy through the same mechanism as electron radiation does: 1) elastic collisions with nuclei and 2) inelastic collisions with shell electrons. In addition, the target atom can capture the ion. This creates a metastable nucleus that eventually decays into fragments that emit beta and gamma radiation [4: 592].

Effects of Photons

X-ray and gamma interactions also affect materials. X-rays are generated through atomic transitions, i.e. shell electrons transitioning from higher to lower energy states. Gammas on the other hand are generated when the nucleus transitions from an excited energy level to a lower energy. For example, gamma rays are produced when radioactive nuclei decays (e.g. Co-60). This is a different definition of x-rays and gammas than often used in electrical engineering textbooks, which differentiates the two by energy.

Since photons have no mass or charge, they interact differently than other types of radiation. They interact with valance band electrons in one of three ways: photoelectric effect, Compton scatter, and pair production. The probability of one of these mechanisms occurring depends on the energy of the photon and the material type.

The photoelectric effect occurs when a photon interacts with an inner shell electron and is most likely to occur at low photon energies. The photon transfers some or all of its energy to the shell electron causing it to excite to a freed state. With an inner electron vacancy left behind, an electron from the outer shell transitions to the empty

state in an effort to achieve the lowest energy state. This transition results in the emission of either an x-ray or an Auger electron [4:608].

The Compton effect is most likely to occur at moderate energies. This is similar to the classical physics “billiard ball” collision. The collision involves an outer shell electron and is assumed to be free for momentum conservation purposes. The photon “collision” with the outer shell electron yields a lower energy photon. The energy difference between the initial and secondary photons is transferred to the electron in the form of kinetic energy [4:610].

The final photon mechanism is pair production. This process requires a higher energy photon, at least twice the rest energy of an electron (1.022 MeV). When one of these higher energy photons passes near the nucleus of an atom, the photon energy is completely absorbed and converted into an electron-positron pair. Excess energy is transferred to the pair in the form of kinetic energy [4:616].

With an understanding of the mechanisms responsible for photon interactions, a discussion of how to quantify photon interactions follows. The fraction of monoenergetic photons that make it through a distance of a particular material is given by

$$\frac{I}{I_o} = e^{-\mu x}, \quad (A-1)$$

where

I is the final intensity of the beam,
 I_o is the initial intensity of the beam,
 μ is the attenuation coefficient, and
 x is the thickness of the material.

The attenuation coefficient can be for a particular interaction (e.g. pair production) or the total attenuation coefficient which combines all three photon

interaction processes. As stated earlier, the interaction probability depends both on photon energy and the material the photon interacts with. For example, lead has a very high coefficient while air does not.

Regardless of the mechanism, the primary effect of photon interactions with matter is to create free electrons. In semiconductors, this is the equivalent to creating electron-hole pairs. Once free, there are a number of fates available for these electron-hole pairs. The electron-hole pair can recombine with each other or other electrons and holes, they can become trapped in latent trap sites, or leave the material and enter the circuit as a spurious current. These possibilities are examined in detail later as they pertain to MEM devices.

Dosimetry

Quantifying the amount of radiation energy deposited in a material requires dosimetry. Knowledge of energy deposition enables the estimation of parameters such as the total number of electron-hole pairs produced and the rate they are produced. Dosimetry also provides a method to compare how different materials absorb radiation.

The term dose refers to the amount of energy absorbed per unit mass. The basic unit of dosimetry is the rad. One rad is defined as 100 ergs per gram. Since each material absorbs 100 ergs differently, the rad must be identified with the material of interest to have meaning. For example rad(Si) is used for absorbed dose in silicon. The rate that absorbed dose changes is referred to as dose rate (e.g. rad(Si) per hour).

In general, the actual energy deposited in a particular unit mass cannot be determined. Instead, a two step process is typically required in testing. First, a reference material, e.g. thermoluminescent dosimeter (TLD), is irradiated; this material

characterizes the radiation environment at a particular location. With knowledge of the radiation environment at that location, the dose in the device and region of interest can be estimated.

Once the dose in one material (say dosimeter) is known, the absorbed dose in a second material can be calculated. The relationship is based on the ratio of mass absorption coefficients.

$$\frac{rad(1)}{rad(2)} = \frac{\mu_1/\rho_1}{\mu_2/\rho_2} \quad (A-2)$$

where

μ_x is the absorption coefficient of material x, and
 ρ_x is the density of material x.

Also, the mass absorption coefficient for a compound is determined using the mass fraction of each element in the compound.

$$\frac{\mu_c}{\rho_c} = \sum_i w_i \frac{\mu_i}{\rho_i} \quad (A-3)$$

where w_i is the mass fraction of each constituent element, i . For example, assume a silicon PIN diode measured a total absorbed dose of D_{Si} rad(Si) over the span of an hour. To convert from rad(Si) per second to rad(SiO₂) per second, first calculate the SiO₂ mass absorption coefficient

$$\frac{\mu_{SiO_2}}{\rho_{SiO_2}} = w_{Si} \frac{\mu_{Si}}{\rho_{Si}} + w_O \frac{\mu_O}{\rho_O} \quad (A-4)$$

(The silicon mass fraction is 0.4674 and the oxygen mass fraction is 0.5326.) Therefore, the equivalent absorbed dose in the silicon dioxide is calculated by

$$D_{SiO_2} = \frac{\mu_{SiO_2}/\rho_{SiO_2}}{\mu_{Si}/\rho_{Si}} D_{Si} \quad (A-5)$$

In a low energy x-ray environment (~ 10 keV photons), the silicon absorption coefficient is $32.89 \text{ cm}^2/\text{g}$, and the oxygen absorption coefficient is $5.565 \text{ cm}^2/\text{g}$. This yields a value of 18.34 for μ_{SiO_2}/ρ_{SiO_2} , and a silicon dioxide total absorbed dose of 0.5576 D_{Si} . That is, the silicon dioxide absorbs approximately half as much energy as silicon in the same amount of time at 10 keV. An important part of the last statement is “at 10 keV.” Mass absorption coefficients are extremely energy dependent. For example, if a Co-60 gamma source is used, the average photon energy is approximately 1.25 MeV. At these energies, the silicon mass absorption coefficient is $0.02652 \text{ cm}^2/\text{g}$ and the silicon dioxide coefficient is $0.02661 \text{ cm}^2/\text{g}$. In this case, the conversion from silicon dose to silicon dioxide dose would be $1.0034 D_{Si}$; the two doses are nearly identical.

This discussion has an implication beyond just dose conversion. It highlights the fact that calculating absorbed dose based on an average energy is not be adequate when a source with a broad spectrum is used. For example, ignoring the low energy portion of the spectrum may overestimate a conversion of silicon dose to silicon dioxide dose by a factor of two.

Deviations from Ideal Case

Charged Particle Equilibrium

The equations to convert absorbed dose from one material to another just described are only valid in a special situation – charged particle equilibrium (CPE). CPE exists when the charged particles of one type and energy leaving a volume are replaced

by particles of the same type and energy [5:75]. Returning to the equation above used to define absorbed dose

$$\varepsilon = (R_{in})_u - (R_{out})_u + (R_{in})_c - (R_{out})_c. \quad (A-6)$$

CPE requires that

$$(R_{in})_c = (R_{out})_c. \quad (A-7)$$

Therefore, the equation for the energy imparted to the volume simplifies to

$$\varepsilon = (R_{in})_u - (R_{out})_u. \quad (A-8)$$

In the case of a beam of x-rays incident on the surface of a material, the impact of not having CPE in a material is non-constant dose deposition. Imagine the material is divided into discrete elements as shown in Figure A-1. Looking at element 1, the x-rays that interact close to the surface create mobile electrons. A larger fraction of these electrons leave this element to enter another element than enter the element. Therefore, CPE does not exist.

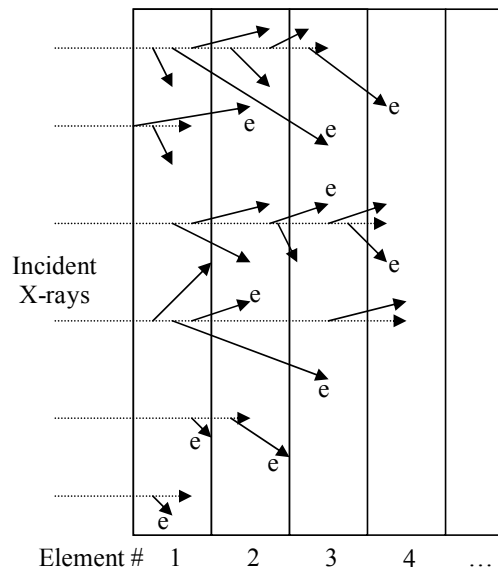


Figure A-1:Schematic shows element 1 not in charged particle equilibrium

The deeper the elements are in the material the smaller the net charged particle energy loss. CPE is achieved at a location that is approximately equal to the range of the most energetic electron. This distance is also called the “equilibrium thickness” as shown in Figure A-2 [2:464].

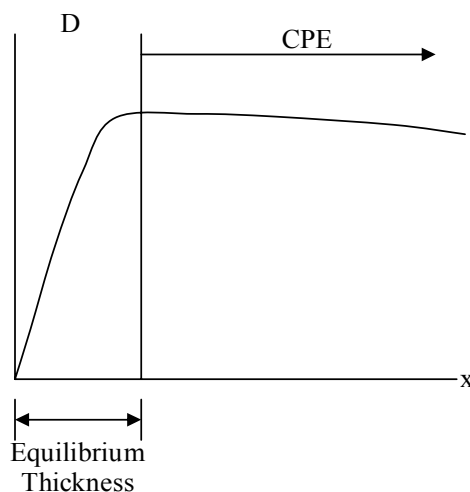


Figure A-2: Absorbed dose through material depth

Figure A-3 compares dose deposition calculations using equation (A-5) to dose deposition including CPE. Notice the dose deviates from the equilibrium case at the two boundaries.

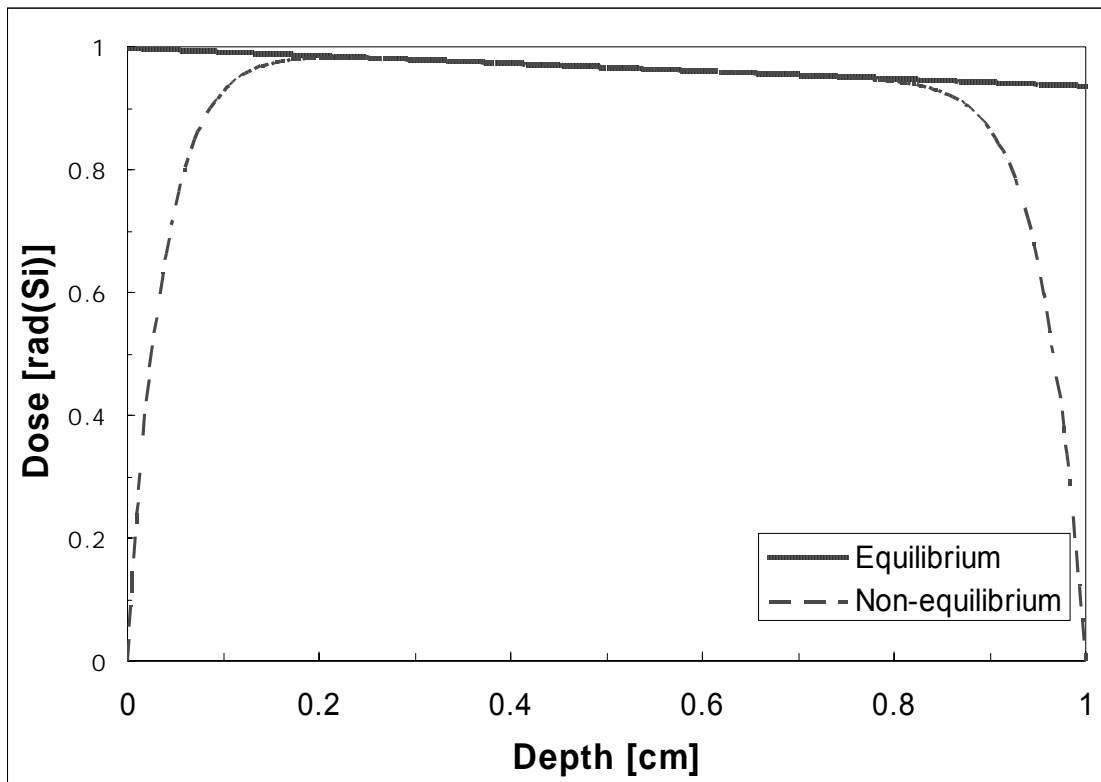


Figure A-3: Plot from PHOTCOEF illustrating equilibrium thickness using 1 cm thick silicon exposed to 1 rad(Si) of 1 MeV photons.

Dose Enhancement

Referring back to Figure A-3, the front and back surfaces of the silicon form an interface of two dissimilar materials - silicon against vacuum. This means that charged particles are leaving the silicon and entering the vacuum. If a different material replaced vacuum at the back interface, the electrons exiting the silicon would be deposited in that adjacent material or would scatter back into the silicon. In both cases this raises the

absorbed dose in those materials as compared to that calculated by the equilibrium equation. Figure A-4 illustrates this behavior at 0.03 cm.

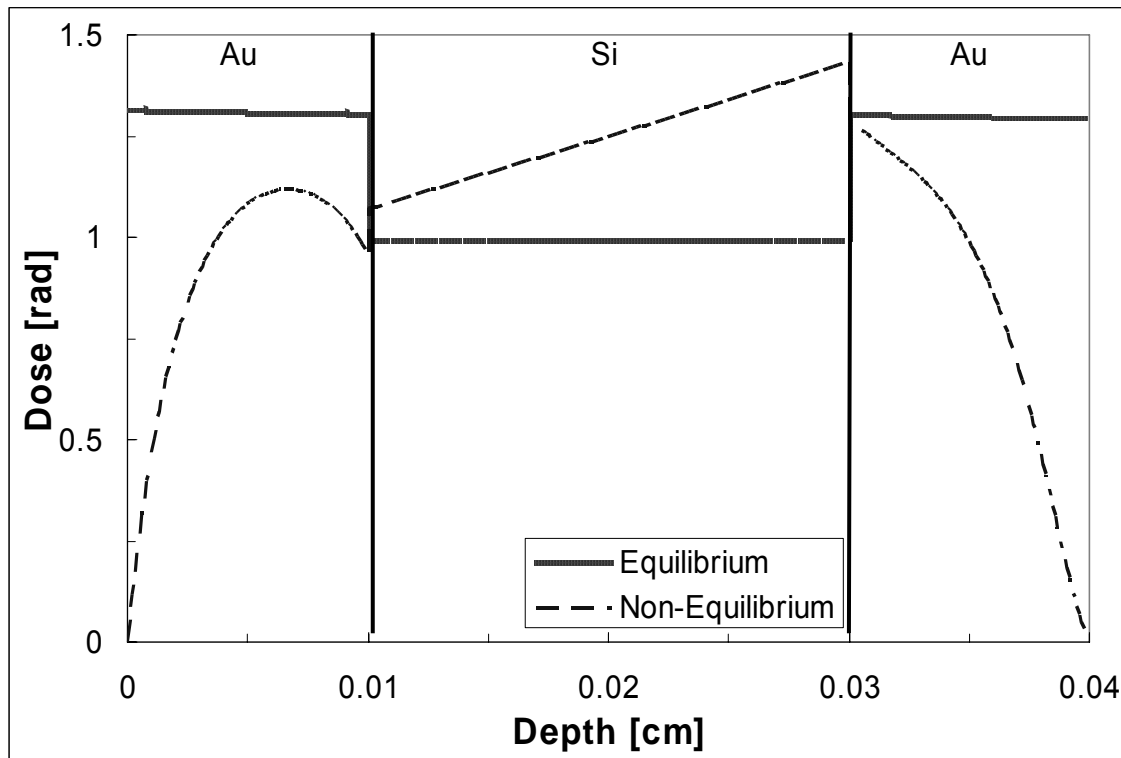


Figure A-4: Plot from PHOTCOEF comparing dose deposition calculations for the ideal, equilibrium assumption, and taking into account non-equilibrium of charged particles. Illustrates dose enhancement in the Au-Si-Au structure.

This is referred to as interface dose enhancement. The ratio of the dose calculation including the non-equilibrium charge transport to the equilibrium dose is the dose enhancement factor, and it is a function of photon energy, incident photon direction, and distance from the interface.

For example, a LEXR source with a nominal energy of 10 keV is incident on a Si/Au interface. It has a dose enhancement factor in the silicon of approximately three

and is independent of photon direction. The same structure exposed to a Co-60 has a dose enhancement factor of 1.64 when the photons pass through the silicon first. It takes approximately one micron to reestablish charged particle equilibrium.

A.2. Modeling Radiation Effects in Insulators

Radiation affects insulators when an incident electron, ion, or quanta deposits enough energy to generate an electron-hole pair. The fate of the electron and hole lies in one of a few options. First, the pair can immediately recombine; when no bias is present, recombination dominates. If the original electron-hole pair does not recombine, they can recombine with other holes and electrons. Second, the charge can become trapped. When a bias is present, charge trapping is possible. Radiation induced trapped charge affects operating characteristics exactly the same way any other trapped charge does – it is seen as a shift of an actuation voltage or flat band voltage. Lastly, the charge can enter the circuit forming a spurious current.

Determining how much charge may be trapped requires knowing how many electron-hole pairs are created per unit of radiation, the likelihood charges will or will not recombine, and the probability that a mobile charge will be trapped. To describe this process, a general model for insulator irradiation is developed. Then, the specifics of silicon nitride irradiation are discussed.

The charge trapping process is described assuming the insulator is biased negatively. Since trap site densities are generally much higher at the interfaces (compared to the bulk), it is assumed all trap sites are located near the two insulator interfaces. For simplicity, the insulator has been evenly divided into 5 cells as shown in

Figure A-5. The shaded regions indicate the location of electron and hole traps. The figure depicts an incident gamma ray creating an electron-hole pair.

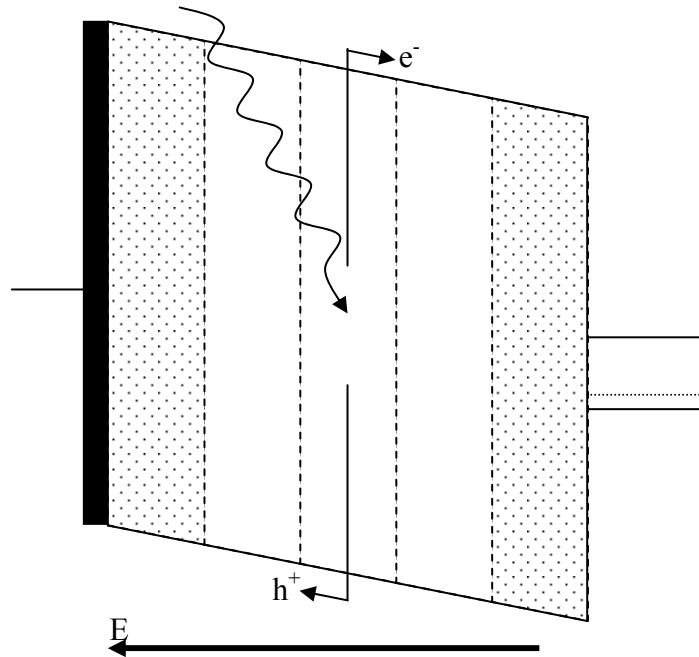


Figure A-5: Schematic diagram of biased insulator

The first step in estimating the amount of radiation induced trapped charge is calculating the number of electron-hole pairs created by radiation. Generally, an empirically derived value specific to the insulator of interest is used. This is referred to as an ionization constant, K_{ins} . K_{ins} is the number of electron-hole pairs generated per unit volume per unit total dose. Multiplying the ionization constant by the width of a particular insulator division and the dose of interest yields the density of electron-hole pairs created in that division during the dose period of interest.

The next step is to determine the fraction of electron-hole pairs surviving recombination. If no bias is applied to the insulator, the electron-hole pairs quickly

recombine with each other yielding no net trapped charge. However, when an electric field is present, the electrons and holes separate from each other. After initial separation, electron-hole recombination is still possible, but with charges born from other electron-hole pairs. The fraction of charge pairs surviving both recombination events is called the fractional charge yield. Fractional charge yield, f_{ins} , is unitless and is a function of electric field. The larger the electric field, the greater the probability that electrons and holes will not recombine. For the bias condition shown in Figure A-5, multiplying the density of electron-hole pairs generated in a cell by the fractional yield gives the density of electrons from that particular cell that will reach one of the two cells that can trap.

This quantity is a fluence and is given by

$$F_{ins,i} = f_{ins} K_{ins} \Delta d_{ins} \Delta D. \quad (A-9)$$

$F_{ins,i}$ is the flux of particles that reach the interface cell and were born in cell i . The next step is determining the fraction of this fluence that becomes trapped in electron (or hole) traps in the interface cell. Trapping rate is a function of the trapping cross-section, $\sigma_{ins,e(h)}$, and the number of trap sites available as shown in the following equation

$$\frac{dn_{e(h)}(t)}{dt} = \sigma_{ins,e(h)} [N_{e(h)} - n_{e(h)}(t)] \sum_i F_{ins,i}. \quad (A-10)$$

where

$N_{e(h)}$ is the total density of electron (hole) trap sites, $n_{e(h)}$ is the density of trapped electrons (holes), and $\sigma_{ins,e(h)}$ is the electron (hole) capture cross-section.

Subtracting $n_{e(h)}$ from $N_{e(h)}$ gives the total number of trap sites available. Therefore, as $n_{e(h)}$ approaches $N_{e(h)}$ the available trap site density approaches zero. The fluences originating in all cells, i , have been considered.

An additional source of charge is needed to complete this description. For the biasing case shown in Figure A-5, holes are attracted to the gate metal and electrons towards the semiconductor. If the electrons or holes pass through the division at their respective interface without being trapped, they will enter the semiconductor or the electrode. The holes will create a spurious current. As electrons enter the silicon, they will cause impact ionization. Impact ionization also creates electron-hole pairs that can recombine or transport. In this case, the holes created may transport back into the insulator. This fluence of holes (or electrons) can be estimated by multiplying the fluence entering the interface cell by a quantum yield, γ , that is empirically derived. This process is repeated for each dose step, and is summarized in Figure A-6.

A.3 Radiation Effects on Silicon Nitride

Applying this process to a MOS device is straight forward. Most of the parameters needed are well known from the large amount of research that has been performed to characterize silicon dioxide. Applying this process to silicon nitride is more difficult. These parameters are not as well known. Takahashi, *et al* investigated MOS devices and metal-nitride-oxide-semiconductor (MNOS) capacitors [6]. They compared MNOS devices to well characterized MOS devices (i.e. an MNOS capacitor with a nitride thickness of zero) and gained information on the silicon nitride parameters not well known. Table A-1 summarizes silicon dioxide properties

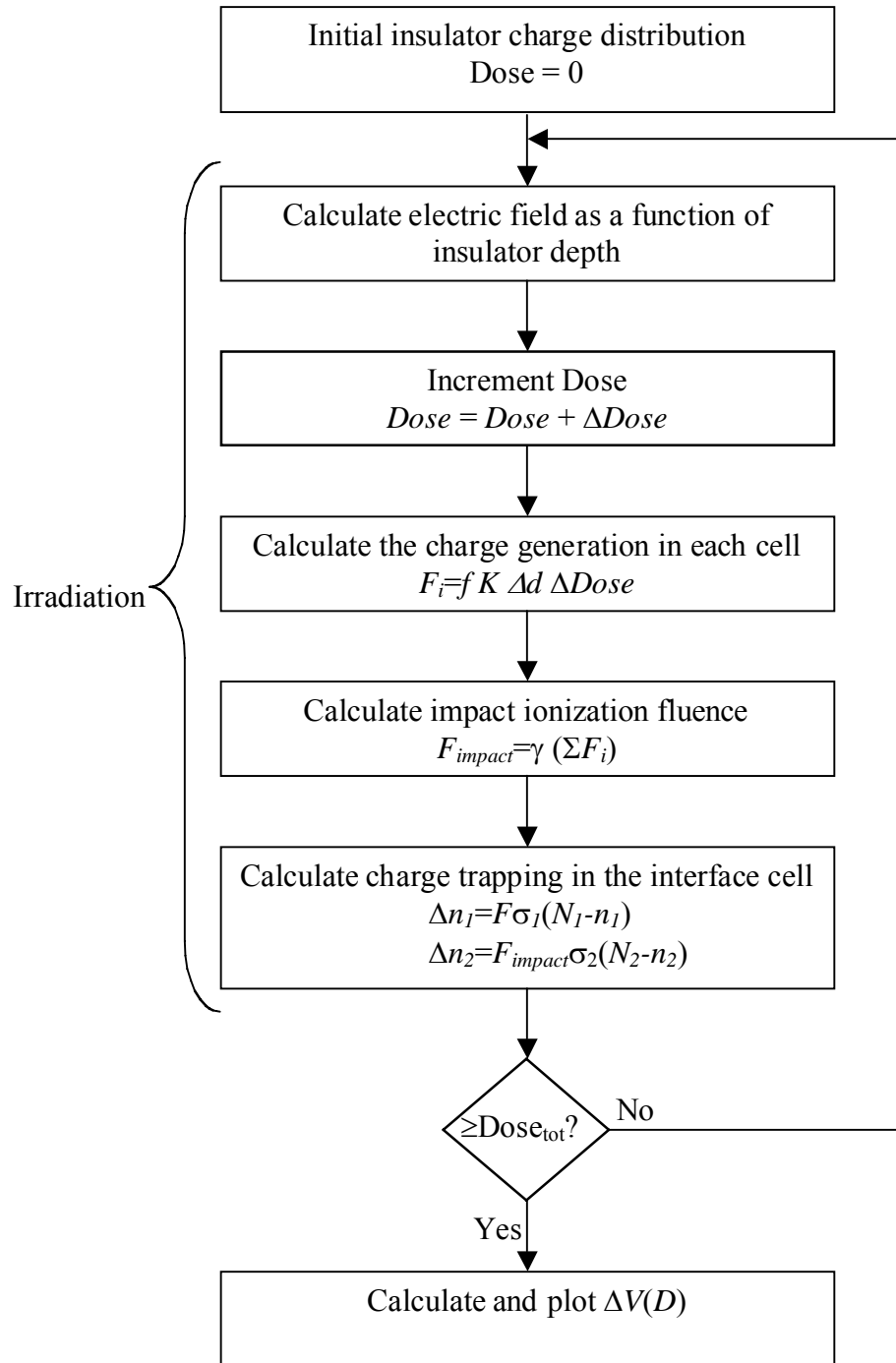


Figure A-6: Irradiation calculation process (based on Figure 9 in [6])

Table A-1: Summary of silicon dioxide parameters [6]

Parameter	Unit	Silicon Dioxide
f_{SiO2}	Unitless	$\left(\frac{0.27}{E_{ox} + 0.084} + 1 \right)^{-1}$
K_{SiO2}	C/cm ³ /rad(SiO ₂)	1.30x10 ⁻⁶
$\sigma_{h, SiO2}$	cm ²	2.0x10 ⁻¹⁴
$\sigma_{e, SiO2}$	cm ²	~0.0

Through experiment and curve fitting, the authors determined values for silicon nitride parameters. Since little is known about the radiation response of silicon nitride, it is difficult to decouple f_{SiN} and K_{SiN} . So, the product of the two were kept together and a factor, α , was used to relate silicon nitride to silicon dioxide.

$$\alpha \equiv \frac{K_{SiN} f_{SiN}}{K_{SiO2} f_{SiO2}} \quad (A-11)$$

Through data fitting, the authors found that $\alpha \approx 0.02 - 0.05$. Also through fitting, they found that the electron and hole cross-sections were 1.5×10^{-16} cm² and 1.5×10^{-14} cm² at an applied electric field of 1 MV/cm. These values are summarized in Table A-2.

The authors found that the MOS test results were best fit when the quantum-yield for the impact ionization term, γ , was 0.25. The last parameter is trap density. Takahashi, *et al.* found that the oxide hole trap concentration, N_{ho} , is 5.0×10^{18} cm⁻³, nitride hole trap concentration, N_{hn} , is 1.2×10^{20} cm⁻³ and the nitride electron trap concentration, N_{en} , is 2.0×10^{19} cm⁻³.

Table A-2: Summary of silicon dioxide parameters [6]

Parameter	Unit	Silicon Dioxide
α	unitless	0.02-0.05
$\sigma_{h, SiN}$	cm^2	1.5×10^{-16}
$\sigma_{e, SiN}$	cm^2	1.5×10^{-14}
N_{hn}	cm^{-3}	1.2×10^{20}
N_{en}	cm^{-3}	2.0×10^{19}
γ	unitless	0.25

The experimentally derived values in the table above allow the radiation response of MNS capacitors to be modeled. The capability to model radiation effects was integrated into the MNS charging model discussed in Chapter 6. The non-irradiation calculations that follow are based on those calculations.

Figure A-7 compares three dose rates to show how irradiation affects charging. The 0 rad(SiO_2)/sec curve was shown earlier in Chapter 3. The 50 rad(SiO_2)/sec curve flattens out to reach a steady state charging level. At the highest dose rate, the curve reaches a maximum shift and actually begins to decrease in magnitude.

An explanation for these results lies in the three processes that occur simultaneously in these calculations. First, holes tunnel from the silicon into the insulator. This explains the negative shift of the 0 rad(SiO_2)/sec curve. The second process involves radiation-induced electrons from the insulator bulk drifting towards the insulator-silicon interface; some of these become trapped. The third process occurs when electrons not initially trapped in the insulator enter the silicon and cause impact ionization events. Impact ionization makes additional holes available for trapping in the insulator. The significance of the latter two processes not only depends on the flux of electrons entering the trapping region, but also the capture cross-section of each carrier.

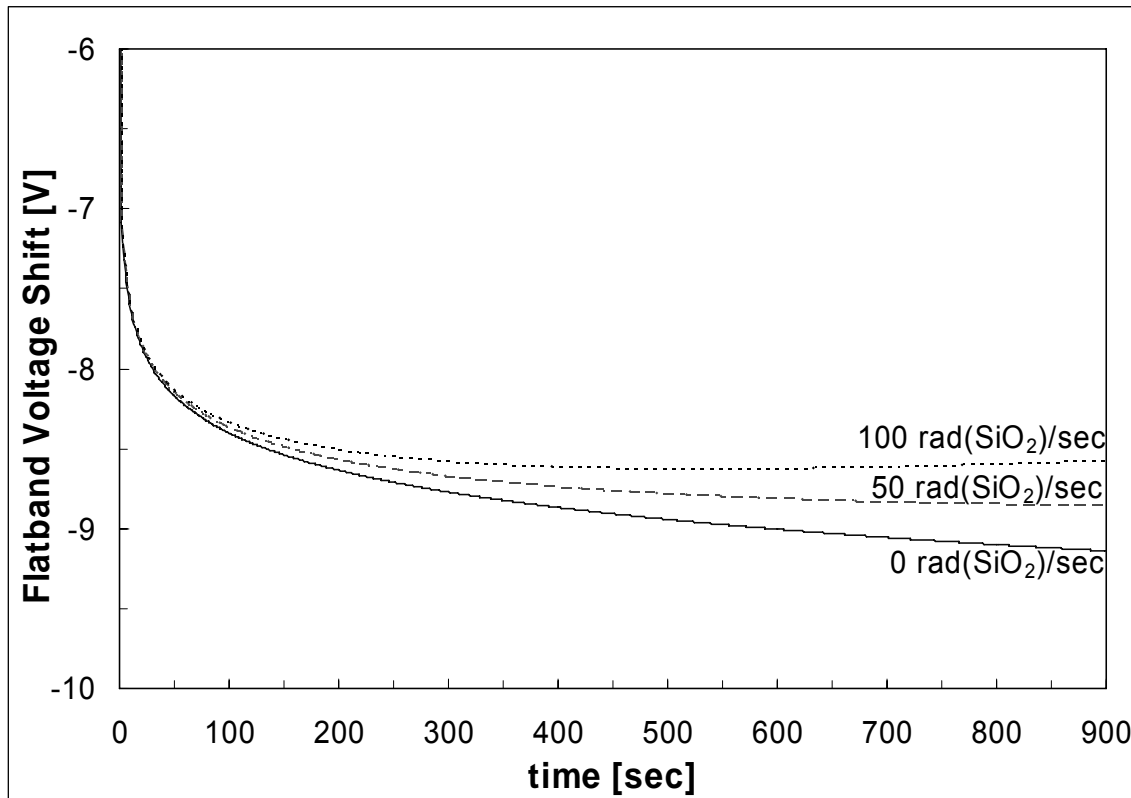


Figure A-7: Charging behavior with -30V applied

In this case, the electron cross-section is approximately two orders of magnitude larger than the hole cross-section. Charge trapping can lead to a softening of the charging curves. At high enough doses, these electrons can meet or even surpass the tunneling rate as illustrated in the next plot.

Figure A-8 shows the same dose rates, but the applied bias is reduced to -10V. Under these conditions, irradiating the capacitor causes the voltage shift curve to reverse polarity. This occurs because the radiation-trapping rate is greater than the tunnel-charging rate.

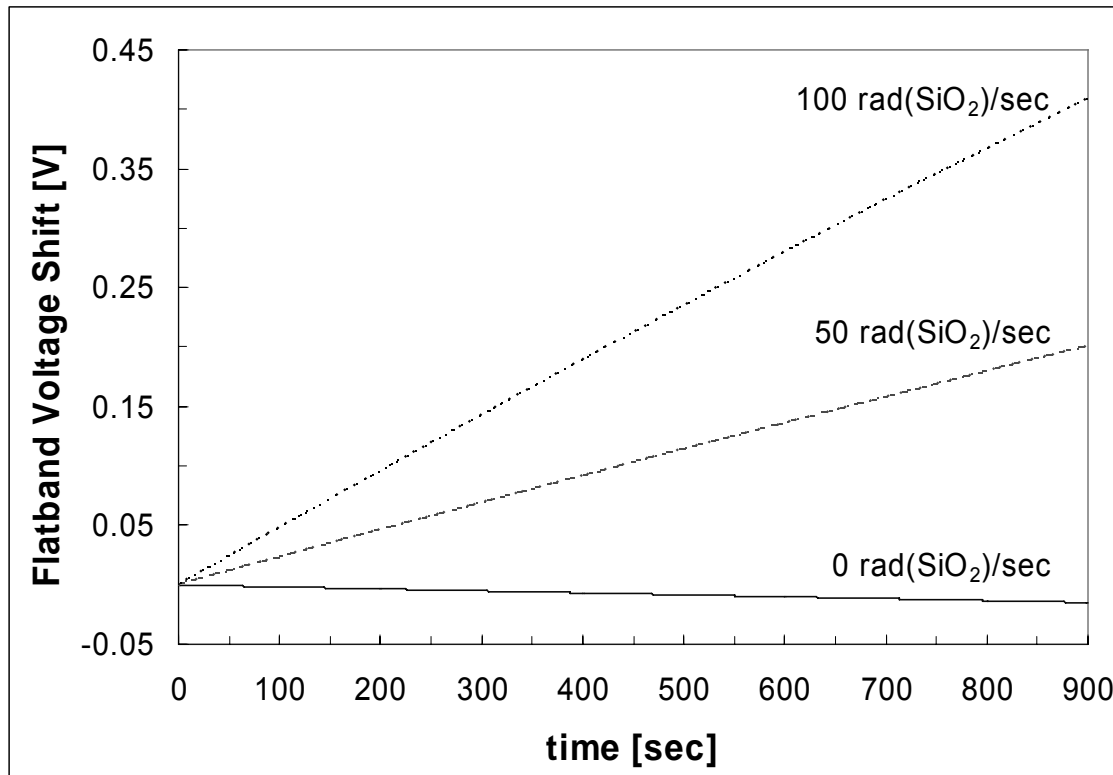


Figure A-8: Charging behavior with -10V applied

Figure A-9 displays the case of a 10V applied bias with the same dose rates.

Notice the results are not a mirror image of the -10V results shown in Figure A-8 - the capacitor charges differently. Electrons are trapped through tunneling and impact ionization events, while hole trapping is not a major factor due to the relatively small hole capture cross-section.

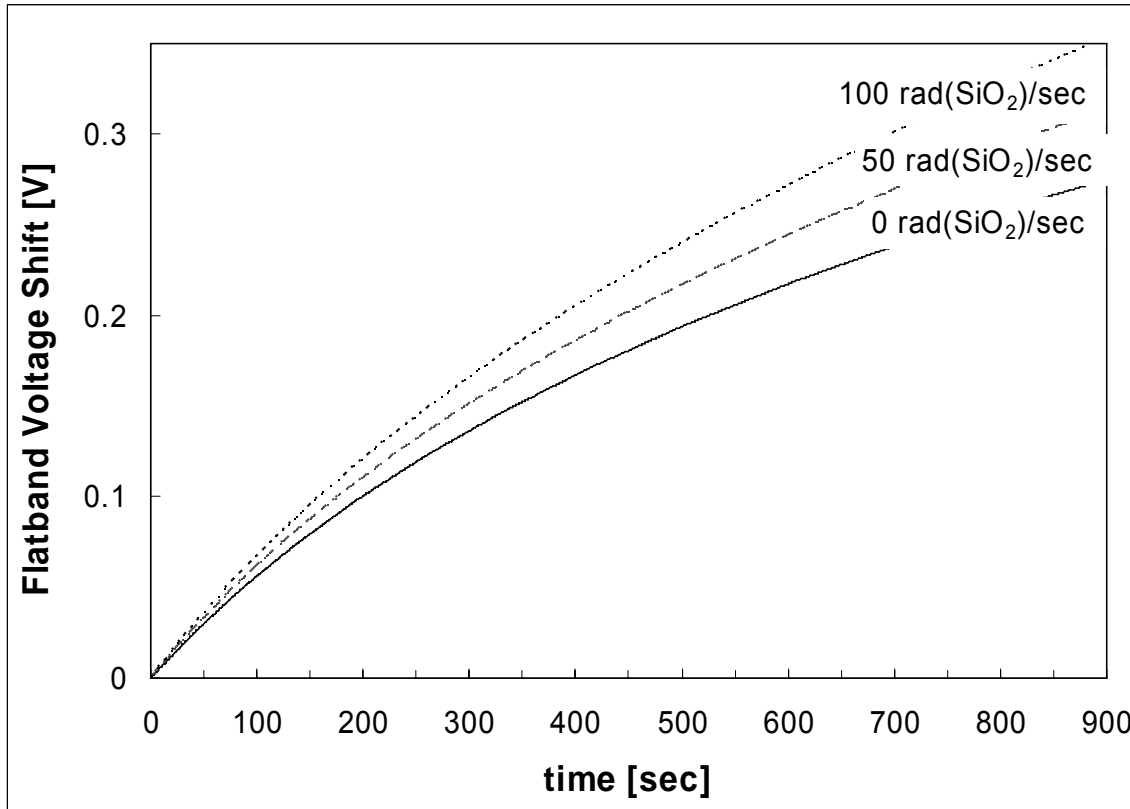


Figure A-9: Charging behavior with 10V applied

However, supplying larger positive biases reduces the impact of radiation charging. When the applied bias is 30V, the tunneling mechanism dominates the other charging processes so irradiation has a negligible effect on capacitor operation.

A.4. Summary of Previous Radiation Experiments

The Jet Propulsion Laboratory and Rockwell Scientific collaborated to perform Co-60 gamma testing on Rockwell's novel RF MEMS switch [7]. The switch design is considerably different than the AFRL switch design. Figure A-10 shows a cross-section. This design uses gold transmission lines (t-line) and drive capacitor plates. The insulating material was not given for proprietary reasons. It is a contact switch, but has

an insulating layer between the two drive electrodes. During normal operation the dielectric never comes in contact with the lower drive electrode. Therefore, a metal-dielectric-metal capacitor is never formed keeping the electric field across the insulator low. This makes the switch design less susceptible to charging than the switch tested in this research, but this design is also more complicated to build and takes up more area on a wafer.

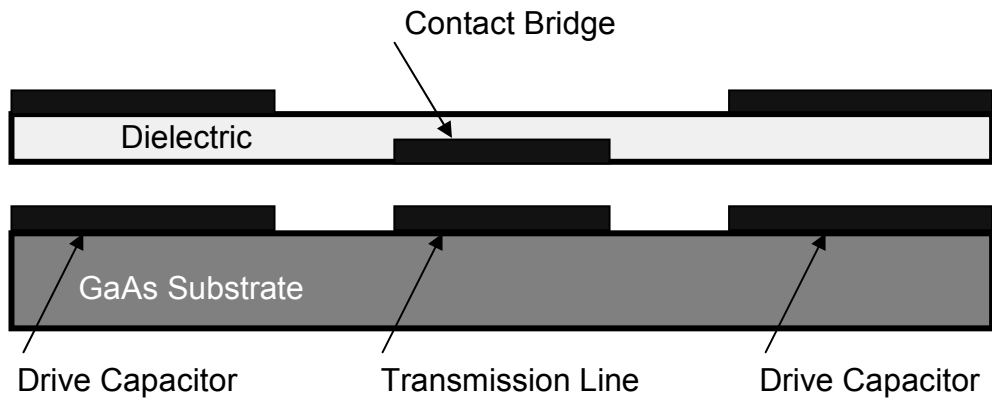


Figure A-10: Rockwell's novel RF MEMS switch design [7]

The switch operates by applying a bias between the top and bottom plates of the two drive capacitors. When the bias is large enough, typically 60V, the bridge deflects causing the contact bridge to come in contact with the t-line. When the bias is removed, the bridge returns to its initial position. At the switch, there is a break in continuity of the t-line. When the contact bridge is pulled down, it comes in contact with both segments of the t-line connecting the two t-line segments. This allows an RF signal to pass through the switch.

During irradiation, they biased the switch statically with $\pm 90V$. When the switch was positively biased, a positive shift in actuation voltage was observed indicating negative trapped charge. When the switch was biased statically with $-90V$, a negative voltage shift was observed and indicated positive trapped charge. The rate the dielectric charges positively and negatively was not the same. The positive charging rate was twice as fast as the negative charging rate.

The authors point out that if charging were only due to charge motion, i.e. mobile electron-hole pairs separating due to an applied field, the results would be the opposite. A different mechanism must dominate. The authors suggest that secondary electrons are responsible for charging. In the negative bias case, electrons are created near the insulator surface so they are able to leave the insulator. They are attracted to the positive, lower electrode leaving behind a positive charge at the insulator surface. For the positive bias case, it is suggested that secondary electrons are created in the lower device structures (gold drive capacitor plates or the GaAs substrate), and are attracted to the insulator surface. Another possibility for negative charge is secondary electrons created in the insulator that leave and return back to the insulator surface. The authors warn that this is speculation without independent verification.

Bibliography

1. Braunig, D. "The Space Radiation Environment," in *Instabilities in Silicon Devices*, Vol 3. Ed. G. Barbottin and A. Vapaille. Amsterdam: Elsevier, 1999.
2. Ma, T.P. and P.V. Dressendorfer. *Ionizing Radiation Effects in MOS Devices and Circuits*. New York: Wiley, 1989.

3. Holmes-Seidel, A. and L. Adams. *Handbook of Radiation Effects*. Oxford: Oxford, 1994.
4. Fahrner, W.R. "An Overview of Radiation-Matter Interactions," in *Instabilities in Silicon Devices*, Vol 3. Ed. G. Barbottin and A. Vapaille. Amsterdam: Elsevier, 1999.
5. Attix, F. Introduction to Radiological Physics and Radiation Dosimetry. New York: Wiley, 1986.
6. Takahashi, Y., K. Ohnishi, Fujimaki, and M. Yoshikawa. "Radiation-Induced Trapped Charge in Metal-Nitride-Oxide-Semiconductor Structure", *IEEE Transactions of Nuclear Science*, 46: 1578-1585 (December 1999).
7. McClure, S.S., L.D. Edmonds, R. Mihailovich, A.H. Johnston, P. Alonso, J. DeNatale, J. Lehman, and C.Yui. "Radiation Effects in Micro-Electromechanical Systems (MEMS): RF Relays," *IEEE Transactions of Nuclear Science*, 49: 3197-3202 (December 2002).

Appendix B: Irradiation Experiment and Results

B.1. MNS

MNS Experiment

As discussed in Chapter 5, tests were performed at AFIT without a radiation source present. Once capacitor charging was characterized, the experimental setup was moved to Ohio State University's (OSU) nuclear research center. The experimental procedure run at AFIT was run again at OSU using their Co-60 gamma irradiator with a dose rate of 162.5 rad(SiO_2)/sec. This allows a comparison of charging between irradiated and non-irradiated silicon nitride.

The predetermined bias times used at AFIT are based on the amount of time required to reach various total dose levels using OSU's cobalt-60 gamma irradiation facility. Total dose levels of 0 krad(SiO_2), 10 krad(SiO_2), 100 krad(SiO_2), and 1000 krad(SiO_2) were used. The times required to reach these total dose values are shown in Table B-1.

Table B-1: Table of Bias/Irradiation Times for MNS Capacitors

Total Dose [krad(SiO_2)]	Total Irradiation Time [hh:mm:ss]
0	00:00:00
10	00:03:42
100	00:36:56
500	03:04:38
1000	06:09:16

When the irradiation experiments occurred, the OSU Co-60 source had an activity of approximately 2600 Ci or 9.62×10^{13} decays per second [Bq]). This activity yields an exposure of approximately 188 kR/hour which corresponds to a dose rate of 162.5 krad(Si)/hr. Figure B-1 depicts a cross sectional view of OSU's facility. The Co-60 source consists of a series of pins surrounding a 10" diameter pipe. The pins sit upright on the bottom of a 15 ft deep pool. The inside of the pipe remains dry.

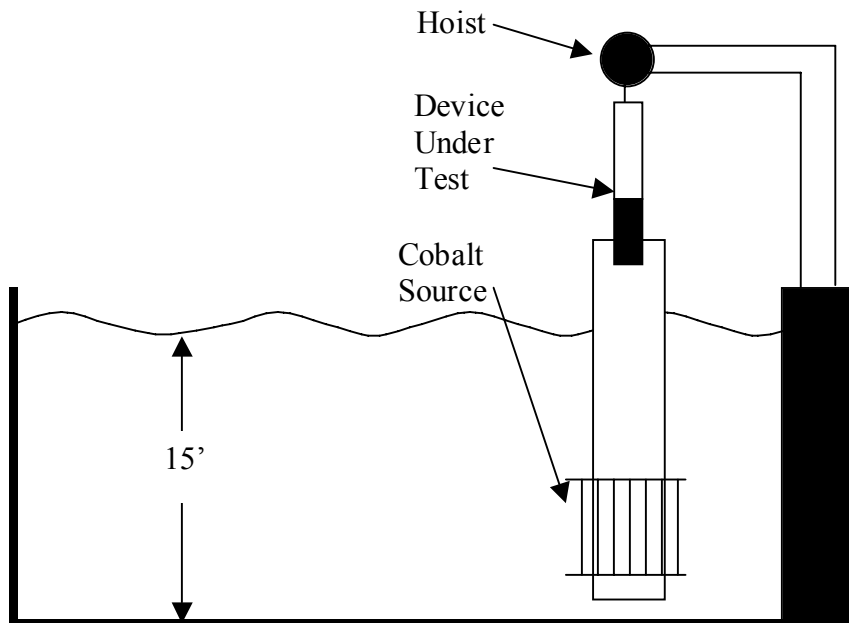


Figure B-1: Ohio State University's Co-60 gamma irradiator [1]

Overall, the experimental procedure required testing capacitors with the same setup shown in Figure 4-4 and Figure 4-5. After completing non-irradiation testing at AFIT, the entire experiment (i.e. same equipment, cables, test fixture, etc.) was moved to Ohio State's irradiation facility for testing at the same bias levels. Therefore, the

experiment required lowering the test fixture box to the bottom of the 10-inch pipe. Figure B-2 shows the test fixture sitting on the elevator positioned at the top of the 10-inch pipe before being lowered into the Co-60 source. Generally, three devices were tested at each bias level, and two biases were tested simultaneously (e.g. +10V and -10V). The same capacitor was never used more than once during this testing.

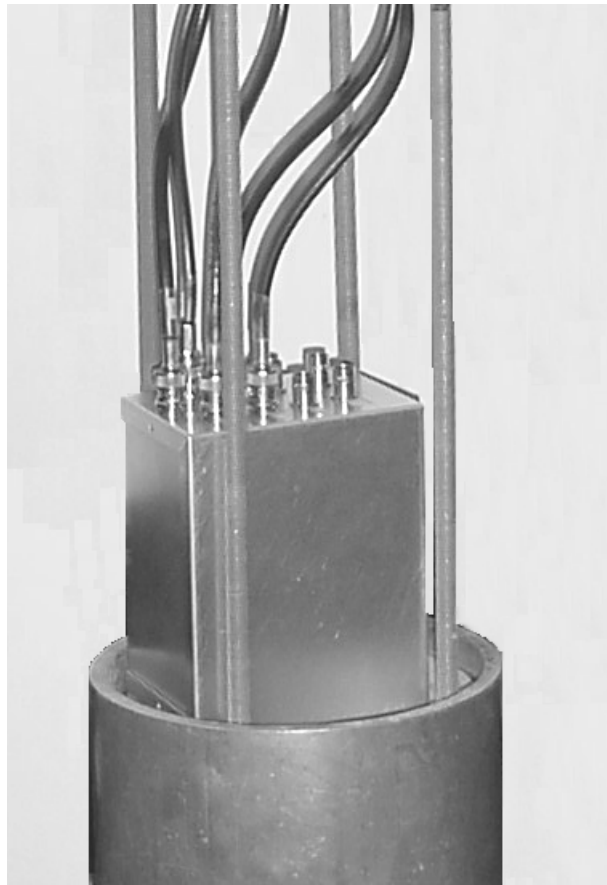


Figure B-2: Aluminum test fixture box at top of Co-60 gamma irradiator

MNS Results

These measurements were made while the capacitors were exposed to ionizing radiation. The data from this section can be compared to the data presented in Chapter 5

– one set with a dose rate of 0 rad(SiO_2)/sec and the other with a dose rate of 162.5 rad(SiO_2)/sec – to determine if radiation has an effect on MNS charging. Figure B-3 shows CV sweeps for an irradiated capacitor biased with +10V. The curve does not change shape appreciably with continued irradiation. Therefore, it is valid to assume the voltage shifts observed over time are due to charge trapping rather than changes in interface state density.

A set of 0V bias sweeps were made in the irradiation facility. This data is used to correct the biasing/irradiation measurements for the charging caused by the CV sweeps. They are not dramatically different from the 0V sweeps shown in section 5.1.

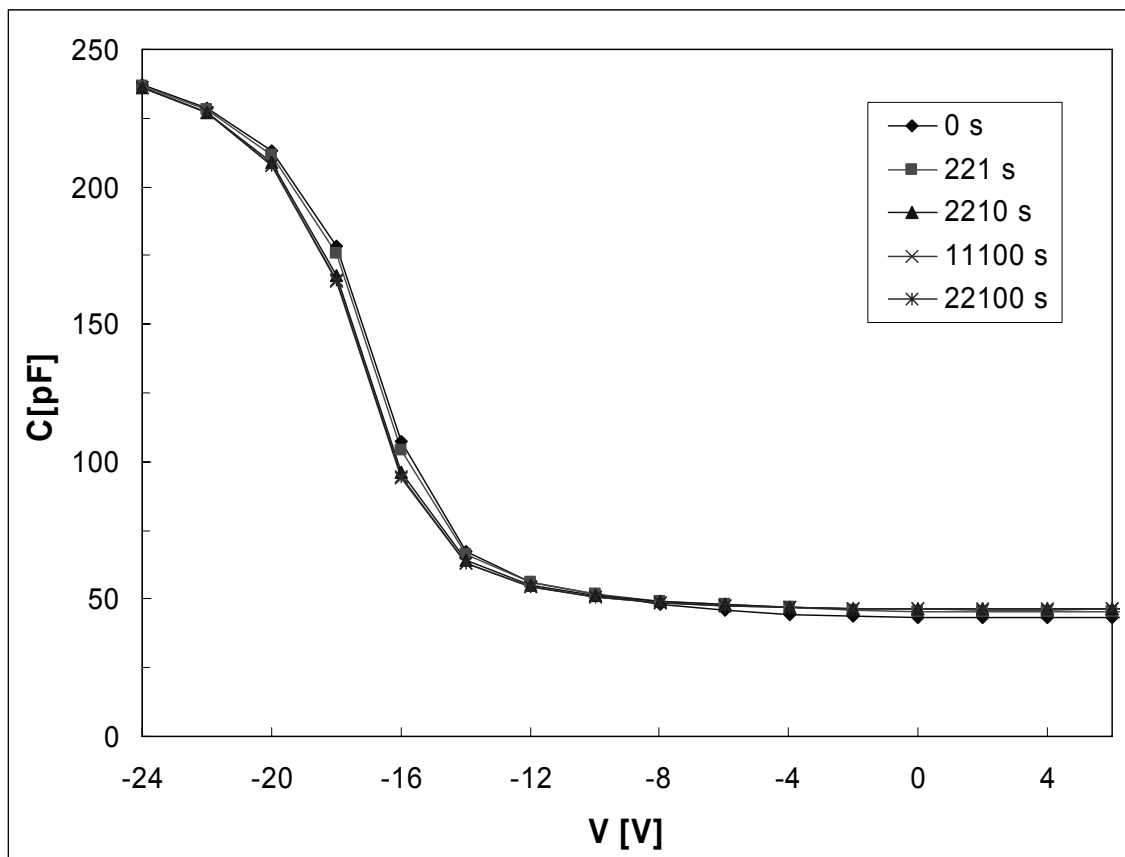


Figure B-3: CV sweeps while capacitor is biased with a +10V and irradiated

The irradiation data shown in Figure B-4 has been plotted as a function of total dose rather than time. 1000 krad(SiO₂) and 22150 sec are equivalent amounts of time for this gamma irradiation facility. The vertical line at 1000 krad(SiO₂) indicates where biasing ended and the capacitors were removed from the source. The remaining data shows charge dissipation with no bias applied or incident radiation present. The use of *krad(SiO₂)* as a unit for tracking dissipation should only be viewed as a unit of time for convenience and is based on a dose rate of 162.5 rad(SiO₂)/sec.

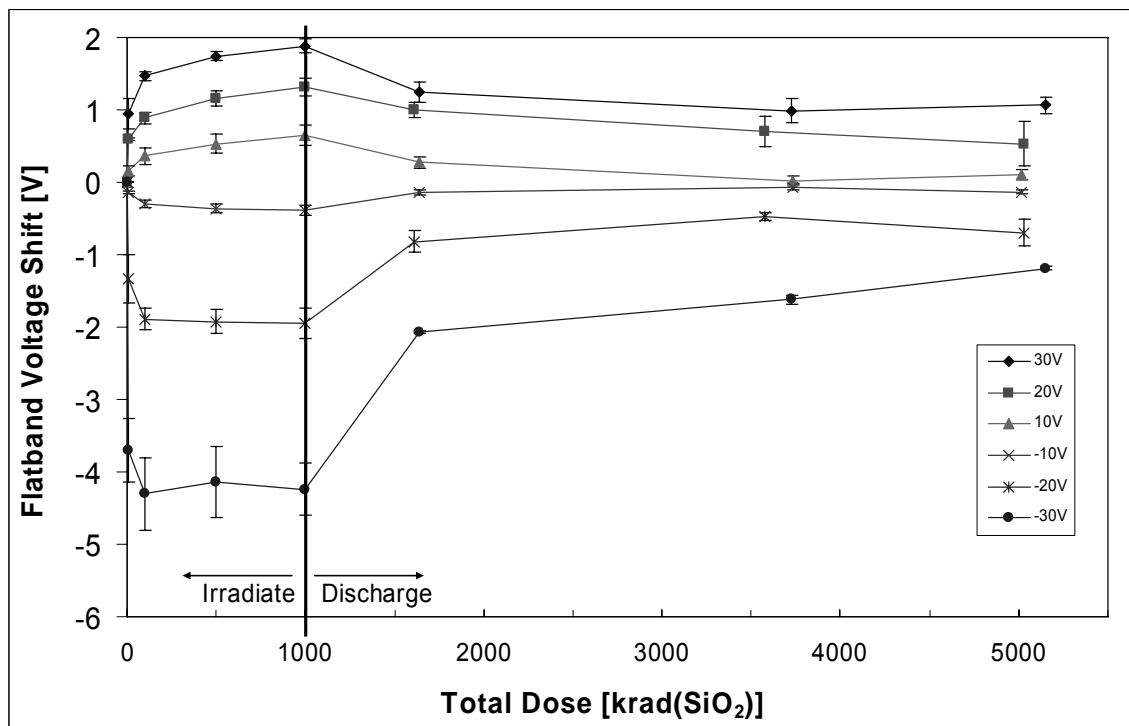


Figure B-4: Summary of biasing data for MNS capacitors. From 0 to 1000 krad(SiO₂) (6 hours, 38 min and 2 seconds) the capacitor is charged. The remainder of plot shows time dependent discharge at room temperature and no bias applied.

Figure B-5 presents only the charging data (≤ 1000 krad(SiO₂)) from Figure B-4. The unirradiated data from Figure 5-4 is also presented on this figure for comparison.

The data is plotted as a function of time rather than total dose. For the positive voltage cases, the unirradiated and irradiated data agree very well, so there is very little if any radiation effect under these conditions.

For the -20 and -30V bias cases, the irradiated curves agree well with the unirradiated curves during the first 100 krad(SiO_2) (or ~ 2215 seconds) then the irradiated curves begin to deviate. The irradiated curve flattens out, while the unirradiated curve steadily increases. For the -20V curve, the difference is never statistically significant, while for the -30V case the difference is numerically significant and the 1000 krad(SiO_2) data points are statistically different than each other. While the differences are mostly not statistically significant, it is noteworthy that the behavior of the -20V and -30V curves is consistent.

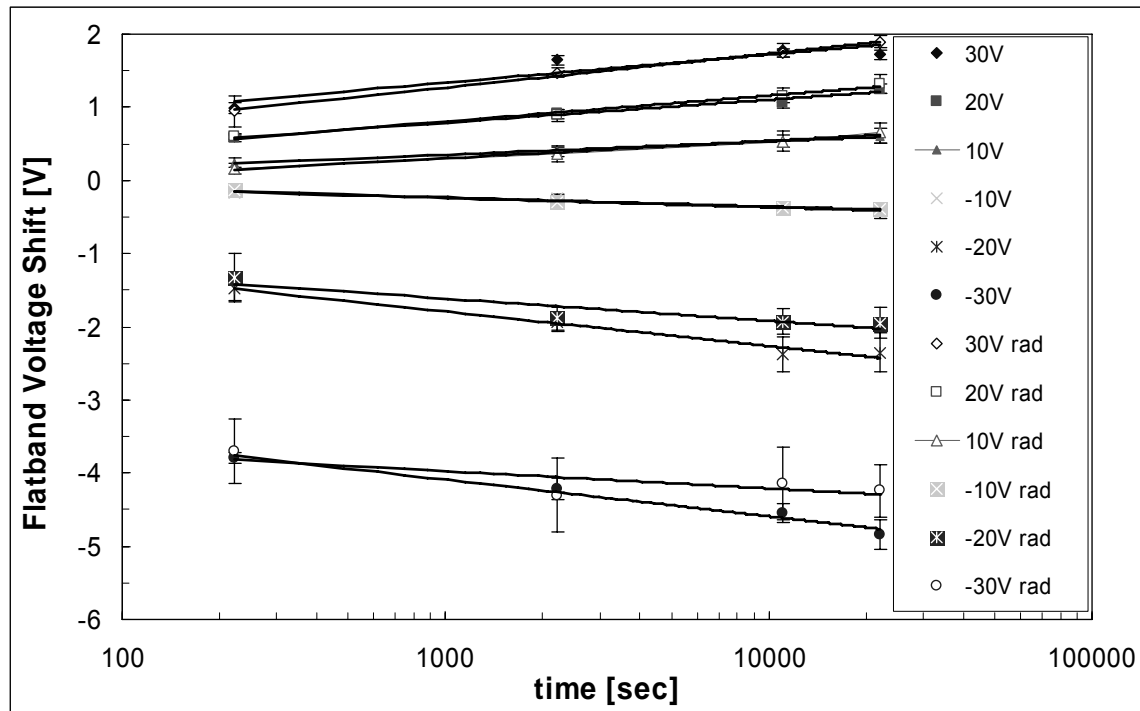


Figure B-5: Comparison of charging data for unirradiated and irradiated capacitors

Least squares estimates are shown in Figure B-2. With a few notable exceptions, there is good agreement between the lines of best fit and the data points. The majority of the R^2 values are well over 0.95 indicating a good estimate. A comparison to Table 5-1 shows there is also good agreement between the non-irradiated and irradiated fits. In the case of the irradiated -20 and -30V curves, the R^2 values are smaller (0.854 and 0.611), and the deviations between the irradiated and non-irradiated equations in these two cases are larger. This may indicate another process (i.e. a radiation effect) begins to dominate.

Table B-2: Equations describing the data in Figure B-5

Bias [V]	Irradiated [V]	R^2 (-)
30	$2.0 \times 10^{-1} \ln(t) + 1.3 \times 10^{-1}$	0.995
20	$1.5 \times 10^{-1} \ln(t) - 2.6 \times 10^{-1}$	0.989
10	$1.0 \times 10^{-1} \ln(t) - 4.2 \times 10^{-1}$	0.987
-10	$-5.4 \times 10^{-2} \ln(t) + 1.4 \times 10^{-1}$	0.973
-20	$-1.3 \times 10^{-1} \ln(t) - 7.0 \times 10^{-1}$	0.845
-30	$-1.0 \times 10^{-1} \ln(t) - 3.2$	0.611

Error bars for the non-irradiated data are small; however, this is not the case for many of the irradiated data points. The large uncertainty in these measurements makes a definitive statement on radiation effects difficult. It is believed the increased error in the irradiated measurements is due to the increased level of complexity in making radiation measurements. Also, the remote nature of the experiment allows more noise in measurement.

Similar to section 6.2, irradiation results for negatively biased capacitors are modeled. The radiation induced charging mechanism was modeled using data provided in Table A-1 and Table A-2. α was chosen as the fit parameter and relates well-known

silicon dioxide material properties to not well-known silicon nitride properties. As shown in Figure B-6, the best fit occurs between 0 and 0.01. For the $-10V$ case, a value for α of 0.0 provides the best fit to the data. This means that there was essentially no radiation effect in this case. When the bias magnitude is increased to $-20V$, the best fit to the data is achieved using an α between 0.005 and 0.01. Finally, at $-30V$, an α of 0.01 provides a very good fit.

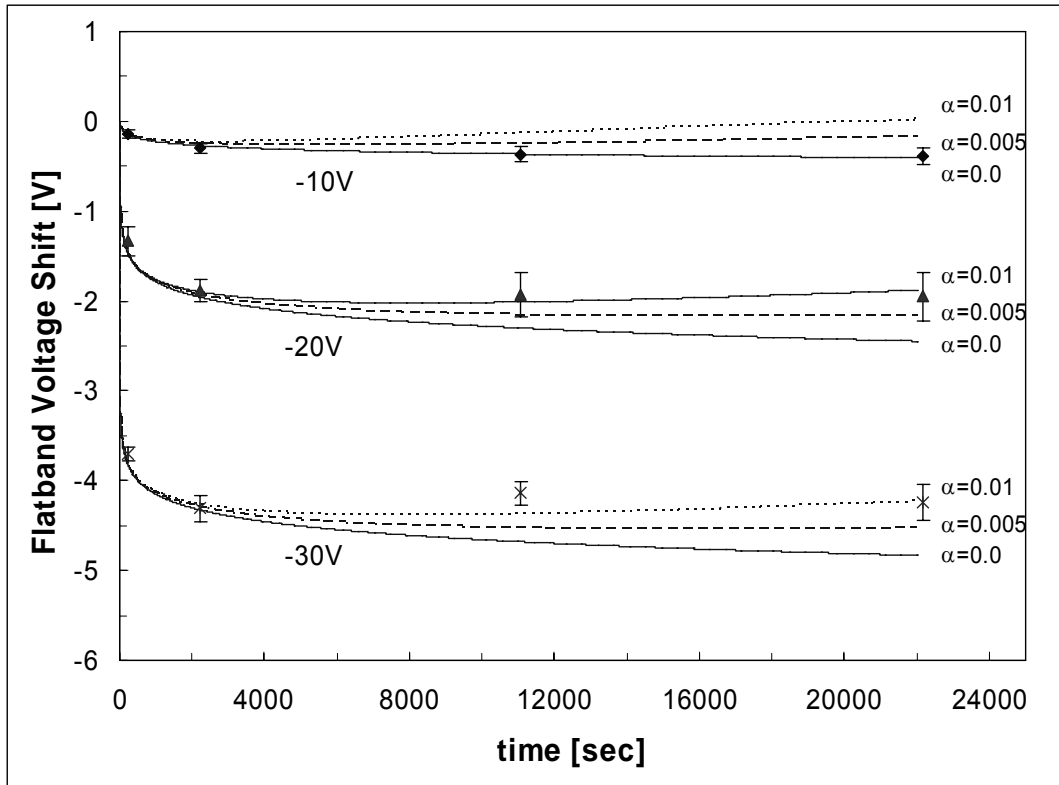


Figure B-6: Irradiated MNS flatband voltage shift results for three applied voltages. Points represent experimental data; lines are modeled results using various α values.

This suggests there is an electric field effect not being taken into account. In Table A-1, a field dependent, fractional charge yield was presented. It is the fraction of

charge created by a unit dose of radiation that survives recombination; it is a function of electric field. The field dependence of this function for silicon dioxide may not apply to silicon nitride directly. Another possibility is field dependence of hole capture cross-sections.

B.2. MEM

MEM Experiment

A low energy x-ray (LEXR) source was used to irradiate the capacitive switches. The LEXR is operated by AFRL's Space Electronics Protection Branch (AFRL/VSSE) at Kirtland AFB, NM. Figure B-7 shows the exterior of the facility. The LEXR facility is a small building built of lead bricks within AFRL/VSSE's high bay laboratory. The x-ray source sits inside of the small building and leaves enough room to set up relatively large experiments. Equipment can be protected from the high dose area by operating them outside of the building and connecting them to the device under test by running cables through envelope slot feed-throughs in the LEXR building's wall.

AFRL/VSSE operates the Philips MG 161 Constant Potential X-ray system with a maximum power output of 3.2 kW. The system produces an x-ray spectrum ranging from 8 to 160 keV [2]. As shown in Figure B-8, the x-ray system consists of a tungsten L line spectroscopic x-ray tube and a number of filters and collimators [3]. The 0.1 cm beryllium layer filters out the low energy component of the spectra. X-rays then pass through a 3.3 cm beam port followed by a 5 cm lead collimator. The end of the collimator is capped with a 2 mil (0.00508 cm) thick aluminum sheet that shields the device under test from the low energy portion of the spectrum caused by spurious fluorescence making dosimetry much more difficult [4]. After passing through the Al,

the x-rays propagate through the nitrogen filled enclosure until reaching the device under test. In this case, the switch was placed 25 cm from the x-ray focal point.



Figure B-7: LEXR facility at AFRL/VS, Kirtland AFB

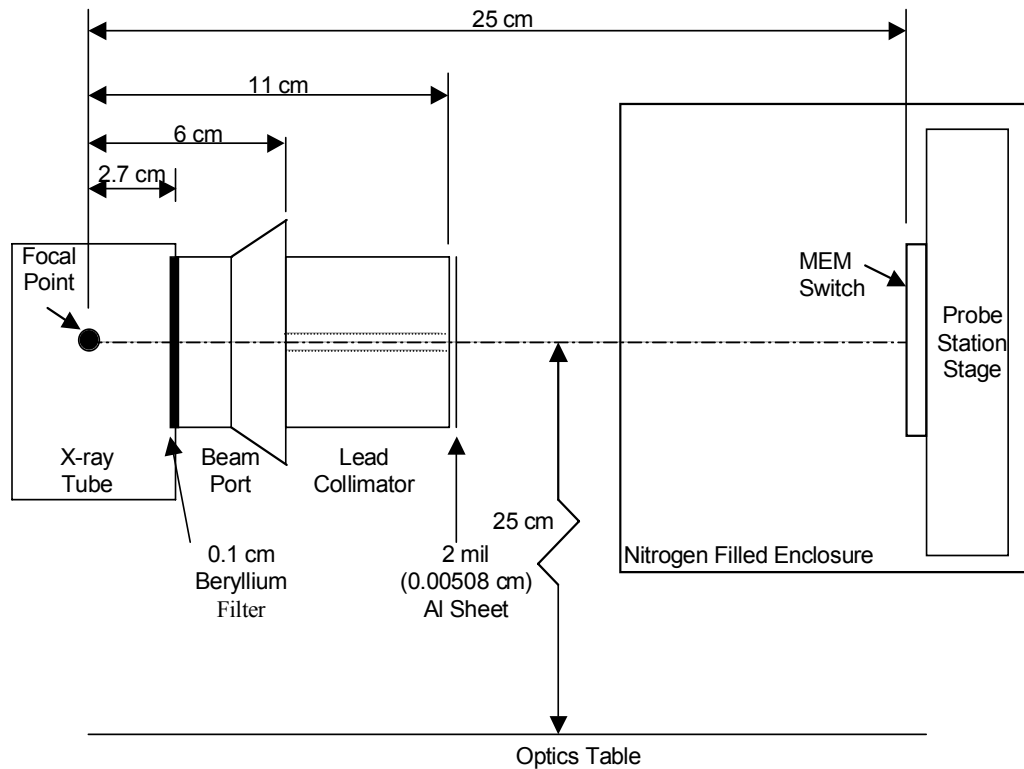


Figure B-8: Experimental setup inside LEXR facility

Dose rate depends on the tube current and the distance from the x-ray focal point to the device. Table B-3 shows the LEXR dose rate determined for a variety of tube currents using a silicon PIN diode for an x-ray voltage source of 100 kV and the diode positioned 25 cm from the focal point.

Table B-3: Tube current-dose rate relationship for the Philips X-ray tube at 100 kV with a 25 cm separation between focal point and Si PIN diode (as of 29 June 2000)

Tube Current [mA]	Dose Rate [rad(Si)/sec]
5.00	145.73
6.00	174.50
10.00	290.70
15.00	435.22
16.00	436.56
20.00	577.29
22.00	632.63
24.00	689.62
26.00	746.79
28.00	802.92
30.00	859.24

The experimental setup in Figure 4-9 must be changed slightly to include the irradiation facility (environmental controls have also been included). Experimental considerations required placing the network analyzer in the LEXR where it would be exposed to irradiation. Therefore, it was shielded using lead bricks. A combination of New Mexico summer heat, lack of air conditioning into the LEXR building and operating the network analyzer for extended periods of time dramatically increased temperatures in the LEXR facility. Therefore, it was necessary to bring cool air into the LEXR building. A 25 ft length of flex duct was used to tap into the laboratory's air conditioning system and divert cooled air into the LEXR facility. A schematic of this setup is shown in Figure B-9.

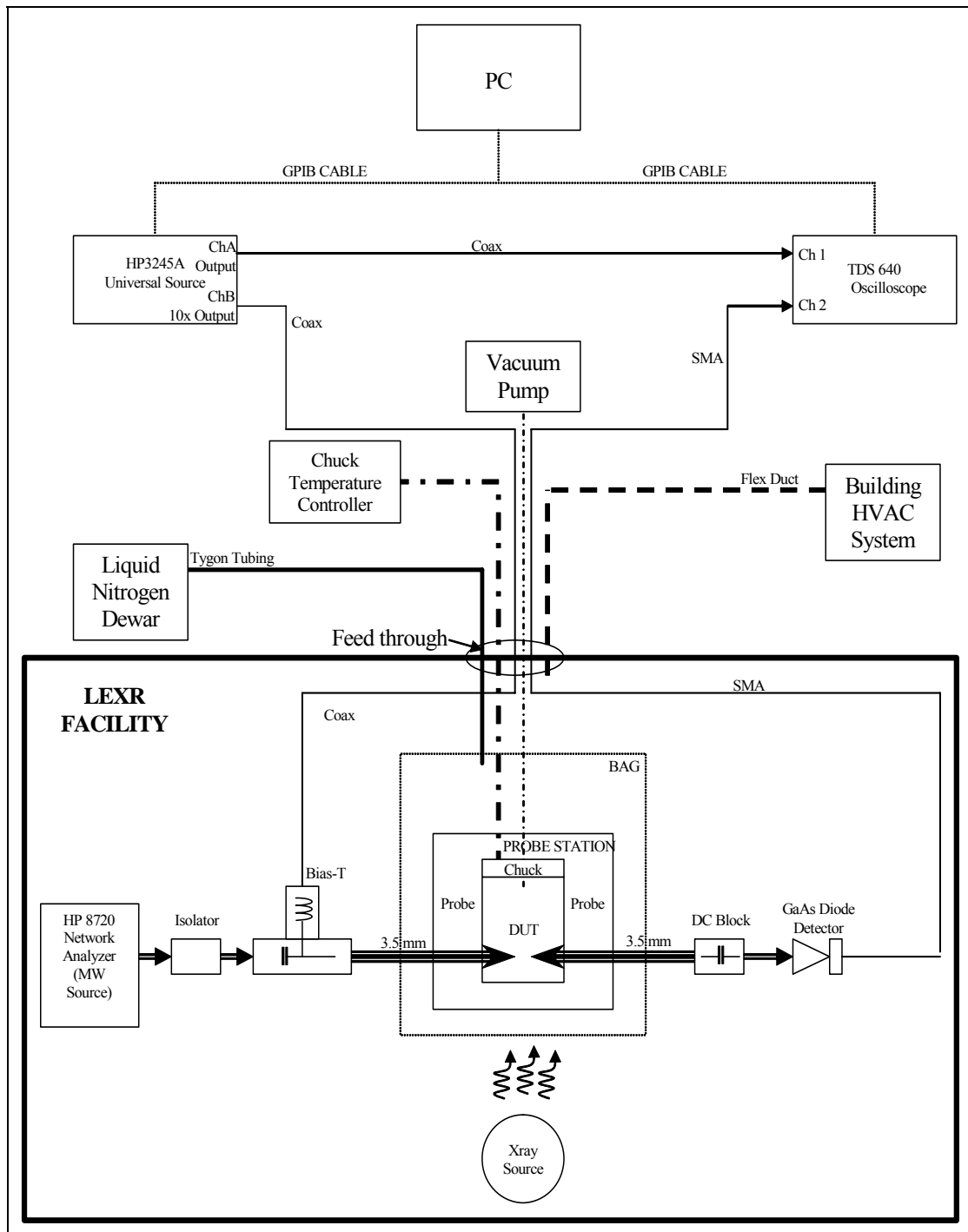


Figure B-9: Experimental setup required to operate and measure capacitive MEM switches

MEM Results

The MEM switches were irradiated using the LEXR source at a dose rate of 859.24 rad(Si)/second. Eight devices were tested in this experiment. These eight devices were of the same design and from the same die. A 48Vpp triangle waveform with +5V and -5V offset voltages was used to operate these switches. Four switches had a $+5V_{off}$ waveform applied - two irradiated, and two were not. A separate set of four switches had a $-5V_{off}$ waveform applied - again, two irradiated, and two were not. Figure B-10 shows the results for pull-in.

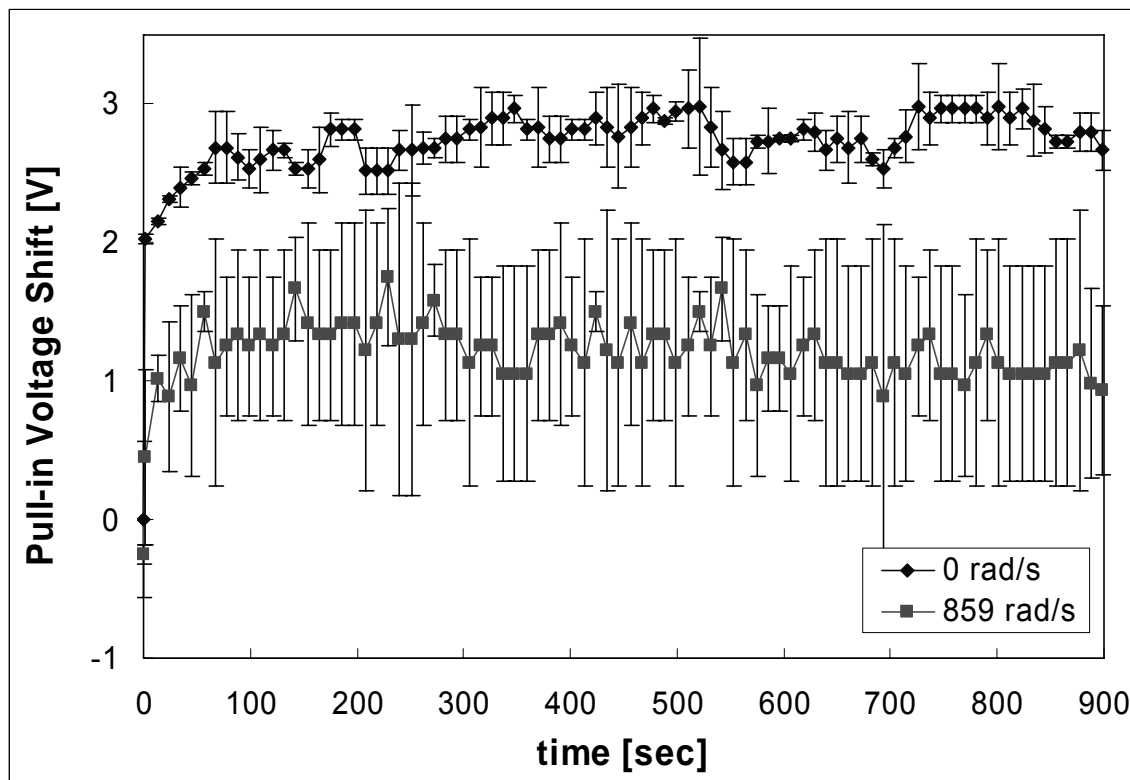


Figure B-10: Change in pull-in voltages for non-irradiated and irradiated switches using the 48Vpp and +5V offset

The non-irradiated curve increases rapidly reaching a 2V shift in the first seconds of operation and eventually reaches a steady state voltage shift of 2.75V. The irradiated curve shifts about 0.5V in the first few seconds and reaches a steady state voltage shift of 1.25V. This is about 1.5V less than the non-irradiated curve. It appears the irradiated curve begins to decrease for remainder of testing.

Figure B-11 shows the release voltage results from the $+5V_{off}$ experiment. Again, there are differences between the irradiated and non-irradiated data. The non-irradiated curve shifts about 1V early in testing and reaches a maximum shift of 1.25V after approximately 200 seconds. The curve then begins a shallow decrease for the remainder of testing, finishing the test with a 1V shift. The irradiated curve reaches a maximum shift of 0.7V in the first 100 sec and declines for the remainder of testing. By the end of testing, the curve approaches the initial offset. For this positive offset case, irradiation appears to dampen the charging mechanism. When the device operated during irradiation, both the charging rate and final charge density are substantially lower than when the switch operates normally.

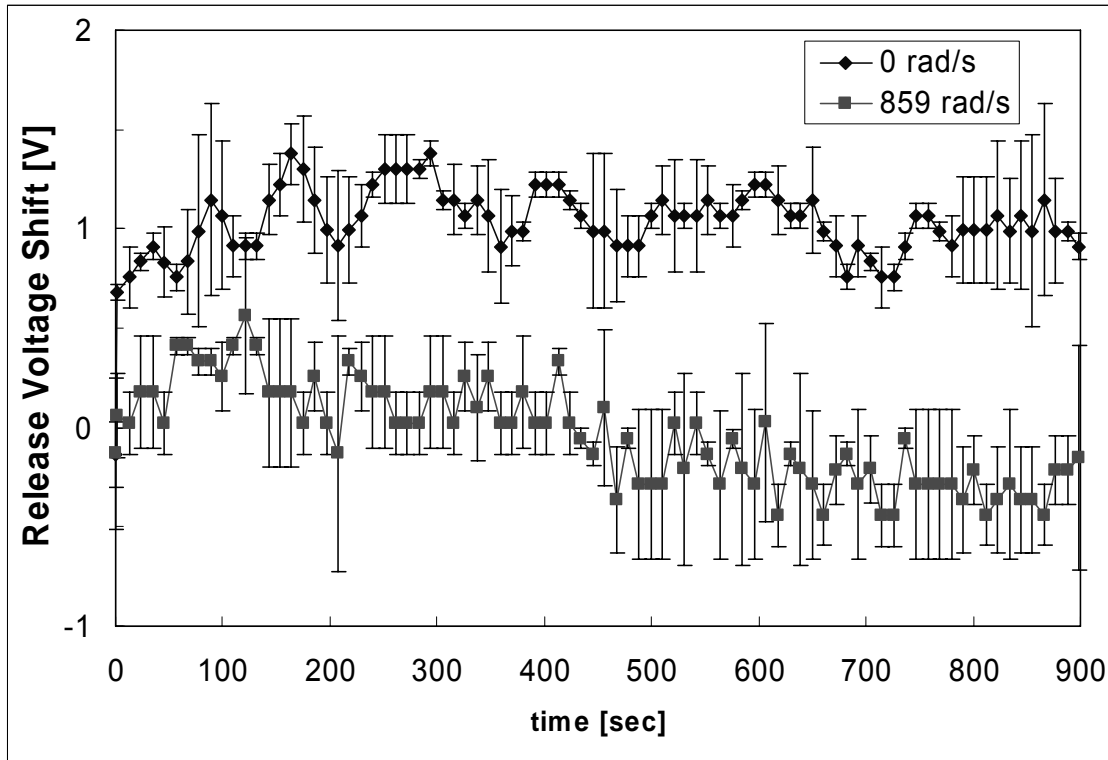


Figure B-11: Change in release voltages for non-irradiated and irradiated switches using the 48Vpp and +5V offset

Figure B-12 displays average pull-in voltage shift curves for irradiated and non-irradiated switches operated with the $-5V_{off}$ waveform. The non-irradiated curve shifts about 1.7V in the first few seconds of testing and maintains this shift for the remainder of testing. The irradiated curve shifts about 1.2V during the first seconds of operation. Following the initial jump, the curve slowly decreases in magnitude for the remainder of testing. By the end of the experiment, the magnitude of the pull-in shift decreases about 0.5V from the initial jump. Although there is a consistent 0.4V difference between the two curves, the irradiated curve falls within the non-irradiated curve's error bars for the

majority of testing. While the effect is consistent for the positive offset case, a high degree of uncertainty still exists in making a statement proclaiming a radiation effect.

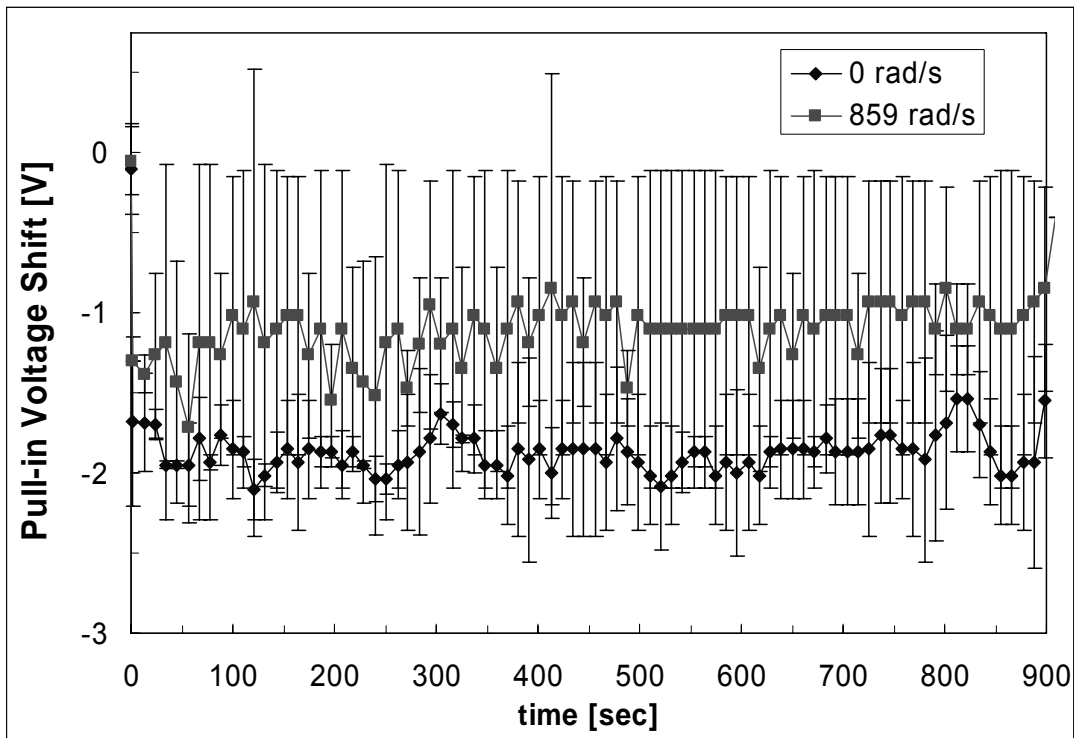


Figure B-12: Change in pull-in voltages for unirradiated and irradiated switches using the 48Vpp and -5V offset

Figure B-13 compares the associated release voltage data that coincides with the pull-in data shown in Figure B-12. The vast majority of data points for the irradiated and non-irradiated curves either fall within the other's error bars, or their error bars overlap. This indicates there is not a strong radiation effect on the release voltage.

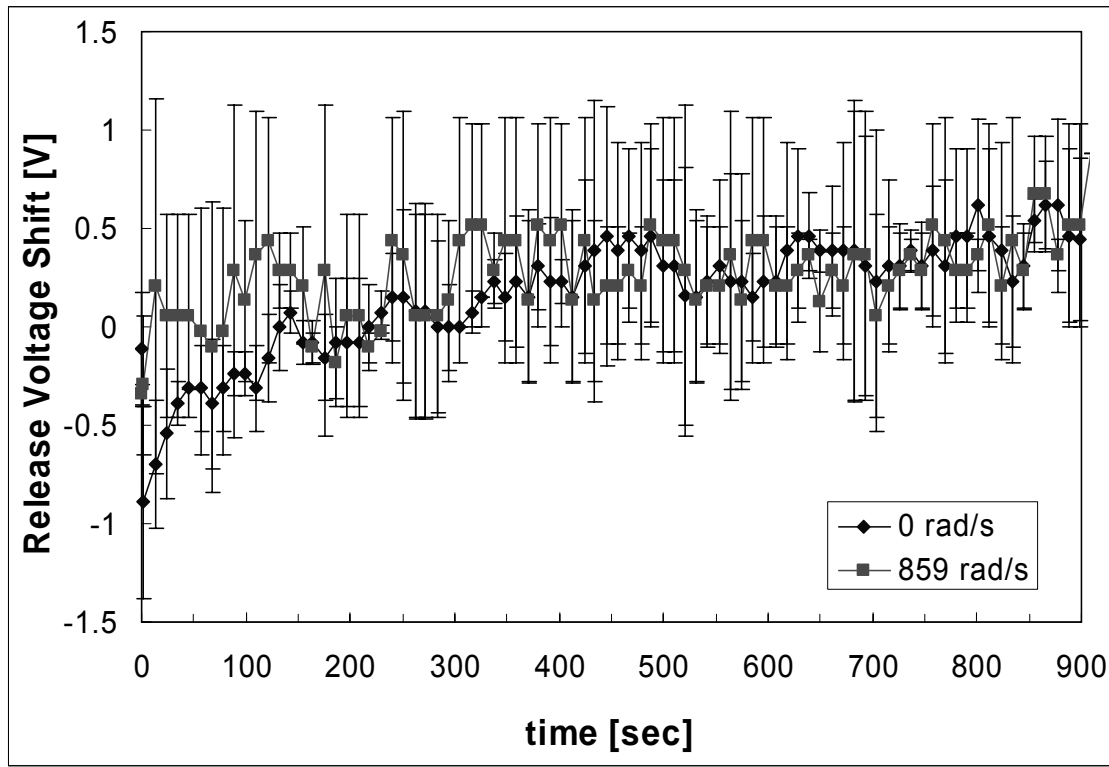


Figure B-13: Change in release voltages for unirradiated and irradiated switches using the 48Vpp and -5V offset

Based on the data and errors shown above, there appears to be a radiation effect when a positive offset voltage is applied; however, the same cannot be said for the negative offset voltage case. The error bars for the negative offset voltage case are much larger than they were for the positive offset case; however, no specific reasons for this difference can be given. These large uncertainties may be covering up a radiation effect. The early stages of a radiation effect appear in the -20V and -30V curves.

Bibliography

1. Ohio State University. "OSU Nuclear Reactor Laboratory Gamma Irradiators." n. pag. <http://www-nrl.eng.ohio-state.edu/facilities/gamma.html>. 8 December 2003.
2. Philips GmbH. *Industrial X-ray MG 161/321: Instructions for Use and Installation*. Manual Number 9499 210 13241, Edition 88 01 02 01, Hamburg, 1988.
3. Ma, T.P. and P.V. Dressendorfer. *Ionizing Radiation Effects in MOS Devices and Circuits*. New York: Wiley, 1989.
4. Palkuti, L.J. and J.J. LePage. "X-ray Wafer Probe for Total Dose Testing," *IEEE Transaction on Nuclear Science*, NS-29: 1832-1837 (December 1982).

REPORT DOCUMENTATION PAGE				Form Approved OMB No. 074-0188	
<p>The public reporting burden for this collection of information is estimated to average 1 hour per response, including the time for reviewing instructions, searching existing data sources, gathering and maintaining the data needed, and completing and reviewing the collection of information. Send comments regarding this burden estimate or any other aspect of the collection of information, including suggestions for reducing this burden to Department of Defense, Washington Headquarters Services, Directorate for Information Operations and Reports (0704-0188), 1215 Jefferson Davis Highway, Suite 1204, Arlington, VA 22202-4302. Respondents should be aware that notwithstanding any other provision of law, no person shall be subject to an penalty for failing to comply with a collection of information if it does not display a currently valid OMB control number.</p> <p>PLEASE DO NOT RETURN YOUR FORM TO THE ABOVE ADDRESS.</p>					
1. REPORT DATE (DD-MM-YYYY) June 2005		2. REPORT TYPE Doctoral Dissertation		3. DATES COVERED (From – To) March 2000 – November 2004	
4. TITLE AND SUBTITLE INSULATOR CHARGING IN RF MEMS CAPACITIVE SWITCHES		5a. CONTRACT NUMBER			
		5b. GRANT NUMBER			
		5c. PROGRAM ELEMENT NUMBER			
6. AUTHOR(S) Kucko, Jay F., Captain, USAF		5d. PROJECT NUMBER 6.1 JON 2305HA01			
		5e. TASK NUMBER			
		5f. WORK UNIT NUMBER			
7. PERFORMING ORGANIZATION NAMES(S) AND ADDRESS(S) Air Force Institute of Technology Graduate School of Engineering and Management (AFIT/EN) 2950 Hobson Way, Building 640 WPAFB OH 45433-8865				8. PERFORMING ORGANIZATION REPORT NUMBER AFIT/DS/ENP/05-02	
9. SPONSORING/MONITORING AGENCY NAME(S) AND ADDRESS(ES) AFRL/SNHA Attn: Dr. J. Robert Reid 80 Scott Dr. Hanscom AFB, MA 01731				10. SPONSOR/MONITOR'S ACRONYM(S)	
				11. SPONSOR/MONITOR'S REPORT NUMBER(S)	
12. DISTRIBUTION/AVAILABILITY STATEMENT APPROVED FOR PUBLIC RELEASE; DISTRIBUTION UNLIMITED.					
13. SUPPLEMENTARY NOTES					
<p>14. ABSTRACT</p> <p>While capacitive radio frequency microelectromechanical (RF MEM) switches are poised to provide a low cost, low power alternative to current RF switch technologies, there are still reliability issues limiting switch lifetime. Previous research identified insulator charging as a primary cause of switch failure. Changes in switch pull-in and release voltages were measured to provide insight into the mechanisms responsible for charging and switch failure. A spatial and temporal dependent model was developed to describe silicon nitride's time-dependent charging as a function of applied bias. This model was verified by applying constant biases to metal-silicon nitride-silicon capacitors and tracking flatband voltage shifts. This knowledge of silicon nitride was then applied to MEM switches. Using novel waveforms and exploiting differences in actuation characteristics allowed the determination of charging characteristics and the investigation of switch failure. Results show tunneling is responsible for changes in the pull-in voltages - this includes a super-saturation effect explained by a steady-state trap charge and discharge condition. A program that models switch actuation was enhanced to include the time-dependent tunneling model. Finally, it was discovered insulator charging cannot explain permanent switch failure; instead, stiction from a contaminant on the insulator surface is likely the cause.</p>					
<p>15. SUBJECT TERMS</p> <p>RF MEMS, Capacitive Switches, Reliability, Dielectric Charging, Radiation Effects</p>					
16. SECURITY CLASSIFICATION OF: U		17. LIMITATION OF ABSTRACT UU	18. NUMBER OF PAGES 231	<p>19a. NAME OF RESPONSIBLE PERSON James C. Petrosky, PhD (ENP)</p> <p>19b. TELEPHONE NUMBER (Include area code) (937) 255-3636, ext 4562 (James.Petrosky@afit.edu)</p>	